R88-01

LARGE-SCALE DISPERSIVE TRANSPORT IN AQUIFERS: FIELD EXPERIMENTS AND REACTIVE TRANSPORT THEORY

by
STEPHEN P. GARABEDIAN
LYNN W. GELHAR
and
MICHAEL A. CELIA

RALPH M. PARSONS LABORATORY
HYDROLOGY AND WATER RESOURCE SYSTEMS

DEPARTMENT
OF
CIVIL
ENGINEERING

SCHOOL
MASSACHUSETTS
Cambridge,

Report Number 315

Prepared with the support of the
U.S. Nuclear Regulatory Commission, No. NRC-04-83-174
National Science Foundation, Grant No. ECE-8311786
U.S. Geological Survey, Grant No. 14-08-0001-A0460

January, 1988

R88-01

LARGE-SCALE DISPERSIVE TRANSPORT IN AQUIFERS: FIELD EXPERIMENTS AND REACTIVE TRANSPORT THEORY

by

STEPHEN P. GARABEDIAN
LYNN W. GELHAR
MICHAEL A. CELIA

RALPH M. PARSONS LABORATORY

HYDROLOGY AND WATER RESOURCES SYSTEMS

Report Number 315

Prepared with the Support of the
U.S. Nuclear Regulatory Commission, No. NRC-04-83-174
National Science Foundation, Grant No. ECE-8311786
The U.S. Geological Survey, Grant No. 14-08-0001-A0460

JANUARY 1988

LARGE-SCALE DISPERSIVE TRANSPORT IN AQUIFERS: FIELD EXPERIMENTS AND REACTIVE TRANSPORT THEORY

by

STEPHEN P. GARABEDIAN
LYNN W. GELHAR
MICHAEL A. CELIA

ABSTRACT

A large-scale natural-gradient tracer test was conducted to examine the transport of reactive and nonreactive tracers in a sand and gravel aquifer on Cape Cod, Massachusetts. The movement and spreading of bromide, a nonreactive tracer, and lithium, a reactive tracer, were monitored over time using a three-dimensional sampling network and analyzed using spatial moments. Calculated total mass of bromide for each sampling date varied between 86 to 105 percent of the total injected mass. The lack of any trend in the calculated mass over time confirms conservative transport of the bromide ion. The horizontal displacement of the bromide center of mass followed a predicted velocity of 0.43 meters per day. During the early part of the test the bromide cloud sank rapidly due to the density difference between the native ground water and the bromide cloud. The bromide cloud moved more slowly downward during the later part of the test due to the accretion of recharge.

A nonlinear trend in the bromide longitudinal variance with travel distance was observed during the first 40 meters of distance traveled, indicating the dispersion process was non-Fickian in the early part of the test. After 40 meters the longitudinal variance followed a linear trend, apparently reaching a Fickian limit. The longitudinal dispersivity, given by one-half the change in variance with travel distance, is about 0.96 meters. Transverse horizontal dispersivity is much smaller, about 1.8 centimeters, and transverse vertical dispersivity is even smaller, about 0.15 centimeters.

The distribution and movement of the reactive solute, lithium, was strongly affected by adsorption to the aquifer sediments. The mass of lithium in solution showed a large decrease during the first

300 days of transport until about 10 percent of the injected mass remained in solution. The velocity of the lithium in solution was initially the same as bromide velocity (0.43 m/d) and then decreased to about 0.05 m/d after 300 days. The distribution coefficient for the lithium adsorption was estimated to be about 2.0 mL/g for the later part of the test. The change in longitudinal variance for lithium showed a strong nonlinear trend, concave upward, which in the later part of the test indicated a dispersivity ten times larger than that for bromide. In contrast, the values of the transverse horizontal and vertical dispersivities did not differ greatly from those for bromide.

A theoretical analysis of reactive solute macrodispersion was developed to explain, in part, the enhanced spreading of reactive solutes relative to nonreactive solutes. The approach used in this analysis was to postulate correlations between hydraulic conductivity and both porosity and the distribution coefficient. Using a spectral analysis method it was found that longitudinal dispersivity can be significantly increased by a negative correlation of hydraulic conductivity to porosity and the distribution coefficient. It was also found that the effective retardation coefficient is the arithmetic mean. Although the theoretical analysis provides an explanation of the enhanced longitudinal mixing for lithium, the enhanced spreading of lithium could also be caused by a kinetically controlled reaction.

Acknowledgements

This research reflects a joint effort of the U.S. Geological Survey and the Massachusetts Institute of Technology. The field experiment was supported through the U.S. Geological Survey's Toxic Waste-Ground-Water Contamination program. At MIT the work was supported in part by the National Science Foundation (Grant ECE-8311786), the Nuclear Regulatory Commission (Contract NRC-04-83-174) and the U.S. Geological Survey (Grant No. 14-08-0001-A0460). The experimental results reported in this thesis are the result of much effort by colleagues at the U.S. Geological Survey, including Denis LeBlanc, Kathryn Hess, Richard Quadri, Warren Wood, and Ken Stollenwerk. Several other people significantly participated in the Cape Cod experiments, including Monique Villars, Karen Wilson, Charles Phillips, Megan Cruise, and Steve Hallem. Several individuals at the U.S. Geological Survey were instrumental in arranging support for this research including Ivan James, New England District Chief, Michael Frimpter, Massachusetts Office Chief, Julio Olimpio, Studies Section Chief, and Steve Ragone, coordinator of the Toxic Waste Program. Thanks also go to Lenny Konikow, the U.S.G.S. graduate studies advisor on this work.

This report is essentially a reproduction of the thesis submitted by the first author in July 1987 in partial fulfillment of the requirements of the degree of Doctor of Philosophy. Lynn W. Gelhar, Professor of Civil Engineering, served as thesis advisor and while he was on sabbatical leave the work was guided by Michael A. Celia, Assistant Professor of Civil Engineering.

TABLE OF CONTENTS

List of Figures

List of Tables

I Introduction

A. Purpose, Objective, and Scope

The purpose of this thesis is to report the results of a large-scale natural-gradient tracer test and a theoretical analysis of reactive solute macrodispersion. The primary objective of the field tracer test was to examine the dispersion process occurring in a sand and gravel aquifer on Cape Cod, Massachusetts, in sufficient detail to answer questions which have arisen about the underlying mechanisms causing dispersion of solutes in aquifers. Therefore, due to the lack of well designed tracer tests for which the magnitude of dispersivity and rate of change of dispersivity can be calculated, the large-scale test was conducted to measure directly the transport of nonreactive and reactive solutes in a sand and gravel aquifer.

The objective of the theoretical analysis of reactive solute macrodispersion was to present a possible explanation of the enhanced spreading observed for reactive solutes in field tracer tests relative to the spreading observed for nonreactive solutes.

The large scale tracer test is part of a larger study of dispersion at the Cape Cod site. In order to answer questions on the relationship between the variability of hydraulic conductivity (K) and the dispersion of solutes, an examination is needed of the relationship between K variability and the dispersion process. This report presents the approach, methods, and results of field tests to examine the dispersion process. Later reports of present (1987) research will present the results of K investigations at the Cape Cod site.

It should also be noted that these dispersion studies are part of a multi-disciplined toxic waste study at this site. Other topics of study include organic and inorganic geochemistry and microbiology.

B. Literature Review

The dispersion of solutes transported in aquifers has been found from field tracer tests (Sudicky and Cherry, 1979) to be quite different than the results of experiments performed in laboratories on columns of porous media. These differences, noted by Anderson (1979), include non-Fickian behavior of the solute spreading when transported in aquifers and much larger apparent dispersivity values (macrodispersivity) when compared to the dispersivity values found in laboratory column tests. This discrepancy can, to some degree, be explained by the scale (volume) over which the samples are taken for the experiment or contamination event (Pickens and Grisak, 1981). For example, if the solute is vertically segregated to a portion of the total aquifer thickness, and samples are taken from fully penetrating wells, then mixing (and dilution) will occur in the well bore during sampling which will indicate more apparent mixing than is actually occurring in the aquifer. However, it has been found from experiments where the solute was sampled using many small intervals (Sudicky and Cherry, 1979; Freyberg, 1986) that there is enhanced mixing occurring in aquifer relative to laboratory column experiments.

It is apparent, both from field experiments and from theoretical studies, that the enhanced mixing in aquifers is caused

by fluid velocity variations. These velocity variations separate packets of the solute, inducing a physical spreading of the solute, and the pore scale dispersion process (that which is measured by laboratory column experiments) results in irreversible mixing between and within the packets moving at different rates. This type of dispersion process is analogous to dispersion in tubes, analyzed by Taylor (1953), where mixing is enhanced due to radial variations in velocity and transverse diffusion of the solute.

The underlying cause of the fluid velocity variations in an aquifer is the heterogeneity of hydraulic conductivity (K) in the aquifer. Typically it has been found that the hydraulic conductivity variations are log normally distributed; Freeze (1975) reports standard deviations (in log base 10 units) that vary from 0.40 to 1.56. Several theoretical studies, including those by Schwartz (1977), Gelhar et al. (l979), Smith and Schwartz (l980), Matheron and deMarsily (l980), Dagan (l982) and Gelhar and Axness (1983), have analyzed the effects of hydraulic conductivity variations on the dispersion of solutes in aquifers using various numerical and analytical methods. All of these studies indicate that the dominant cause of enhanced mixing is hydraulic conductivity variations. These studies also demonstrate that for some situations there is a significant period in which the spreading of solute can not be described using a Fickian assumption. The studies by Gelhar et al. (1979) and Dagan (1982) also show that an eventual asymptotic limit is reached in the value of macrodispersivity.

There are issues of scale which are relevant to a discussion of macrodispersion as analyzed by Gelhar and Axness (1983). The issue

of scale is very important because it defines the context in which the results of Gelhar and Axness (1983) are meaningful. First, an assumption is made that the variations in aquifer properties are of a scale greater than the representative elementary volume (Bear, 1972) that defines the local properties (hydraulic conductivity, porosity, pore-scale dispersion, and chemical properties). A second assumption is that these properties vary continuously and randomly such that a correlation scale can be defined. A third assumption is that the scale of the tracer or contaminant plume is large with respect to the correlation scale of the hydraulic conductivity. This latter assumption is particularly important because ergodicity is assumed in the analytical approach. Therefore a major assumption is that solute transport in an ensemble of aquifers with the assigned statistical properties approximates the real field situation, a single heterogeneous aquifer. This assumption will only be reasonable if flow of the tracer or contaminant plume has occurred over many correlation scales of hydraulic conductivity.

The scale of the problem is also important because an assumption is made that the concentration gradient is "locally" constant, that is the variation of the concentration gradient is small relative to the scale of the hydraulic conductivity variations. This assumption will also be valid only if the size of the problem (i.e. the solute cloud) is large in comparison with the variations in aquifer properties. Therefore the results of the analysis by Gelhar and Axness (1983) can be applied to problems which are large either due to long travel distances (where significant spreading has already occurred) or due to initial conditions for the solute which involve

large volumes and gradual (rather than steep) concentration gradients.

A major review of available literature reporting values of field-scale longitudinal dispersivities (Gelhar et al., 1985) not only demonstrates the scale effect of reported dispersivities, but also the wide range of dispersivity values for the same type of aquifer and scale of study (fig. 1). This information, indicating widely diverging values of dispersivity, is somewhat tempered by a companion illustration, figure 2, showing the relative reliability of the data on the graph. Generally the highly reliable data show dispersivities less than a few meters for travel distances of less than 100 meters. These reliable data do not indicate any asymptotic behavior in dispersivity values, although this may be due to the short travel distances that have been reported. These data point out the need for highly reliable tests which can be used to measure the spreading rate of solutes in aquifers, particularly for travel distances exceeding 100 meters.

There are several reliable tracer test results reported in the literature, and the recently reported (Mackay et al., 1986; Freyberg, 1986; Sudicky, 1986) test, conducted at the Borden Air Force Base in Ontario, Canada, is an excellent example. A solution containing two inorganic tracers (chloride and bromide) and five halogenated organic chemicals (bromoform, carbon tetrachloride, tetrachloroethylene, 1,2-dichlorobenzene, and hexachloroethane) in 12 m^3 was injected as a pulse into a sand aquifer and monitored vertically and horizontally as the tracers moved under natural gradient conditions (Mackay et al., 1986). Tracers were monitored

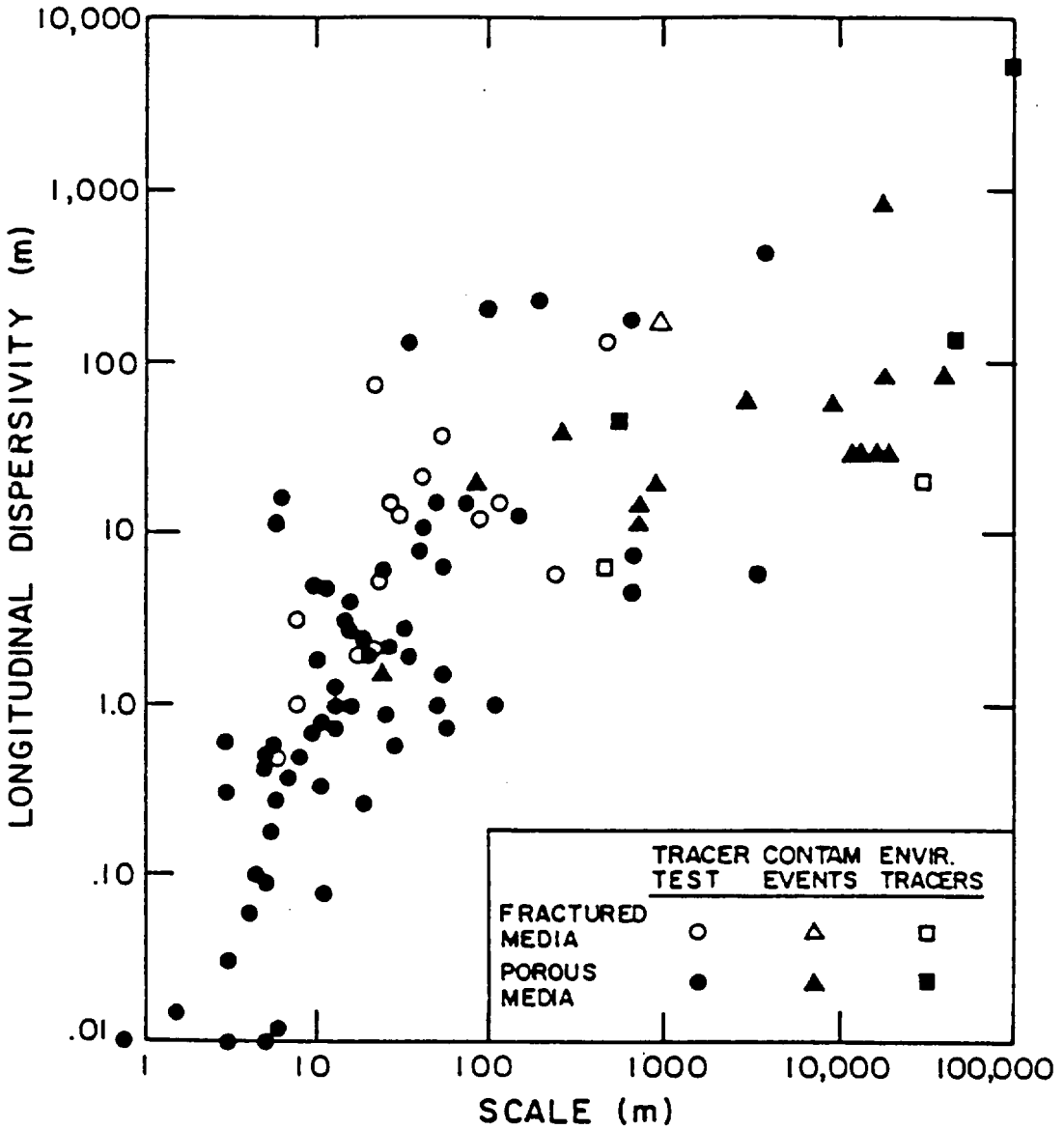

Figure 1. Scale of observation versus longitudinal dispersivity for the saturated zone, from Gelhar et al., 1985

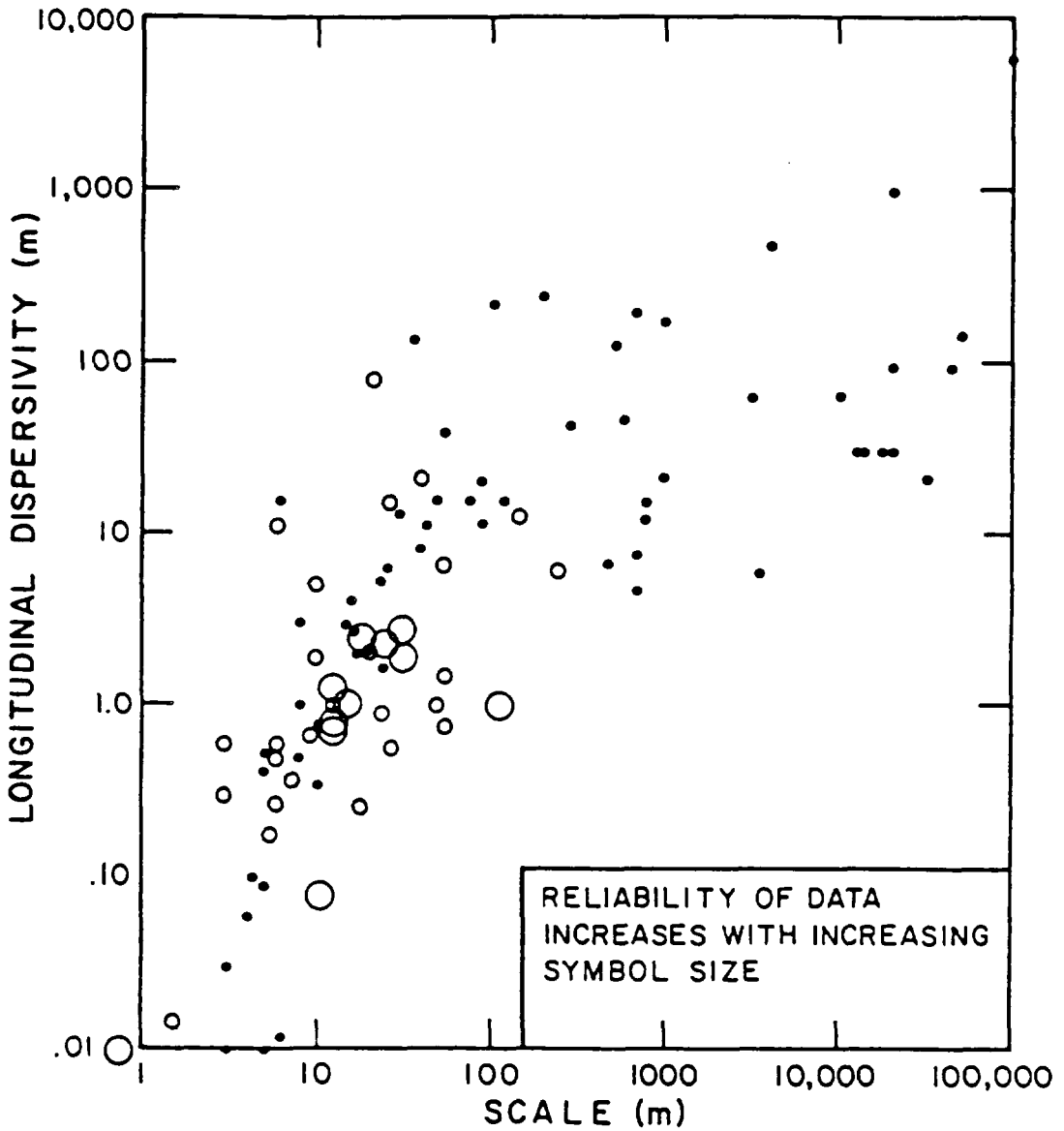

Figure 2. Scale of observation versus longitudinal dispersivity for the saturated zone: reliability classification, from Gelhar et al.,1985

for about 2 years and the nonreactive tracers traveled about 90 meters. All of the organic compounds were significantly retarded, with retardation factors ranging from 2.5 for carbon tetrachloride to 9.0 for dichlorobenzene after 650 days of travel (Roberts et al., 1986).

The analysis of the dispersion of nonreactive tracers (Cl, Br) was made using spatial moments (Freyberg, 1986). Spatial moments were calculated using trapezoidal integration in the vertical and Gaussian quadrature for the horizontal integration. Horizontal interpolation to Gauss points was performed using the Surface II Graphics system (Freyberg, 1986; Sampson, 1978). Results of mass estimation are shown in figure 5 (fig. 3) from Freyberg. These estimates show that initial calculations underpredicted the total injected mass, but that later calculations generally were within 20 percent of the injected mass. The later mass calculations indicate a decrease in mass with travel distance; this trend could be due to a true change in mass in solution (reactive behavior) or merely to inaccuracies in the method.

First moment estimates indicate the location of the center of mass in the three coordinate directions (X, Y, Z). Figure 6 (fig. 3) from Freyberg (1986) indicates an unusually linear, unidirectional, flow path for chloride and bromide. The direction of solute movement (N47.5°E) is in the center of the range observed for the direction of the hydraulic gradient (Freyberg, 1985, pg. 2040). This suggests that the mean horizontal anisotropy is small; Sudicky (1986) reached the same conclusion after an analysis of 1279 core samples taken from the aquifer adjacent to the tracer test site.

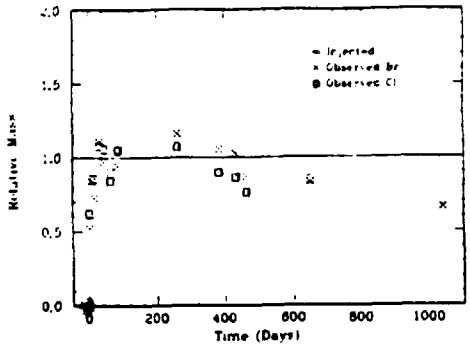

Fig. 5. Estimated masses in solution of chloride and bromide, normalized by injected mass (10.7 kg for chloride, 3.87 kg for bromide).

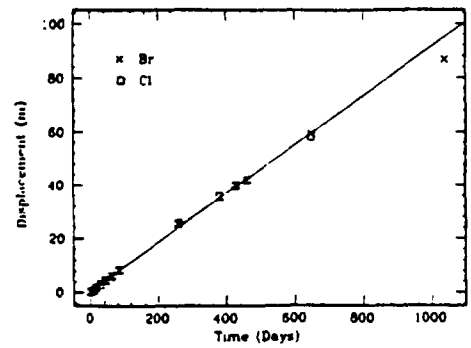

Fig. 8. Horizontal displacement of the centers of mass of the chloride and bromide plumes along the linear trajectory of Figure 6 as a function of time since injection.

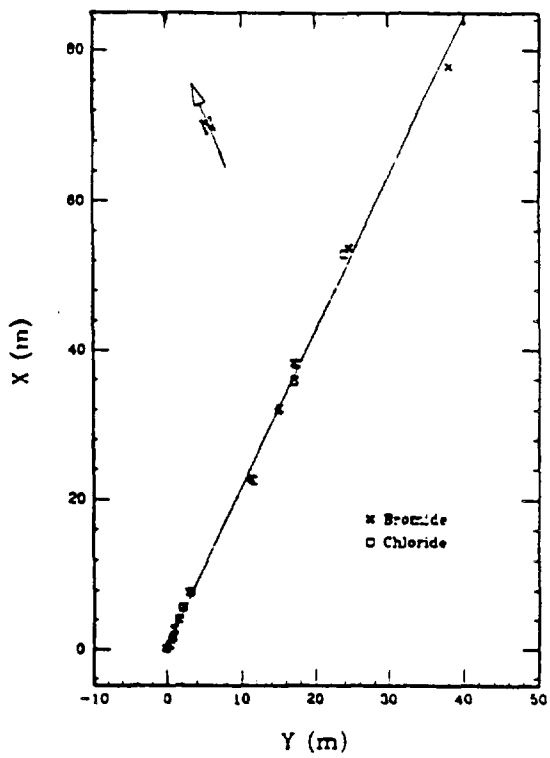

Fig. 6. Horizontal trajectories of the centers of mass of the chloride and bromide plumes.

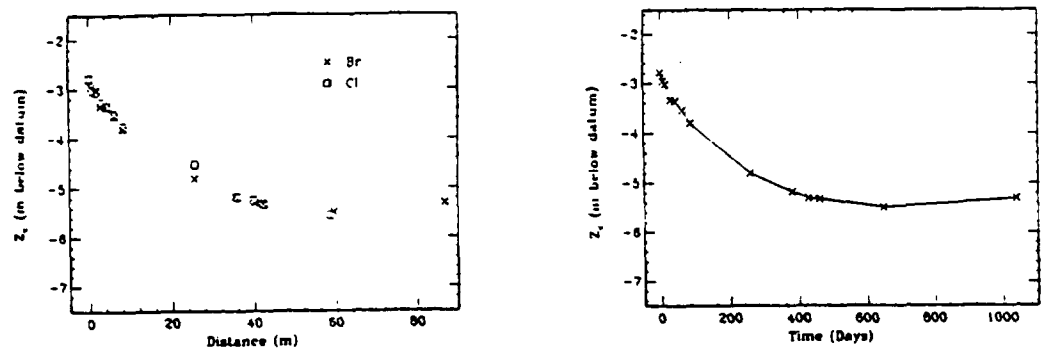

Fig. 7. Vertical displacement of the centers of mass of the chloride and bromide plumes. (left) Vertical location of the center of mass for each plume as a function of horizontal displacement along the linear trajectory shown in Figure 6. (right) Average vertical coordinate of the centers of mass of the bromide and chloride plumes as a function of time. Straight line segments connect the points.

Figure 3. Illustrations from Freyberg, 1986

Vertical locations of the center of mass are plotted versus travel distance and time in figure 7 (fig. 3). The trajectory of the vertical movement show a downward displacement of 2.7m after 647 travel days. The concave upward shape indicates that the downward vertical velocity decreases with time. Freyberg notes that possible explanations for this movement include a small vertical component in the regional velocity field, the density contrast between the plume and the native groundwater, local infiltration and recharge, and (at later times) interaction with an underlying, denser landfill plume.

The nearly constant horizontal solute velocity is illustrated in Freyberg's figure 8 (fig. 3). The rate of horizontal movement is 0.091 m/day; this measured value agrees well with estimates calculated from measurements of hydraulic conductivity (average K is 7×10^{-5} m/s) and the hydraulic gradient (Mackay et al., 1986). The last sampling period falls off the earlier trend in horizontal displacement, indicating a lower velocity. Freyberg states that the plume had a bimodal shape and that this increased by the last sampling period; he reasons that a large-scale inhomogeneity was encountered by the plume such that most of the solute plume slowed.

The second moment (variance) analysis of this test describes the change in solute plume shape over time as it moved through the aquifer. The initial rectangular shape, with the longer side transverse to flow, developed over time into an elipsoid shape, with the longest direction oriented in the direction of flow (Mackay et al., 1986). This change in angle between the major principal axis of the covariance tensor and the flow direction is shown in Freyberg's

figure 9 (fig. 4). Changes in the magnitude of the covariance tensor (horizontal components only) are shown in figure 10 (fig. 4). The slopes of the lines in figure 10 (fig. 4) indicate that the values of the covariance tensor are σ_{xx} = 0.36m, σ_{yy} = 0.039 m, σ_{xy} = 0.023 m. The value of longitudinal dispersivity at the end of the test is estimated to be about 0.43 m. The vertical covariance terms were not calculated because the temporal variations in the vertical covariance terms could not be distinguished from sampling noise.

As part of the test analysis, Freyberg applies the two dimensional results of Dagan (1982, 1984) to the change in variance with travel distance. By calibrating Dagan's curves to the measured change in variance, Freyberg finds a reasonable fit with the variance of log hydraulic conductivity (lnk) equal to 0.24 and the correlation scale of lnk equal to 2.7 m. These values agree well with those found by Sudicky (1986). An asymptotic value of 0.49 m is calculated for longitudinal dispersivity by taking the calibrated model to large time. Freyberg indicates that the experimental evidence shows increasing dispersivity with travel distance and that the asymptotic limit had not been reached after 90 m of travel.

These important results form a framework for discussing the results of the Cape Cod test, and parallels can be drawn between the two, along with important differences.

C. Site Description and Otis Plume Study Results

The site of the large-scale tracer test is located in the northern part of Falmouth, Massachusetts on Cape Cod (figure 5). The study area is in a broad sand and gravel outwash plain, formed

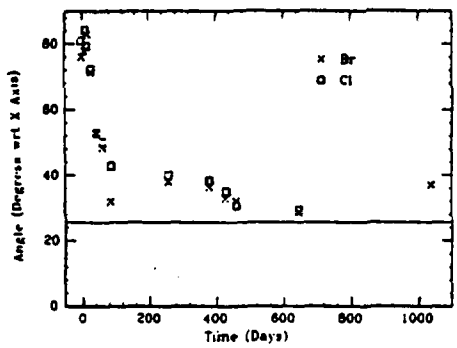

Fig. 9. Angle between the major principal axis of the estimated spatial covariance tensor and the x axis as a function of time. Angles are measured as clockwise rotations from the x axis. Solid line indicates the angle between the estimated mean velocity vector and the x axis (25.5).

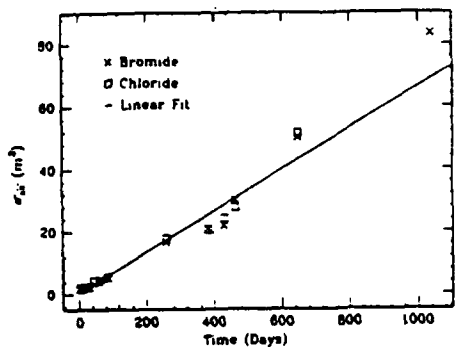

Fig. 10a.

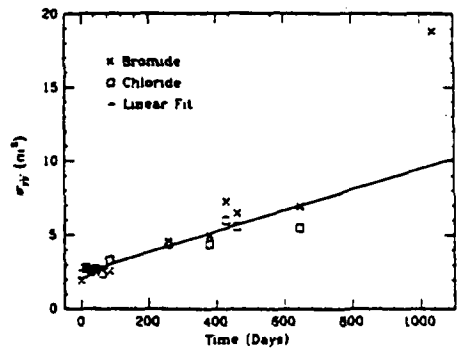

Fig. 10b.

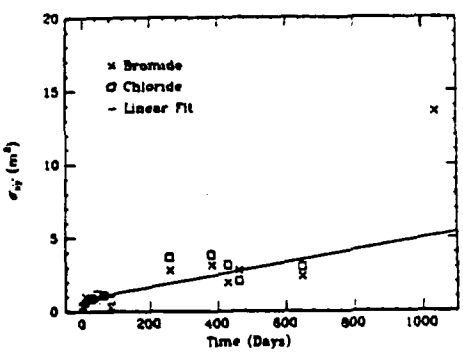

Fig. 10c.

Fig. 10. Components of the estimated spatial covariance tensor of chloride and bromide as functions of time. Coordinate system is aligned with the estimated mean velocity vector, with x' parallel and y' perpendicular to the velocity, respectively. (*a*) Longitudinal variance $\sigma_{x'x'}$ (*b*) Transverse variance $\sigma_{y'y'}$ (*c*) Covariance $\sigma_{x'y'}$

Figure 4. Illustrations from Freyberg, 1986

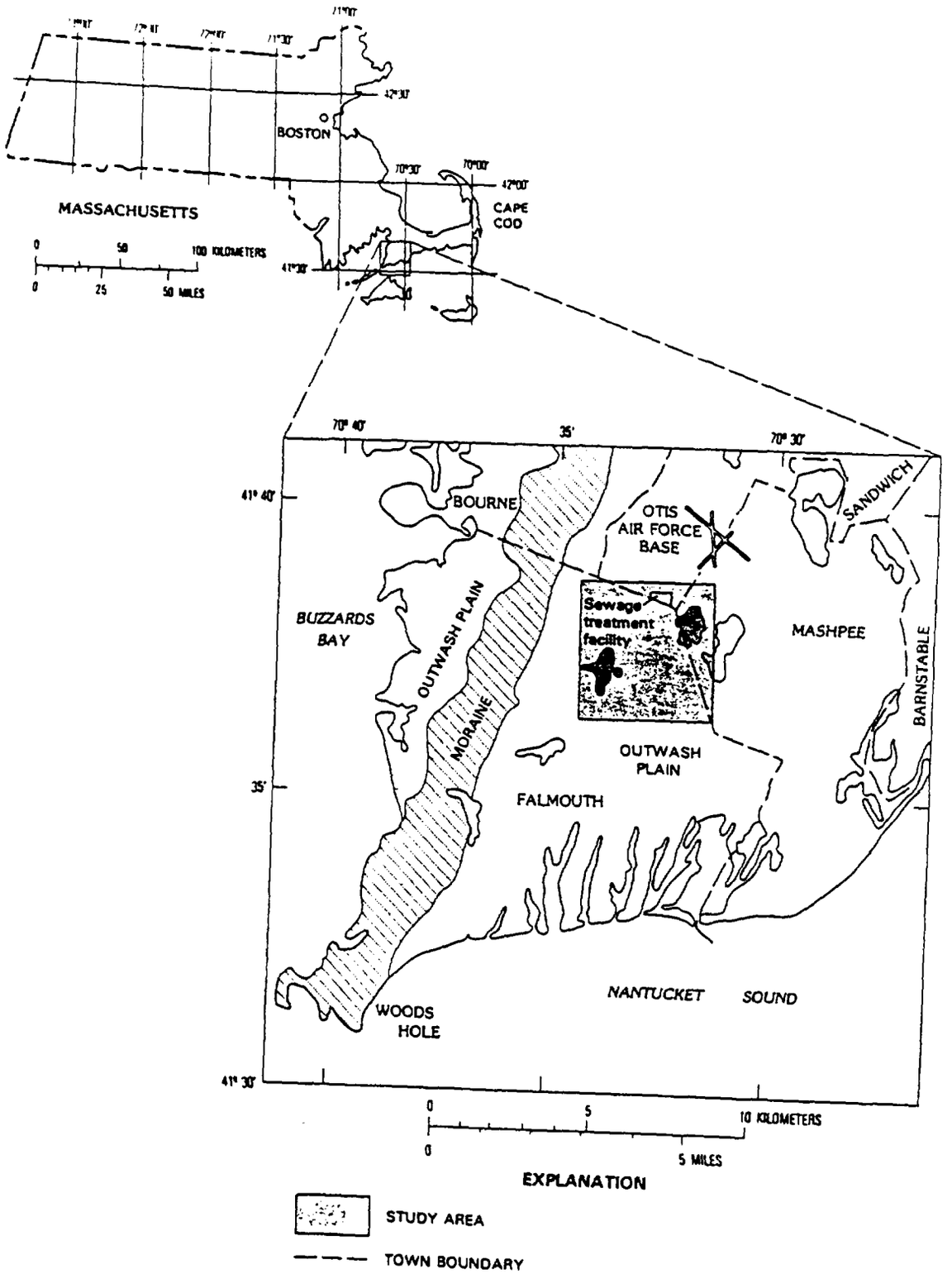

Figure 5. Study area location, from LeBlanc, 1984a

during the last Pleistocene glacial advance, which slopes southward to Nantucket Sound. The outwash plain is pitted with many kettle holes, some of which contain ponds (figure 6). Kettle holes were formed during the glacial retreat when abandoned, stagnant blocks of ice slowly melted away while sediments were deposited around and on the ice. When the ice block eventually melted, a hole was formed in the otherwise flat outwash plain; typically the sediments show slump features around the edges of the kettle holes. Another major topographic feature of the study area are the dry valleys which generally run north to south. Most of these valleys, typically 500 to 900 feet wide and 30 feet deep, do not contain streams but can have wetlands, particularly in the southern ends of the valley. A prevailing opinion is that these valleys were formed during the Pleistocene when frozen soils limited infiltration and surface streams could form.

A hydrogeologic cross section showing the vertical distribution of sediment types is shown in figure 7. The top 90 to 140 feet of sediment is a well sorted, medium to coarse sand with some gravel. North of route 151, the sand and gravel overlies a fine sand and silt. South of route 151, the outwash overlies fine sand, silt, and dense sandy till. The till contains lenses of silt and clay along with sand and gravel. These unconsolidated sediments overlie crystalline (granodiorite) bedrock, which generally slopes from west to east through the study area (Oldale, 1969).

Using a comparison with other measured values of similar sediments on Cape Cod (Guswa and LeBlanc, 1985), LeBlanc (1984a) gives a range of 200 to 300 ft/day for sand and gravel hydraulic

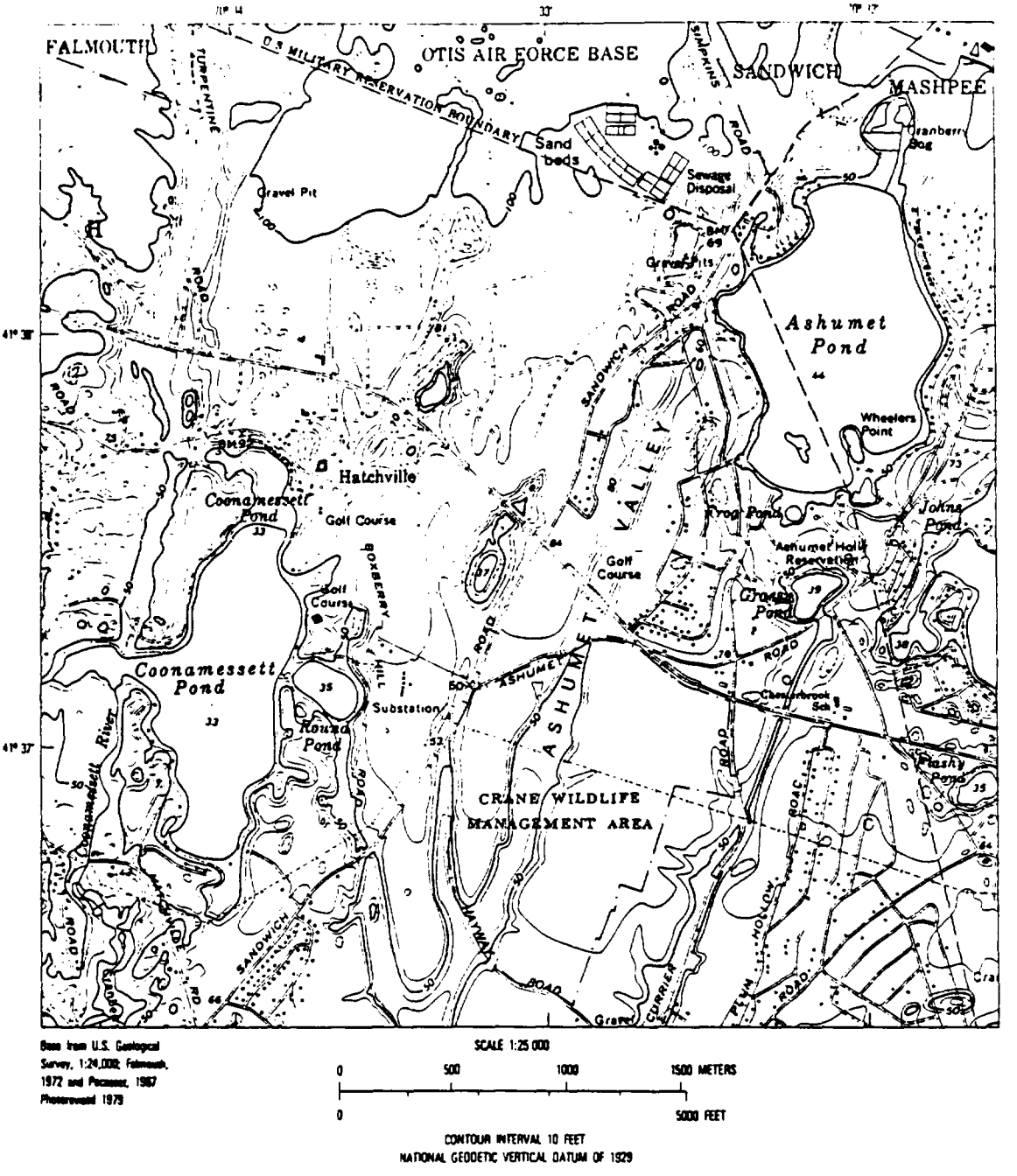

Figure 6. Physical and cultural features, from LeBlanc, 1984a

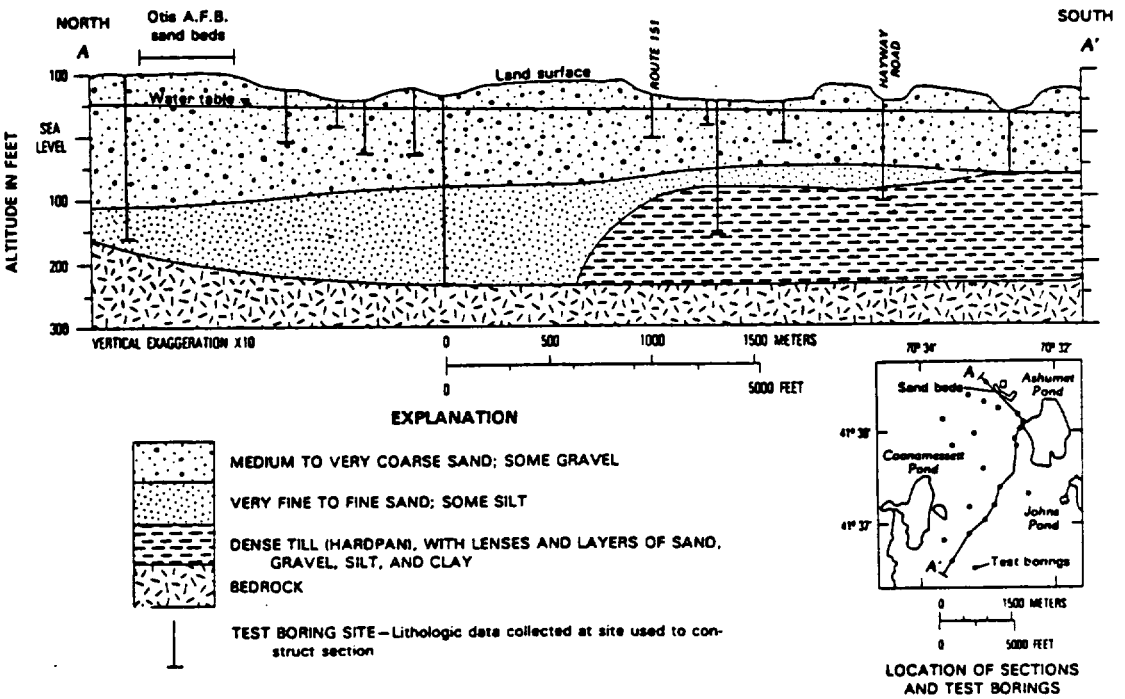

Figure 7. Geologic section showing hydrogeologic units in the study area, from LeBlanc, 1984a

conductivity in the study area. Hydraulic conductivities of the unconsolidated sediments were also estimated by LeBlanc (1984b) using grain size analysis (table 1). The hydraulic conductivity of the fine sand and sandy till was estimated to be about ten times lower than that of the sand and gravel. The crystalline bedrock is assumed to have a very low hydraulic conductivity and the bedrock surface is assumed to be the bottom of the regional ground-water flow system.

Groundwater in the unconsolidated sediments occurs under unconfined (water table) conditions in the study area. The water table slopes to the south and southwest at about 8 ft/mile (figure 8). Water-table altitudes shown in figure 8 were near the average for the period 1963-76 (Guswa and LeBlanc, 1985). Seasonal variations in aquifer recharge cause the water table to fluctuate 1 to 3 feet per year, with highest levels in the spring and lowest in the fall (figure 8a and table 2).

Groundwater recharge to the study area occurs primarily from precipitation and underflow from upgradient areas. Surface water runoff is small because the sandy soils are very permeable. Estimated recharge to the aquifer is 21 in/yr, about 45 percent of the total precipitation (LeBlanc, 1984a). Estimated rates of horizontal groundwater velocity in the sand and gravel range from .8 to 2.3 ft/day (LeBlanc, 1984a). This estimate is based on an average hydraulic gradient (8 ft/mi), hydraulic conductivity (200 to 300 ft/day), and porosity (.20 to .40).

LeBlanc (1984a) describes the extent of contamination occurring in the study area aquifer due to sewage disposal at the southern end of the Otis Air Base (fig. 6). Secondarily treated

Table 1. Estimated hydraulic conductivity of sediment samples of sand and gravel, silty sand, and sandy till, from LeBlanc, 1984a

Geohydrologic unit shown in figure 4	Well number (sites shown in figure 5)	Depth of sample below land surface, in feet	Grain-size diameter, in millimeters, Percent finer by weight: 10 percent	50 percent	Estimated hydraulic conductivity,[1] in feet per day[2]
Sand and gravel	FSW 233	41	0.32	0.80	254
		42	.51	1.03	562
		72	.29	.54	182
	FSW 234	72	.30	.63	181
	FSW 237	63	.27	.58	155
	FSW 239	83	.16	.36	60
	FSW 244	98	.28	.58	172
	FSW 254	107	.26	.66	141
	FSW 262	87	.07	.34	15
		88	.29	.65	170
	FSW 279	148	.09	.21	20
	FSW 282	79	.15	.66	57
Average			.35	.59	164
Silty sand	FSW 254	138	.014	.125	1.6
		168	.092	.20	19
		198	.078	.16	13
		268	—	.155	5.8
Average			—	.16	10
Till	FSW 262	155	.115	.22	28
		160	.068	.26	13
Average		179	—	.23	14

[1] Assumes ground-water temperature of 10°C.
[2] From Krumbein and Monk, 1943.

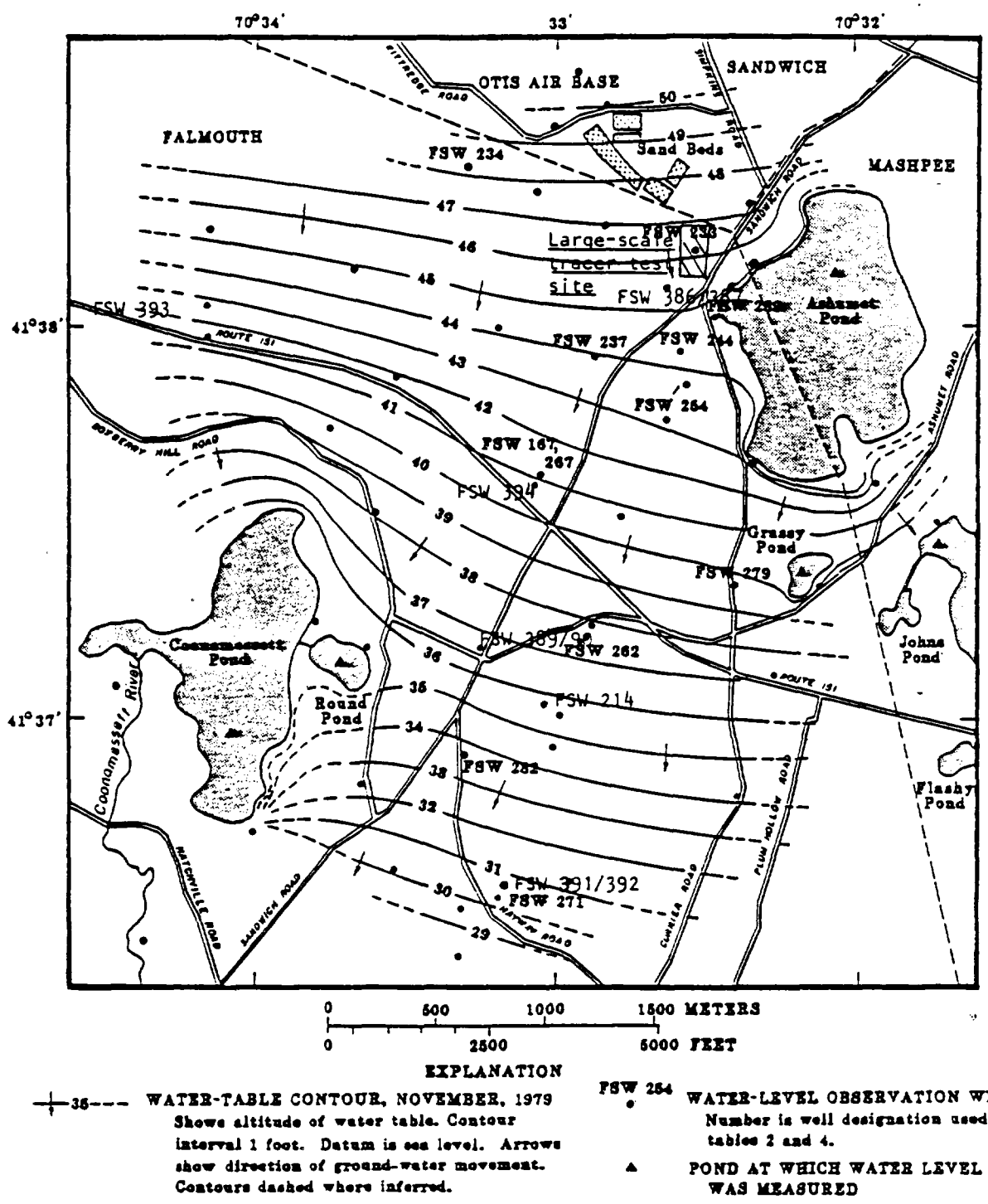

Figure 8. Water-table contour map, from LeBlanc, 1982

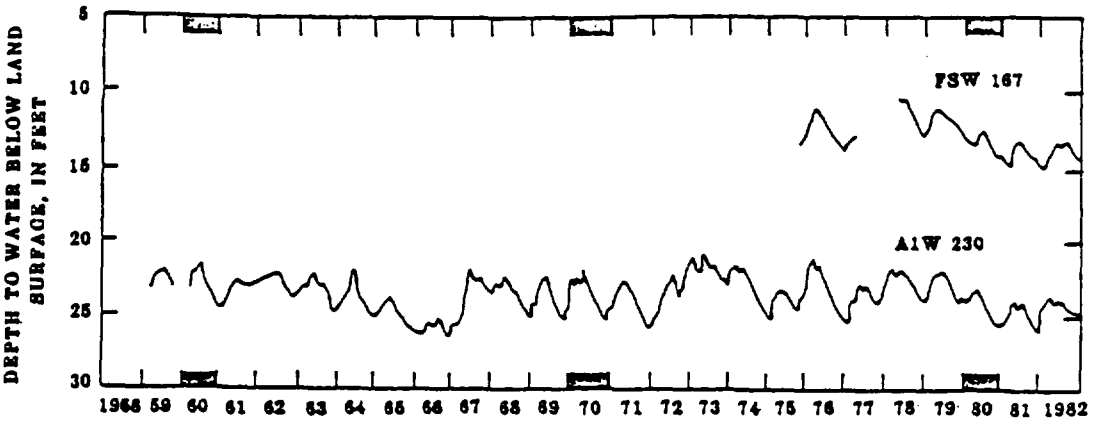

Figure 8. Hydrograph of observed water levels in wells FSW 167 and A1W 230 for the period 1959-82, from LeBlanc, 1984a

Table 2. Observed hydraulic head in clusters of observation wells, November 1979, from LeBlanc, 1984a

[Well sites are shown in figure 8.]

Well cluster	Well depth, in feet below land surface	Hydraulic head, in feet above sea level	Well cluster	Well depth, in feet below land surface	Hydraulic head, in feet above sea level
FSW 254	26	43.84	FSW 167, 267	55	41.33
	54	43.88		88	41.33
	72	43.89		[1]111	41.30
	107	43.88		[1]136	41.32
	[1]140	43.93		[1]155	41.26
	[1]168	43.91			
	[1]216	43.91	FSW 271	41	30.45
				[1]85	30.45
FSW 262	41	37.69		[1]141	30.49
	69	37.69		[1]165	30.49
	85	37.68			
	[1]109	37.72	FSW 282	49	33.67
	[1]159	37.53		70	33.68
				94	33.70
				[1]123	33.69

[1] Well screened below the bottom of the sand and gravel outwash.

sewage, disposed on to rapid infiltration beds, has formed a plume of contaminated ground water 2,500 to 3,500 feet wide, 75 feet thick, and more than 11,000 feet long (figure 9). The plume moves with the ambient flow to the south and southwest, and is overlain by up to 50 feet of uncontaminated ground water derived from precipitation that recharges the aquifer (figure 10).

The plume of sewage contaminated ground water is characterized by elevated concentrations of boron, chloride, sodium, phosphorus, ammonia, nitrate, detergents (LeBlanc, 1984a), and in some locations, volatile organic compounds (figure 11, Thurman et al., 1984). Boron, chloride, and sodium appear to be moving conservatively and to be attenuated primarily by hydrodynamic dispersion. Phosphorus movement is greatly retarded by adsorption on to the sediments. Ammonia in the plume is oxidized to nitrate as the anoxic contaminated ground water mixes with uncontaminated ground water containing up to 11 mg/L dissolved oxygen. Detergent concentrations exceeding 0.5 mg/L MBAS (methylene blue active substances) are located 3,000 to 10,000 feet downgradient of the sewage infiltration beds. This distribution of detergents reflects the use of nonbiodegradable detergents on the Air Base between 1946 and 1964 (LeBlanc, 1984a).

LeBlanc (1984b) simulated the transport of boron using a two dimensional method of characteristics ground-water transport model (Konikow and Bredehoeft, 1978). Although a comparison of the simulated plume (figure 12) and the measured plume (figure 9) indicates that the flow direction was closely matched, the actual concentration values are a poor match. This is due to the two

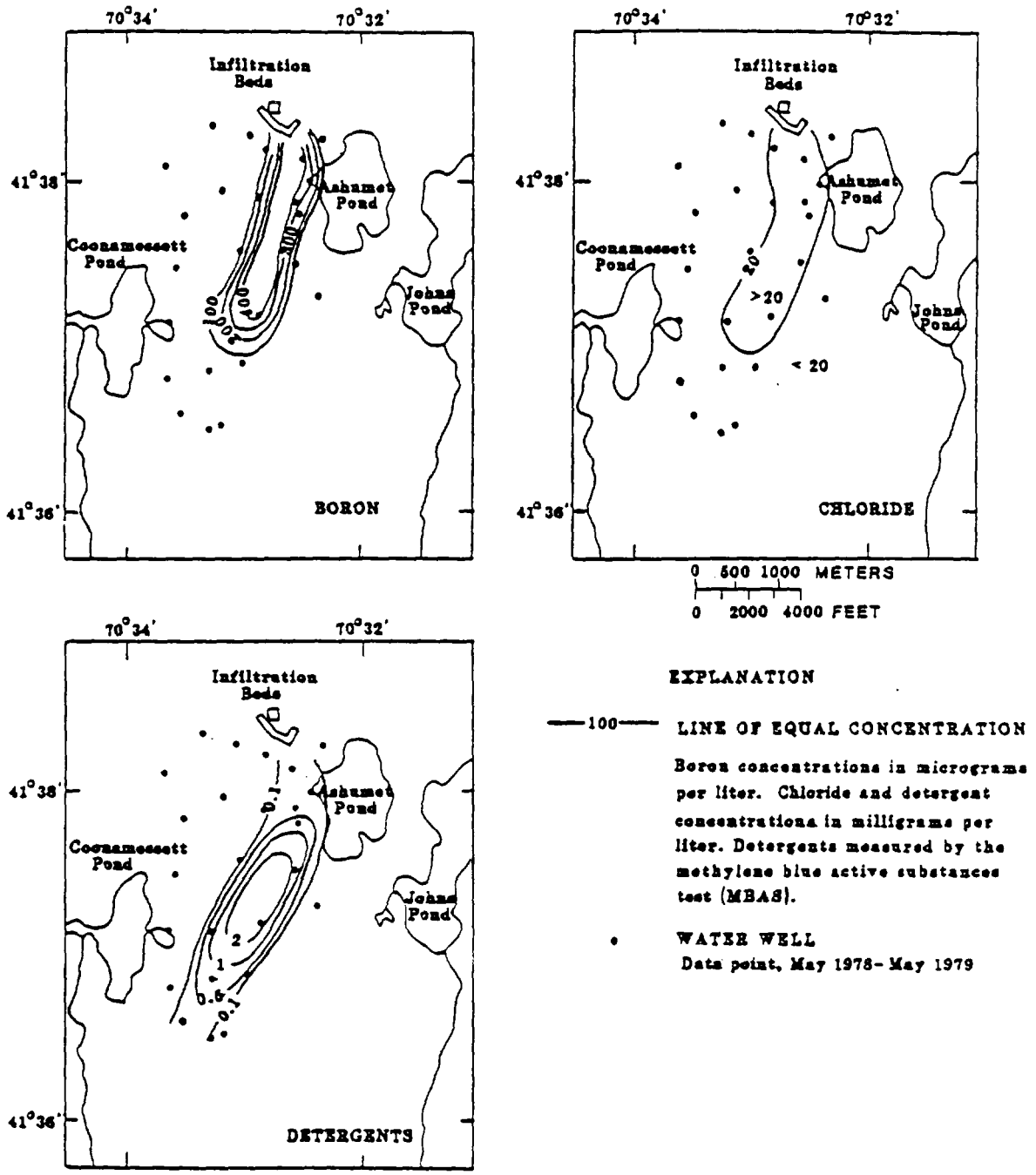

Figure 9. Observed areal distributions of boron, chloride, and detergents in ground water, May 1978 through May 1979 (from LeBlanc, 1982).

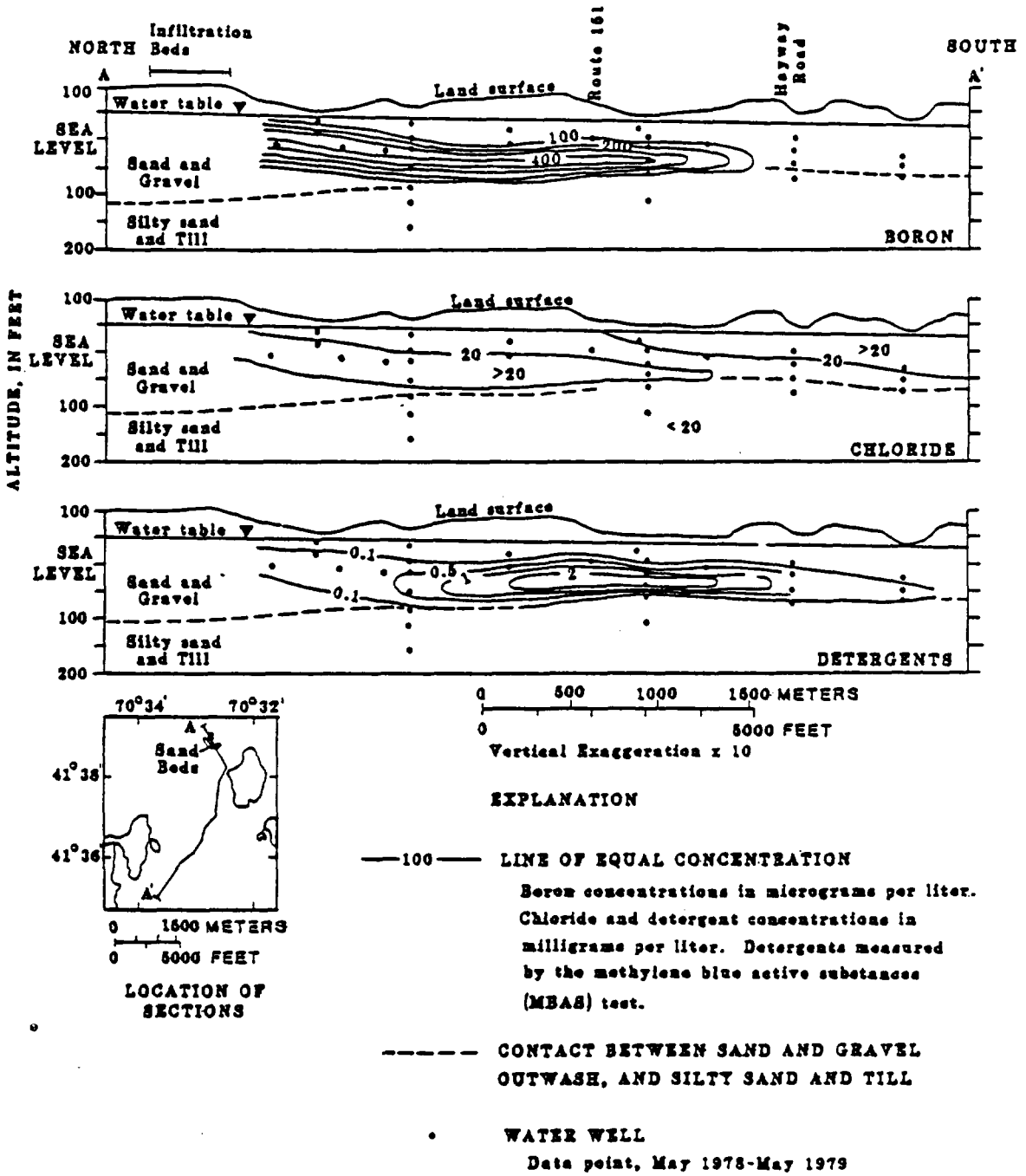

Figure 10. Observed vertical distributions of boron, chloride, and detergents in ground water, May 1978 through May 1979 (from LeBlanc, 1982).

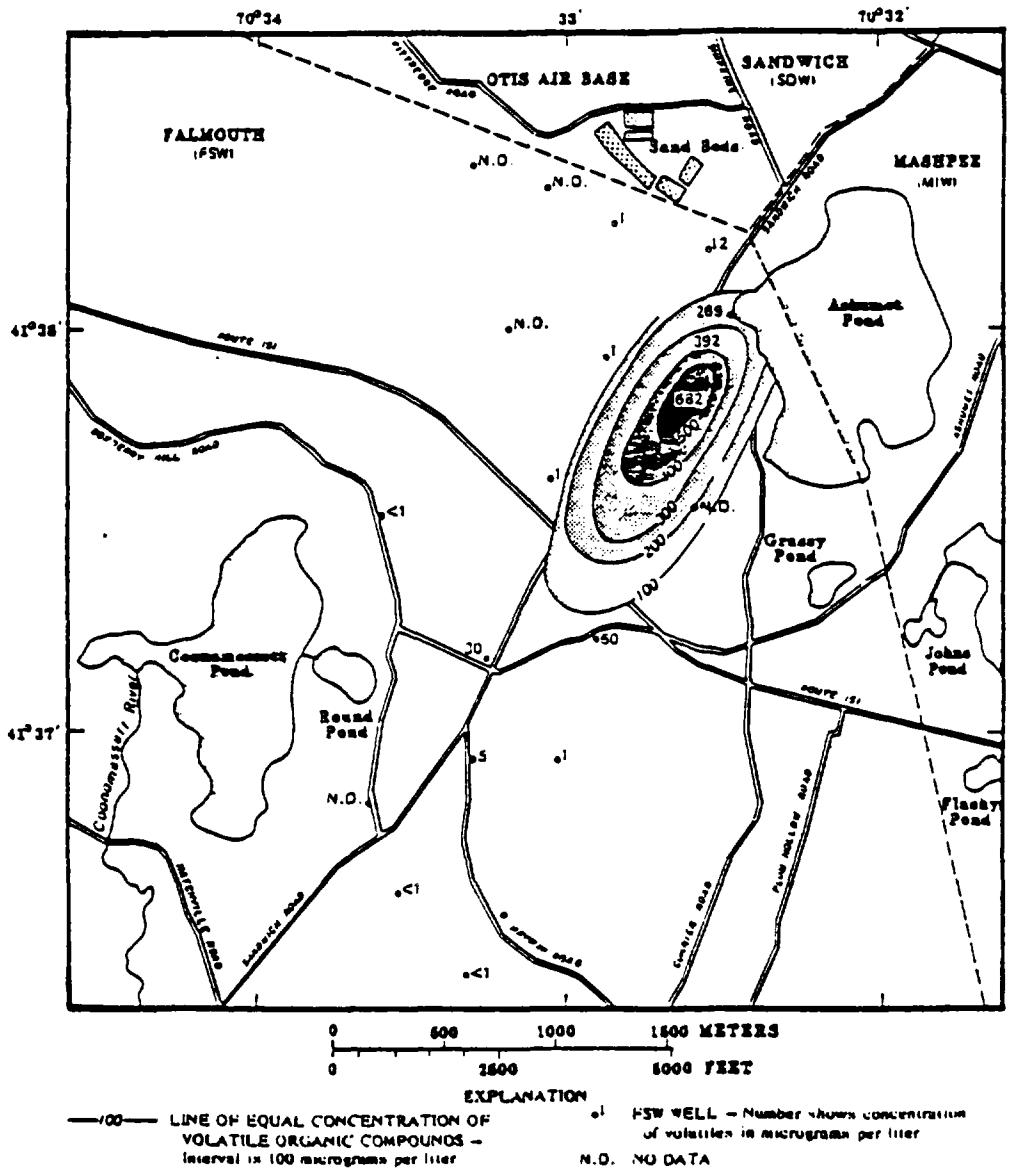

Figure 11. Areal distribution of volatile organic compounds in ground water, 1983.
from Thurman et al.,1984

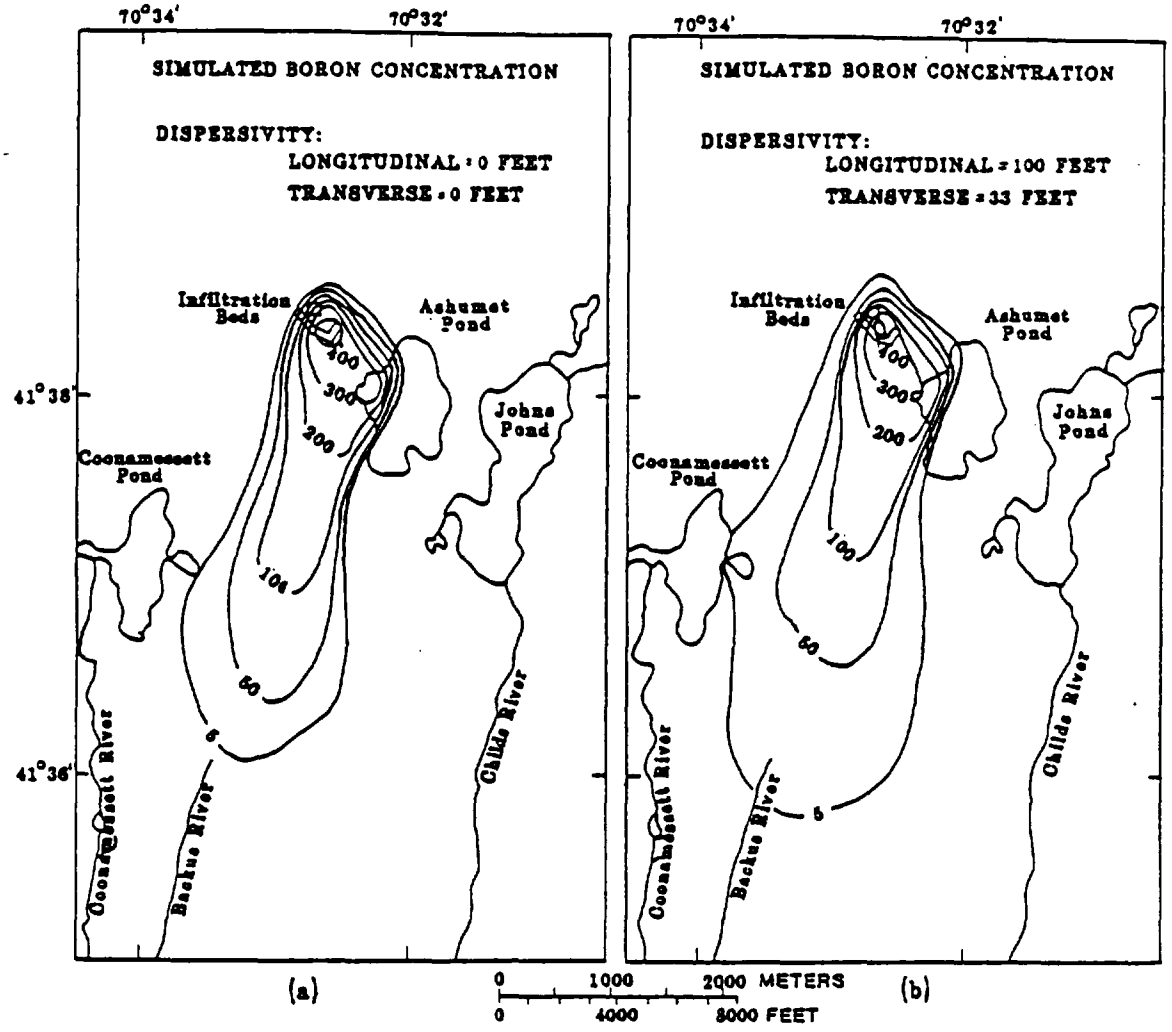

Figure 12. Computed boron concentrations after 40 years of disposal of treated sewage containing 500 ug/L, assuming (a) zero dispersivity and (b) longitudinal dispersivity of 100 feet and transverse dispersivity of 33 feet, from LeBlanc, 1984a

dimensional assumption in the model. As recharge accretes on the water-table aquifer the actual plume sinks, with very little vertical mixing (see figure 10). The model, however, treats the system as fully mixed and predicts a much more rapid decrease in concentrations than actually occurred. Figure 12 also shows the effects of uncertainty in the longitudinal and transverse horizontal dispersivity values. It is readily apparent that matching the large plume scale data set will not uniquely identify aquifer dispersivity values.

There are several major reasons for conducting a large-scale natural-gradient tracer test at the Cape Cod site. These reasons include the differences between the mean hydraulic conductivity at the Borden site and at the Cape Cod site. The Borden test results are important findings, and the range of sediments for which these types of dispersion experiments are performed needed to be extended to coarser, more permeable, and more variable sediments such as the sand and gravel aquifer at the Cape Cod site. Another reason is the lack of definitive information from the Borden test on the vertical mixing of solutes, which needed to be examined in a field tracer test.

The results of the Borden test showed the longitudinal dispersivity approaching an asymptotic value. Therefore, another reason to conduct the Cape Cod test was to go beyond the 90 meter travel distance of the Borden test to observe if indeed the longitudinal dispersivity does reach an asymptotic (i.e. Fickian) value in a field tracer test.

II Pre-Experiment Data Collection

To conduct a large-scale tracer test at the Cape Cod site effectively, it was necessary to collect information for proper test design. After reviewing the available literature, particularly the tests being conducted at the Borden site, it was decided that small scale tracer tests and a pump test would provide the initial data necessary for large-scale test design. This section outlines the approach and methods used in these tests, along with the analysis of test results.

A. Ashumet Well Pump Test

In order to establish a reliable estimate of hydraulic conductivity, an aquifer test was designed and conducted at the Ashumet well (FSW 214, fig. 8) in July 1984. The Ashumet well was constructed in the Crane Wildlife Management area in Falmouth, Massachusetts, to supply water for the town of Falmouth. The well was installed in February 1976, and was used as a water supply until 1978, when the well was found to be contaminated by the sewage plume. The well was shut down until July 1984, when it was restarted for the aquifer test. As part of the test, the water quality of the pump discharge was tested for possible remediation by mixing with uncontaminated water. Unfortunately, the volatile organics plume had moved within the cone of depression for the well and the discharge was contaminated with volatile organics. The Ashumet well remains unused at present (summer, 1987), and will likely be unused for years in the future.

The observation well network for the aquifer test, shown in figures 13 and 14, was designed to measure the vertical and horizontal head variations in the aquifer during the test. A three-dimensional numerical groundwater flow model (McDonald and Harbaugh, 1984) was used to estimate the range of drawdown expected at various radial distances and depths. These drawdown estimates were used in designing the observation well locations to insure sensitivity to hydraulic conductivity, anisotropy, and storage coefficients. Wells were placed at different horizontal distances for observing drawdown versus distance relations, and at the same radial distance about 90° apart to observe possible drawdown differences due to horizontal anisotropy (fig. 13). Two sets of wells were also placed at various depths to observe vertical drawdown changes with depth (fig. 14).

Heads in several of the wells were monitored using a gas bubbling, pressure transducer arrangement. This system can take head measurements every 30 seconds, ensuring a reasonable record of early-time data. Other wells were measured using either a system which senses water level changes using electrical conductance at a probe, or using electric tapes and steel tapes with chalk. The accuracy of the head measurements generally were .02 feet.

The Ashumet well is 60 feet deep with a 10 foot screen at the bottom. The well has a 2 foot diameter with a 48 to 60 inch diameter gravel pack outside the well screen and casing. The well penetrates the sand and gravel outwash aquifer, which is about 75 feet thick at this site. Beneath the sand and gravel is about 20 feet

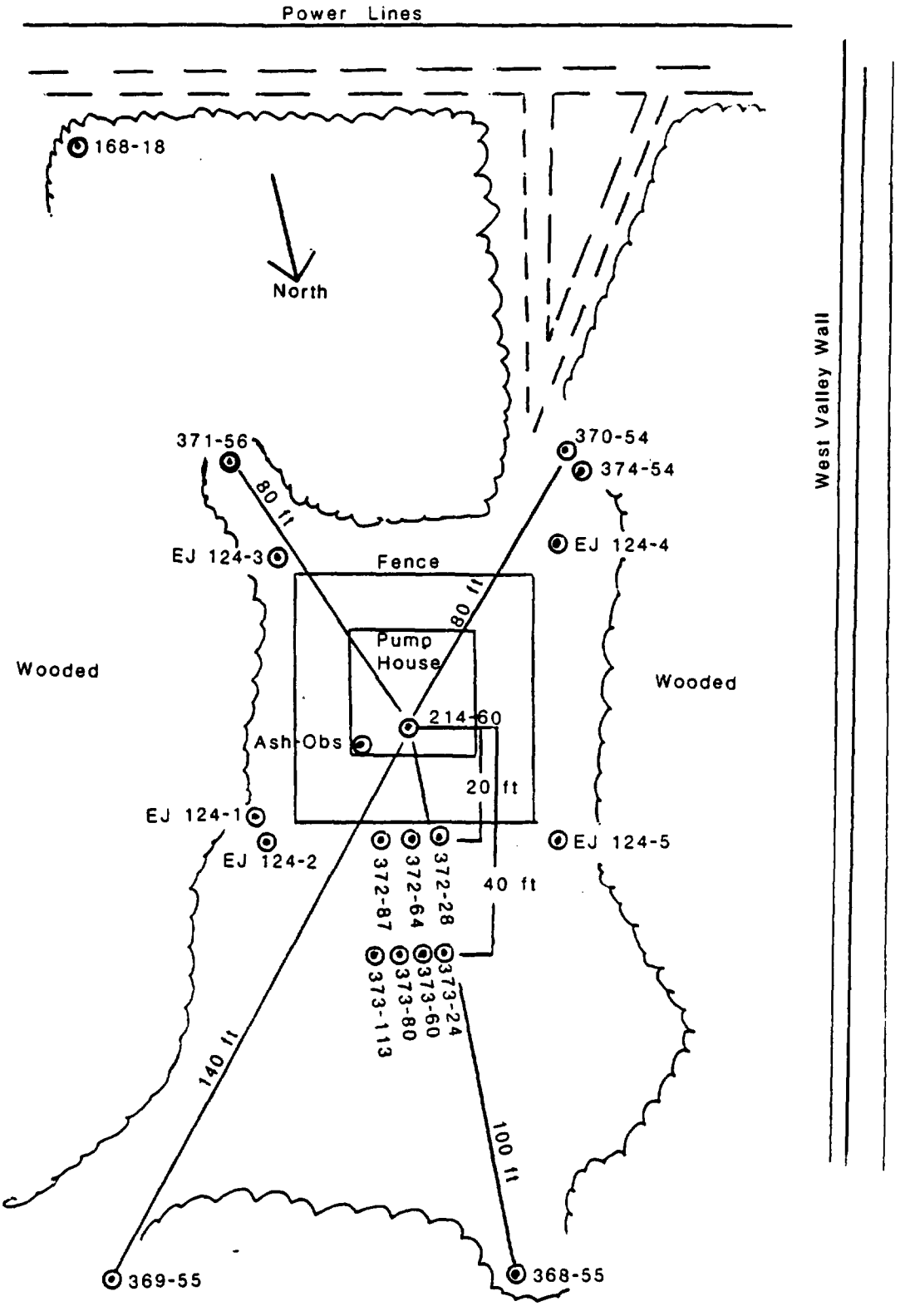

Figure 13. Observation well network for the Ashumet well pump test. All U.S. Geological Survey wells have the prefix FSW (ex: FSW 371-56)

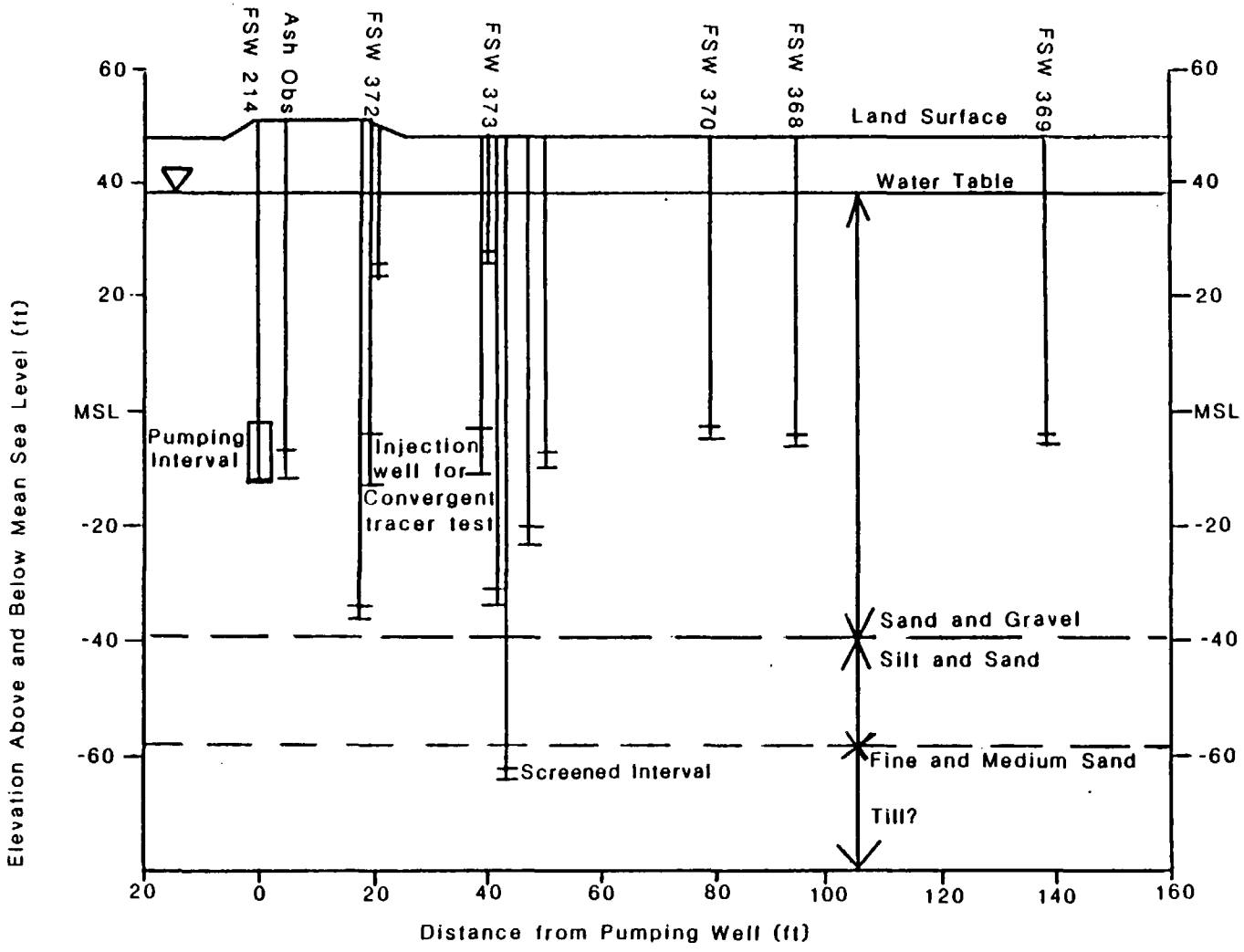

Figure 14. Vertical locations of observation wells for the Ashumet pump test

of silt and sand, which is further underlain by about 160 feet of sandy till. The water table is about 10 feet below the land surface at the Ashumet well.

The aquifer test was conducted at 475 gallons per minute; the pump discharge was piped to waste, 1,500 feet south in Ashumet valley. Although the total duration of the test was about 90 days, only the first seven days of drawdown data were used for analysis. After seven days, a significant rainfall occurred, causing a dip in the drawdown versus time curves (fig. 15).

The drawdown versus time curves for wells FSW 372-28, -64, -87 (fig. 15) show the sigmoid shape of a water-table response to pumping. Neuman (1972, 1973, 1974, 1975) has explained this response using three segments of the drawdown versus time curve. The first steep segment of the curve falls along a Theis solution and is due to water released from elastic storage (compaction of the aquifer and expansion of the water). The second stage entails gravity drainage from vertical movement of the water table, which temporarily stabilizes the drawdown response and is analogous to leakage from a source. The third segment is an increase in drawdown with time as the cone of depression gradually expands outward with a resultant water-table drop (Neuman, 1972).

The Neuman type curve method was used to analyze the drawdown versus time curves for wells FSW 372-28, -64 and 373-60. The application method for partially penetrating wells (Neuman, 1975) involved the use of computer programs to compute the type curves for each of the three wells. The drawdown data are plotted with time on log-log paper and the procedure outlined by Neuman

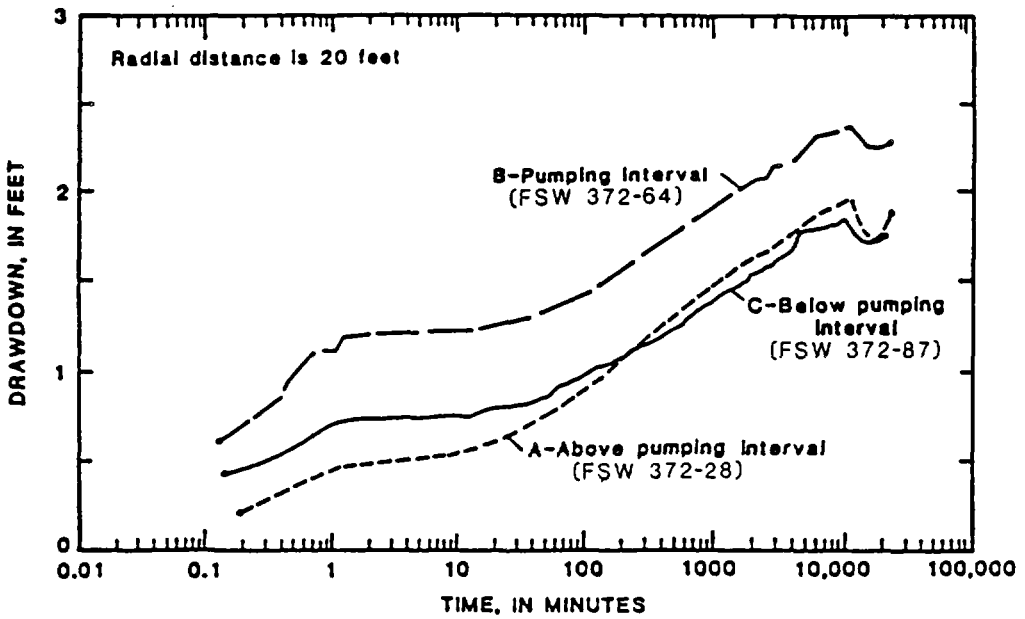

Figure 15. Observed drawdown in observation wells located 20 feet from the pumping well screened above (A), opposite (B), and below (C) the pumping interval, July 7–14, 1985. Pumping-well screen is 10 feet long.

(1975, pages 330-1) is used to generate values of confined storage, specific yield, transmissivity, and the ratio of horizontal to vertical hydraulic conductivity. The drawdown data curves are fitted to the type curves and values of dimensionless drawdown, time, and anisotropy ratio at match points are recorded. After calculating transmissivity, the horizontal hydraulic conductivity is calculated by dividing transmissivity by the aquifer thickness.

The results of this analysis are shown in table 3. A comparison of the values of transmissivity shows large differences between the values, particularly between the wells open in the same zone as the pump (FSW 372-64, 373-60) and the well completed above the pumped interval (FSW 372-28). The differences in the analysis values can be explained by examining the drawdown curves (fig. 15). The later time portions of the curves show different slopes, when the slopes should only be sensitive to transmissivity, and the same for both. A match between type curves and observed drawdown versus time therefore could not be obtained with a consistent set of parameters. These difficulties were thought to be due to a violation of assumptions and led to the application of a numerical model to the aquifer test analysis.

The three-dimensional finite-difference groundwater flow model developed by McDonald and Harbaugh (1984) was used in this aquifer test analysis. After comparing the drawdown records at FSW 370-54 and 371-56 (fig. 13), which are located at the same radial distance from the pump and recorded identical drawdowns, the conclusion was made that there was no horizontal anisotropy. To take advantage of the radial symmetry, the model actually

Table 3

Results of Neuman Type Curve Analysis for Ashumet Well Pump Test

	FSW 372-28	FSW 372-64	FSW 373-60
Transmissivity (ft^2/min)	9.83	21.5	21.7
Hydraulic Conductivity* (ft/day)	184	401	406
Vertical/Horizontal Hydraulic Conductivity	1.0	0.42	0.37
Specific Yield	0.43	0.17	0.14
Specific Storage*	5.31×10^{-5}	8.70×10^{-5}	4.42×10^{-5}
Radial Distance from Pump (ft)	20.5	20.5	39.9

*Assumed aquifer thickness: 77 ft.

covered only one quarter of the area, with the pump in one corner of the model pumping one quarter of the actual rate (475 gpm). The modeled area was subdivided horizontally into 7229 blocks (27 x 27). The block size was expanded outward from the pump to include all the observation well radial distances. The total model distance along each horizontal side was 5,880 feet. The boundary conditions along the sides were no flow; for the duration of the simulations the drawdown along these sides was 0.01 feet or less. The model was subdivided vertically into 11 layers; the upper 9 were in sand and gravel, the tenth represented the silt and sand, and the eleventh represented the till. The crystalline bedrock beneath the till was assumed to be impermeable.

Starting with parameter values from the Neuman type curve analysis, these values were adjusted until the drawdown curve for FSW 372-64 was matched. Using this simulation as a base run, parameter values were increased and decreased to yield the sensitivity of a number of the drawdown curves to each parameter (fig. 16-19). After examining each set of curves, it becomes readily apparent that each parameter has a different effect on the drawdown curves. For example, horizontal hydraulic conductivity (K_r, fig. 16) strongly affects the slope of the drawdown curves at later times. This indicates that the curves are sensitive to this parameter. For the ratio of vertical to horizontal hydraulic conductivity (K_D, fig. 17) the largest effects occur to well FSW 372-64 and causes a uniform increase in drawdown with a decrease in K_D. The specific yield (S_y, fig. 18) has the largest impact on well FSW 372-28 and causes an increase in drawdown in later time with a

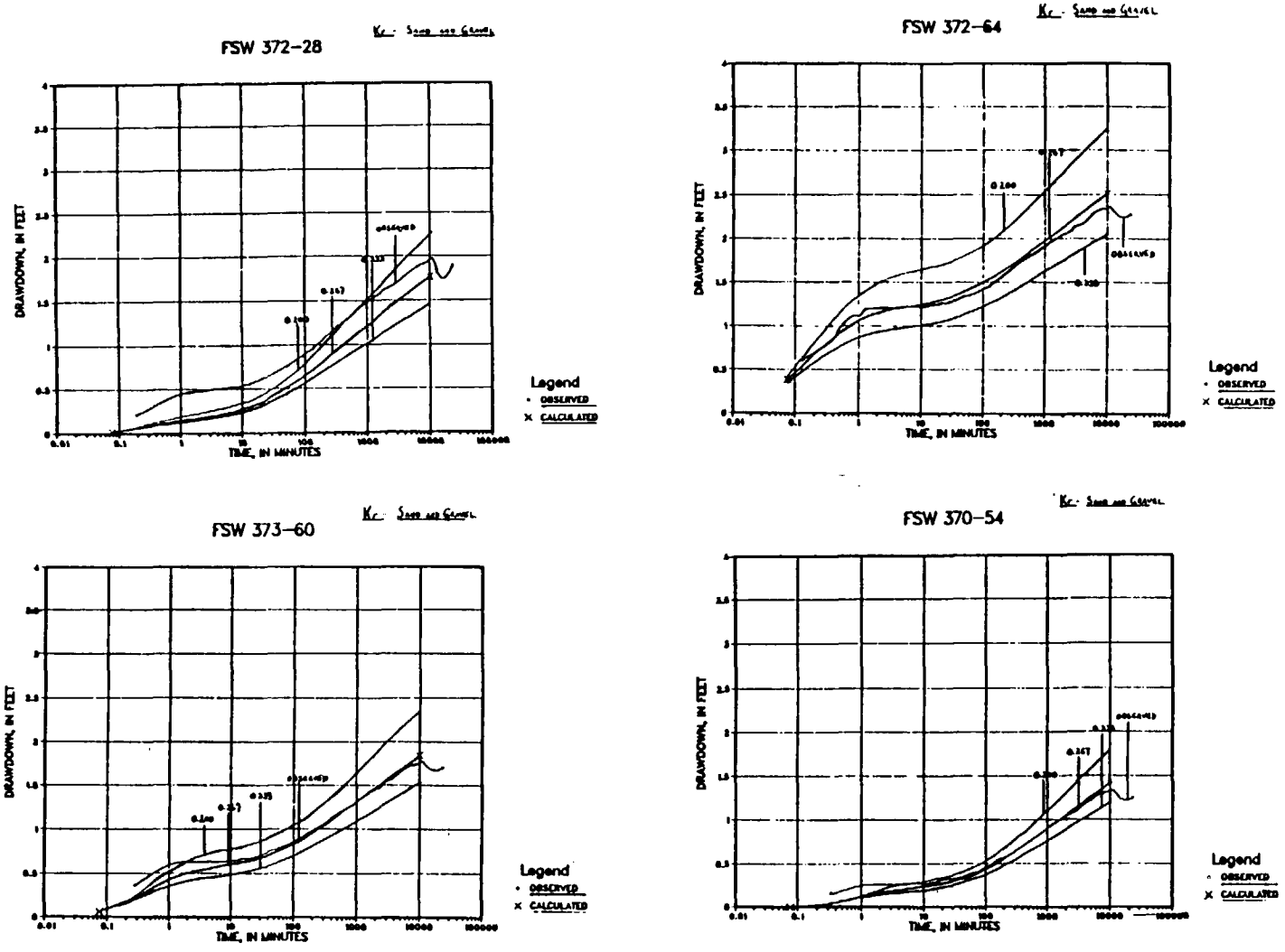

Figure 16. Model response to variations in horizontal hydraulic conductivity

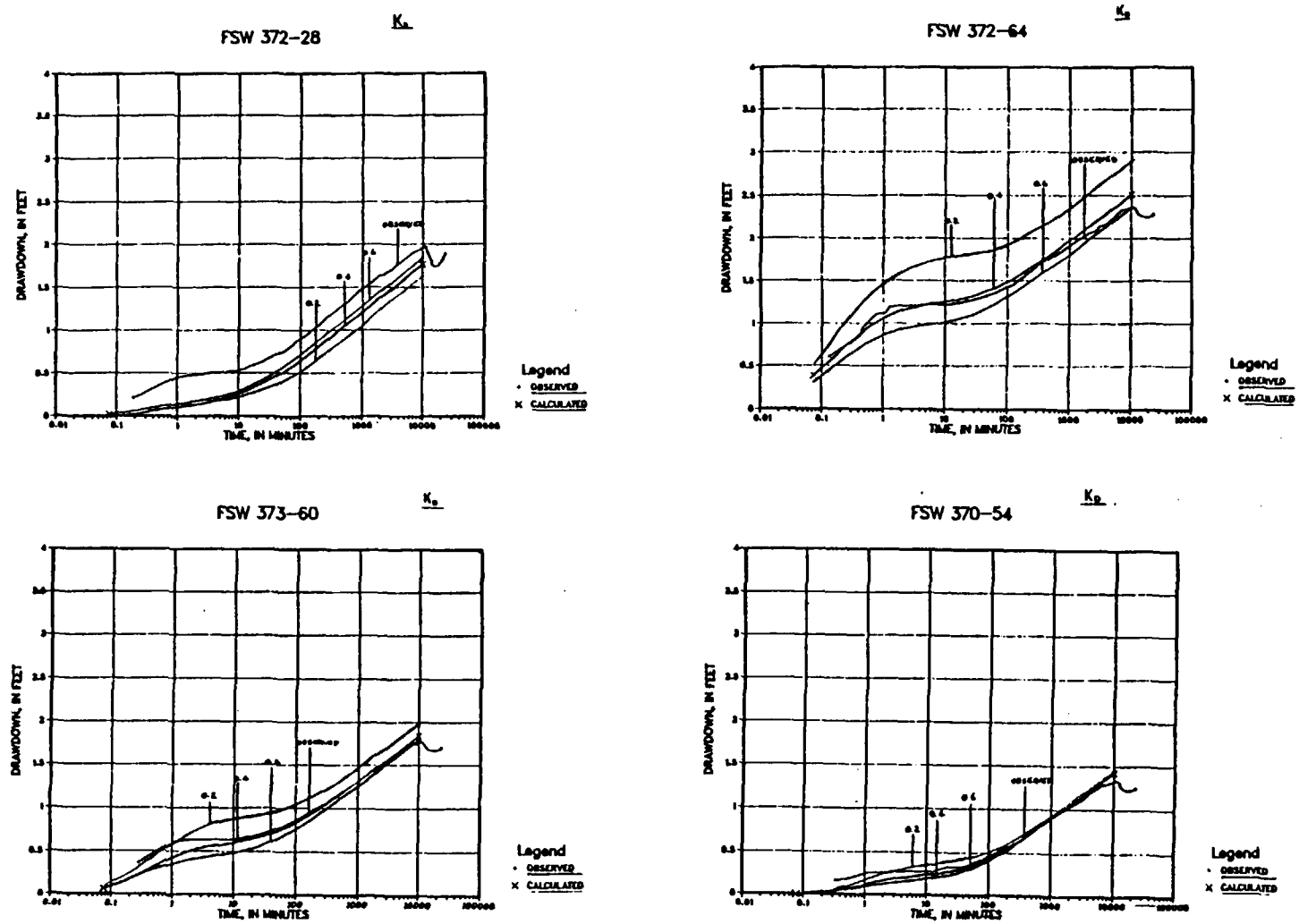

Figure 17. Model response to variations in the ratio of vertical to horizontal hydraulic conductivity

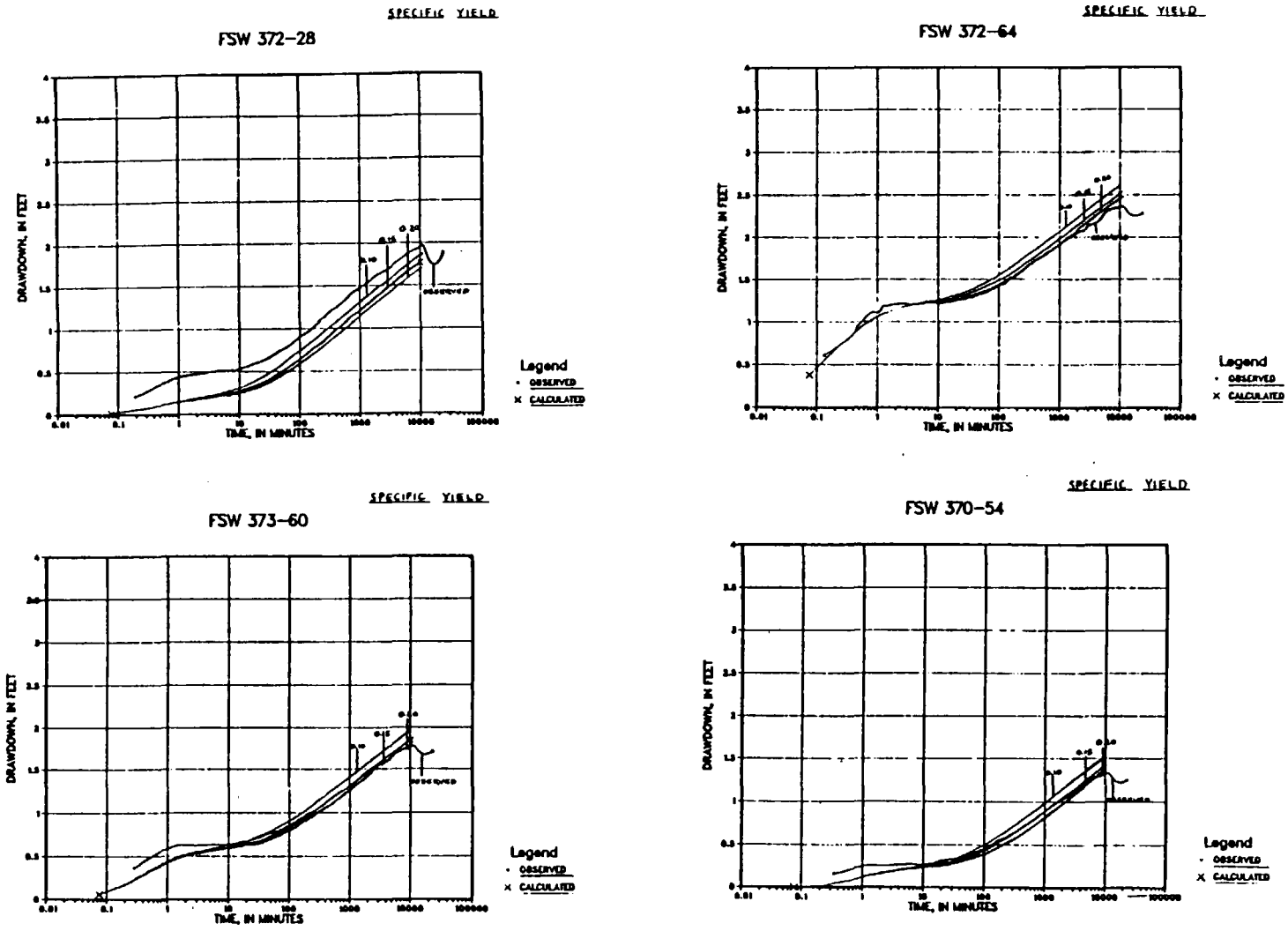

Figure 18. Model response to variations in specific yield

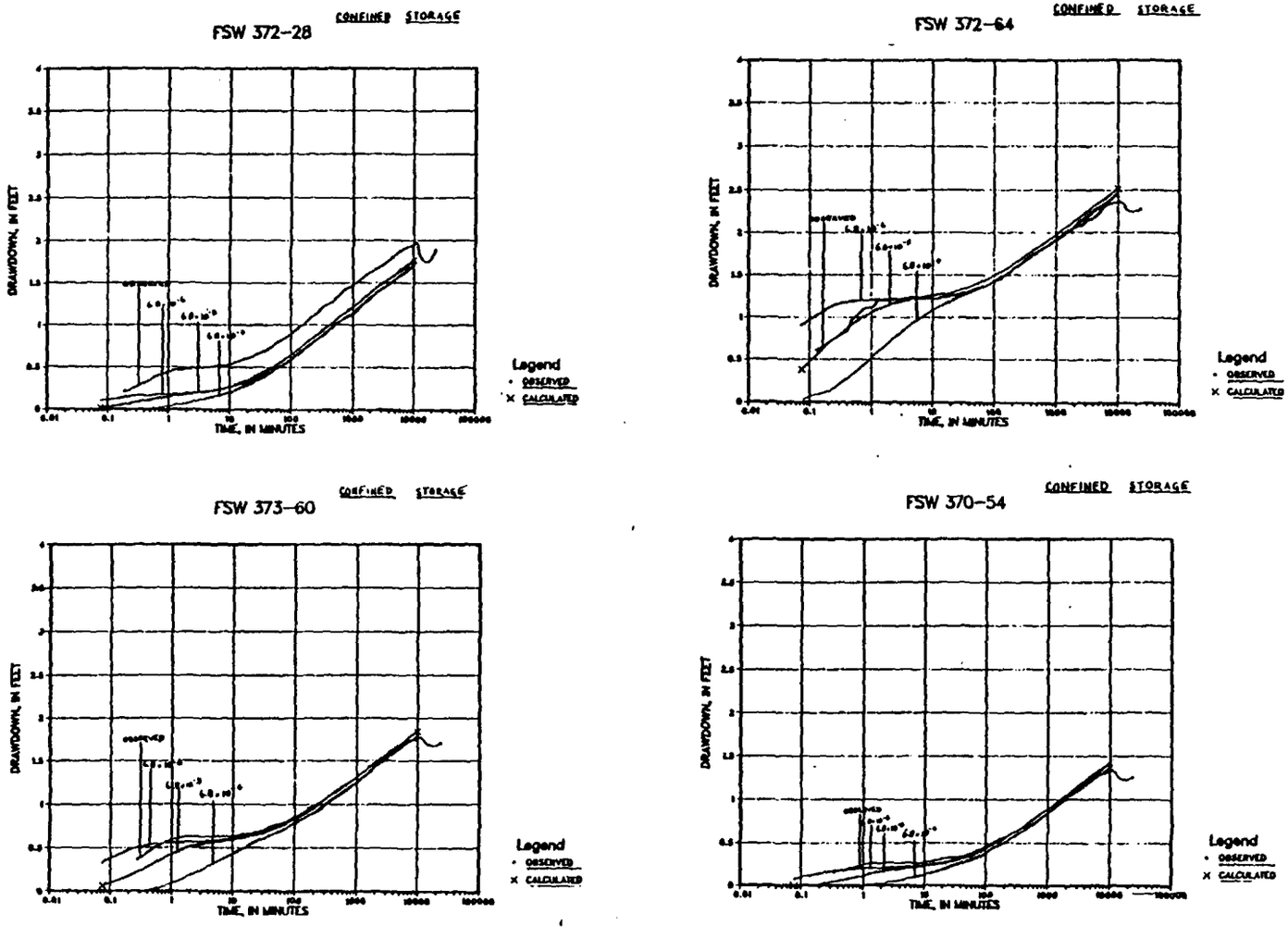

Figure 19. Model response to variations in confined storage

decrease in Sy. Confined storage (S_s, fig. 19) causes an increase in drawdown in early time with decreasing S_s, occurring strongest at FSW 372-64. The model simulation with the best overall fit of calculated to measured drawdown had the following parameter values: K = 0.267 ft/min., K_D = 0.4, S_y = 0.15, S_s = 6.8 x 10^{-5}.

After carefully reviewing the effects of each of the four major parameters (K_r, K_D, S_y, S_s) it was apparent that any adjustment to better fit the calculated response to observed drawdown at FSW 372-28 would be at the expense of degrading the match at FSW 372-64. This realization prompted a careful examination of the test and analysis, leading to the pumped well construction diagram. The Ashumet well was installed with a 10 foot screen and a gravel pack surrounding the well for the full length of the casing and screen (50 feet). The Ashumet well gravel pack is composed of 1.5 mm and 4.5 mm sized gravel and has a higher hydraulic conductivity than the aquifer. The effect of the gravel pack was modeled by increasing K_r and K_D in the pump node for the first seven layers, those which have the gravel pack. The model response to the increase in K_r and K_D in the pump node (K_w) is shown in figure 20. Comparing the effect of Kw on the calculated drawdown curves to the four major parameter effects leads to the conclusion that K_w is very similar to K_D.

The additional parameter, K_w, was calibrated along with the other four to match the shallow and deep drawdown curves. As shown in figure 21 the match was better with K_r = 0.267 ft/min., K_D = 0.5, S_y = 0.I, S_s = 6.8 x 10^{-6}, and the K_r in the well node increased by 2.42 and the K_D in the well node increased by 5.48.

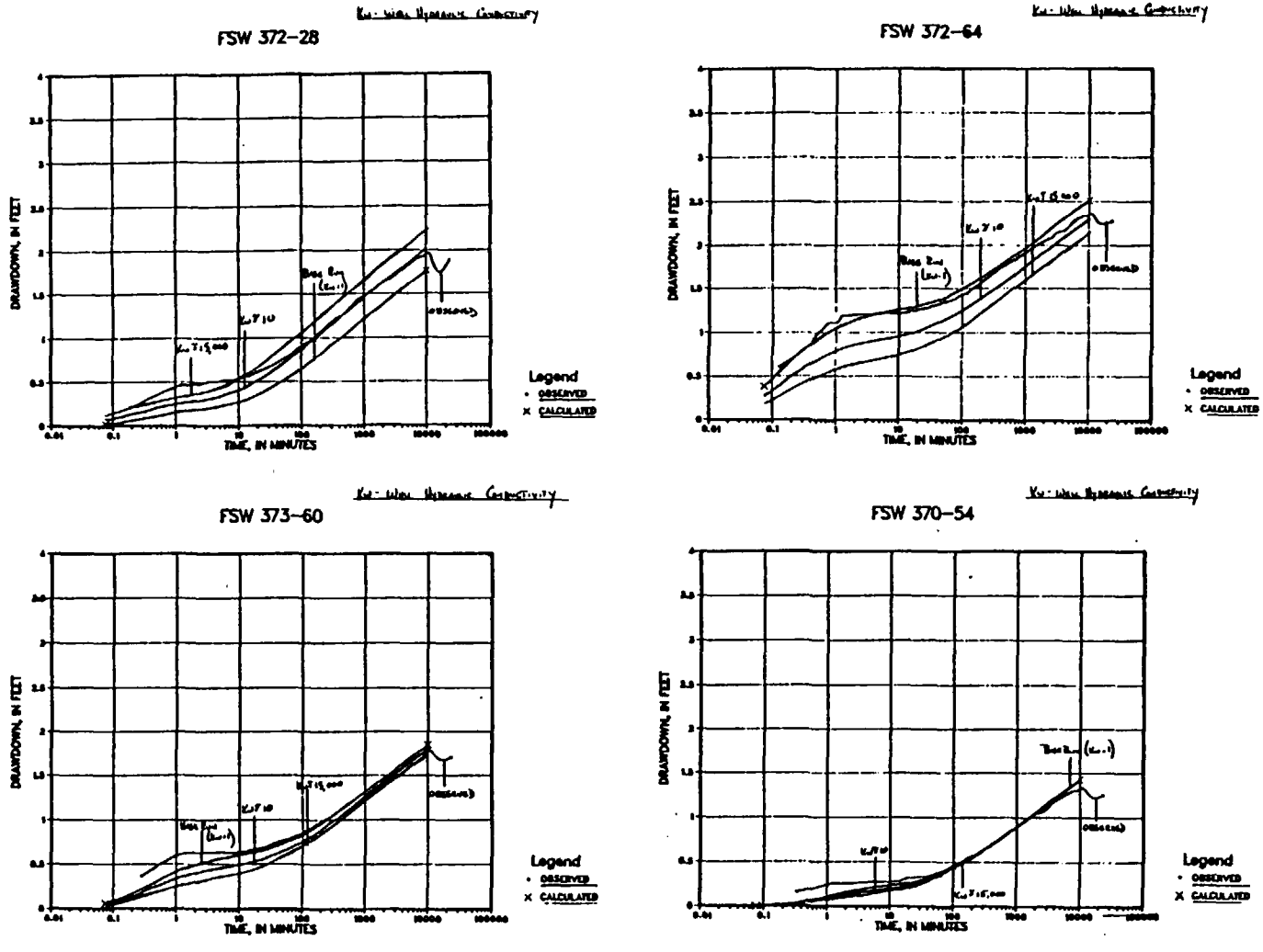

Figure 20, Model response to variations in the hydraulic conductivity around the pumping well

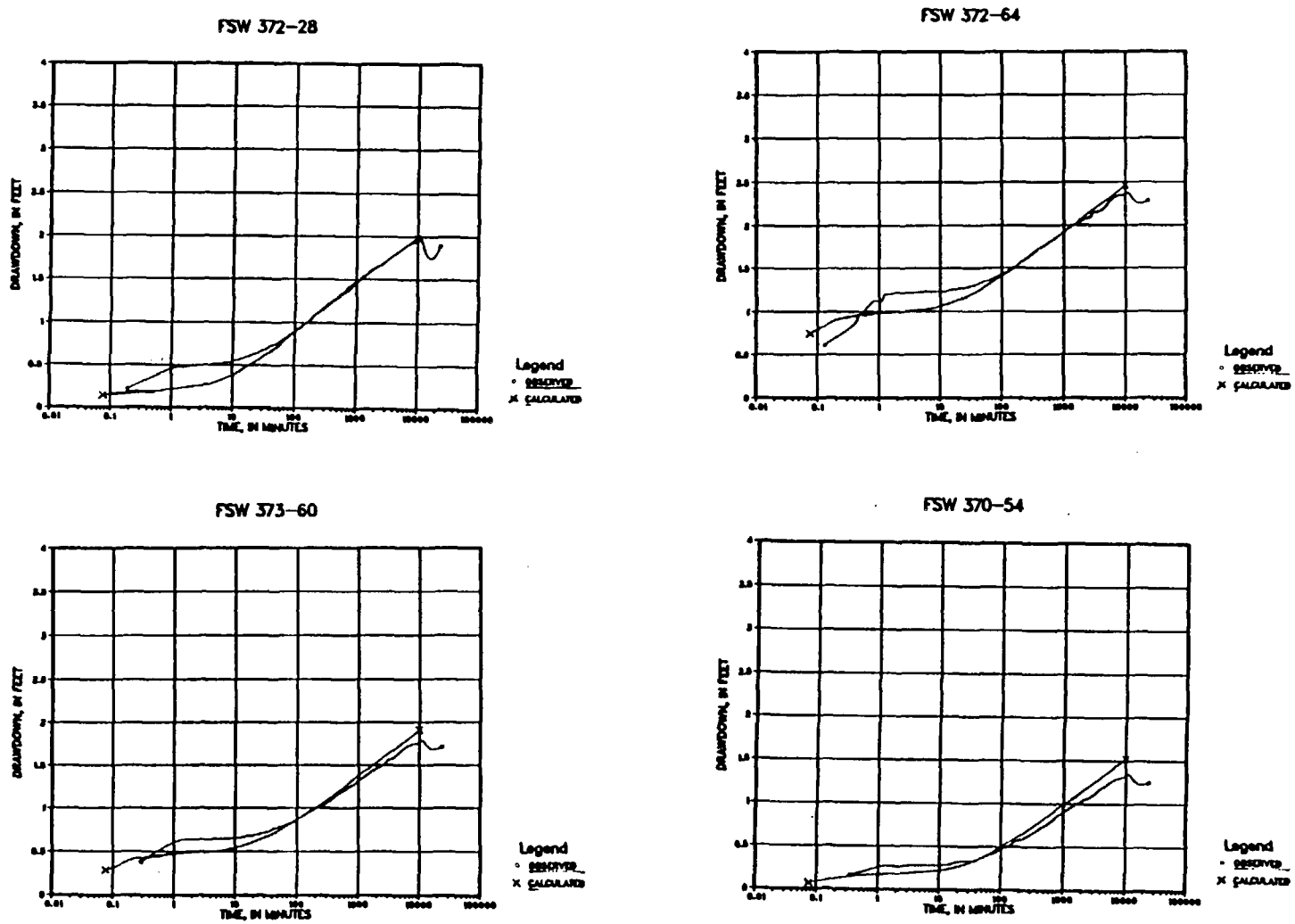

Figure 21. Model response to the calibrated parameters

Although the match to the wells FSW 372-28, 372-64, and 373-60 were good, the match at FSW 370-54 was not as good; obviously there is room for further improvement. In particular it would appear that increasing the specific yield would improve the fit for wells greater than 40 feet from the pumped well.

In conclusion, the results of this analysis indicate the following: 1) the observed drawdown curves are very sensitive to horizontal hydraulic conductivity with the calibrated value about 380 ft/day (.267 ft/min); 2) the vertical hydraulic conductivity affects the wells at smaller radial distances the strongest and as a parameter is highly correlated with the hydraulic conductivity of the gravel pack around the pumped well; 3) the best fit to vertical to horizontal hydraulic conductivity was about 0.5, but the range of this parameter may include values to 0.4 or lower; 4) the specific yield is in the range from 0.I to 0.2 and the specific storage is from 7×10^{-6} to 7×10^{-5}. The Ashumet well test was considered a success because the most important parameter for large-scale test design purposes, horizontal hydraulic conductivity, was accurately measured. It became clear, however, that the other parameters, in particular the ratio of vertical to horizontal hydraualic conductivity, were difficult to measure precisely due to the gravel pack extending above the screen along the well casing.

B. Small-scale Tracer Tests

In addition to the aquifer test, six small-scale tracer tests were conducted during the summer of 1984. The purpose of the small-scale tracer tests was to test equipment, tracer analysis

methods, and obtain estimates of aquifer porosity. These tests were particularly important for the experience gained in testing methods and approaches for application to the large-scale experiment.

1. Convergent Tracer Test

After the seven day Ashumet well aquifer test, a convergent tracer test was performed at the FSW 214 site. The convergent tracer test was conducted by injecting a slug of water, with 770 grams of bromide (diluted in 135 gallons, ≈ 1500 mg/l Br) as a nonreactive tracer, down observation well FSW 372-64 and collecting samples of the pump discharge. The tracer test lasted about eight hours and the concentration versus time curve is shown in figure 22. Analysis of the water samples for the bromide concentrations was performed both on site using an ion selective electrode method and by the U.S. Geological Survey's National Laboratory, which used an ion chromatographic method. The close comparison between the field and lab values indicated the ion selective electrode method was suitable for bromide analyses.

Convergent tracer test porosity estimates were calculated using two methods. In both cases steady-state flow to the pumped well was assumed and the time to peak concentration (210 minutes) was used to represent the average transit time for the solute to move through the aquifer to the pumped well. In the first approach to calculating porosity, the pattern of flow to the well is assumed to be either uniformly spherical:

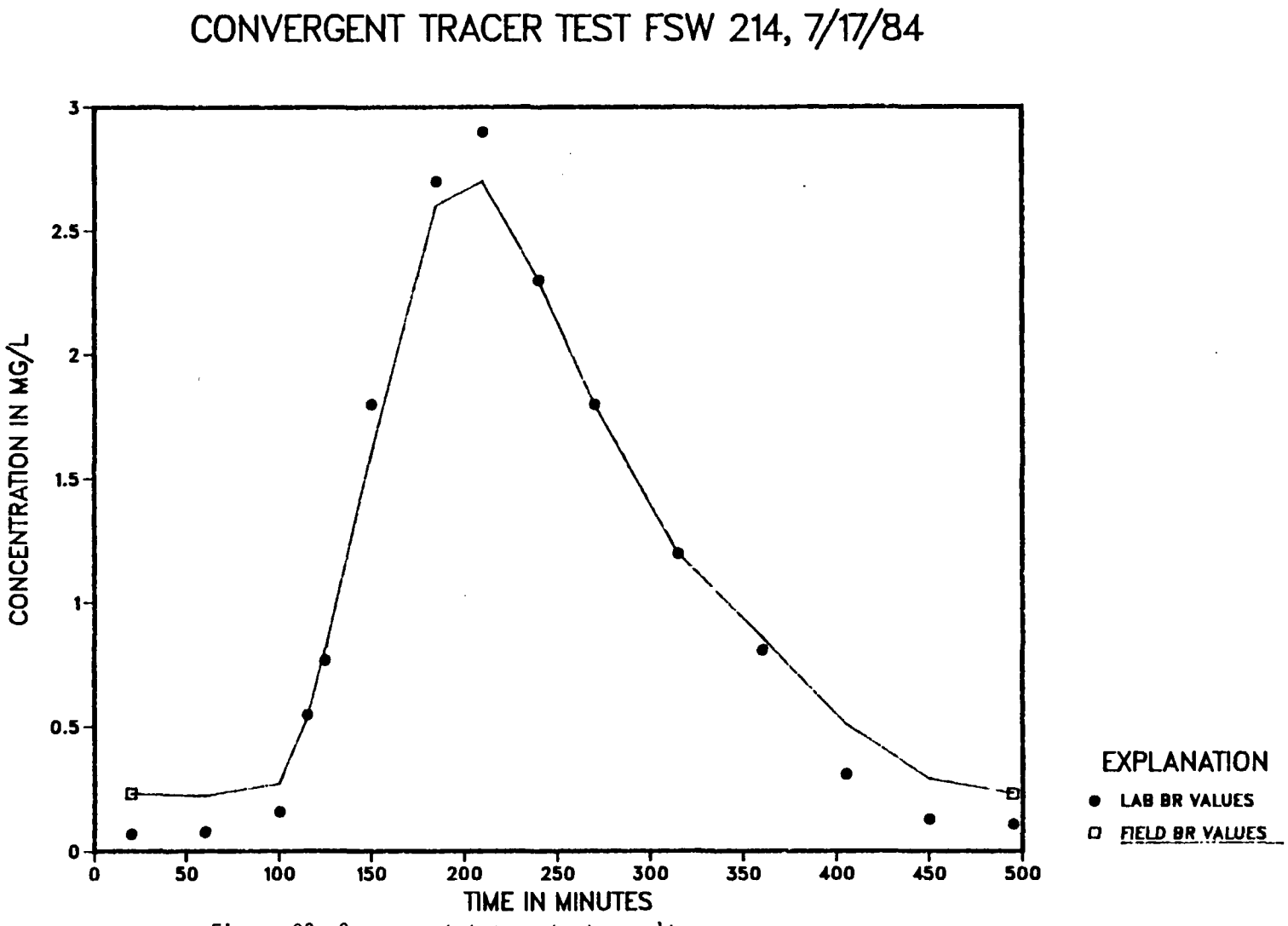

Figure 22. Convergent tracer test results

radial distance = 20.5 ft.

volume of sphere $= \frac{4}{3}\pi (20.5)^3 = 36{,}087\ ft^3$,

pumping rate = 475 gpm

time to peak = 210 minutes

volume pumped in time to peak = 13,336 ft^3,

$$\text{porosity} = \frac{\text{volume pumped}}{\text{volume of aquifer}} = 0.37;$$

or uniformly radial:

screened interval = 10 ft

volume of cylinder $= \pi(20)^2 10 = 12{,}566$

$$\text{porosity} = \frac{\text{volume pumped}}{\text{volume of aquifer}} = 1.06$$

It is obvious that the radial flow model is physically unrealistic and that the spherical model appears to give a much better representation of the flow regime close to the pump.

The other method used to calculate porosity for the convergent tracer test is based on the numerical model results. By rearranging the Darcy equation and using the time to peak concentration, an expression can be formed for porosity:

$$T = \text{total time} = t_1 + t_2 + ... + t_i,$$

$$= \frac{X_1}{V_1} + \frac{X_2}{V_2} + ... + \frac{X_i}{V_i},$$

$$= \sum_{i=1}^{N} \frac{nX_i}{K_i I_i}$$

solving for n:

$$n = \frac{T}{\sum_{i=1}^{N} \frac{X_i}{K_i I_i}}$$

where I is the gradient calculated using model simulated drawdowns and N is the number of interblock distances traveled by the solute from the injection well to the pumping well. Two porosity calculations were made using this method, one for the base run results (n=.41) shown in figure 16 (K_r = 0.267), and the other for the simulation with an increased hydraulic conductivity in the gravel pack around the well (n=.33), figure 21. It is apparent from this series of calculations that the calculated porosity is quite sensitive to the flow field around the pumped well, showing 20 percent changes in calculated porosity from two differing model simulations. These porosity estimates are close to the estimate (.35) used by LeBlanc (1984b) in solute transport modeling of the Otis contaminant plume and give a useful range for designing and interpreting the large-scale tracer test.

2. Doublet Tracer Tests

Three doublet tracer tests were conducted at separate locations (fig. 8) in the study area during summer 1984. The doublet tests were conducted using a pair of wells, one for injection, the other for pumping. For a given test, injection and pumping rates were equal, however, the rates varied from test to test (table 4). For two doublet tests (FSW 389-390, FSW 391-392) the pumped water was not injected back into the aquifer but was allowed to discharge about 100 feet from the pumping well. The water for injection was obtained from supply wells about 100 feet from the injection well. One double test (FSW 386-387) was conducted by recirculating the pump discharge into the injection well.

The change in concentration at the pumped well with time for each doublet test is shown in figures 23, 24, and 25. The FSW 389-390 test (fig. 23) has three peaks in the breakthrough curve. The second and third peaks cannot be explained using a solution of the advective-dispersion equation with uniform hydraulic properties; this suggests that aquifer hydraulic properties at this location are spatially variable. The breakthrough curve for the FSW 386-387 test shows a second peak, but this second peak is at double the time of the initial peak. Test FSW 386-387 was conducted using recirculation of pumped water and the second peak may be the rearrival of the first peak due to this recirculation. Test FSW 391-392 shows a small second peak, but of the three tests appears to most closely follow the theoretical doublet breakthrough curve. Generally, field analyses of bromide for the three tests closely match the USGS National laboratory measurements.

Table 4

Doublet Tracer Test Data and Porosity Calculations
(approach from Gelhar, 1982)

Date Well No.	Discharge (Q) (m^3/min)	Time (T) to Peak (min)	Distance (L) between wells (m)	Screened Interval (H)(m)
6/27/84				
FSW 389-390	0.0682	200	3.66	1.37
7/26/84				
FSW 386-387	0.0720	295	3.66	1.22
8/15/84				
FSW 391-392	0.0511	160	3.66	1.22

porosity, $n = Qt/T_pHL^2$, T_p = dimensionless time to peak

Date	Porosity $T_p = 1.1$	Porosity $T_p = 1.3$	Injected mass of B_r^- (g)
6/27/84	0.68	0.57	155
7/26/84	1.18	1.0	311
8/15/84	0.45	0.38	311

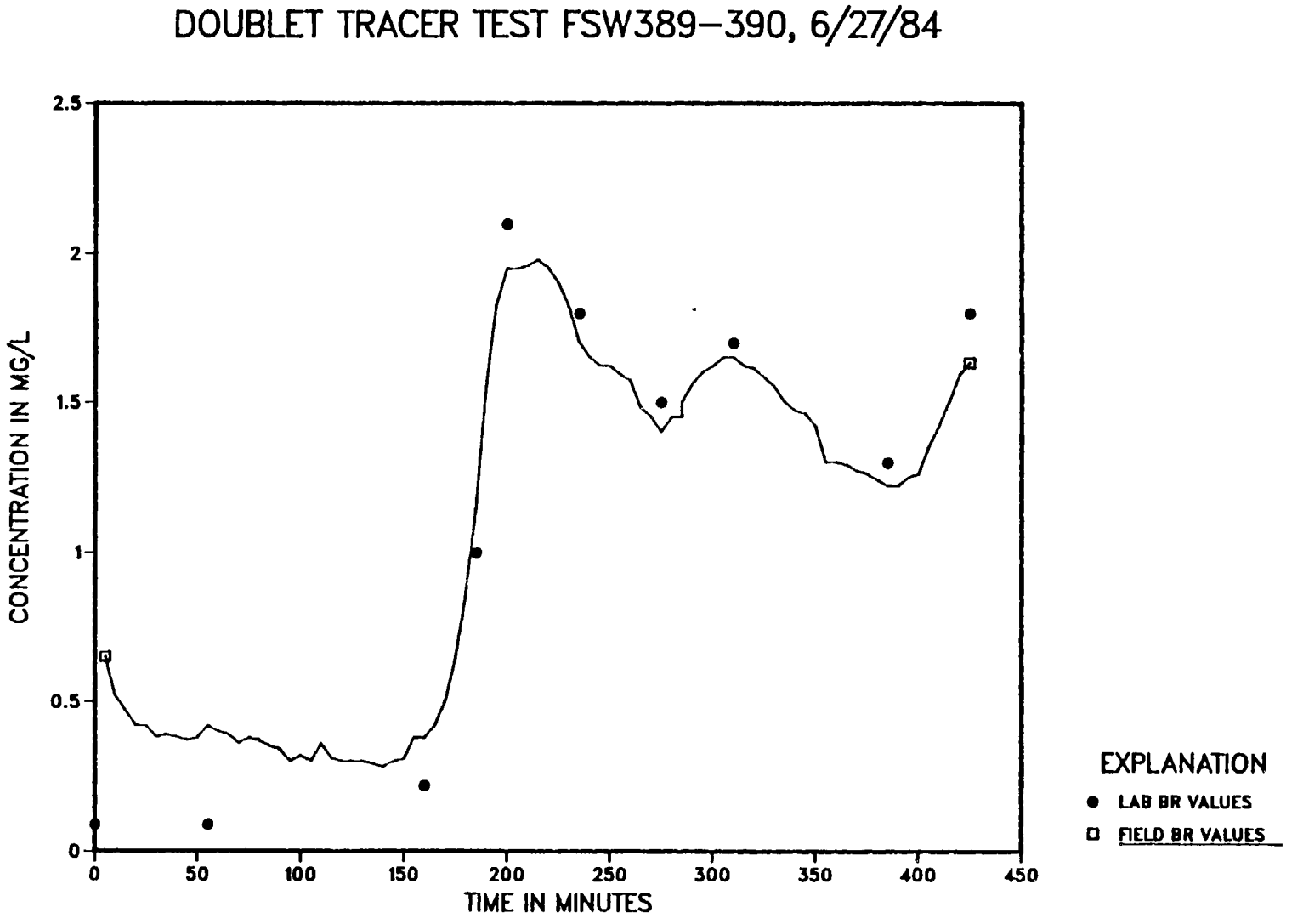

Figure 23. Doublet tracer test at FSW 389-390 results

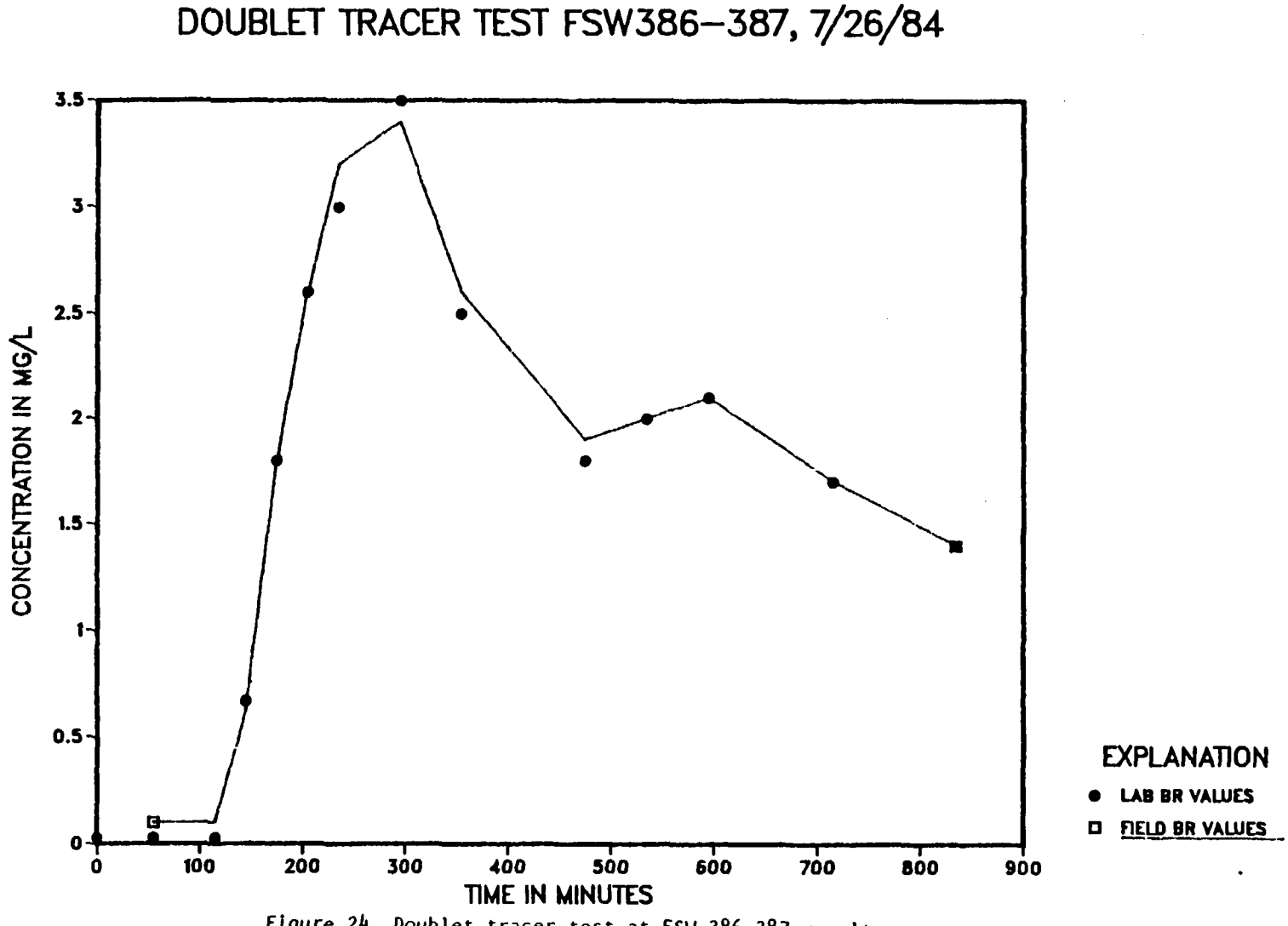

Figure 24. Doublet tracer test at FSW 386-387 results

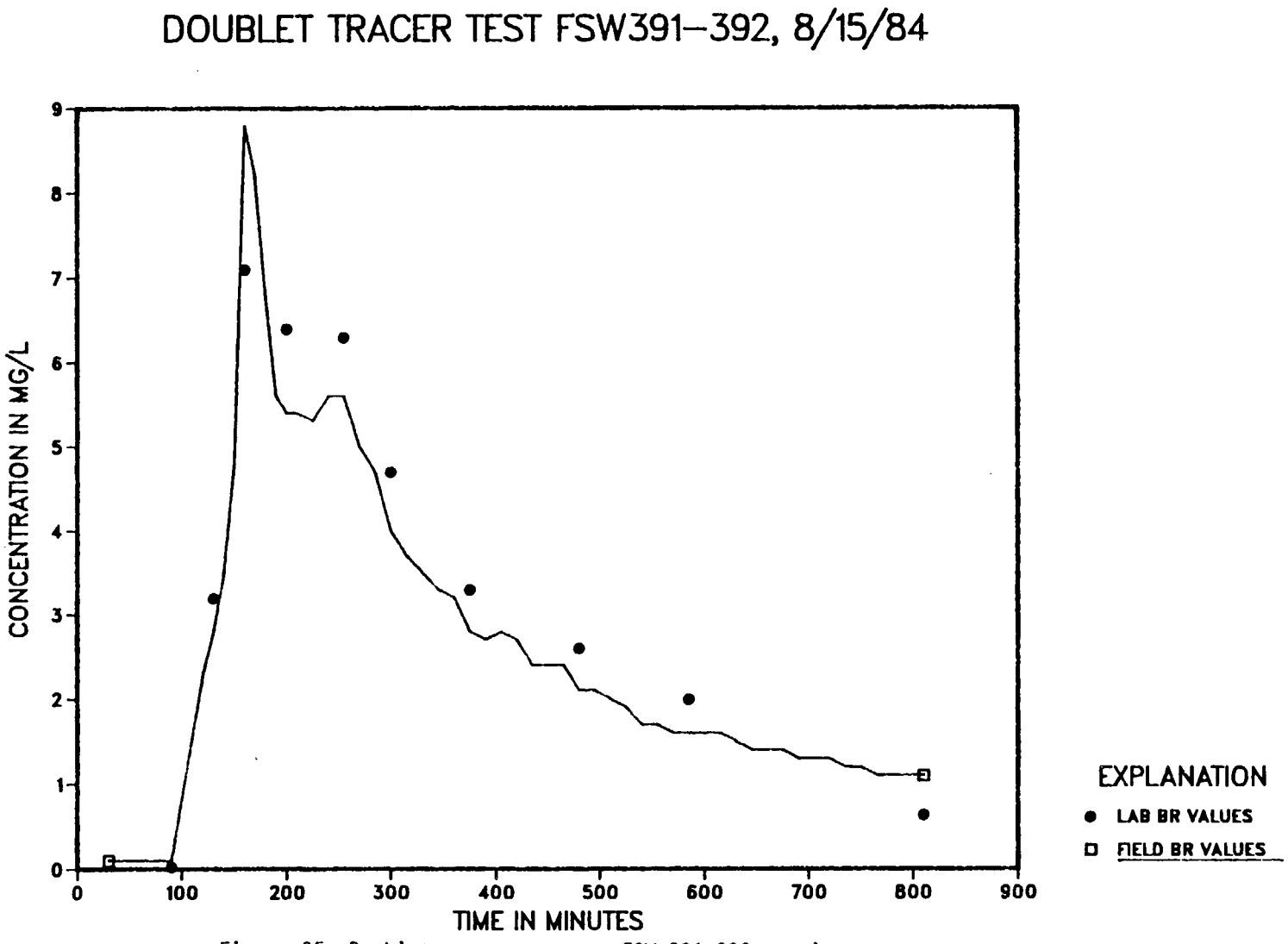

Figure 25. Doublet tracer test at FSW 391-392 results

Analysis of the three doublet tests for porosity, using the approach outlined by Gelhar (1982), is shown in Table 4. The dimensionless time (T_p) to peak concentration is varied from 1.1 to 1.3 in order to cover a range of longitudinal dispersivity values. The results of this analysis give porosity values which exceed the expected range (.33 to .41 from the convergent test) for tests FSW 389-390 and FSW 386-387. The calculated porosity for test FSW 391-392 overlaps the expected range and gives the most reasonable results.

The differences between calculated porosity for the three tests are due to the discharge rate - time to peak relationship. As shown in Table 4, the time to peak concentration increases as the pumping rate increases. The expected relationship for an aquifer with constant porosity would be for a decreased time to peak with an increased pumping rate. Therefore one or more of the major assumptions used in this analysis must be violated; the most likely is the assumption of two-dimensional flow. The well screens are 4 feet long and do not fully penetrate the sand and gravel aquifer, which varies from 80 to 140 feet thick across the study area. The flow field near the pumping and injection wells should include a vertical component and increasing the flow rate could cause a larger vertical component of flow. Therefore, the large calculated porosities for tests FSW 389-390 and FSW 386-387 are likely the result of the solute moving through a thicker section of the aquifer than the screened interval. For example, if porosity is fixed at 0.39 and the screened interval (ft) is calculated for test FSW 386-387, the result is an apparent thickness of 10 to 12 feet. This indicates a

strong vertical component of flow for this test, with flow between the doublet pair traveling through 2.5 to 3 times the thickness of the screened interval.

Test FSW 391-392 is compared to type curves for varying dispersivity values in figure 26 and table 5. Test FSW 39l-392, because of a lower pumping rate, most closely matches a theoretical doublet test breakthrough curve. It is apparent that although the peak concentration most closely matches the curve with epsilon (α/l, a ratio of longitudinal dispersivity to the distance between injection and pumping wells) equal to 0.2 (α = 2.4 ft or 0.73 m), the initial part of the FSW 39l-392 curve is too steep for a good match. The steep rise in the FSW 391-392 curve would indicate a smaller value of epsilon, perhaps from 0.02 to 0.002, but the peak concentrations would not match with this range of dispersivity values.

The difficulty in matching the FSW 391-392 curve points out a major problem in using doublet tracer tests to measure aquifer dispersivity at the Cape Cod site. It is likely that the breakthrough curves for doublet tests in sand and gravel aquifers are very sensitive to the local heterogeneities in hydraulic conductivity. For a perfectly stratified aquifer, one in which the hydraulic conductivity varies vertically but not laterally, the total breakthrough curve is the superposition of the individual breakthrough curves for each layer of the aquifer. The total breakthrough curve then has greater spread around the peak concentration than a curve for a homogeneous aquifer because of the different transit times for each layer in the aquifer. For the sand

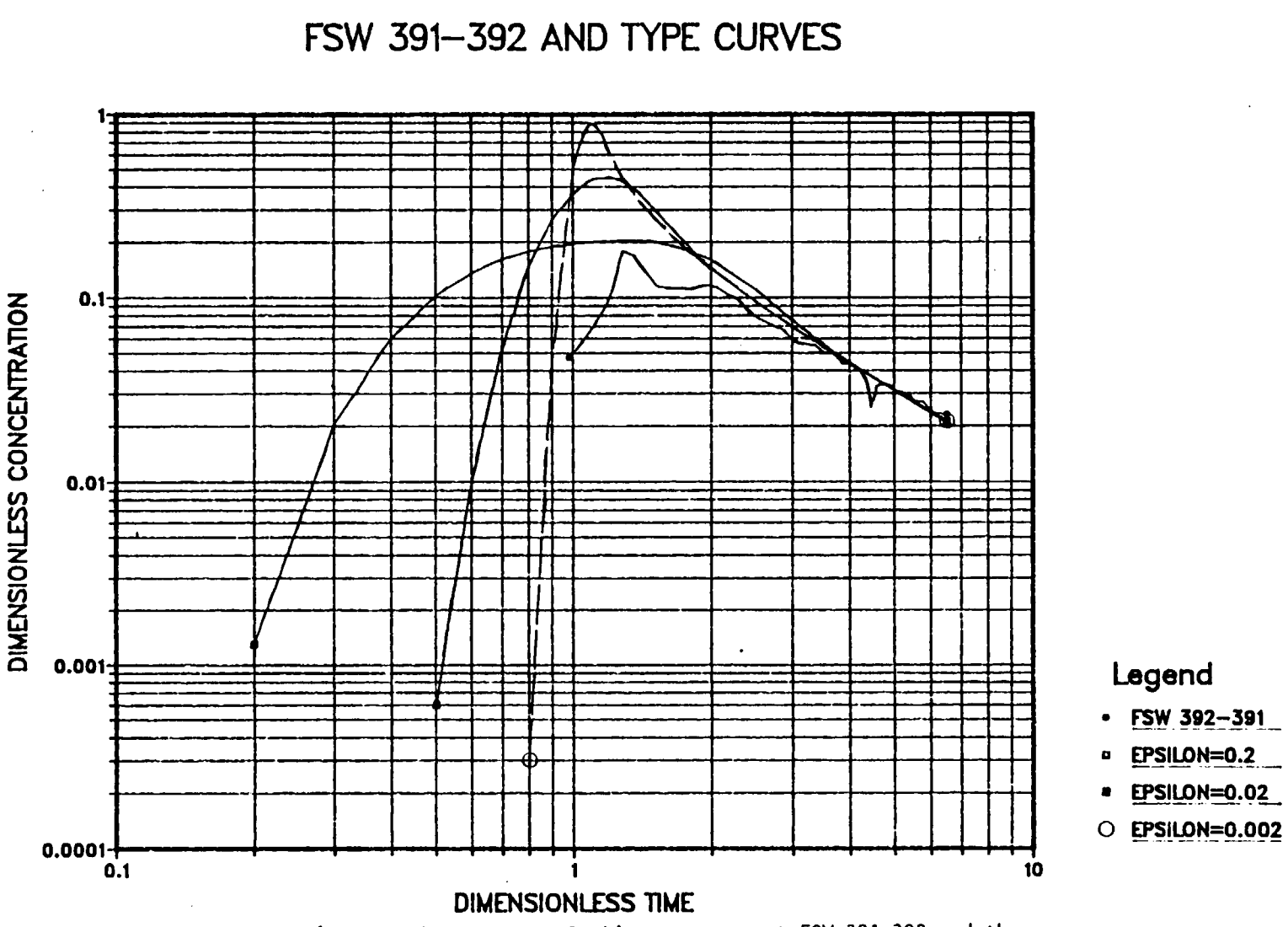

Figure 26. Comparison between Doublet tracer test FSW 391-392 and the results using a type curve analysis

Table 5

Analysis of Doublet Tracer Test FSW 391-392
(approach from Gelhar, 1982)

Time (min)	T*	Concentration (mg/L)	$\hat{C}$**
0-90	0-0.722	0.0	0.0
120	0.979	2.3	0.047
130	1.04	2.8	0.057
140	1.12	3.5	0.072
150	1.20	4.8	0.098
160	1.28	8.8	0.180
170	1.36	8.2	0.168
180	1.44	6.8	0.139
190	1.52	5.6	0.115
200	1.60	5.4	0.111
210	1.69	5.4	0.111
225	1.81	5.3	0.109
240	1.93	5.6	0.115
255	2.05	5.6	0.115
270	2.17	5.0	0.102
285	2.29	4.7	0.096
300	2.41	4.0	0.082
315	2.53	3.7	0.076
330	2.65	3.5	0.072
345	2.77	3.3	0.068
360	2.89	3.2	0.066
375	3.01	2.8	0.057
390	3.13	2.7	0.055
405	3.25	2.7	0.055
420	3.37	2.7	0.055
435	3.49	2.4	0.049
450	3.61	2.4	0.049
465	3.73	2.4	0.049
480	3.85	2.1	0.043
495	3.97	2.1	0.043
510	4.09	2.0	0.041
525	4.21	1.9	0.039
540	4.33	1.7	0.035

Table 5 continued

Time (min)	T*	Concentration (mg/L)	$\hat{C}$**
555	4.45	1.7	0.035
570	4.57	1.6	0.033
585	4.69	1.6	0.033
600	4.81	1.6	0.033
615	4.94	1.6	0.033
630	5.06	1.5	0.031
645	5.18	1.4	0.029
660	5.30	1.4	0.029
675	5.42	1.4	0.029
690	5.54	1.3	0.027
705	5.66	1.3	0.027
720	5.78	1.3	0.027
735	5.90	1.2	0.025
750	6.02	1.2	0.025
765	6.14	1.1	0.023
780	6.26	1.1	0.023
810	6.50	1.1	0.023

* $T = \frac{Qt}{nHL^2} = 0.008025\ t$

$Q = 0.0511\ m^3/min$

$n = .39$

$H = 1.22\ m$

$L = 3.66\ m$

** $\hat{C} = \frac{nHL^2C_w}{M} = 0.0205\ C_w$

$M = 311g$

and gravel aquifer at the Cape Cod site, the perfectly stratified model is likely not appropriate for distances greater than a few feet because individual lenses can not be identified for longer distances. The total breakthrough curve for greater distances then becomes an integrated measure of individual transit times of flow lines that do not follow the assumed curvilinear path in the doublet pair analysis. Therefore, dispersivity was not uniquely identified in test FSW 391-392, most likely due to unknown hydraulic conductivity variations.

3. Divergent tracer tests

Two divergent tracer tests were conducted at separate locations (Fig. 8) in the study area during summer 1984. The divergent tests involved injecting bromide as a pulse in a constant flow of water into the aquifer and collecting samples for analysis at increasing distances (5 to 20 feet) from the injection well. For each test the water for injection was pumped from a supply well at least 150 feet from the injection well and the water was injected into the aquifer through a four foot screened interval. Samples were collected using multilevel samplers, each with nine ports one foot apart, which straddled the injection zone. A list of sampler distances, pump rates, and other test data is given in table 6; a schematic of the test wells and equipment is shown in figure 27.

The objectives of the divergent tracer tests were to test the multilevel sampler design and completion method, and to obtain qualitative information on hydraulic conductivity contrasts in the sand and gravel outwash aquifer. The multilevel samplers (MLS) were constructed using 1 1/4 inch PVC pipe, with 1/4 inch

Table 6

Divergent Tracer Test Data

Well Number	FSW 393	FSW 394
Depth below surface	37 ft.	36 ft.
Date of test	9/5-6/84	8/8-9/84
Distance from supply well to injection well	153 ft.	160 ft.
Pumping rate	25 gpm	22 gpm
Injection mass of B_r^-	462g	462g
Initial B_r^- concentration	1500 mg/L	1500 mg/L

Sampler distances from injection well and completion method	distance	drilling method	bentonite seal	
	5.45	auger	yes	5.5, 10, 20 ft. all drilled using an auger & bentonite seals
	10.30	drive & wash	no	
	10.30	auger	yes	
	10.50	drive & wash	yes	
	10.75	auger	no	
	19.80	auger	yes	

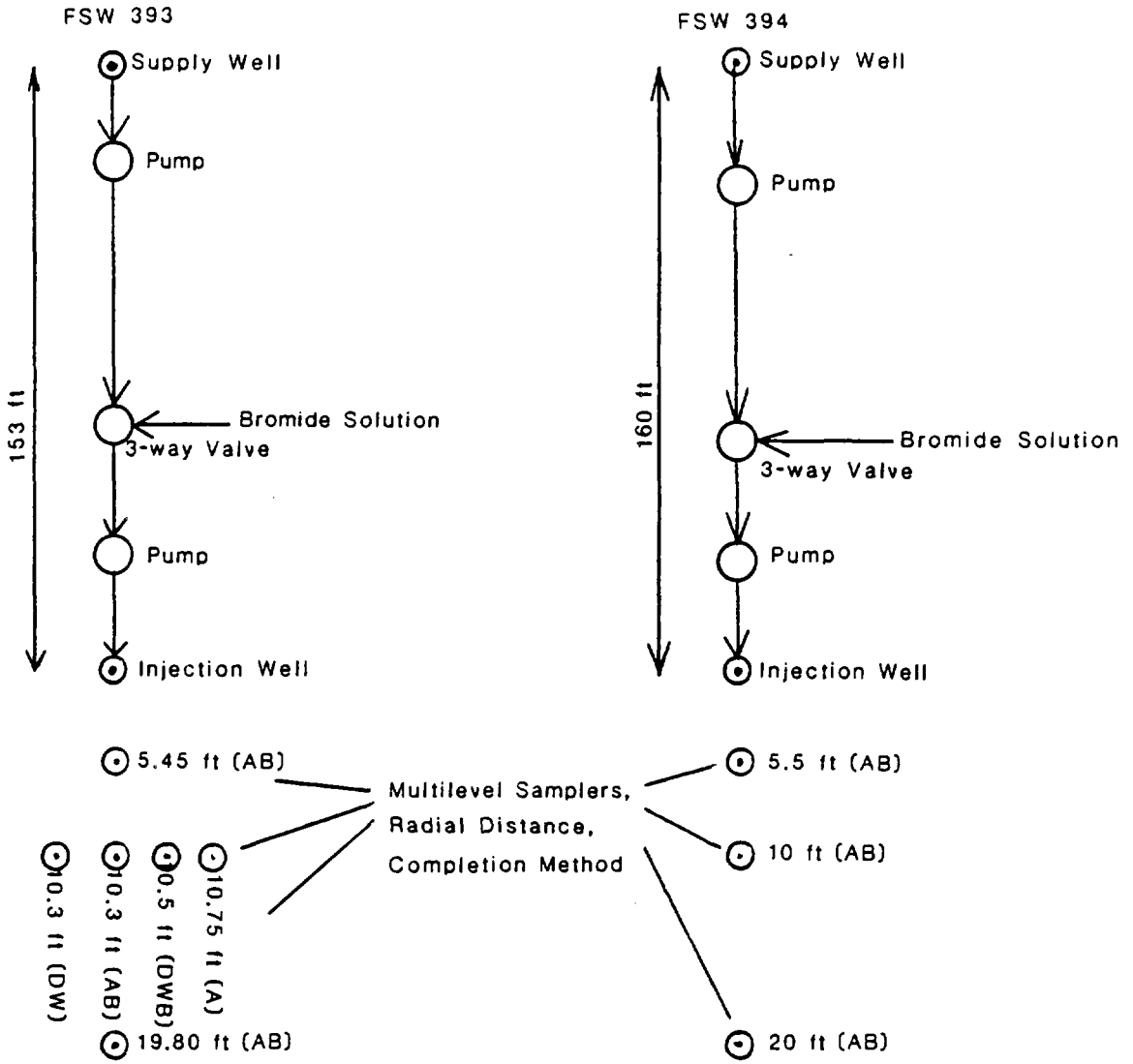

Figure 27. Schematic diagram of divergent test operation.

Completion of multilevel samplers included:

A - auger drilling with no bentonite

AB - auger drilling with bentonite seals

DW - drive and wash drilling with no bentonite

DWB- drive and wash drilling with bentonite seals

polyethylene tubing strung inside the pipe and brought outside through a hole drilled just above the desired interval. The tubing was cut and wrapped with nylon cloth and bound with stainless steel wire to the pipe; tubing openings (ports) were spaced one foot apart for the divergent tracer tests. The tubes were marked with colored tape at the surface and were named (from top to bottom) red (R), double red (RR), blue (B), double blue (BB), green (G), double green (GG), and black (BL). This MLS design is not only inexpensive and relatively easy to construct, but it also protects the tubing inside the pipe during installation.

Four variations of MLS construction and installation methods were tested as part of the 9/5-6/84 experiment at FSW 393. Most of the MLS were constructed with bentonite packs between each sampling port. The bentonite packs were made using plastic screening to hold bentonite pellets as bundles around the 1 1/4 inch PVC pipe. Two of the MLS were constructed without the bentonite packs. Most of the MLS were installed using a 3 1/4 inch internal diameter hollow-stem auger; two of the MLS were installed using a drive and wash drilling method. The four variations (auger or drive and wash, with or without bentonite) were used at the same radial distance at FSW 393 (see table 6 and figure 27).

Examples of the breakthrough curves for the 9/5-6/84 test at FSW 393 are shown in figure 28. It is apparent that there is a two-fold difference in peak concentration arrival times between the slowest and fastest zones sampled in this test. It is also apparent that the order of peak arrival times (bottom, top, middle samplers) were the same for the 5 and 10 foot samplers. Although most of the

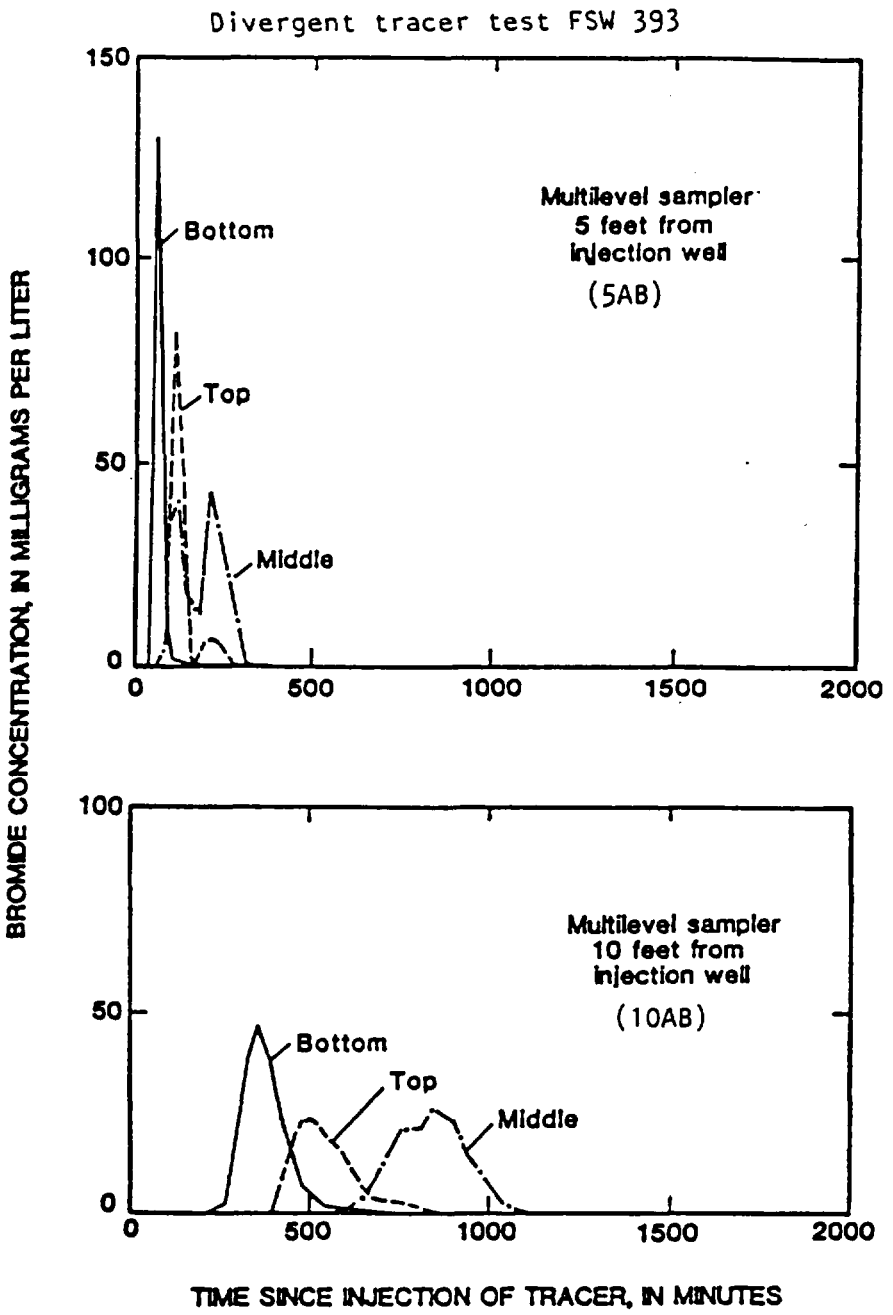

Figure 28. Breakthrough of conservative bromide tracer at top, middle, and bottom of injection zone in two multilevel samplers, divergent-flow tracer test, September 1984. Injection-well screen is 4 feet long.

breakthrough curves have single peak values, there are two distinct peak values for the 5 foot middle sampler (Y). This double peak result could not have been predicted using a solution of the advective-dispersion equation with homogeneous aquifer properties. It is likely that the double peak was due to the heterogeneity of aquifer hydraulic conductivity and porosity, causing the local variations in velocity necessary to create the arrival of two distinct pulses of solute at different times.

A comparison of peak arrival times at different depths and distances for the two divergent tracer tests is shown in figures 29 and 30. The peak arrival times for the FSW 394 (8/8-9/84) test (fig. 29) showed that the solute cloud spread above and below the injection zone and that these arrival times were up to five times longer than the arrival times at the center of the injection zone. This pattern of solute movement is due to the induced vertical movement of water flowing from the partially penetrating injection well. This general pattern is modified for the FSW 393 (9/5-6/84) test (fig. 30) by the presence of a low velocity zone (Y) in the middle of the injection zone. The peak arrival time for the slow zone (Y) is about double that of the fastest zone. This indicates that the ratio of hydraulic conductivity to porosity (K/n) varies by at least a factor of two in this aquifer. This observation assumes that the flow is axisymmetric and constant, but in comparison to the peak arrival times for FSW 394 (fig. 29) it is noted that the middle sampler (Y) should have the shortest arrival time. Therefore the contrast in K/n should actually be greater than the two fold difference indicated by the FSW 393 test.

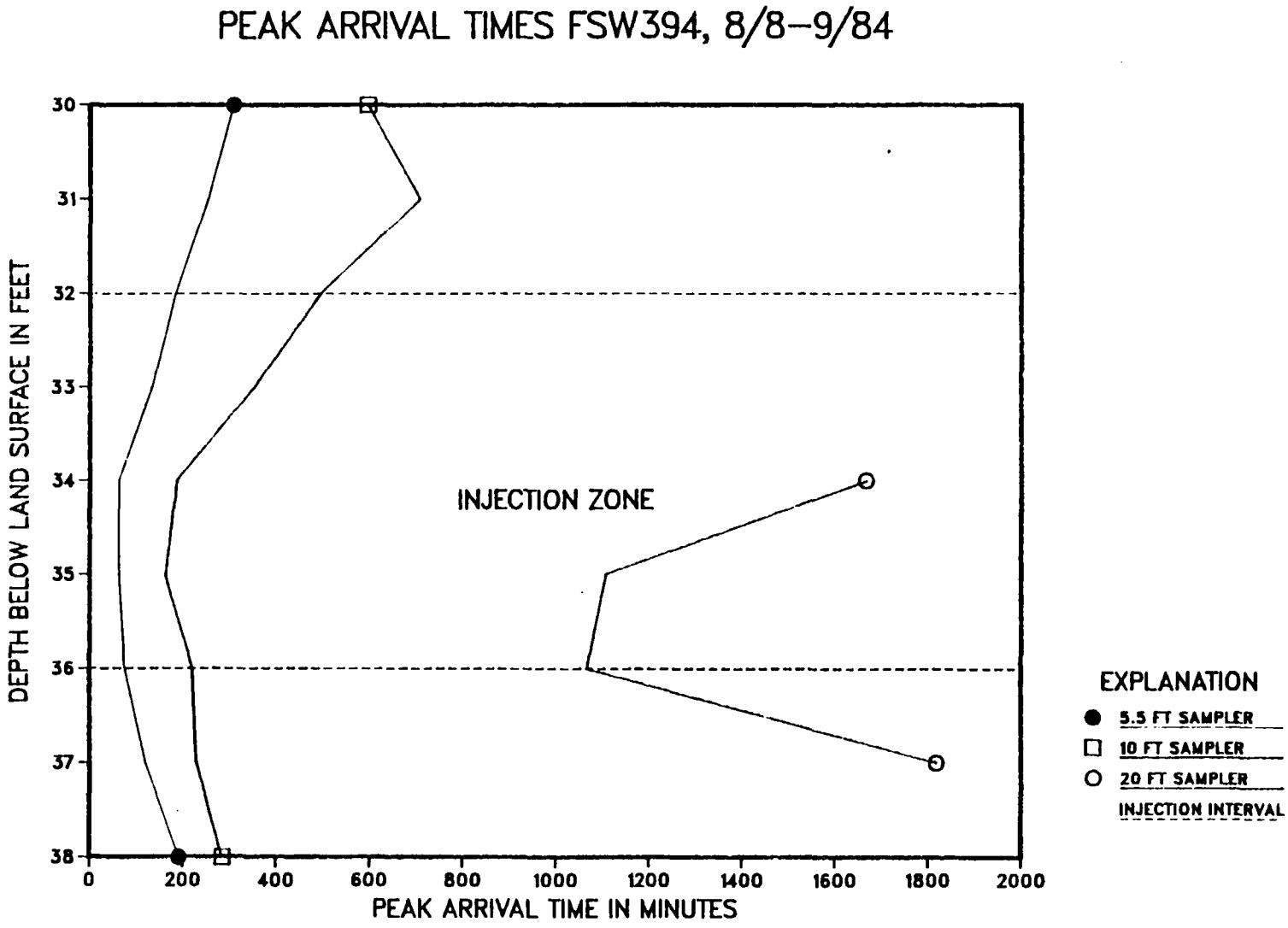

Figure 29. Peak arrival times by depth for divergent tracer test FSW 394

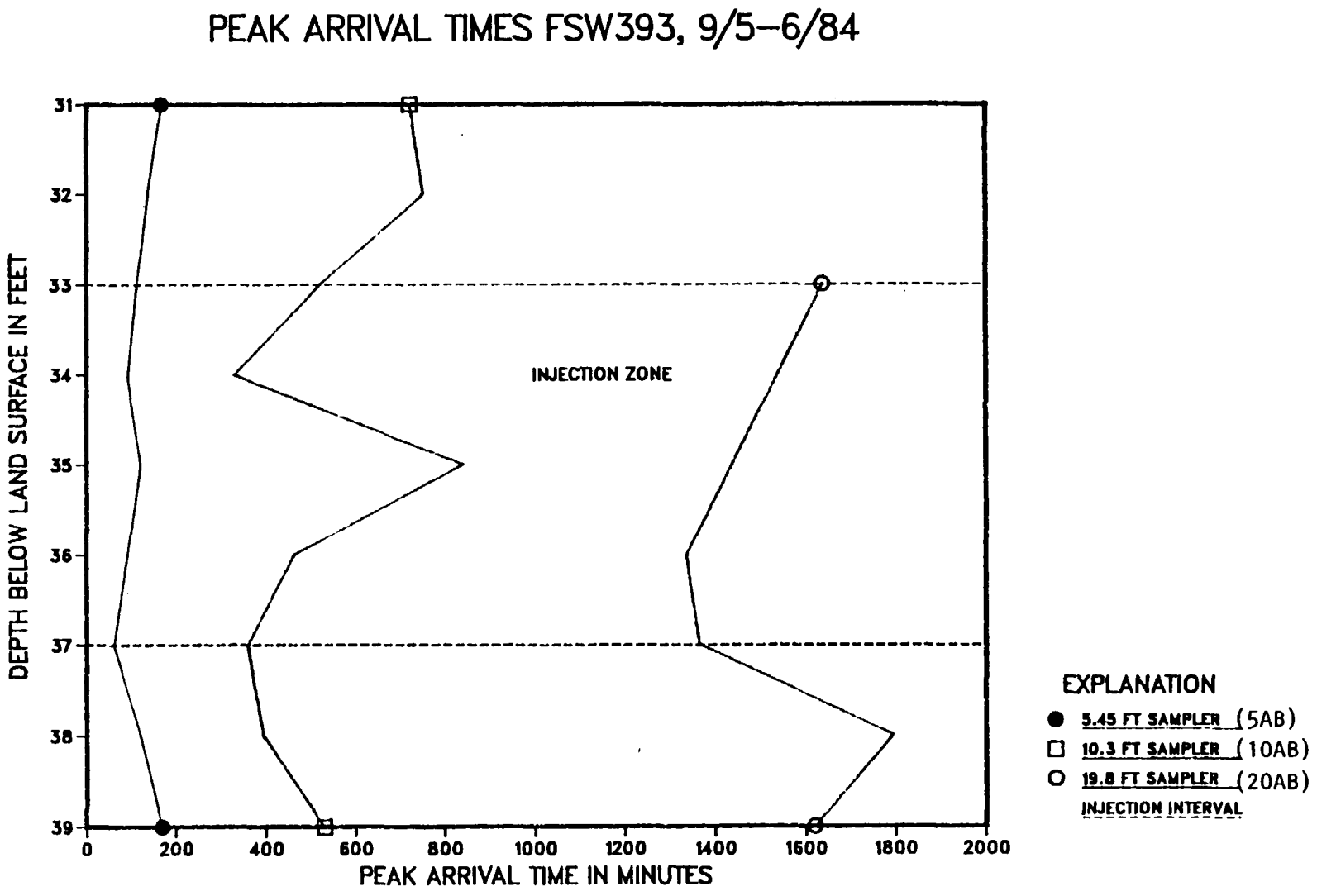

Figure 30. Peak arrival times by depth for divergent tracer test FSW 393

A comparison of the ratio of peak arrival times at different radial distances to the calculated ratios based on radial or spherical flow is given in tables 7 and 8. This comparison indicates that the ratio of arrival times for the FSW 393 test (table 7) were generally between the ratios expected for radial and spherical flow. This result seems reasonable for a partially penetrating well where a significant vertical flow is expected to occur. The ratio of arrival times ($T_{10}/T_{5.5}$) for the FSW 394 test (table 8) were consistently less than the expected ratio for radial flow. This result, along with the significant differences between the T_{10}/T_5 and T_{20}/T_{10} ratios for both tests, indicates that the flow fields were not only complex due to partial penetration causing three dimensional flow, but that the spatial variation in the K/n ratio was causing other velocity differences.

The spatial variations in the velocity field are illustrated by a comparison of MLS peak arrival times for the FSW 393 test (fig. 31), all at about a 10 foot radial distance. Each of these samplers was installed using a different drilling or completion technique. The most apparent difference between the samplers is the consistent increase in average peak arrival time from left to right (facing toward the injection well). The differences that occur are not due to type of well or drilling method, but due primarily to position. Within some intervals there is greater than a 3 fold difference in the peak arrival times. There are apparently consistent slow and fast zones in this illustration; however; it is difficult to estimate the size of the features which have caused this pattern.

Table 7

Peak Arrival Times for FSW 393 (9/5-6/84) Divergent Tracer Test (in minutes) For Samplers with Auger Installation and Bentonite Seals

Level (Depth, ft)	5.45 ft. sampler	10.30 ft. sampler	19.80 ft. sampler	$T_{10.3}/T_{5.45}$	$T_{19.8}/T_{10.3}$
R (31)	166	724	/	4.36	
RR (32)	135	754	/	5.59	
B (33)	110	520	1637	4.73	3.15
BB (34)	90	329	/	3.66	
Y (35)	120	841	/	7.01	
YY (36)	90	462	1335	5.13	2.89
G (37)	60	359	1365	5.98	3.80
GG (38)	120	395	1794	3.29	4.54
BL (39)	168	530	1619	3.16	3.06

	Expected Time Ratio ($T_1/T_2 = r_1^n/r_2^n$)	
	radial (n = 2)	spherical (n = 3)
$T_{10.3}/T_{5.45}$	3.57	6.75
$T_{19.8}/T_{10.3}$	3.70	7.10

Table 8

Peak Arrival Times for FSW 394 (8/8-9/84) Divergent Tracer Test (in minutes)

Level (Depth, ft)	5.5 ft. sampler	10. ft. sampler	20 ft. sampler	$T_{10}/T_{5.5}$	T_{20}/T_{10}
R (30)	307	597	/	1.95	
RR (31)	251	708	/	2.82	
B (32)	181	495	/	2.74	
BB (33)	131	352	/	2.69	
Y (34)	60	185	1666	3.08	9.01
YY (35)	63	161	1105	2.56	6.86
G (36)	75	222	1065	2.96	4.80
GG (37)	119	230	1817	1.93	7.90
BL (38)	190	285	/	1.50	

	Expected Time Ratio ($T_1/T_2 = r_1^n/r_2^n$)	
	radial (n = 2)	spherical (n = 3)
$T_{10}/T_{5.5}$	3.31	6.01
T_{20}/T_{10}	4.0	8.0

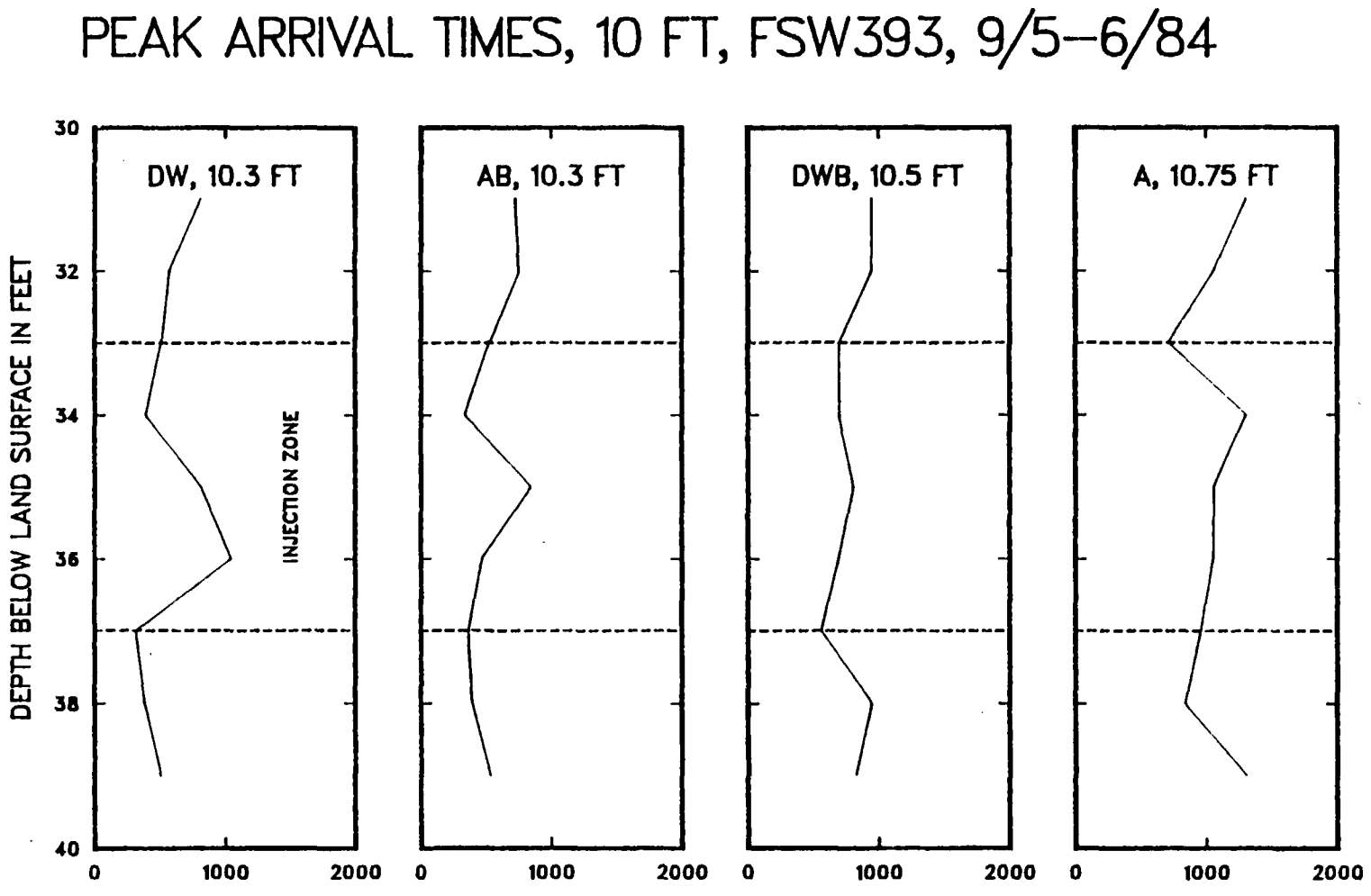

Figure 31. Divergent tracer test FSW 393

Conclusions that can be drawn from the divergent tracer test include the following. There is no apparent difference in the performance of differing MLS due to construction or installation methods in this type of aquifer. There is significant vertical movement of solutes during divergent tracer tests using partially penetrating injection wells. The three-dimensional nature of the flow field, combined with the variation in aquifer hydraulic properties, make a quantitative interpretation of these tests difficult; however, valuable qualitative information was obtained. In particular, there was little indication of smearing due to vertical mixing along the samplers. Along with this MLS performance data, these tests indicated up to a 3 fold variation in the velocity of solutes in the aquifer. This information was useful during the design of the large-scale test, covered in the next section.

III. Large Scale Tracer Test

A. Design of the Large-scale Tracer Test

I. Purpose and Scope

The purpose of the large-scale tracer test was to measure the dispersivity of the aquifer in the sewage plume area in Falmouth, Massachusetts. As indicated in the introduction, several theoretical studies (Gelhar and Axness, 1983; Dagan, 1982) have shown that it should be possible to predict the applicable field value of dispersivity for conservative solutes using statistical measures of the hydraulic conductivity variations in an aquifer. An experimental program was initiated to perform the necessary measurements to test these theoretical results. The general approach in the program was to measure the dispersivity of the aquifer using tracer tests and also to measure the statistical properties of the aquifer hydraulic conductivity. The statistical measures could then be used to calculate a predicted dispersivity which would be compared with the measured dispersivity from the tracer tests. Along with this major objective, the large-scale tracer test was used to examine methods to estimate average distribution coefficients, and to examine the degree to which laboratory values of geochemical model parameters would represent conditions observed during transport of reactive solutes in the field.

In this section the design, implementation, and analysis of the large-scale natural-gradient tracer test is presented. The design of the large-scale test included site selection, measurement of head at the site for solute velocity estimation, design of a sampling network, further refinement of multi-level sampler design, a pre-

test tracer experiment, selection of tracers and mass, and design of sample collection and analysis. The implementation of the large-scale test involved sampling and analysis for nonreactive and reactive tracer distributions, projection of tracer movement, and installation of samplers to stay ahead of the tracer cloud. Analysis of the tracer test included calculations of the spatial moments and the interpretation of these results.

2. Location of the Large-Scale Natural-Gradient Tracer Test

The large-scale tracer test location is in an abandoned sand and gravel pit in the northeast corner of Falmouth, Massachusetts (fig. 8) between the sewage disposal beds on Otis Air Base and Ashumet Pond. This location was chosen for the following reasons. The depth to water was less than 25 feet and therefore was within suction limit, a requirement for use of the multi-level samplers. The property is owned by the State of Massachusetts, operated by the Division of Fisheries and Wildlife as part of the Crane Wildlife Management Area. The state gave its permission to use the sand and gravel pit for this test, which included cutting trees and altering the terrain. The sewage contaminated ground-water plume, originating from Otis Air Base, is under the sand and gravel pit area. Although this presented problems with analyses for solute concentration, the presence of the plume made this water unpotable. Therefore the Massachusetts Department of Environmental Quality Engineering (DEQE) had little problem with the introduction of the tracers into the aquifer. The sand and gravel pit is close to USGS field operations on Otis Air Base; this made coordinating activities

at the test site much easier. The sand and gravel pit is about 700 feet long and this was considered a large enough travel distance for the large-scale test. These reasons, particularly the access and DEQE permission, made the sand and gravel pit an attractive site for the large-scale test.

3. Water Table, Direction of Ground-Water Flow, and Initial Grid

A network of observation wells was installed in the sand and gravel pit area to measure ground-water levels and to define the water table for the large-scale tracer test. Observation wells were generally 2 inch PVC with 2 foot screens. Most wells were set 10 to 20 feet below the water-table, with some set deeper to measure head differences with depth. Observation well locations and the water-table altitude contours are shown in figure 32.

The water table slopes to the southeast, toward Ashumet Pond, and the water-table gradient ranges between 0.0014 and 0.0018 in the sand and gravel pit area. The water table fluctuates seasonally on Cape Cod, with high levels in early spring and low levels in late fall. The water-level trends for three wells in the sand and gravel pit area over the period of the large-scale tracer test are shown in figure 33. During the tracer test period (July 1985 to December 1986) water levels were low, with small increases in September 1985 and spring 1986. Water-level variations were about 1 foot during the 1.5 year period of the test. Also apparent from these hydrographs are the large drop before the test and large increases after the test. These hydrograph fluctuations were in direct response to the amount of recharge available from precipitation.

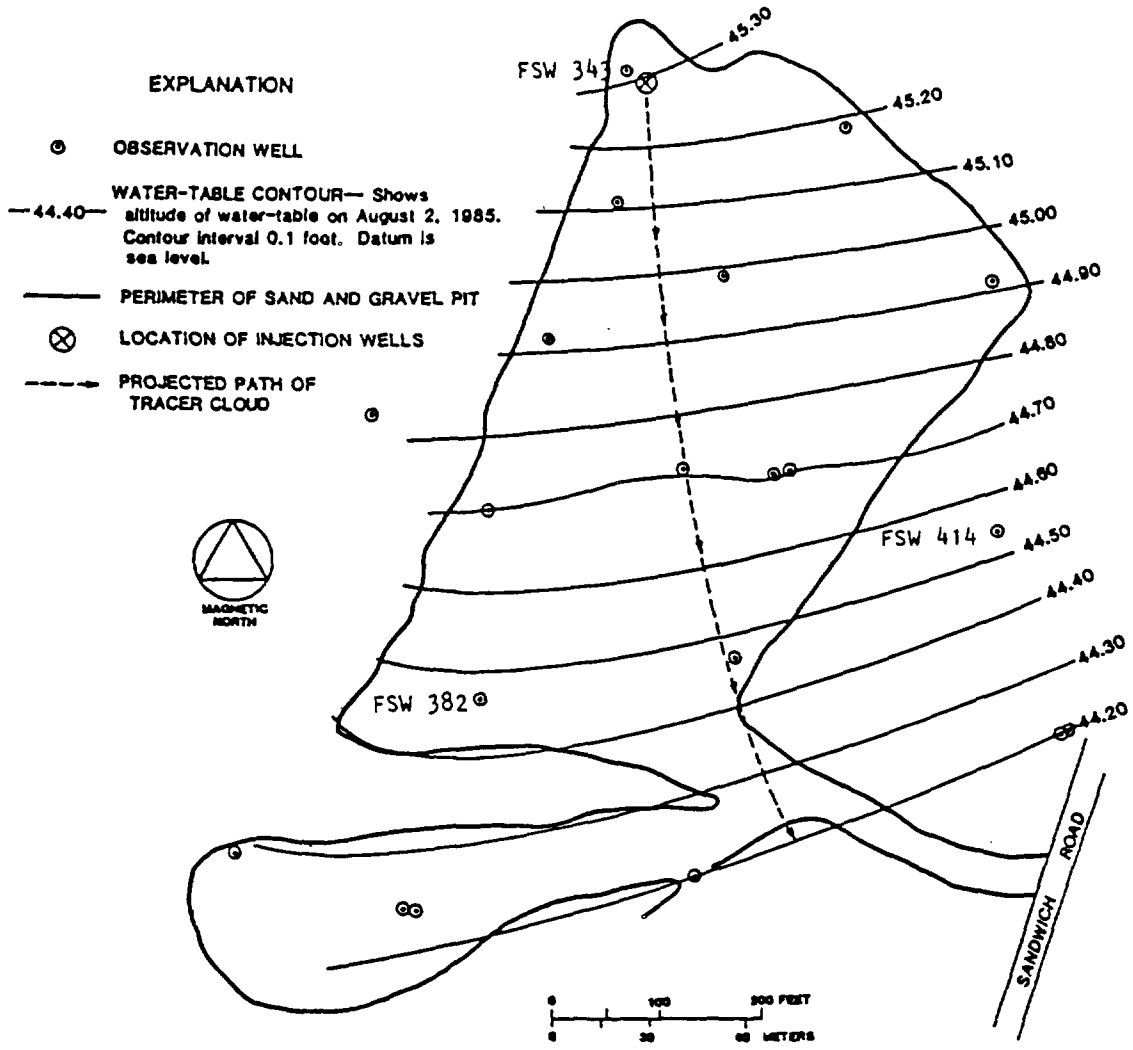

Figure 32 Water-table contour map, location of injection wells, and projected path of tracer cloud for the large-scale tracer test.

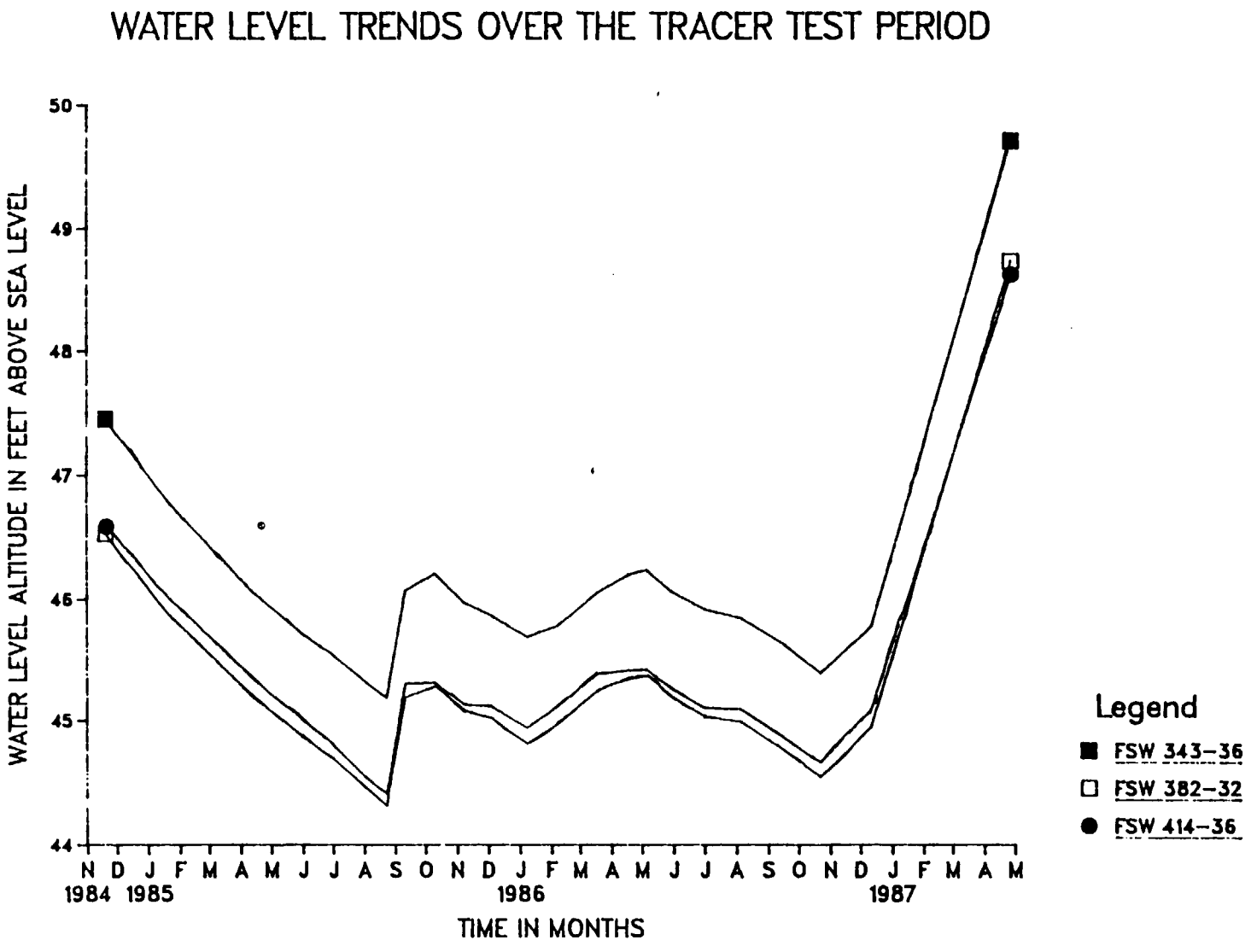

Figure 33. Water level trends over the tracer test period

The water-table gradient and direction, as indicated by three wells (FSW 343, FSW 382, FSW 414), are shown in figures 34 and 35. The changes in the magnitude and direction of the water-table gradient correlate very well with the water-level trends shown in figure 33. It can be seen that as water levels rose, the gradient increased and shifted to a more southeasterly direction. As this is in the direction of Ashumet Pond, it is likely that as the water table rises the pond exerts a stronger influence on the water table. Generally the changes in the magnitude and direction of the water-table gradient were small during the test, with the magnitude varying between 0.0014 to 0.0018 and the direction between 7 to 16 degrees east of south.

Vertical head gradients in the sand and gravel are small. Measured head differences in wells completed at different depths were 0.01 feet or less. These differences were within the range of measurement and leveling errors, but when observed show decreasing head with depth, indicating a potential for downward flow.

The direction of tracer movement across the sand and gravel pit was predicted by drawing a flow line perpendicular to the water-table contours. It was assumed that the water-table map used for prediction represented average conditions and that the aquifer hydraulic conductivity was horizontally isotropic. The water-table configuration in August 1985 (fig. 32), as indicated by water-level hydrographs (fig. 33), appears to be lower than the average conditions during the tracer test period. As was pointed out, however, the variation in gradient magnitude and direction was

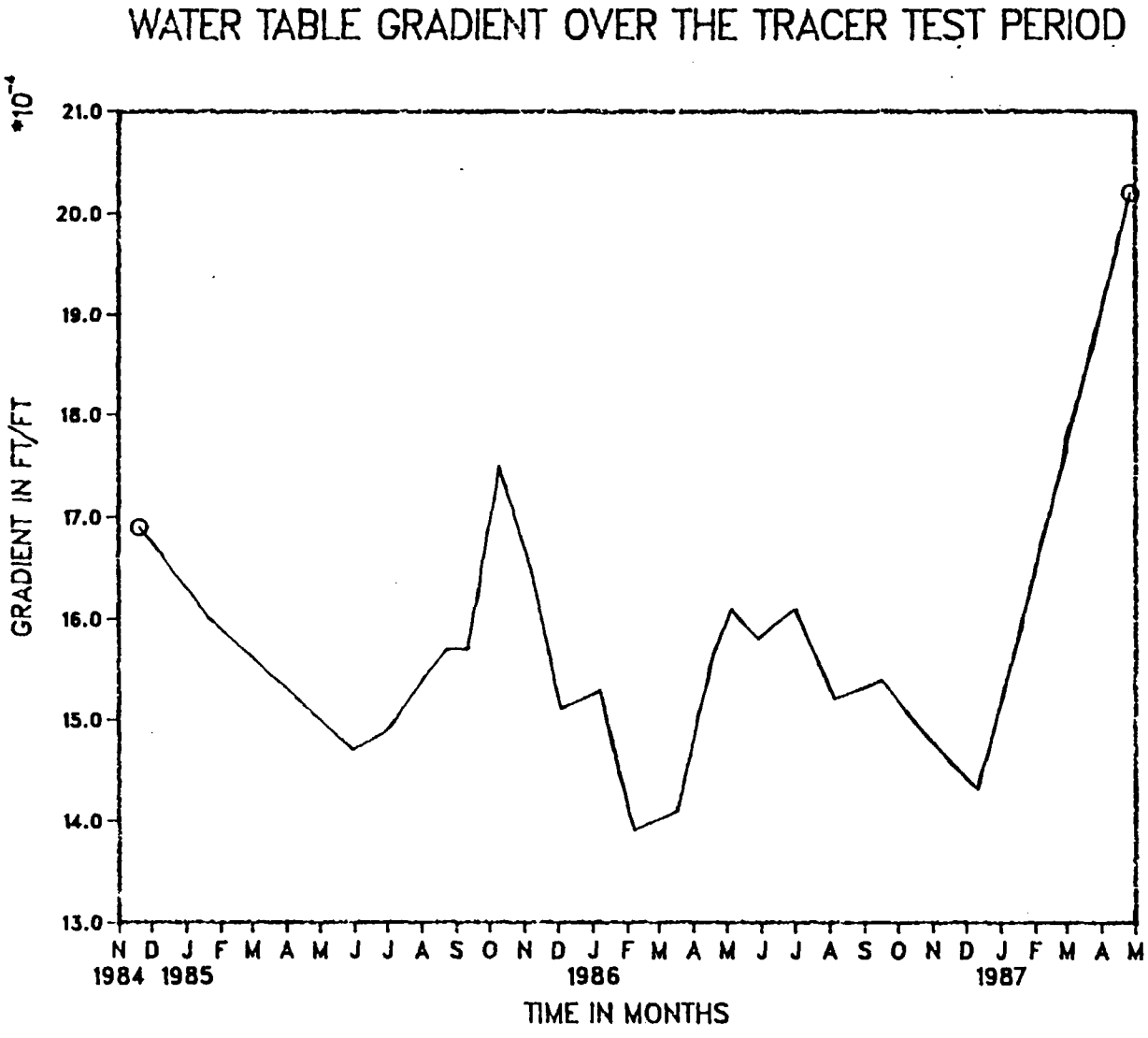

Figure 34. Water table gradient over the tracer test period

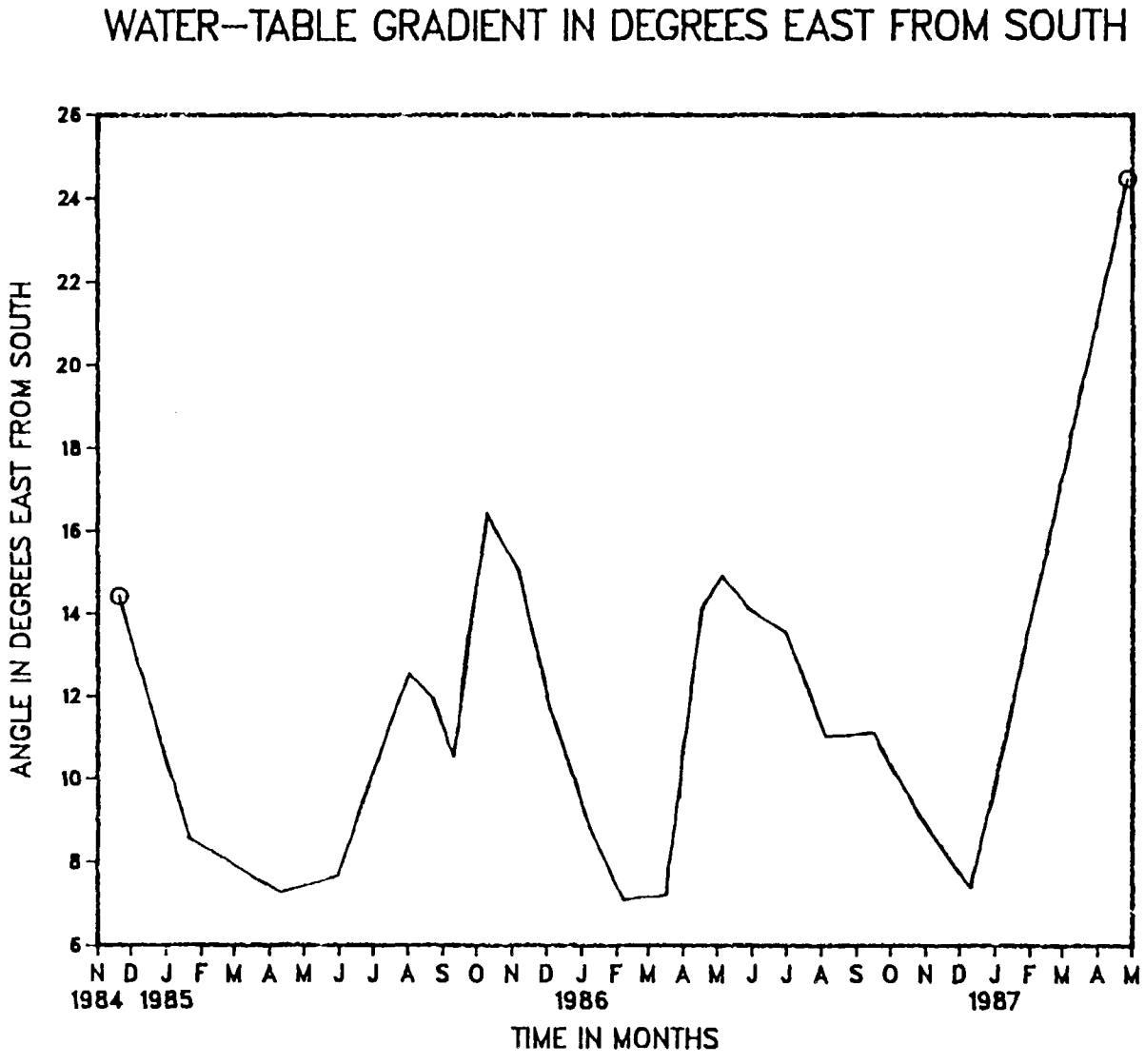

Figure 35. Water table gradient direction over the period of the tracer test

small during the tracer test period and the prediction was a useful guide for test planning. The assumption of horizontal isotropy for hydraulic conductivity appeared reasonable as there was no evidence of anisotropy during the Ashumet well aquifer test.

An estimate of the horizontal solute velocity was made at this point (spring 1985) in the test design using Darcy's equation

$$V = KI/n$$

where

K = estimated horizontal hydraulic conductivity (380 ft/d)

I = water-table gradient (0.0014)

n = porosity (0.35)

resulting in an estimate of 1.5 ft/day. As will be shown later, this early estimate was very close to the measured rate of solute velocity.

An initial grid of multilevel samplers (fig. 36) was designed with the use of the predicted solute path (fig. 32). The initial grid included the first six rows of samplers and had expanding distances between samplers in anticipation of the rapid spreading of the solute after injection. Three injection wells, each with four foot screens, were set in the middle of the vertical span of the samplers (33.5 to 45.17 feet above MSL). These three injection wells were used to inject a large solute volume in the aquifer with as low an injection rate as possible to reduce vertical movement of the solute.

After the observation wells and initial grid were established, several tests of the multilevel samplers and a short duration tracer test were conducted. The design and results of testing the

TRACER TEST SAMPLER LOCATIONS

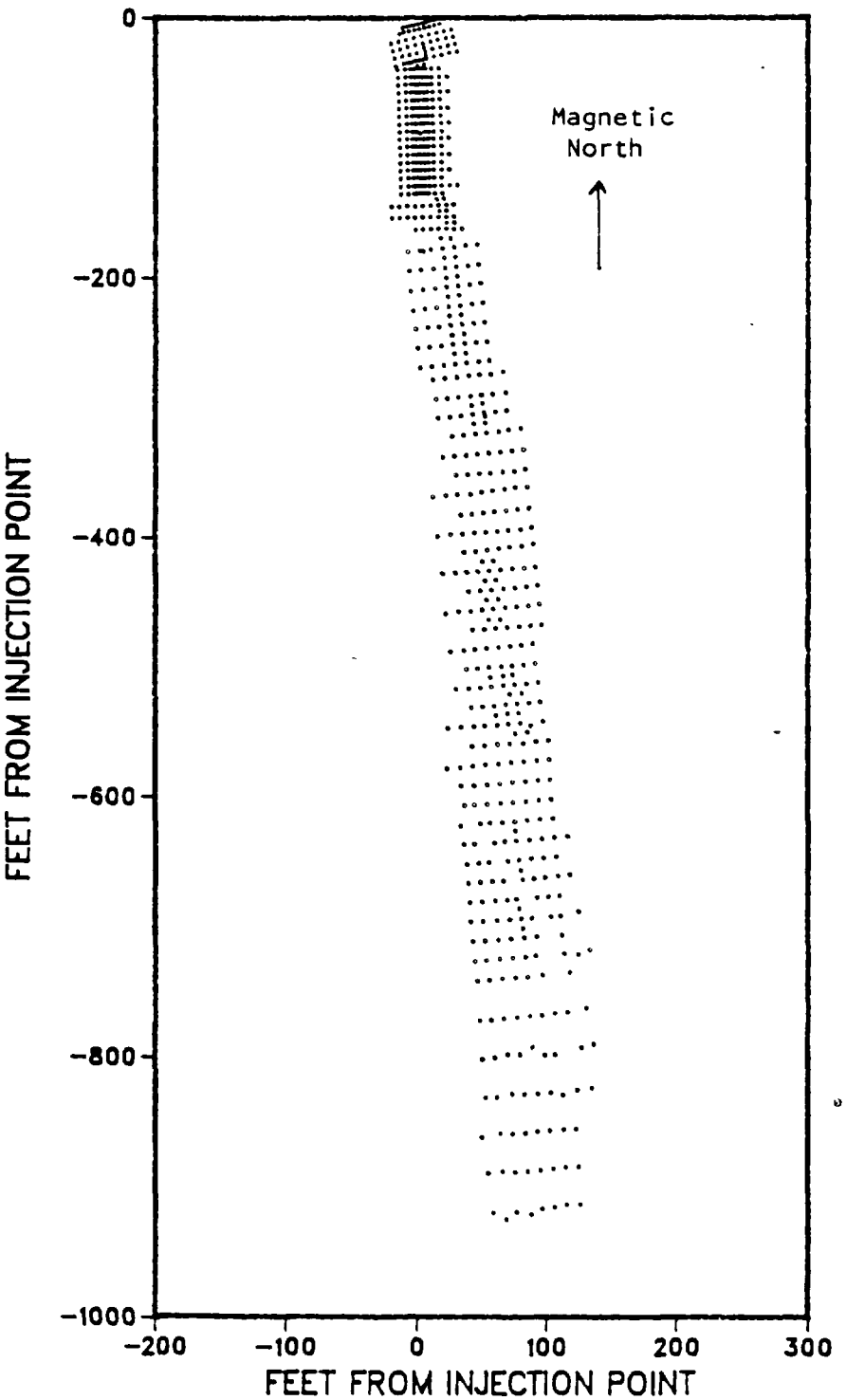

Figure 36. Tracer test sampler locations

multilevel samplers are presented in the next section. The results of the short duration test are then presented.

4. Multi-Level Sampler Design and Tests

The sampling devices used in the large-scale tracer test were similar to those constructed for the small-scale divergent tracer tests (Section II.B.3). Because the large-scale test at the Borden site (MacKay et al, 1986; Freyberg, 1986) had indicated sharp vertical concentration gradients, it was anticipated that small vertical intervals would be needed to capture the vertical variations in solute distributions. Therefore 15 sampling ports were used in each multi-level sampler (MLS). This was the largest number of polyethylene tubes which could be accommodated inside the PVC tubing. The spacing between each of the ports was varied from 10 to 30 inches, increasing downgradient from the injection site (figure 37 and table 9) in order to span the complete thickness of the solute cloud.

Sampling tubes were labeled by the tubing color and from bottom to top were: white (W), black (BK), blue (BU), red (R), green (GN), purple (P), yellow (Y), gray (GY), orange (O), white tape (WT), black tape (BKT), blue tape (BUT), red tape (RT), green tape (GNT), and purple tape (PT). MLS locations were labeled by row and sequence number; an example is 4-15, the fifth sampler in row 4. This sequencing scheme allowed for additional samplers to be placed at the beginning of the row and be labeled 4-10 or lower, if needed.

The MLS were initially installed by a combination of auger and drive and wash drilling. The hollow-stem auger (3 1/4 inch ID) was

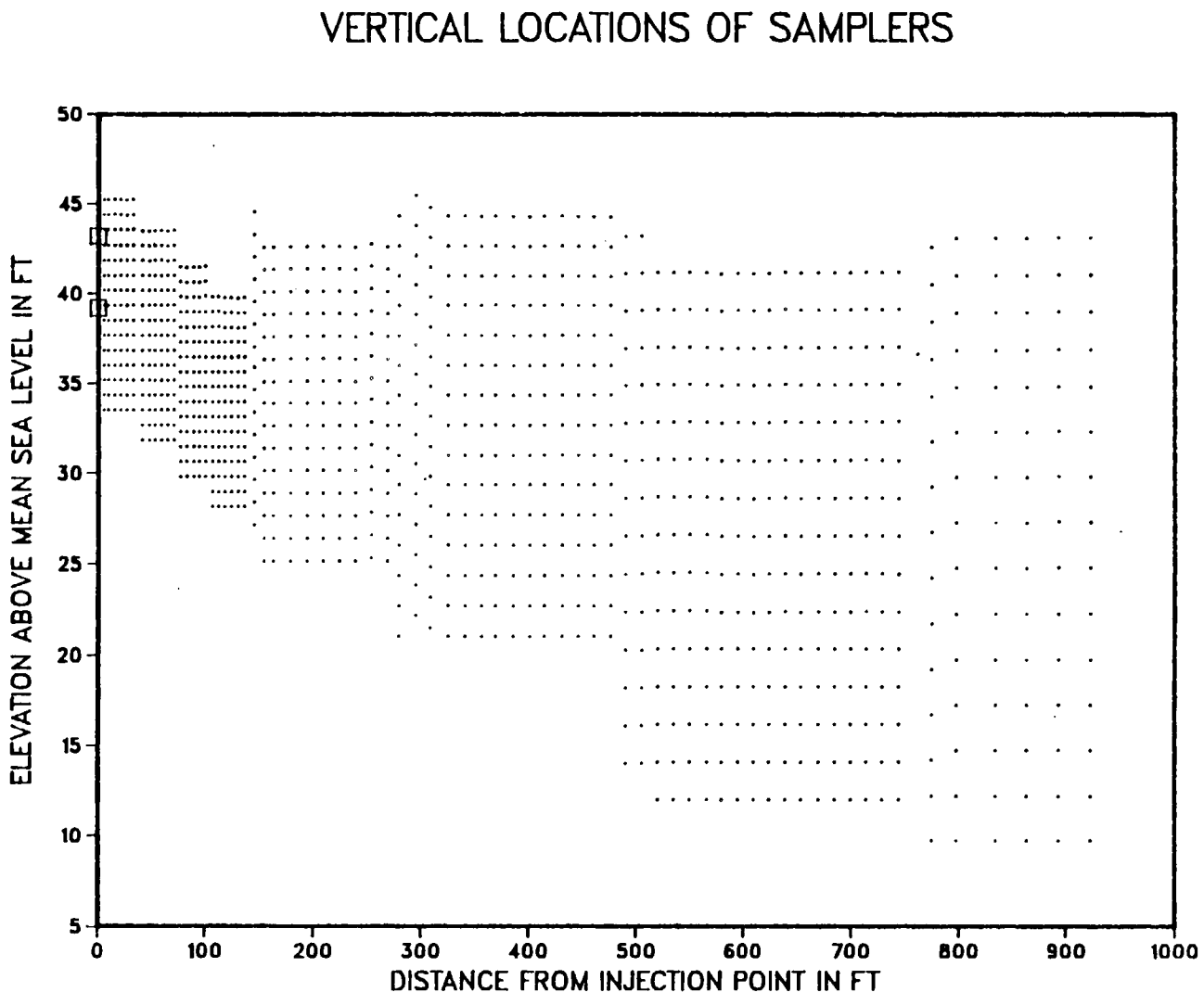

Figure 37. Vertical locations of multilevel samplers for the large-scale tracer test

Table 9 Elevations* of Multi-level Samplers for the Large-scale Tracer Test

Rows	1-6	7-12	13-17	18-23	24	25-31 33	32	34, 37-47	35	36	48-49	50-65	66-71
Spacing (in)	10	10	10	15	15	15	20	20	20	25	25	25	30
PT	45.21	43.48	41.48	39.80	44.52	42.55	42.75	44.29	45.43	44.77	43.17	41.16	43.06
GNT	44.38	42.65	40.65	38.97	43.27	41.30	41.50	42.62	43.76	43.10	41.09	39.08	40.98
RT	43.55	41.82	39.82	38.14	42.02	40.05	40.25	40.96	42.10	41.44	39.00	36.99	38.90
BUT	42.67	41.00	38.96	37.29	40.77	38.80	39.00	39.30	40.47	39.79	36.92	34.91	36.81
BKT	41.83	40.16	38.12	36.45	39.52	37.55	37.75	37.63	38.80	38.12	34.84	32.83	34.73
WT	41.00	39.33	37.29	35.62	38.27	36.30	36.50	35.96	37.13	36.45	32.75	30.76	32.25
O	40.17	38.50	36.46	34.79	37.02	35.05	35.25	34.30	35.47	34.79	30.66	28.67	29.75
GY	39.33	37.66	35.62	33.95	35.87	33.87	34.07	32.63	33.80	33.12	28.58	26.59	27.25
Y	38.50	36.83	34.79	33.12	34.62	32.62	32.82	30.96	32.13	31.45	26.50	24.51	24.75
P	37.67	36.00	33.96	32.29	33.37	31.37	31.57	29.33	30.48	29.80	24.41	22.42	22.23
GN	36.83	35.16	33.12	31.45	32.12	30.12	30.32	27.67	28.82	28.14	22.33	20.33	19.73
R	36.00	34.33	32.29	30.62	30.87	28.87	29.07	26.00	27.15	26.47	20.25	18.25	17.23
BU	35.17	33.50	31.46	29.79	29.62	27.62	27.82	24.33	25.48	24.80	18.17	16.17	14.73
BK	34.33	32.66	30.62	28.95	28.37	26.37	26.57	22.67	23.82	23.14	16.08	14.08	12.20
W	33.50	31.83	29.79	28.12	27.12	25.12	25.32	21.00	22.15	21.47	14.00	12.00	9.70

*All elevations in feet above mean sea level; does not include the elevations of samplers between rows.

used through the unsaturated zone and the drive and wash casing was driven to the desired depth. After washing the casing out, the sampler was lowered down the hole, the casing was pulled out, and the augers were backed out. Collapse of the aquifer sands below the water table around the sampler was immediate and although the sampler could be moved for a short time after installation, they could not be moved after a day. This was good indication that the aquifer sands were collapsing tightly up against the MLS and gaps along the MLS were not likely.

The maximum amount of aquifer disturbance which occurred during MLS installation can be found by calculating the ratio of the drive casing area (0.05 ft^2) to the minimum area around each MLS (9 ft^2). This calculation indicates about 0.5 percent of the aquifer was disturbed during MLS installation, a very small impact on the aquifer volume. Therefore, it was expected that MLS installation did not disrupt the natural flow of ground water at the tracer test site.

Three short duration tracer tests (cross-talk tests) were performed on three different locations, two on sampler 4-19 (BK, BUT) and one on sampler 4-11 (BK). The purpose for these tests was to establish if there was any evidence for rapid vertical movement of solutes due to incomplete sealing around the MLS. The two tests in 4-19 involved pumping down a sodium chloride (NaCl) solution in one port as a pulse and observing the breakthrough of increased specific conductance (indicating increased concentrations of NaCl) in a vertically adjacent port. In the case of 4-19-BK, about 400 ml of a 2000 microsiemens/cm (μs/cm) solution was injected in 4-l9-W (10 inches below BK) with water continuously injected at 320 ml

per minute in W and pumped at 220 ml per minute from BK. Specific conductance measured at BK began to rise 11 minutes after injection and peaked at 260 µs/cm 15 minutes after injection (fig. 38). For 4-19-BUT, about 400 ml of a 1970 µs/cm solution was injected in 4-19-BKT (10 inches below BUT) with water continuously injected at 320 ml per minute in BKT and pumped at 320 ml per minute from BUT. Specific conductance measured at BUT began to rise 18 minutes after injection, and peaked at 106 µs/cm 25 minutes after injection (fig. 38).

In both of these tests rapid dilution of the injected solution occurred, about 8 fold dilution for 4-19-BK and 20 fold dilution for 4-19-BUT. The higher conductance values for 4-19-BK are due to the higher background conductance at depth; this increase is due to the presence of the sewage contaminated groundwater at this site.

The test in 4-11-BK involved injecting about 1 liter of sodium chloride solution with a specific conductance of 1975 µs/cm down 4-11-W (10 inches below 4-11-BK) and pumping about 325 ml/minute from 4-11-BK. After injecting the solution, injection was stopped and pumping was continued for about 320 minutes. Specific conductance began to rise after 35 minutes and peaked at 147 µs/cm, 100 minutes after injection (fig. 38).

The crosstalk experiments at 4-19 and 4-11 are distinctly different due to the differing flow systems created by injecting and pumping. In the case of 4-19, simultaneous injection and pumping led to a more rapid breakthrough and higher peak concentrations relative to background. For 4-11 the peak is very broad and shows a very slow downward trend. In each of these tests however, there is

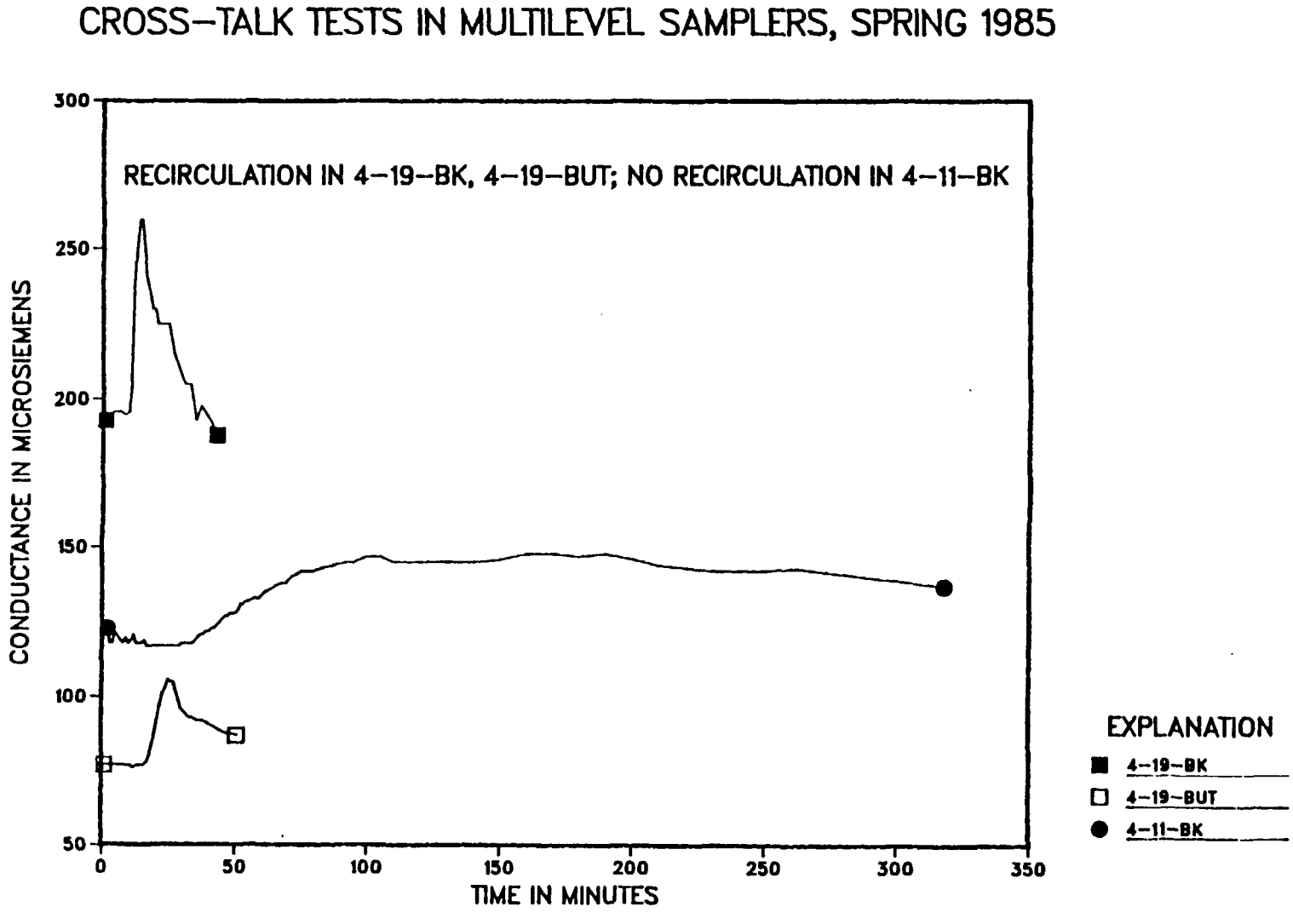

Figure 38. Breakthrough curves for the cross-talk tests

a significant initial period of time before the tracer arrives and a rapid dilution of the solution from injection concentration.

If it can be assumed that the solute moved from sampling port to sampling port through a cylindrical volume, a radius of the cylinder can be calculated. A known volume of water was pumped during the period of time until the peak concentration arrived. If this volume is divided by the porosity (0.39) and the distance between ports, a cylinder radius can be calculated. For example, in the 4-I9-BK test, time to peak was 15 minutes and a volume of about 3.3 liters was pumped. Using a spacing of 10 inches (25.4 cm) a cylindrical radius of I0.3 cm can be calculated. For the 4-I9-BUT test the radius was I6.0 cm. If for the 4-11-BK test the flow was assumed to be spherical, the peak arrival time for something injected 10 inches away should have been 82 minutes, this matches the observed breakthrough time of I00 minutes closely. The above results, although not conclusive, do indicate the solute movement is through a significant portion of the aquifer around the sampling ports. Therefore it appeared that the sampling ports were sampling ground water in the aquifer and there wasn't a rapid vertical mixing (i.e. short circuiting along the sampler) of the solutes during sampling.

B. Preliminary Tracer Test Using Sodium Chloride

A preliminary tracer test was conducted at the large-scale tracer test site from March 7, I985 to March 27, I985. The purpose of this experiment was to test the equipment, injection procedure, sampling protocol, and to obtain an estimate of solute velocity

before commitment to the large-scale test. About 2.5 kilograms of sodium chloride was diluted in 1,000 gallons of water and injected in the center well as shown in figure 39. Water samples were collected 7, 13, and 20 days after injection and analyzed for specific conductance in µs/cm. Specific conductance was used as a general indicator of solute concentration primarily for the ease of field analysis. Specific conductance varies with depth in the sand and gravel pit due to the presence of the sewage plume, increasing from about 50 µs/cm in the top sampler (45.12 ft above MSL) to about 200 µs/cm in the bottom sampler (33.50 ft above MSL). As the tracer solution was about 2350 µs/cm, specific conductance was a good indicator of high tracer concentrations for the short distances in the preliminary tracer test, but would not have been suitable for the large-scale test.

Contour maps of vertically-averaged concentrations of the specific conductance distribution 7, 13, and 20 days after injection are shown in figure 39. The vertical averages were calculated by taking the arithmetic mean of the 12 lowest sampler values. As can be seen in a cross section through the solute cloud 7 days after injection (fig. 40), the 12 lowest samplers showed specific conductance values above background values (greater than 200 µs/cm).

Horizontal movement of the cloud was a few degrees west of due south. Using the peak concentration as the center of mass, the average velocity of the cloud was about I.5 ft/day. This agrees with the original estimate using the Darcy equation. The leading edge, as indicated by the 200 µs/cm contour, was moving more rapidly,

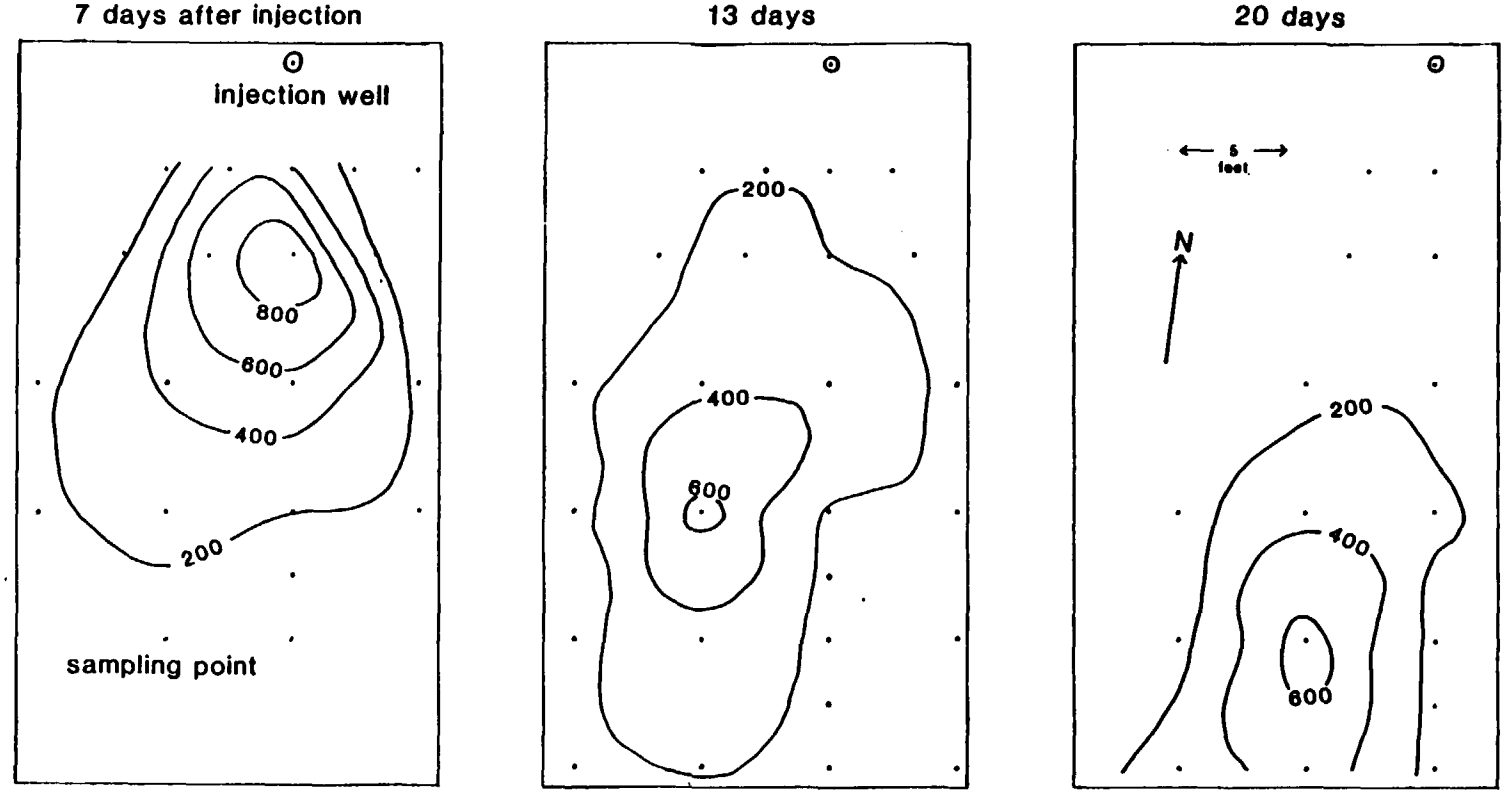

Figure 39. Vertically-Averaged Concentrations of Specific Conductance (μs/cm) for a Short-Term Preliminary Tracer Test, March, 1985

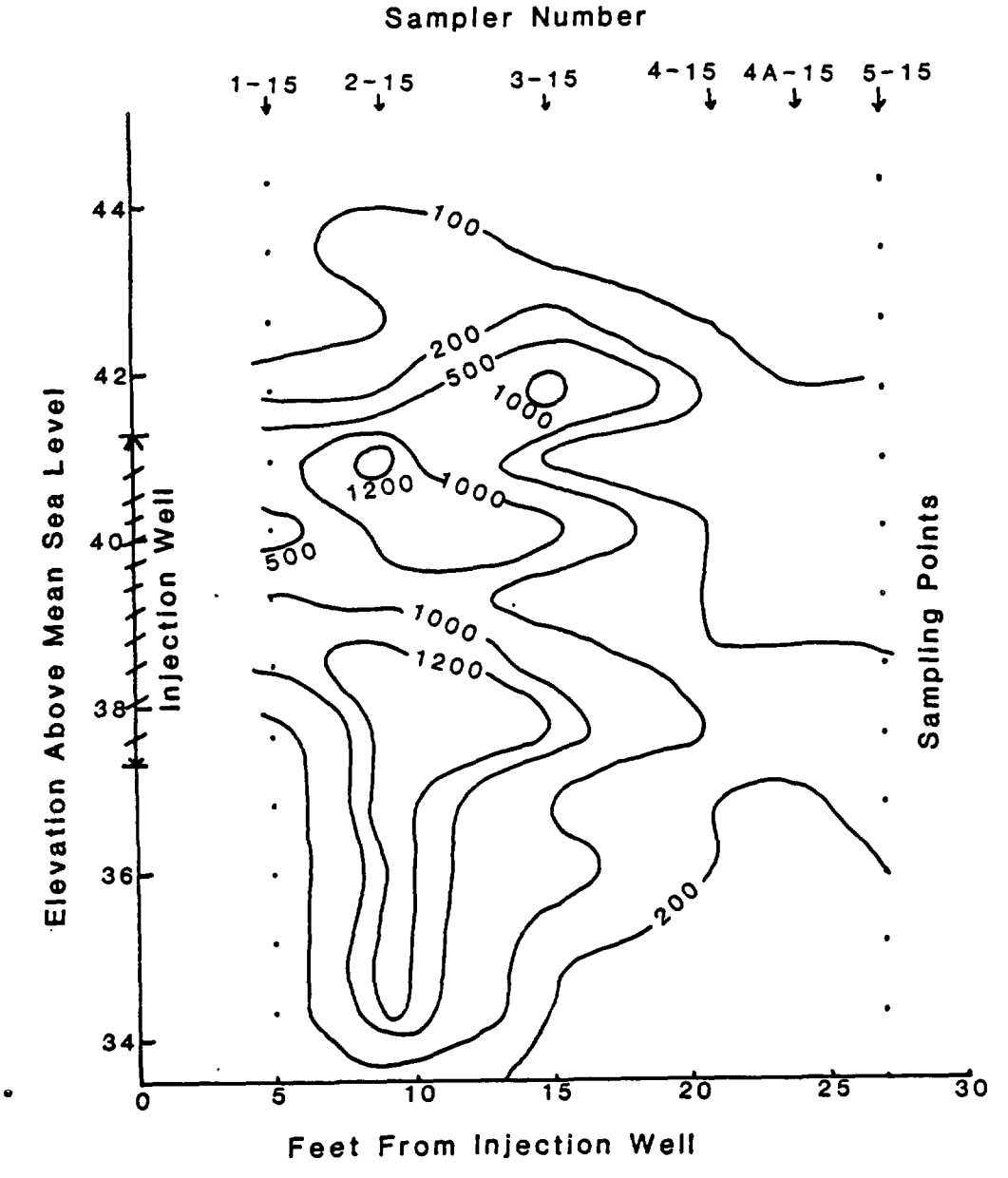

Figure 40. Crossection of Specific Conductance (µs/cm) for a Short-Term Tracer Test, 7 Days After Injection, March,1985

averaging about 3.0 ft/day. This higher velocity indicated possible problems with sampler installation, as the intention was to stay ahead of the large-scale test cloud without over-extending the grid. The initial grid was extended for 17 more rows in a southward direction in response to the lateral movement measured in the sodium chloride tracer test (figure 39).

The cloud moved downward relative to the injection interval, as indicated by the cross section in figure 40. The downward movement was likely the result of a density contrast or possibly to local heterogeneity in the hydraulic conductivity distribution. New samplers were put deeper into the aquifer (figure 37) in response to the sinking observed during the sodium chloride tracer test. The injection wells were also pulled up 1.67 feet to inject the tracers higher in the section. This put the bottom of the screen at 39 feet above MSL and the top at 43 feet above MSL.

After the sodium chloride tracer test, several modifications were made to the test procedures. The tank truck used in March leaked and other trucks were secured for the large-scale test. Single head peristaltic pumps were used for the preliminary sampling and pumping hundreds of samples took a full day. Therefore a more rapid method for sampling was required to pump the thousands of samples anticipated for the full-scale test. Finally it was readily apparent that a rapid analysis method for tracers would be needed in order to accurately predict the cloud movement. The information obtained from the sodium chloride pre-test helped anticipate the problems and needs of the large-scale tracer test.

C. Large-Scale Test Operation

I. Tracers

The tracers were chosen for the large-scale test using the following criteria:

- low background concentration in the aquifer
- sensitive and inexpensive analysis method
- low toxicity
- compatibility with research objectives.

The four tracers injected in the large-scale test included three anions: bromide (Br^-), molybdate (MoO_4^{2-}), and fluoride (F^-); and one cation, lithium (Li^+).

Bromide was used as the conservative tracer because of the low background concentrations in the aquifer, which ranged from 0.03 to 0.10 mg/L and averaged about 0.05 mg/L. Background samples were analyzed by the USGS National Laboratory in Atlanta, GA, using ion chromatography. Bromide concentrations can be accurately determined to about 0.5 mg/L with an ion selective electrode and down to about 0.01 mg/L with ion chromatography. With an input concentration of 500 mg/L or more there would be about a 10^3 dilution possible before the tracer would be difficult to detect using an ion-selective electrode analysis method. With ion chromatography a 10^4 dilution is possible before bromide concentrations would be indistinguishable from background concentrations. Because background chloride concentrations are from 7 to 30 mg/L, only a 10^2 dilution would be possible with an

input tracer concentration of about 1,000 mg/L, making chloride a less desirable tracer for this experiment.

Molybdate was used as a nonconservative tracer to address specific research questions which are not part of the scope of this report. The molybdate tracer was used as a chemical analog for other, more toxic, oxyanions such as arsenate (AsO_4^{3-}), chromate (CrO_4^{2-}), and selenate (SeO_4^{2-}) (Stollenwerk and Grove, 1987). Research goals in this effort were: a) to identify the type of data needed to adequately model the transport of a nonconservative solute in ground water, b) to study the geochemistry of the system and identify mechanisms responsible for adsorption and desorption of the solute, and c) to model the transport and reaction of the solute in laboratory and field environments (Stollenwerk and Grove, 1987). A preliminary discussion of the molybdate movement during the large-scale tracer test and laboratory experimental results is given in the above report.

Fluoride and lithium were included as tracers to examine: a) the enhanced transport of a cation (Li^+) by a complexing anion (F^-) and b) the number and type of retardation data necessary to characterize cation movement in the aquifer. It was found during the tracer test that the fluoride was significantly retarded and concentrations quickly dropped to background concentration (0.03 to 0.2 mg/L) (Warren Wood, personal communication, 1986). More discussion of the lithium movement is included later in this report.

2. Injection Data

The large-scale natural gradient tracer test began on July 18, 1985, with the injection of 7.6 m^3 (2015 gallons) of tracer solution over 17 hours; injection ended early on July 19, 1985. The tracer solution was injected in three wells with a combined flow of about 2 gallons per minute. The tracer solution contained 4,900 g of bromide, 380 g of fluoride, 610 g of molybdate, and 595 g of lithium. Tracer concentrations in the injected solution were 640 mg/L bromide, 50 mg/L fluoride, 80 mg/L molybdate (as Mo), and 78 mg/L lithium. The tracer solution was prepared by mixing salts (lithium bromide, lithium fluoride, lithium molybdate) with uncontaminated ground water in two insulated 1,000 gallon tanks. Water was circulated between the tanks to equalize tracer concentrations. Temperature of the tracer solution rose from 13.5°C just after the tanks were filled to 16°C when the injection stopped.

D. Data Collection and Analysis for Tracers (Br, Li)

1. Sampling

Seventeen sampling rounds were taken from July 1985 to May 1987, occurring about every month. During each round, water samples were collected for three laboratories performing the bromide (Boston, MA), molybdate (Denver, CO), and lithium and fluoride (Reston, VA) analyses. As many as 10,000 water samples were collected from 40 to 300 MLS during each sampling round to obtain a three-dimensional "snapshot" of the tracer distribution.

Water samples were collected at each MLS location using a specially constructed sampling cart. Two carts were built of wood

and each had two multihead peristaltic pumps. The multihead peristaltic pumps can simultaneously pump all 15 tubes in each MLS. This significantly decreased the time needed to sample each MLS. An obvious limitation of the MLS-sampling procedure is that the depth to water can not be greater than the suction limit, which for the peristaltic pumps is about 28 feet, but this was not a problem at the tracer test site. Typical sampling rounds lasted from two to three days. Along with pumps, the sampling carts also contained a waste trough and buckets for collecting waste water. All waste water was collected, sampled, measured for volume, and dumped off-site to prevent recirculation of the tracer.

Varying volumes of water were pumped to waste, ensuring fresh ground water was sampled. It was found through direct measurement that each foot of polyethylene tubing would hold 4.4 ml of water. Because the length of tube below water table could be calculated from the water table elevation and sampler depths (fig. 37), a volume of standing water in the tube was calculated. By pumping in excess of this amount prior to collection of the samples, it was ensured that fresh ground water was sampled. Mass removed by this procedure was small, varying between 2 to 5 grams of bromide for each sampling round.

Water samples were pumped untreated and unfiltered (raw) into 60 ml polyethylene bottles. All bottles were labeled with the sampling round date (usually the middle of three days), the sampler number (ex: 4-I5-W), and the analysis (Br, Li-F, Mo). Bottles were packaged as groups of fifteen (each MLS) in plastic bags and stored

at room temperature until analyzed. For most sampling rounds analysis of constituents was completed within 60 days.

2. Bromide Analysis

The analysis of bromide concentration in tracer test samples was performed by ion-selective electrode (probe) and ion chromatographic (IC) methods. Probe measurements were made by following the procedure outlined by the manufacturer (Orion) without any ionic strength adjustment of the samples because of the low concentrations of the vast majority of samples. Ion-selective electrode analysis consists of two electrodes placed in a solution. The bromide electrode has a silver bromide/silver sulfide membrane bonded into the tip of an epoxy electrode body (Orion Research, 1982). When the membrane is in contact with a bromide solution, silver ions dissolve from the membrane surface and the electrode develops a potential due to the silver ion concentration. This concentration is, in turn, determined by the sample bromide concentration. This potential is measured against a constant reference potential (second probe) with a digital pH/mV meter or specific ion meter. The measured potential corresponding to the level of the bromide ion in solution is described by the Nernst equation:

$$E = E_0 - S \log A$$

where

E = measured electrode potential

E_0 = reference potential (a constant)

A = bromide ion level in solution

S = electrode slope (about 57 mV at 20°C).

The level of bromide ion in solution (A) is the activity or effective concentration (Orion Research, 1982). Due to the low ionic strength of the water samples, the measured activity of the bromide in solution is effectively the true concentration.

Probe measurements were made using the following procedure: a) bromide standards were prepared using distilled water and measured amounts of sodium bromide, b) water samples and standards were allowed to come to ambient (and measured) room temperature, c) millivolt readings of the standard solutions were taken and used to form a log concentration-millivolt relationship, d) sample millivolt readings were taken and using the logC-mV relationship a concentration was assigned to the sample. All samples were stirred during the probe measurements.

The log-linear relationship between concentration and millivolt readings breaks down below about 0.5 mg/L bromide (Orion Research, 1982). Meter response is also much slower below 0.5 mg/L bromide and the meter readings had a tendency to drift with the low concentration samples and standards. Along with the above problems, other dissolved constituents can cause interference effects. This particular problem will be discussed later.

Ion chromatography is an analysis method in which a small amount of the sample is introduced in a carrier solution and then passed along a resin column. As the solution moves along the column the ionic species (either cations or anions) are adsorbed onto the column and move at different rates dependent on the ion's affinity for the column resin. After passing through the column the solution

goes through a conductivity detector. Because each ion has a different rate of movement through the column, the conductivity detector records the concentration (via the strength of conductance variation) of the ion in the original solution. The area of the conductivity peak is calculated and compared to that of a standard solution to quantify the ion concentration.

The accuracy of the ion chromatographic method for bromide is dependent on the strength of surrounding peaks and the column efficiency in separating the different ions in solution. The USGS National laboratory indicates a minimum detection of about 0.01 mg/L for the IC method. Although the IC method can detect bromide at lower concentration than the probe method, the IC method is more costly for equipment and supplies and cannot analyze as many samples per day (~ 50/day for IC, ~ 200/day for the probe). For these reasons all the samples were analyzed for bromide using the ion-selective electrode and the ion-chromatographic method was used as a check and backup for the probe analyses.

3. Interference in Ion-selective Electrode Bromide Analysis

It became apparent soon after the large-scale test began that there were interfering ions for the ion-selective electrode analysis in the sewage contaminated ground water. The interfering ions included chloride (Cl^-), ammonia (NH_3), and iodide (I^-). Using the maximum allowable ratio of interfering ion to bromide for chloride (400), ammonia (2), and iodide (2×10^{-4}) (Orion Research, 1982), along with maximum interfering ion concentrations in the plume ($[Cl^-]$ = 30 mg/L = 8.5×10^{-5} moles/L, $[NH^+_3]$ = 2.1 mg/L = 1.5×10^{-4}

moles/L, [I^-] = 0.002 mg/L = 1.6 x 10^{-8} moles/L), the concentration of bromide at which there should be an expected 1 percent error is about 13 mg/L (1.6 x 10^{-4} moles/L).

A comparison of probe and IC methods of bromide analysis was made for 143 water samples from the large-scale tracer test (fig. 41). The interference effects caused the probe measurements to be, on average, 0.12 mg/L higher than the IC measurements. This bias was observed only for probe measurements which were less than 1.0 mg/L bromide. Above 1.2 mg/L the errors in both methods mask the small bias observed in the probe measurements at lower concentrations (fig. 41).

The interference in probe measurements is depth dependent at the large-scale tracer test site. This is shown in figure 42, in which the probe values are plotted with depth for samples which had 0.05 mg/L bromide (or less), the background level as determined by IC measurement. The reason for the apparent increase in probe bias with depth is the sewage contaminated ground water. The presence of the sewage plume (and interfering ions) is indicated by the change in specific conductance with depth (fig. 43). The specific conductance in the sand and gravel pit area first increases with depth, levels out, and then decreases at the bottom of the plume.

Calibration curves for water collected at different depths (fig. 44) were used to estimate corrections for the probe bias. These calibration curves show that a wide variation occurs in the probe values below 1.0 mg/L using water collected at different depths. The information in these calibration curves was used to produce a table of correction factors (table 10). The correction

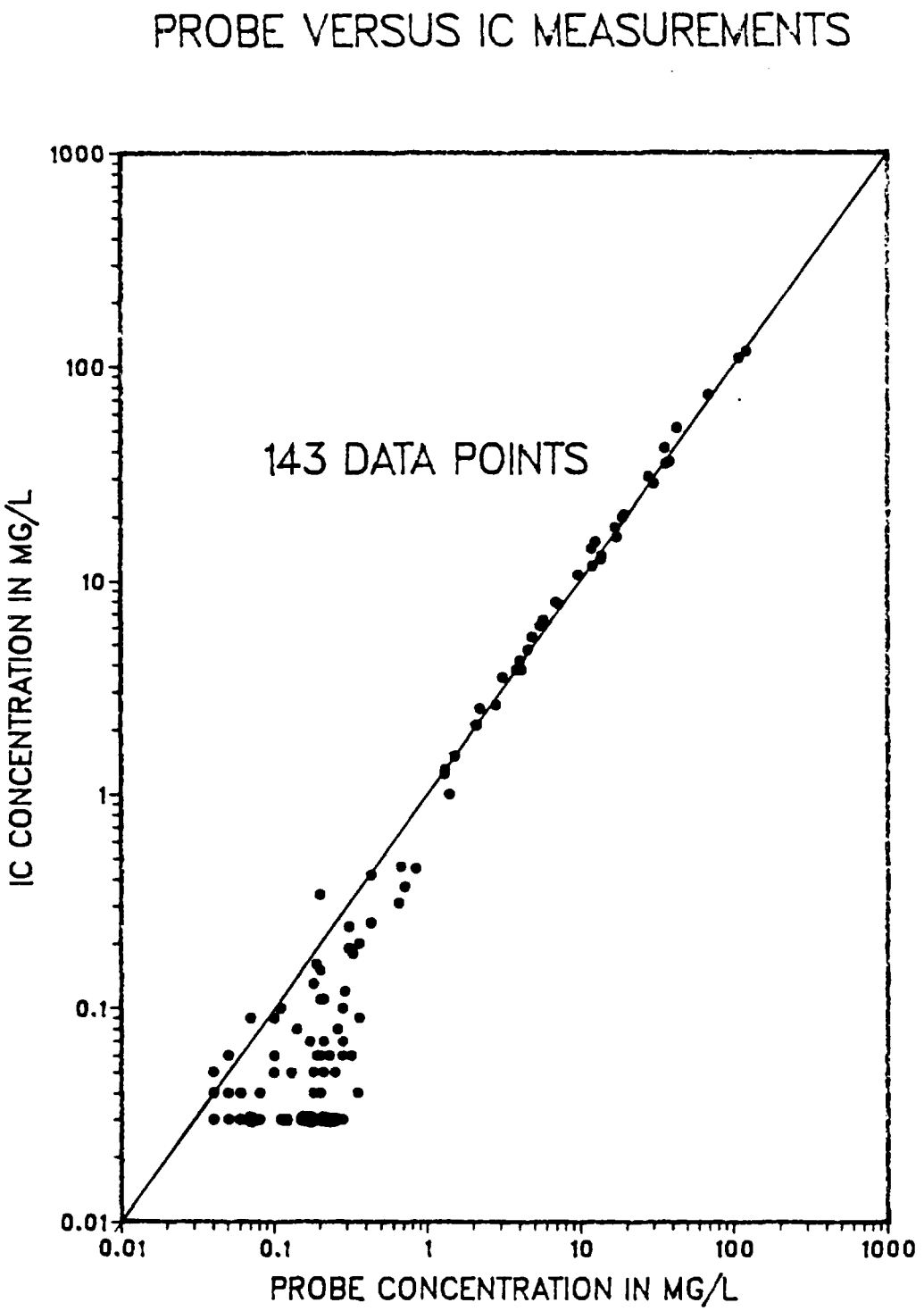

Figure 41. A comparison of analysis methods for bromide

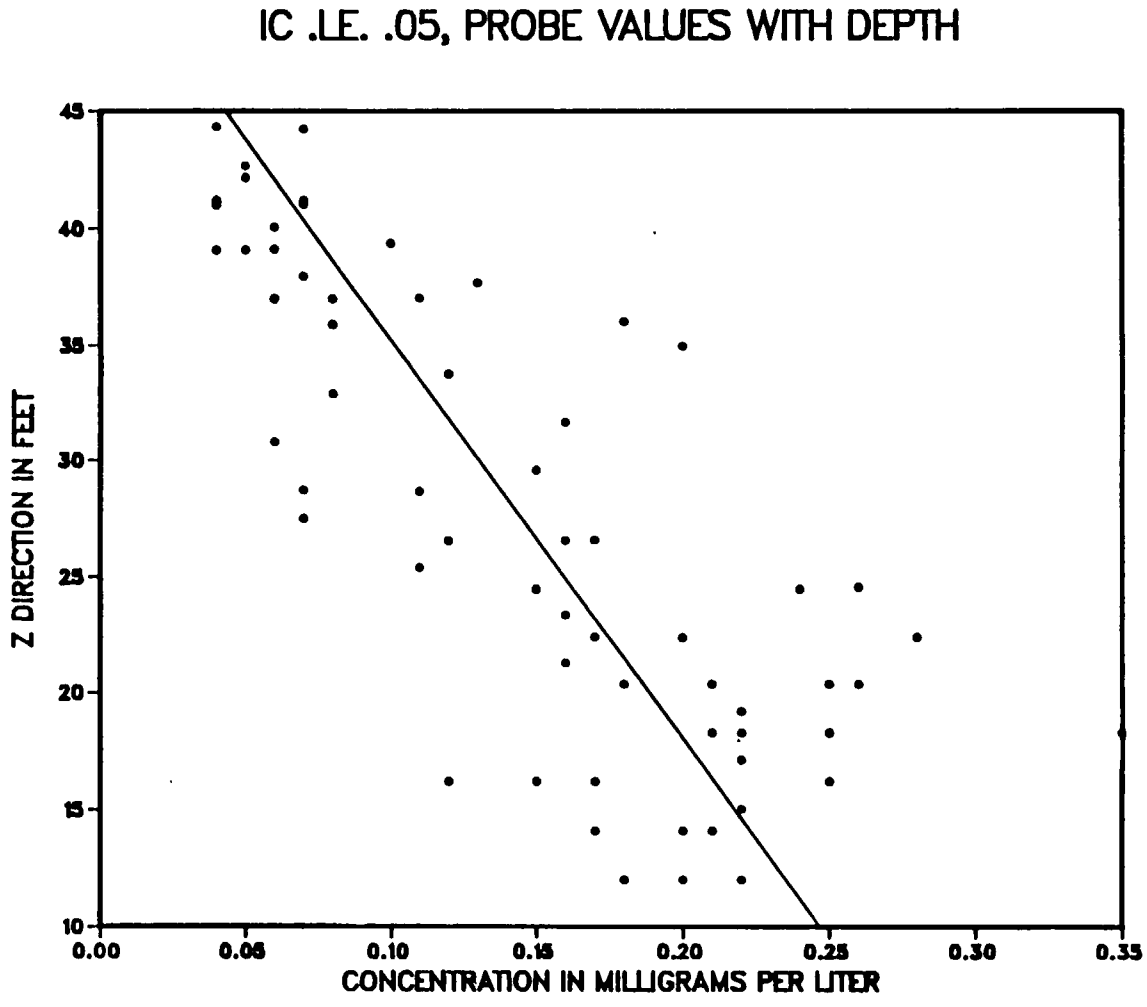

Figure 42. Change in apparent concentration with depth for ion specific electrode (probe) measurements

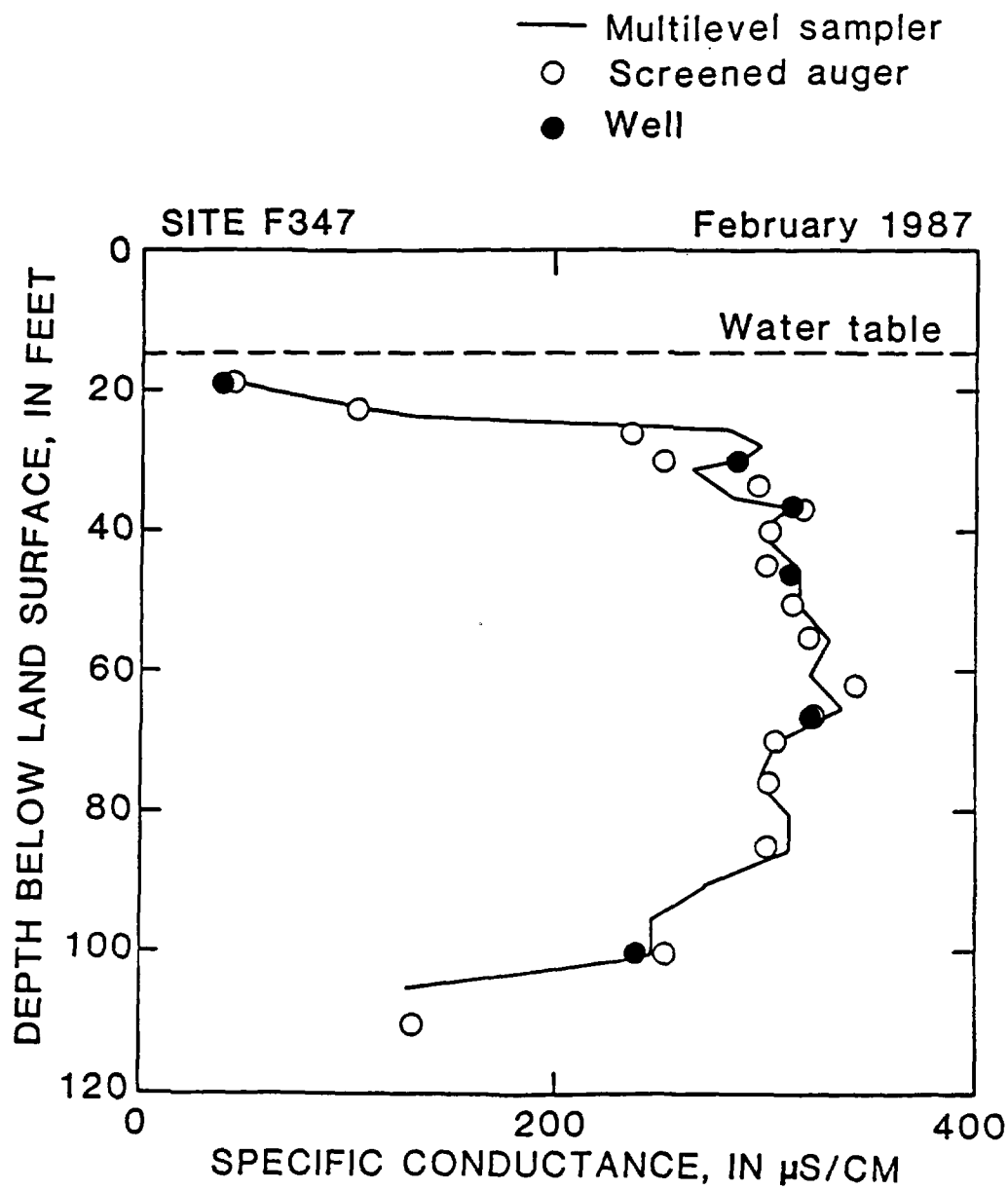

Figure 43. Change in specific conductance with depth in the tracer test area

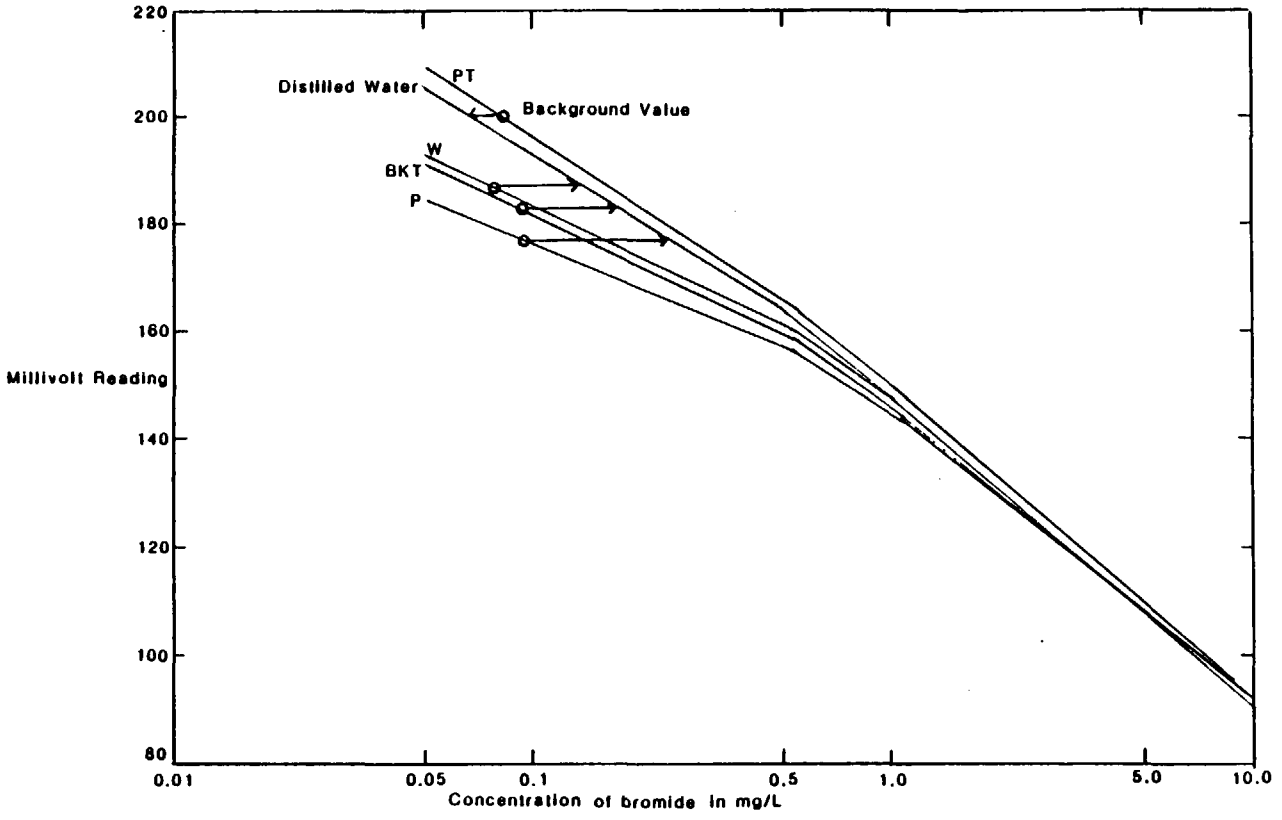

Figure 44. Calibration curves for bromide analysis at the W, P, BKT, and PT levels in MLS 58-18

Table 10

Corrections to Ion-Selective Electrode Measurements for Interference Effects*

Altitude of Sample above Mean Sea Level	Concentration Ranges (mg/L) 1.2-0.75	0.75-0.3	0.3-0.05	< 0.05
> 39.00	0.0	0.02	0.03	0.05
39.00 - 30.00	0.1	0.14	0.15	0.05
30.00-12.00	0.1	0.21	0.23	0.05
< 12.00	0.1	0.1	0.12	0.05

*All corrections were subtracted from the probe values. If a negative value results after subtraction, the value was set to 0.0.

factors include the small (0.03-0.05 mg/L) background value of bromide. The probe values for the 108 samples shown in figures 41 were corrected using table 10. A comparison of corrected probe values and IC values is shown in figure 45. The average difference between the corrected probe values and IC values (fig. 45) is 0.02 mg/L. Therefore, with the correction factors the probe values gave reasonably accurate estimates of the bromide concentrations.

4. Li Analysis

Analysis of water samples for lithium concentration was performed by atomic absorption spectrophotometry (AA). AA analysis involves aspirating a sample into a flame which atomizes the sample. A light beam is directed through the flame, into a monochromator, and onto a detector that measures the amount of light adsorbed by the atomized element in the flame (Standard Methods, 15th ed.). The amount of energy of the characteristic wavelength adsorbed in the flame is proportional to the concentration of the element in the sample. The background concentration of Li in the aquifer is below the detection limit of 0.01 mg/L. All lithium analyses were performed at a USGS laboratory in Reston, VA under the supervision of Dr. Warren Wood.

5. Lithium Adsorption onto Sediments

Laboratory experiments were conducted on sand and gravel samples obtained from dug pits and cores in the large-scale test area to measure the amount of lithium that would be adsorbed from a tracer solution. A set of experiments were run on splits of sand in

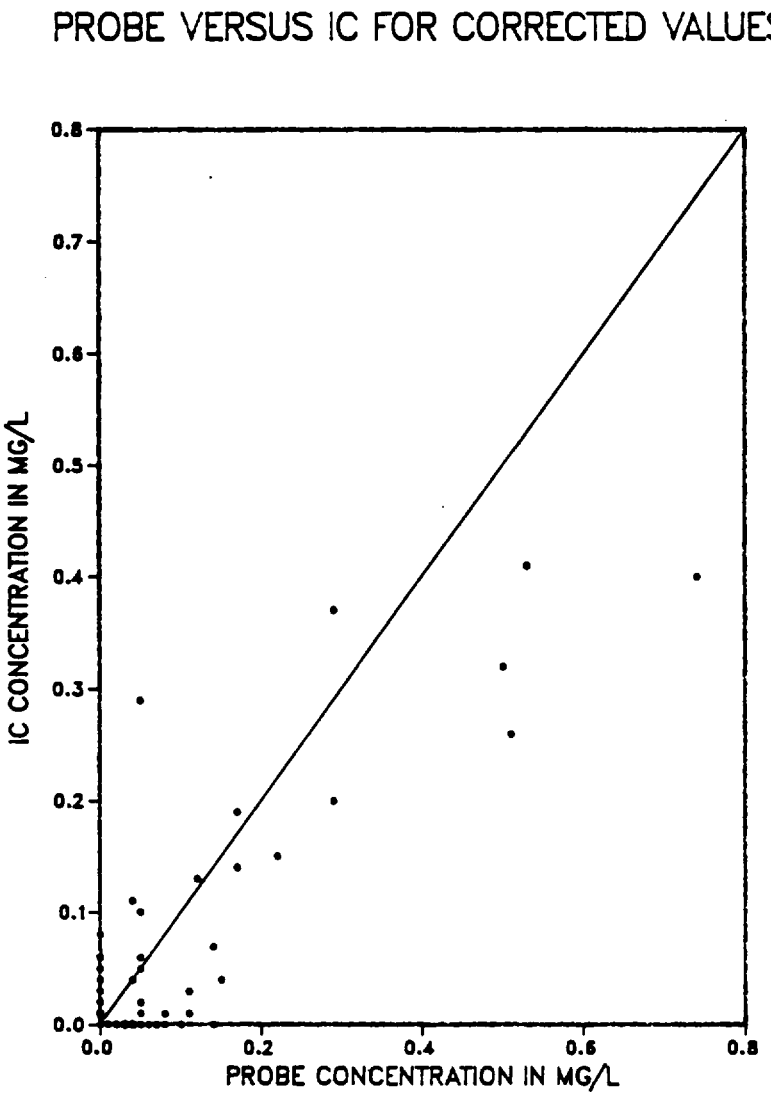

Figure 45. Ion specific electrode measurements after correction for interference effects

which varying concentrations of lithium in solution were added to measured amounts of sand. By measuring the concentration of the solution after mixing with the sand it is possible to calculate the amount of adsorbed lithium per gram of sediment. The concentration on the solid is plotted versus the concentration in solution after one and seven days (fig. 46, written communication, Warren W. Wood, 1987). These relationships are the adsorption isotherms at various times.

The lithium adsorption isotherms shown in figure 46 are nonlinear. A nonlinear least squares fit for each resulted in the equations:

$S = 0.178C^{0.558}$, one day,

$S = 0.373C^{0.384}$, seven days,

where

S = concentration on the solid (µg/g), and

C = concentration in solution (mg/L).

The correlation coefficient of the log transform of the one-day equation is 0.984 and 0.986 for the seven-day equation. These isotherms show the rate of lithium uptake on the solid decreases as the concentration in solution increases. This effect has been explained by way of limited sites (fewer are then available for each increased concentration increment) or by varying energies at sites (whereby the higher energy sites are occupied first and lower energy sites at higher concentrations). The amount of adsorption is time dependent, showing a two-fold increase from one to seven days (fig. 46).

To examine the spatial variability of the adsorption of Li on the sediments a set of one-day adsorption experiments were

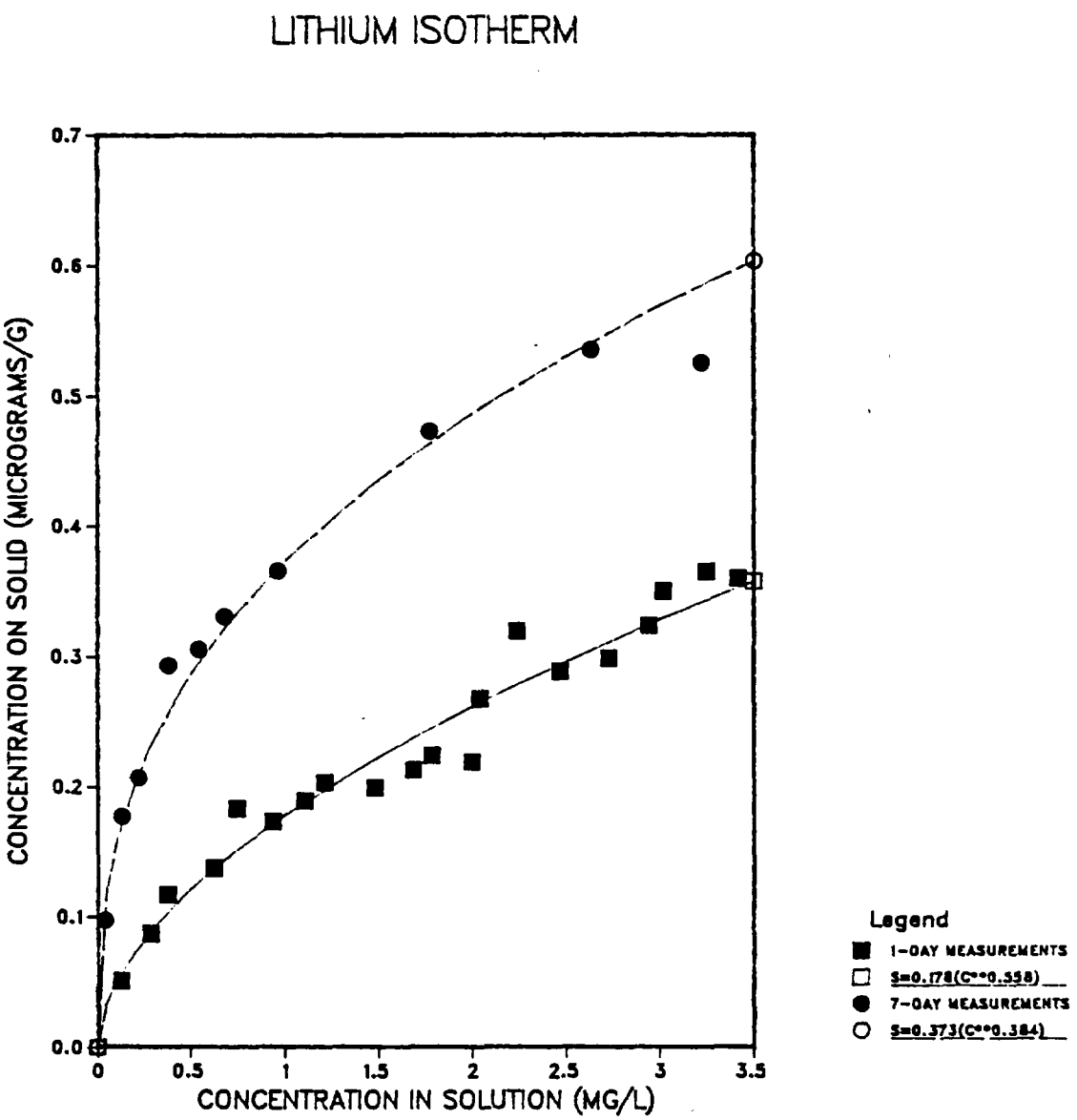

Figure 46. Absorption isotherms after 1 day and 7 days for lithium

on to Cape Cod sediment, (written communication, Warren Wood, 1987)

conducted on cores from the large-scale tracer test site. The results of these experiments are shown in table 11. The amount of Li adsorption to the core sediments at the specified concentration is very similar to that shown for the one-day nonlinear isotherm (fig. 46). The reader should note that the distribution coefficient (Kd) calculated in table 10 assumes a linear isotherm and that the slope of the one-day nonlinear isotherm at C=0.275 mg/L is 0.175, significantly lower than the average Kd (0.303). It is interesting, however, to note that there is variability in Li adsorption with a maximum Kd value of 0.414, a minimum of 0.221 and a standard deviation of 0.054 (about 18% of the mean, 0.303).

It is apparent from both the nonlinear isotherms and the Kd measurements that a significant amount of lithium is adsorbed on the sediments. The relative amount adsorbed can be calculated using a ratio of the amount adsorbed to the total:

$$\text{fraction of Li adsorbed} = \frac{\rho s}{nc+\rho s}$$

and substitution into the one-day nonlinear isotherm gives

$$\text{fraction of Li adsorped} = \frac{\rho(0.178\ c^{0.558})}{nc + \rho(0.178\ c^{0.558})}$$

Using n=0.4 L/L and ρ = 1.7 g/mL, the amount of adsorbed lithium is 68% at C=0.1 mg/L, 58% at C = 0.25 mg/L, and 43% at C = 1.0 mg/L. This indicates that as the concentration in solution decreases there is a larger relative amount of Li adsorbed onto the solid. As will be

Table 11

Vertical Variations in Kd for Li Adsorption, F415 C6
(written communication, Warren W. Wood, 1987)

Depth in feet below land surface	Concentration in in solution (mg/L)	Li Adsorption per gram of sediment (µg/g)	Distribution coefficient (Kd) (mL/g)
19-19.5	0.257	0.091	0.354
I9.5-20.0	0.257	0.081	0.315
20.0-20.46	0.257	0.072	0.280
20.46-20.92	0.257	0.067	0.26I
20.92-21.42	0.267	0.073	0.273
21.42-21.92	0.267	0.068	0.255
21.92-22.38	0.267	0.073	0.273
22.38-22.86	0.267	0.068	0.255
24.0-24.54	0.272	0.107	0.393
24.54-25.08	0.272	0.080	0.294
25.08-25.64	0.272	0.075	0.276
29.0-29.46	0.276	0.104	0.377
29.46-29.92	0.276	0.085	0.308
29.92-30.38	0.276	0.061	0.221
30.38-30.82	0.276	0.073	0.265
30.82-31.32	0.278	0.094	0.338
31.32-31.82	0.278	0.098	0.351
31.82-32.32	0.278	0.112	0.402
32.32-32.78	0.278	0.115	0.414
35.0-35.50	0.279	0.096	0.345
35.5-36.13	0.279	0.081	0.289
36.13-36.71	0.279	0.076	0.271
36.71-37.29	0.279	0.067	0.241
37.29-37.87	0.279	0.072	0.258
37.87-38.48	0.279	0.077	0.277

shown, the movement and distribution of lithium in the large-scale test was affected by the nonlinear adsorption onto the sediments.

E. Bromide and Lithium Distributions

1. Solute Distributions in Areal and Vertical Views

Graphical views of solute distributions were used throughout the tracer test to plan sampler installation (areally and vertically) and sampling round choices. The raw data were plotted in several ways; the most useful were vertical averages, maximum concentrations, and cross-sections. Vertical averaging was done by vertically integrating over the length of each sampler and dividing each by the sampler length. Vertical averages give a strong indication of the bulk tracer mass location in the horizontal plane. Therefore they are a good indicator of the center of mass. However, vertical averages are generally poor indicators of the solute cloud edges and overall extent of the cloud because of the dampening effect of the averaging process.

A plot showing the distribution of maximum concentration in each sampler does a better job of delineating the edges and general extent of the solute cloud. The maximum concentration plots from previous rounds were used to predict the direction of solute movement for planning the next round of sampling and sampler installation. Obtaining a complete sampling of the solute distribution (particularly bromide) was a major objective because the spatial variance calculations are more sensitive to the lower concentration edges than either mass or center of mass calculations.

Cross-sections along the longitudinal axis of the bromide cloud were used to plan the vertical placement of samplers. Cross-sections are also more detailed illustrations of the complex concentration information than either vertical averages or maximum concentration plots. Cross-sections were also used for interpolating and extrapolating data for samplers which did not fully penetrate the cloud thickness.

Vertically averaged bromide concentrations at 13 and 32 days after injection are shown in figures 47 and 48. The rate of horizontal movement of the bromide cloud was about 1.4 ft/day, which matches the velocity predicted by Darcy's law from estimated hydraulic parameters. The direction of the bromide movement also closely follows the projected path based on water-table configuration. A comparison of figures 47 and 48 shows a decrease over time in peak concentration along with a rapid longitudinal spreading of the bromide cloud caused by the velocity differences between the leading (3 ft/day) and trailing (0.4 ft/day) edges. This range in velocity is likely due to heterogeneity in aquifer hydraulic conductivity.

Longitudinal cross-sections of the bromide cloud are shown in figures 49-52. In the early stages of the tracer test the concentration distribution was highly variable both vertically and longitudinally. This variability in concentration was likely due to velocity differences caused by heterogeneity in hydraulic conductivity. Although the vertically averaged values plotted in figures 47 and 48 are useful in visualizing the solute cloud location,

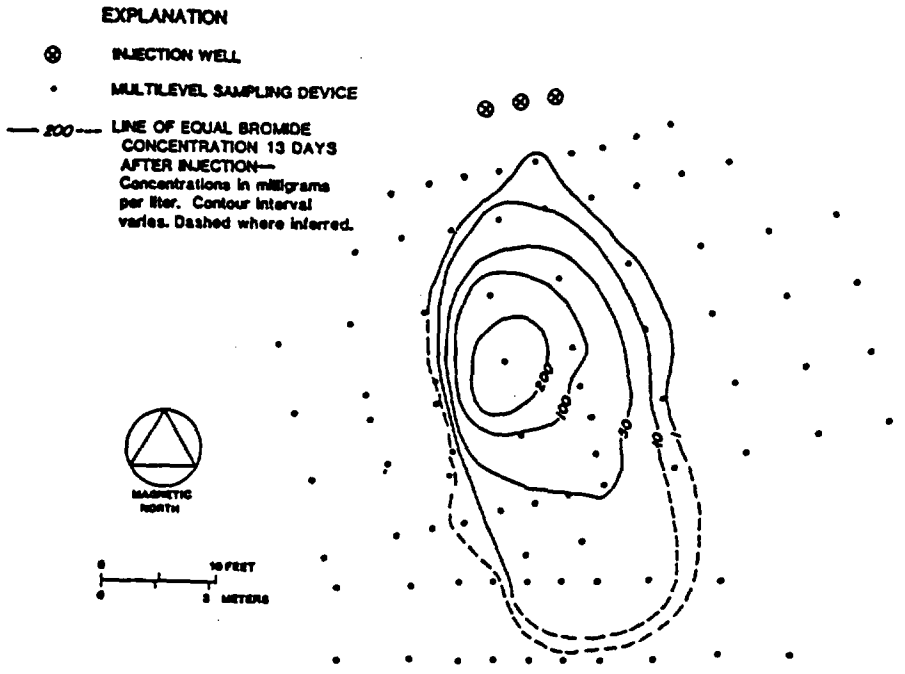

Figure 47.—Vertically averaged bromide concentration distribution in the aquifer 13 days after the injection of the tracer solution.

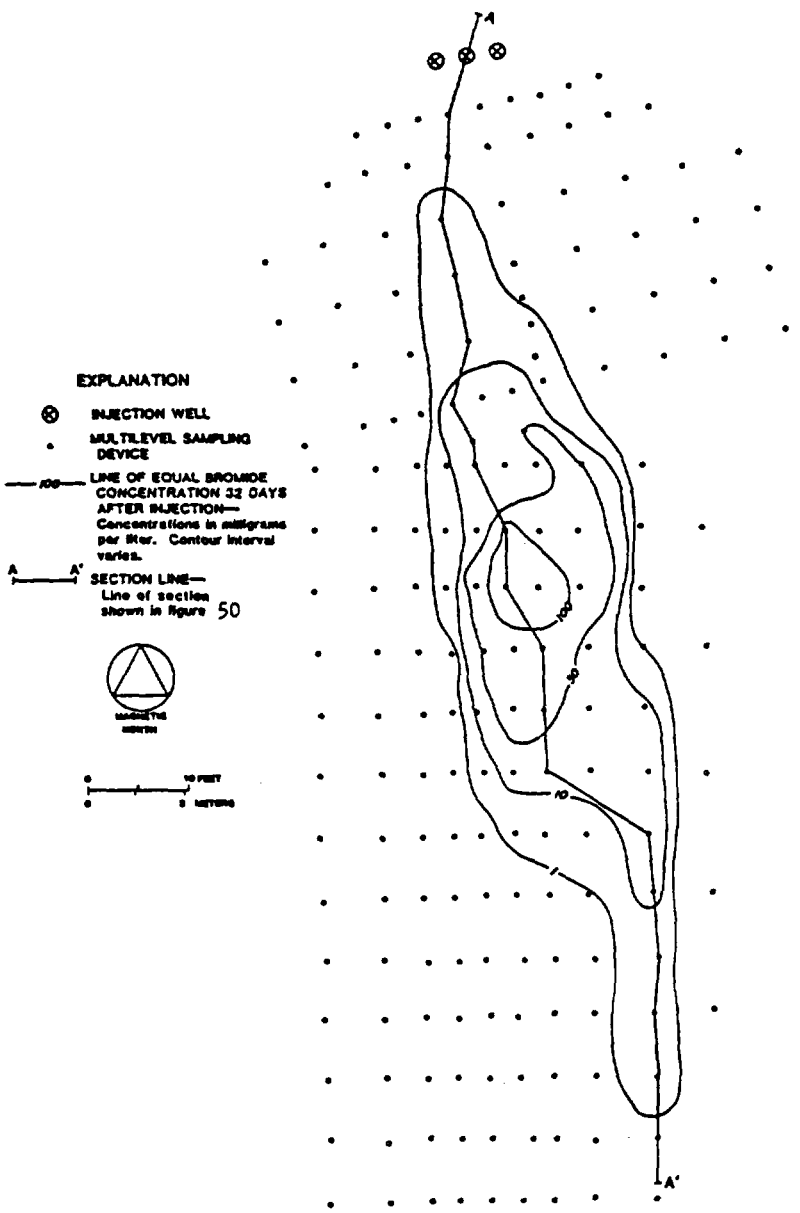

Figure 48 Vertically averaged bromide concentration distribution in the aquifer 32 days after injection of the tracer solution

Longitudinal Cross-section of Bromide Concentration (mg/L),
13 Days after Injection

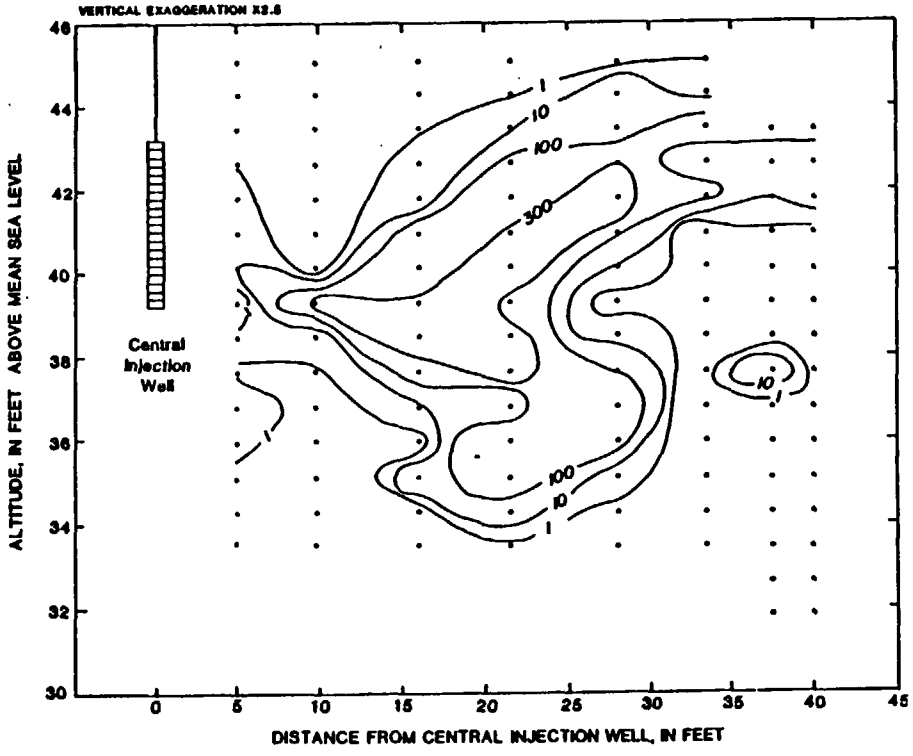

Figure 49. longitudinal crossection of bromide 13 days after injection

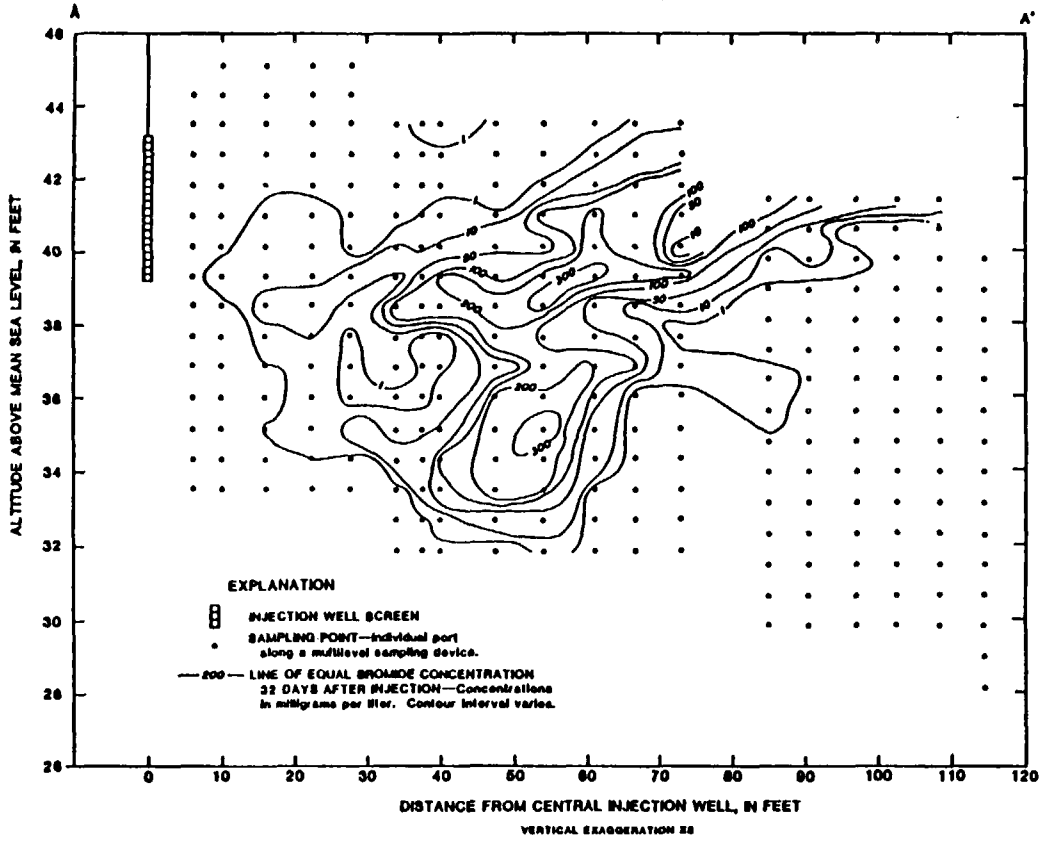

Figure 50 Longitudinal cross-section of bromide-concentration distribution in the aquifer 32 days after injection of the tracer solution. Location of section shown in figure 48

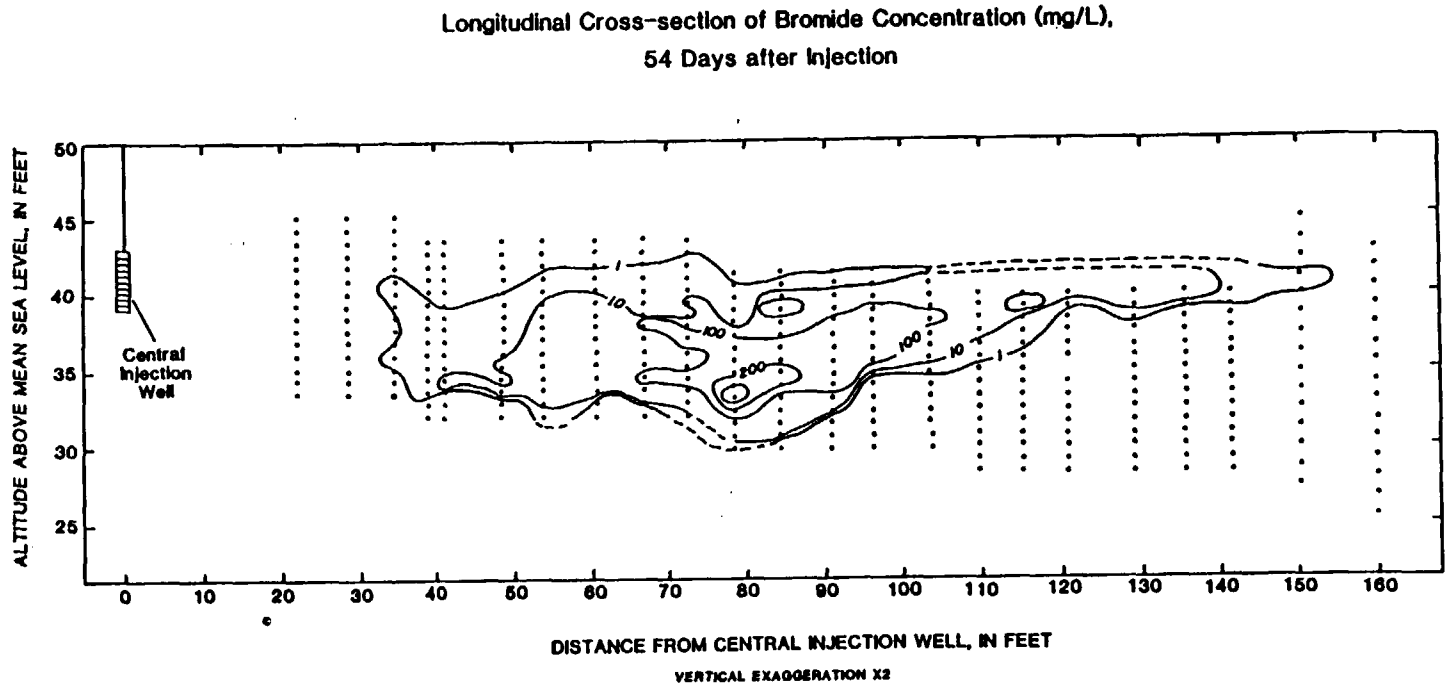

Figure 51. Longitudinal crossection of bromide 54 days after injection

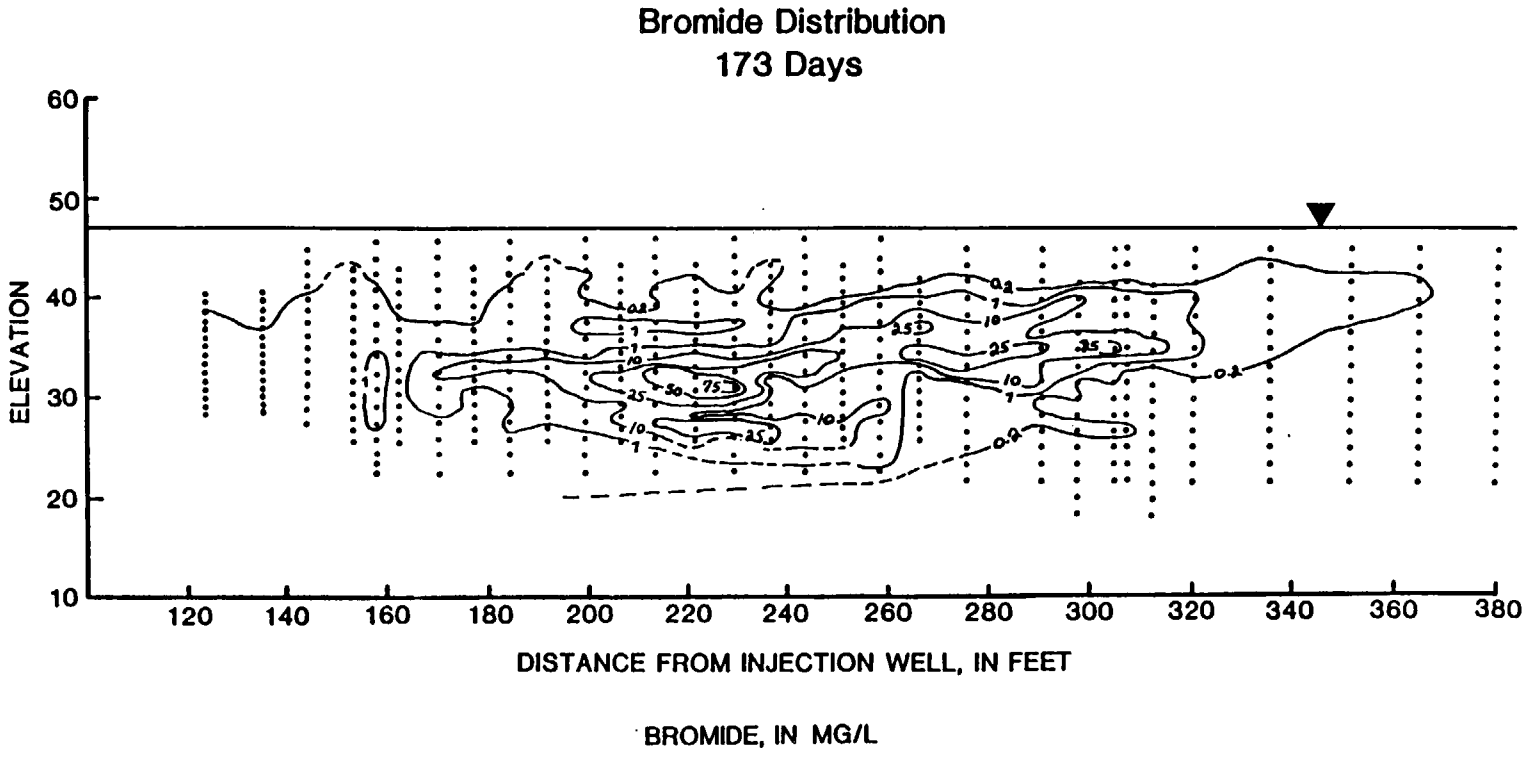

Figure 52. Longitudinal crossection of bromide, 173 days after injection

real distributions, as indicated in figures 49-52, are much more varied and complex.

2. Vertical Movement of the Bromide Cloud

The bromide cloud moved vertically downward about 10 feet during the first 200 days of transport (fig. 53). This vertical movement was probably caused by the difference in density between the injected solution and the native ground water as well as by the accretion of recharge at the water table. The initial concentration of dissolved solids in the tracer solution was about 890 mg/L; dissolved solids concentration of the native ground water ranged from 40 to 150 mg/L. The tracer test at Borden, Canada also showed sinking of the tracer cloud during the early part of the test (Freyberg, 1986).

Using Hubbert's (1953) method, it is possible to calculate the potential for sinking due to density contrasts (Denis LeBlanc, written communication, 1987). Hubbert's approach assumes that a small volume of immiscible fluid, with a different density than the surrounding fluid, moves in response to the sum of the surrounding fluid's potential and a potential due to the density contrast. It is also assumed that there are no other hydrodynamic effects, particularly the potential needed for surrounding fluid displacement, influencing the volume movement. An angle can be calculated for the fluid volume trajectory as it moves vertically. The calculations are shown in fig. 54. The results show that an expected range of the angle, for a Kz/Kx ratio of 0.2, is between 1 to 6 degrees downward. This range brackets the observed angle of 4 degrees, thus supporting

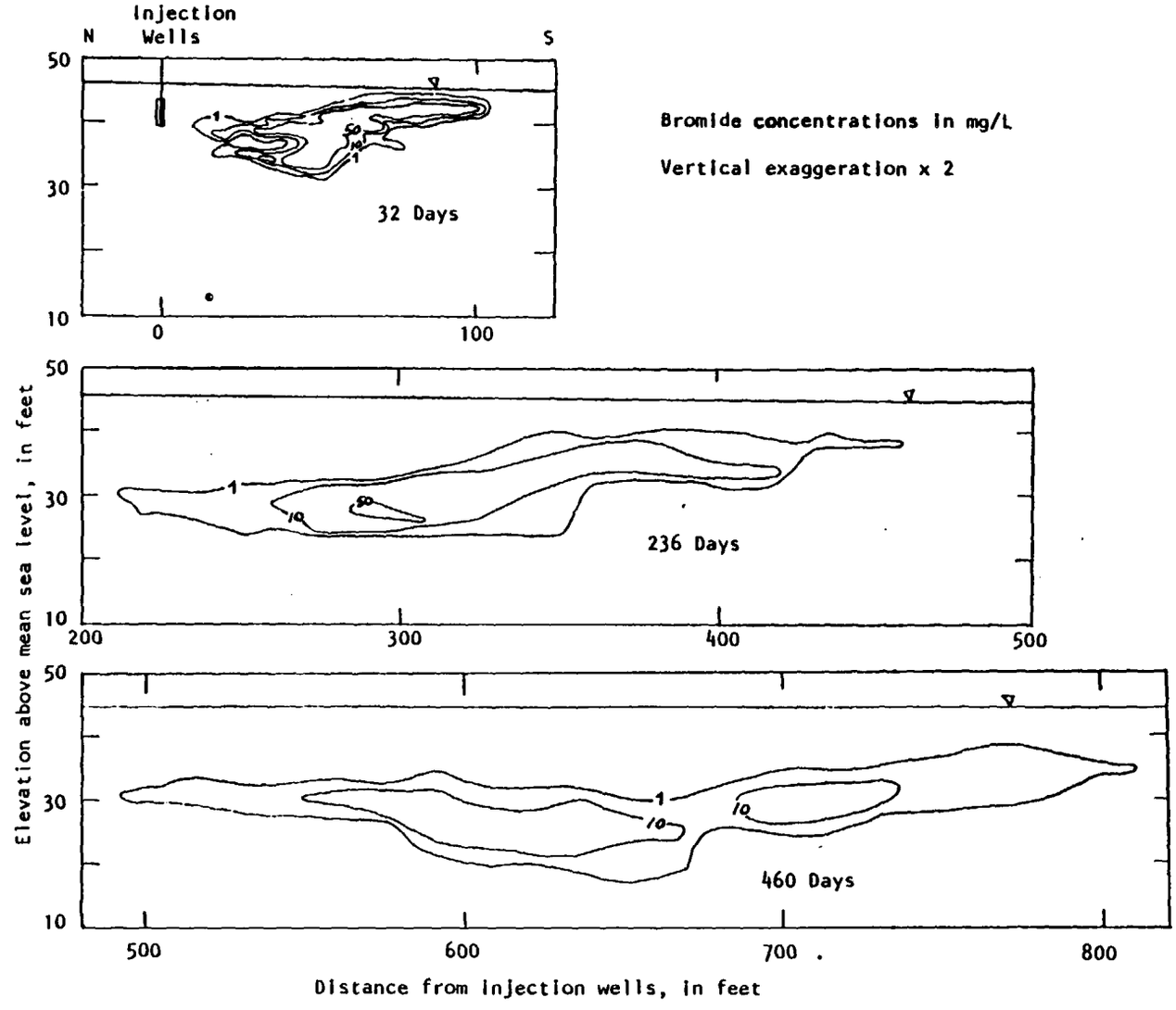

Figure 53. Longitudinal crossection of bromide after 32, 236, and 460 days

DENSITY EFFECT

Theory

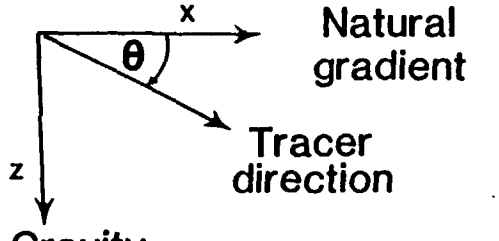

$$\theta = \tan^{-1}\left[\frac{K_z}{K_x} \cdot \frac{-\frac{[\rho_w - \rho_t]}{\rho_w}}{\frac{\delta h}{\delta x}}\right]$$

Hubbert (1953)

Predicted

$\frac{K_z}{K_x}$	Tracer Density 1.00089	1.00023
1	28°	3°
0.2	6°	0.7°

$\rho_w = 1.00015$ g/cm^3

$\delta h/\delta x = -0.0014$

Observed

$\theta \approx 4°$

Figure 54. Calculation of the angle from the horizontal for the vertical movement of a fluid with a greater density

the argument for density-driven sinking in the early part of the tracer test.

When bromide concentrations declined from more than 500 mg/L to 62 mg/L, the downward movement of the cloud was slower but did not stop. Therefore, part of the vertical movement of the tracer cloud may also be due to vertical flow caused by areal recharge. During the first 200 days of the test, total precipitation was 32 inches and the water table rose about 8 inches, indicating a significant accretion of recharge. The angle of vertical flow that would be expected from recharge can be calculated by using the ratio of the rate of vertical recharge to the rate of horizontal specific discharge:

$$\tan^{-1}\left(\frac{\varepsilon}{q}\right) = 0.5 \text{ degrees}$$

where

$$\varepsilon = 21 \text{ inches/yr} = 1.75 \text{ ft/yr}$$

$$q = 380 \frac{\text{ft.}}{\text{day}} \cdot (0.0014) \cdot \frac{365 \text{ days}}{\text{yr}} = 194 \text{ ft/yr.}$$

The above calculated angle matches the observed angle of about 0.5 degrees during the later part of the tracer test (after 250 days).

3. Bromide Cloud Spreading and Shape

The bromide cloud spread significantly in the longitudinal direction during transport, but spread much less transverse to flow

(figs. 47 and 48). At 460 days after injection, the cloud was over 300 feet long but only 45 feet wide. After the initial vertical spreading during injection, the bromide cloud spread vertically only slightly and remained about 12 to 20 feet thick as it moved downgradient (fig. 53). During transport there was significant dilution of the tracers and peak concentrations decreased from over 500 mg/L just after injection to about 40 mg/L after 460 days.

The tracer cloud was asymmetrical along the longitudinal axis and exhibited two zones of elevated bromide concentrations. One zone of high concentration was near the water table and ahead of a second, lower zone (fig. 53). The two zones were observed in the first view of the cloud taken 13 days after injection (fig. 49) and persisted in all subsequent views. The two zones were probably formed during injection because of variations in hydraulic conductivity near the injection wells and persisted because vertical mixing was small during transport. The leading edge of the bromide cloud occurred near the water table and moved forward at over 3 ft/day during the early part of the test. The average velocity of the leading edge was about 2 ft/day over the length of the test. The higher velocity near the water table may reflect a zone of higher hydraulic conductivity that caused the leading edge to move well ahead of the main bromide cloud.

4. Lithium Distribution and Movement

The lithium cloud followed a similar trajectory to the bromide cloud (fig. 55). However, its average rate of movement was much slower than the bromide. After 460 days the lithium cloud has

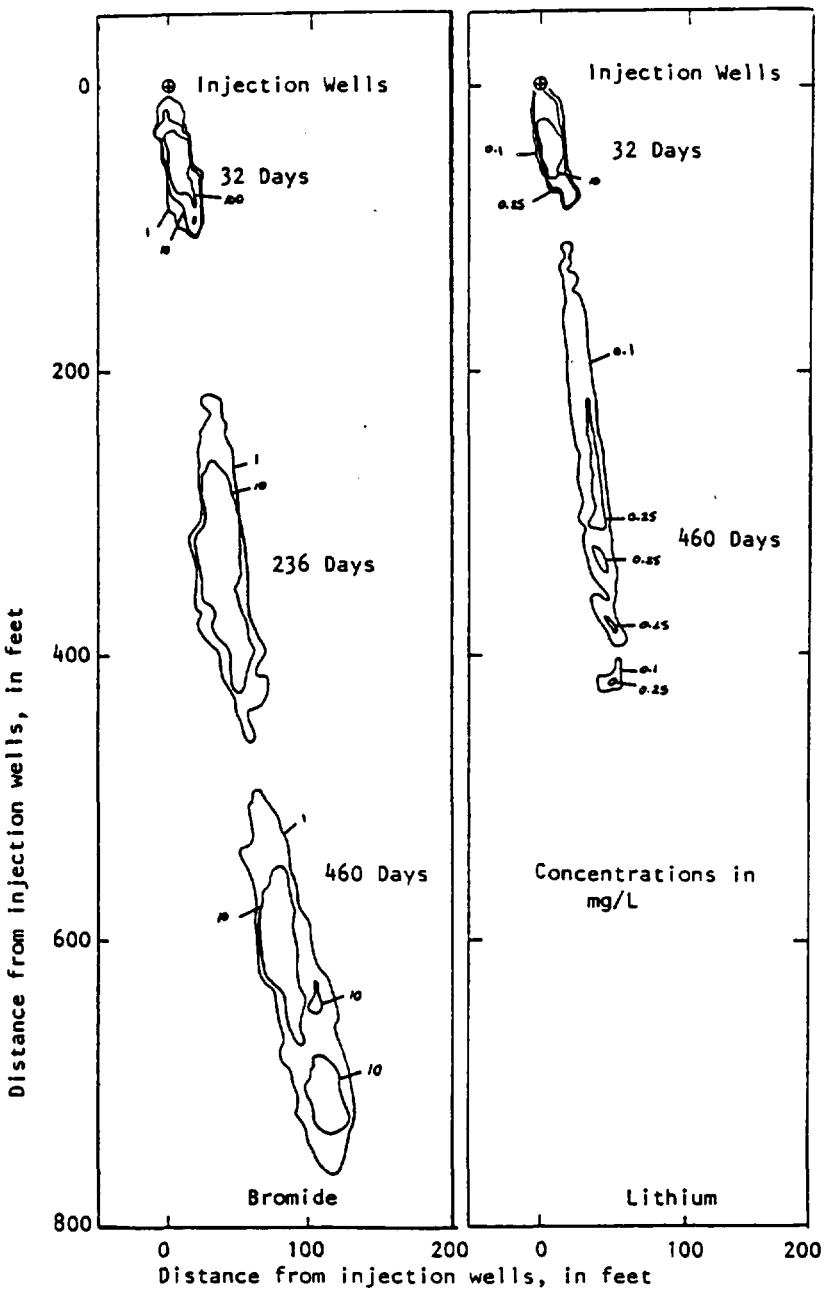

Figure 55. Contours of maximum lithium concentration in mg/L in comparison to those for bromide

spread longitudinally more than the bromide cloud had at about the same travel distance (236 days). The lithium distribution is also more asymmetric, with higher concentrations closer to the leading edge and a long tail extending back toward the injection wells (fig. 55). It is very evident from these characteristics that the transport of the lithium cloud is strongly affected by adsorption to the sediments.

F. Moments Analysis

1. Spatial Moments and Model Parameters for a Nonreactive Solute

The spatial moments of the bromide distribution were used to calculate the total bromide and lithium mass, velocity, and dispersivity during the large-scale tracer test. The relationship between the spatial moments and these parameters can be derived using an approach developed by Aris (1956). Using the one dimensional (this approach can easily be extended to three dimensions) advective-dispersion equation for a nonreactive solute (modified from eq. 7-49, Bear, 1979),

$$\frac{\partial c}{\partial t} + \frac{\partial (vc)}{\partial x} - \frac{\partial}{\partial x}\left(D \frac{\partial c}{\partial x}\right) = 0 \qquad (1)$$

where

V = seepage velocity,

D = solute dispersion coefficient,

and the general moments equation,

$$M_m = \frac{1}{M_T}\int_{-\infty}^{\infty} ncx^m dx \qquad (2)$$

where

n = porosity

M_T = total solute mass $= \int_{-\infty}^{\infty} ncdx$

the change in moment with respect to time is:

$$\frac{\partial M_m}{\partial t} = \frac{1}{M_T}\cdot\frac{\partial}{\partial t}\int_{-\infty}^{\infty} ncx^m dx = \frac{1}{M_T}\int_{-\infty}^{\infty} nx^m \frac{\partial c}{\partial t}\,dx \qquad (3)$$

$$= \frac{1}{M_T}\int_{-\infty}^{\infty} nx^m\left[\frac{\partial}{\partial x}\left(D\frac{\partial c}{\partial x}\right) - \frac{\partial (vc)}{\partial x}\right]dx \qquad (4)$$

For the first moment M_1:

$$\frac{\partial M_1}{\partial t} = \frac{1}{M_T}\int_{-\infty}^{\infty} nx\left[\frac{\partial}{\partial x}\left(D\frac{\partial c}{\partial x}\right) - \frac{\partial (vc)}{\partial x}\right]dx \qquad (5)$$

Integration by parts is now applied:

$$\frac{\partial M_1}{\partial t} = \frac{n}{M_T}\left|_{-\infty}^{\infty} x\left[D\frac{\partial c}{\partial x} - vc\right] - \frac{n}{M_T}\int_{-\infty}^{\infty}\left[D\frac{\partial c}{\partial x} - vc\right]dx \qquad (6)\right.$$

and it is assumed that both c and $\partial c/\partial x$ go to zero at the limits ($\pm\infty$), leaving:

$$\frac{\partial M_1}{\partial t} = \frac{n}{M_T} \int_{-\infty}^{\infty} \left[-D \frac{\partial c}{\partial x} + vc \right] dx \qquad (7)$$

If D and v are assumed constant in space then this produces:

$$\frac{\partial M_1}{\partial t} = v - \left| \frac{nDc}{M_T} \right|_{-\infty}^{\infty} = v, \qquad (8)$$

where c is zero at the limits. Therefore the change in mean position ($M_1 = \bar{x}$) is the average solute velocity. If D and v are not constant the result is:

$$\frac{\partial M_1}{\partial t} = \frac{n}{M_T} \int_{-\infty}^{\infty} c \frac{\partial D}{\partial x} dx + \frac{n}{M_T} \int_{-\infty}^{\infty} vc dx \qquad (9)$$

$$= \overline{\frac{\partial D}{\partial x}} + \bar{v} \qquad (10)$$

This result indicates that the change in the first spatial moment is the sum of the average change in the dispersion coefficient (w.r.t. space) and the average solute velocity.

For the second moment, equation (4) is modified to produce a central moment:

$$\frac{\partial M_2}{\partial t} = \frac{n}{M_T} \int_{-\infty}^{\infty} (x-\bar{x})^2 \left[\frac{\partial}{\partial x} \left(D \frac{\partial c}{\partial x} \right) - \frac{\partial (vc)}{\partial x} \right] \qquad (11)$$

Applying integration by parts reveals

$$\frac{\partial M_2}{\partial t} = \frac{n}{M_T}\left|_{-\infty}^{\infty}(x-\bar{x})^2\left(D\frac{\partial c}{\partial x} - vc\right) - \frac{n}{M_T}\int_{-\infty}^{\infty} 2(x-\bar{x})\left(D\frac{\partial c}{\partial x} - vc\right)dx \right. \tag{12}$$

and as c and $\partial c/\partial x$ go to zero at the limits,

$$\frac{\partial M_2}{\partial t} = \frac{n}{M_T}\int_{-\infty}^{\infty} 2(x-\bar{x})\left(vc - D\frac{\partial c}{\partial x}\right)dx \tag{13}$$

Now if v is assumed constant,

$$\frac{n}{M_T}\int_{-\infty}^{\infty} 2(x-\bar{x})vc\,dx = \frac{2v}{M_T}\int_{-\infty}^{\infty} ncx\,dx - \frac{2v}{M_T}\int_{-\infty}^{\infty} nc\bar{x}\,dx$$

$$= 2v\bar{x} - 2v\bar{x} = 0. \tag{14}$$

Proceeding with integration by parts again:

$$\frac{\partial M_2}{\partial t} = \frac{-2n}{M_T}\left|_{-\infty}^{\infty}(x-\bar{x})\,Dc + \frac{n}{M_T}\int_{-\infty}^{\infty} 2c\,\frac{\partial}{\partial x}\left(D(x-\bar{x})\right)dx \right. \tag{15}$$

$$= \frac{2}{M_T}\int_{-\infty}^{\infty} nc\left(D + (x-\bar{x})\frac{\partial D}{\partial x}\right)dx \tag{16}$$

If $\partial D/\partial x$ is assumed constant, then

$$\frac{2}{M_T}\int_{-\infty}^{\infty} nc(x-\bar{x})\frac{\partial D}{\partial x}\,dx = \frac{2}{M_T}\frac{\partial D}{\partial x}\left[\int_{-\infty}^{\infty} ncx\,dx - \bar{x}\int_{-\infty}^{\infty} nc\,dx\right]$$

$$= \frac{2}{M_T}\frac{\partial D}{\partial x}\left[\bar{x}\,M_T - \bar{x}\,M_T\right] = 0 \qquad (17)$$

This leaves

$$\frac{\partial M_2}{\partial t} = \frac{2}{M_T}\int_{-\infty}^{\infty} ncD\,dx \qquad (18)$$

or equivalently,

$$\bar{D} = \frac{1}{2}\frac{\partial \sigma_x^2}{\partial t} \qquad (18a)$$

and therefore one half the change in variance w.r.t. time is equal to the average dispersion coefficient for the solute distribution. If it is assumed that the dispersion coefficient is proportional to the average solute velocity,

$$D = \alpha_x \bar{v} \qquad (19)$$

then substitution into equation 18a produces a relation between the dispersivity, α_x and the change in variance w.r.t. travel distance, $\bar{x} = vt$,

$$\bar{D} = \alpha_x \bar{v} = \frac{1}{2}\frac{\partial \sigma_x^2}{\partial \bar{x}} \cdot \frac{\partial \bar{x}}{\partial t} = \frac{\bar{v}}{2}\frac{\partial \sigma_x^2}{\partial \bar{x}}$$

and

$$\alpha_x = \frac{1}{2} \frac{\partial \sigma_x^2}{\partial \bar{x}}. \qquad (20)$$

Equation 20 was used in the large-scale test analysis to find the macrodispersivity of the solutes. It is important to point out that a major assumption in this analysis is that of constant velocity. This assumption was carefully examined during the test analysis.

As was noted in the introduction there is field evidence that the dispersivity (α_x) increases with travel distance (or time) during transport. It is important that this time dependence of the dispersivity should not be confused with spatial dependence. In the moments analysis for the large-scale test α_x is held constant in space but allowed to vary with time. Furthermore, because moments are evaluated at points in time and not continuously, the value of α_x that is calculated is the time averaged (i.e. bulk) value over the period of time between the sampling rounds.

2. Spatial Moments and Model Parameters for a Reactive Solute

The spatial moments of the lithium distribution can be related to solute mass, velocity, and dispersivity using the same approach used for bromide. For lithium the advective-dispersive equation (eq. 1) is modified to include a term representing the instantaneous, reversible adsorption of lithium:

$$n \frac{\partial c}{\partial t} + \rho \frac{\partial s}{\partial t} = \frac{\partial}{\partial x}\left(nD \frac{\partial c}{\partial x}\right) - q \frac{\partial c}{\partial x} \qquad (21)$$

where

ρ = bulk density

s = concentration on the solid

q = specific discharge.

The total mass in the aquifer is defined as a sum of the mass in solution and the mass adsorbed onto the solid:

$$M_T = \int_{-\infty}^{\infty} (nc + \rho s)\, dx = M_c + M_s \tag{22}$$

and the change in total mass over time is zero,

$$\frac{\partial M_T}{\partial t} = 0, \quad \frac{\partial M_c}{\partial t} = -\frac{\partial M_s}{\partial t} \tag{23}$$

The total first moment can be defined,

$$\bar{x}_T = \int_{-\infty}^{\infty} \frac{x\,(nc + \rho s)}{M_T}\, dx \tag{24}$$

with the solute and adsorbed first moments

$$\bar{x}_c = \int_{-\infty}^{\infty} \frac{xnc}{M_c}\, dx \tag{25}$$

$$\bar{x}_s = \int_{-\infty}^{\infty} \frac{x\rho s}{M_s}\, dx \tag{26}$$

and $\bar{x}_T M_T = \bar{x}_c M_c + \bar{x}_s M_s$. The change in $\bar{x}_T$ with respect to time is then

$$\frac{\partial \bar{x}_T}{\partial t} = \int_{-\infty}^{\infty} \frac{x}{M_T} \frac{\partial}{\partial t} (nc+\rho s)dx \tag{27}$$

and substituting in the right hand side of equation 21,

$$\frac{\partial \bar{x}_T}{\partial t} = \int_{-\infty}^{\infty} \frac{x}{M_T} \left[\frac{\partial}{\partial x} \left(nD \frac{\partial c}{\partial x} \right) - q \frac{\partial c}{\partial x} \right] dx \tag{28}$$

Using integration by parts and assuming q and dD/dx are constant, the result is:

$$\frac{\partial \bar{x}_T}{\partial t} = \frac{M_c}{M_T} \left(\frac{q}{n} + \frac{dD}{dx} \right) = \frac{M_c}{M_T} \left(v + \frac{dD}{dx} \right). \tag{29}$$

This result shows that the change in total first moment with respect to time is equal to the retarded fluid velocity and change in dispersion coefficient with distance. If the adsorption isotherm is linear ($s = K_d c$), the coefficient M_c/M_T, is constant:

$$\frac{M_c}{M_T} = \frac{\int_{-\infty}^{\infty} nc\, dx}{\int_{-\infty}^{\infty} (nc+\rho s)dx} = \frac{n \int_{-\infty}^{\infty} c\, dx}{(n+\rho Kd) \int_{-\infty}^{\infty} c dx} = \frac{1}{1 + \frac{\rho Kd}{n}}, \tag{30}$$

where $1 + \frac{\rho Kd}{n}$ is the retardation coefficient.

If the isotherm is nonlinear however, the ratio M_c/M_T will change with time as the concentrations decrease. In the case of the lithium adsorption isotherm it would be expected that more mass will be on the sediment as the concentrations decrease, and as a result the Li velocity will decrease.

The total second moment is defined as:

$$\sigma_x^2 = \int_{-\infty}^{\infty} \frac{(x-\bar{x}_T)^2\,(nc+\rho s)}{M_T}\,dx, \tag{31}$$

and the change with respect to time is:

$$\frac{\partial \sigma_x^2}{\partial t} = \int_{-\infty}^{\infty} \frac{(x-\bar{x}_T)^2}{M_T}\,\frac{\partial (nc+\rho s)}{\partial t}\,dx. \tag{32}$$

After substituting in the right-hand side of equation (21) the change in the second moment is:

$$\frac{\partial \sigma_x^2}{\partial t} = \int_{-\infty}^{\infty} \frac{(x-\bar{x}_T)^2}{M_T}\left[\frac{\partial}{\partial x}\left(nD\,\frac{\partial c}{\partial x}\right) - q\,\frac{\partial c}{\partial x}\right]dx. \tag{33}$$

Using integration by parts and assuming q and dD/dx are constant the result is:

$$\frac{\partial \sigma_x^2}{\partial t} = \frac{2M_c}{M_T}\left[\bar{D} + (\bar{x}_c - \bar{x}_T)\left(v + \frac{dD}{dx}\right)\right] \tag{34}$$

where $\bar{D} = \frac{1}{M_c} \int_{-\infty}^{\infty} Dnc\, dx$, the average dispersion coefficient.

The above result shows that the change in the total variance with respect to time is equal to a retarded dispersion coefficient and additional terms. If the adsorption isotherm is linear the difference between the solute first moment and total first moment $(\bar{x}_c - \bar{x}_T)$ is zero.

$$\bar{x}_T = \int_{-\infty}^{\infty} \frac{x(nc+\rho s)}{M_T}\, dx = \frac{(n+\rho Kd)}{(n+\rho Kd)} \frac{\int_{-\infty}^{\infty} cx\, dx}{\int_{-\infty}^{\infty} c\, dx} = \frac{\int_{-\infty}^{\infty} cx\, dx}{\int_{-\infty}^{\infty} c\, dx}$$

$$\bar{x}_c = \int_{-\infty}^{\infty} \frac{xnc}{M_c}\, dx = \frac{n\int_{-\infty}^{\infty} cx\, dx}{n\int_{-\infty}^{\infty} c\, dx} = \frac{\int_{-\infty}^{\infty} cx\, dx}{\int_{-\infty}^{\infty} cdx},$$

and therefore $\bar{x}_T = \bar{x}_c$.

If the isotherm is nonlinear however, it is possible that the solute and total first moments will not be equal and the second term in equation (34) will have an effect on the change in variance with respect to time.

It can be shown that the relationship in equation 20 also holds for a solute with linear adsorption. For a solute with a linear adsorption isotherm equation 34 becomes:

$$\frac{\partial \sigma_x^2}{\partial t} = \frac{2M_c}{M_T} \bar{D} \qquad (35)$$

It is assumed that $\bar{D}$ is composed of a fluid velocity and dispersivity ($\bar{D} = v\,\alpha_x$), and integrating equation 29 for travel distance:

$$\bar{x}_T = \frac{M_c}{M_T} vt\ , \qquad (36)$$

it is possible to obtain the following relation:

$$\frac{\partial \sigma_x^2}{\partial t} = \frac{M_c}{M_T} \frac{v\,\partial \sigma_x^2}{\partial \bar{x}_T} = \frac{2M_c}{M_T} v\alpha_x \qquad (37)$$

and

$$\alpha_x = \frac{1}{2} \frac{\partial \sigma_x^2}{\partial \bar{x}_T} \qquad (38)$$

Equation 38 is analogous to equation 20 and shows that one half the change in variance w.r.t. travel distance is equal to the reactive solute dispersivity when the solute has a linear adsorption isotherm.

3. Numerical Approach to Moment Calculations

An estimate of the spatial moments was calculated for each sampling round using a numerical integration of the solute distribution. The values of concentration at the sampling points were linearly interpolated over the domain and then integrated to

obtain the moment estimates. For this analysis the three-dimensional spatial moments expression is,

$$M_{ijk} = \int\int\int_{\Omega} \frac{nc(x-\bar{x})^i(y-\bar{y})^j(z-\bar{z})^k dz\, dy\, dx}{M_T} \qquad (39)$$

where

- n = porosity
- c = solute concentration
- x,y,z = coordinate directions
- M_T = total mass = M_{ooo}
- Ω = test domain.

For this analysis porosity was assumed constant (0.39) and for all moments greater than zero (i.e., total mass) can be canceled from the calculations.

Because the solute concentration was sampled at points (averaging volume = .006 ft^3) in space, rather than continuously, a numerical integration procedure was used to calculate the moments. First the integration over the vertical is performed at each sampler location because the x and y positions are the same for each set of vertical samples (typically 15):

$$Z1(k) = \int_{z_{i-1}}^{z_i} c(z-\bar{z})^k\, dz, \qquad (40)$$

for example,

$$M_0 : \int_{z_{i-1}}^{z_i} c\,dz \tag{40a}$$

$$M_1 : \int_{z_{i-1}}^{z_i} cz\,dz \tag{40b}$$

$$M_2 : \int_{z_{i-1}}^{z_i} c(z-\bar{z})^2\,dz. \tag{40c}$$

The integration over z is performed numerically using trapezoidal quadrature, which assumes a linear interpolation between sampling points:

$$C = Az + B, \tag{41}$$

where

$$A = \frac{(c_i - c_{i-1})}{(z_i - z_{i-1})},$$

$$B = c_i - AZ_i$$

Substituting (41) into (40) for each sampling interval results in:

$$\int_{z_{i-1}}^{z_i} (Az+B)(z-\bar{z})^k dz, \tag{42}$$

which can be split into two pieces. The first piece is calculated using repeated application of integration by parts:

$$\int_{z_{i-1}}^{z_i} Az(z-\bar{z})^k dz = A \left|_{z_{i-1}}^{z_i} \frac{z^2}{2}(z-\bar{z})^k \frac{-kz^3}{6}(z-\bar{z})^{k-1} + \ldots \right.$$

$$= A \left|_{z_{i-1}}^{z_i} \sum_{n=2}^{k+2} \frac{(-1)^n k! z^n (z-\bar{z})^{K+2-n}}{n!(K+2-n)!} \right. . \qquad (43)$$

and the second piece is:

$$\int_{z_{i-1}}^{z_i} B(z-\bar{z})^k = B \left|_{z_{i-1}}^{z_i} \frac{(z-\bar{z})^{k+1}}{(k+1)} \right. . \qquad (44)$$

It should be pointed out that for the total mass (k=0) and the mean position (k=1), $\bar{z}$ is equal to zero.

With the z integration completed the next step is to integrate over the x and y plane. As an interpolation scheme between points is necessary, a linear interpolation between three sampling points (triangular subregion) is used:

$$ZI(k) = A+Bx+Cy \qquad (45)$$

k = counter-clockwise numbering of triangle points

where ZI(k) = vertically integrated value,

$$A = \frac{ZI_1(x_2y_3-x_3y_2) + ZI_2(x_3y_1-x_1y_3) + ZI_3(x_1y_2-x_2y_1)}{D}, \qquad (45a)$$

$$B = \frac{(ZI_1-ZI_3)(y_2-y_1) + (ZI_2-ZI_1)(y_3-y_1)}{D}, \qquad (45b)$$

$$C = \frac{(ZI_3 - ZI_1)(x_2 - x_1) - (ZI_2 - ZI_1)(x_3 - x_1)}{D}, \tag{45c}$$

$$D = (y_3 - y_1)(x_2 - x_1) - (y_2 - y_1)(x_3 - x_1). \tag{45d}$$

Substituting (45) into (39) produces:

$$M_{ijk} = \int_{\Omega_T}\int \frac{n(A+Bx+Cy)(x-\bar{x})^i(y-\bar{y})^j dy\, dx}{M_T}, \tag{46}$$

which is applied to each triangular subregion, Ω_T, for the total domain area, Ω. Equation 46 can be easily solved using a set of equations borrowed from finite element analysis. Each of the expressions within parentheses in equation 46 is a linear function over the triangular subdomain and can be represented as a sum of linear basis functions. For example:

$$ZI = A + Bx + Cy = \sum_{i=1}^{3} ZI_i\, \phi_i \tag{47}$$

where

ZI_i = value of ZI at point i

ϕ_i = 1 at i

= 0 at j or k,

$$= \frac{1}{2A_t}[(x_j y_k - x_k y_j) + x(y_j - y_k) + y(x_k - x_j)],$$

A_t = area of the triangular subdomain,

$$= \frac{1}{2}[(x_2y_3 - y_2x_3) - x_1(y_3 - y_2) + y_1(y_3 - x_2)$$

A counter-clockwise numbering index of the triangle points is required for these calculations. The other expressions are also represented using basis functions:

$$(x-\bar{x}) = \sum_{i=1}^{3} (x-\bar{x})_i \, \phi_i \tag{48}$$

$$(y-\bar{y}) = \sum_{i=1}^{3} (y-\bar{y})_i \, \phi_i \tag{49}$$

If equations (47), (48), and (49) are substituted into (46) the result is:

$$M_{ijk} = \int\int \frac{\left(\sum_{L=1}^{3} Zl_L \phi_L\right)\left(\sum_{m=1}^{3} (x-\bar{x})_m \phi_m\right)^i \left(\sum_{n=1}^{3} (y-\bar{y})_n \phi_n\right)^j dy \; dx}{M_T} \tag{50}$$

A useful formula for the integration of linear basis functions over triangular area is:

$$\int_{\Omega_T}\int \phi_1^i \phi_2^j \phi_3^k dx \; dy = \frac{2A_t \, i! \; j! \; k!}{(i+j+k+2)!}, \tag{51}$$

where A_t = area of triangular region.

Equation (51) is used in solving (50) by expanding (50) and sequentially applying (51), summing each component until the total integral is calculated.

Calculation of the second moments for the solute distribution will, in general, produce a symmetric tensor of solute variance terms:

$$\begin{bmatrix} \sigma^2_{xx} & \sigma^2_{xy} & \sigma^2_{xz} \\ \sigma^2_{yx} & \sigma^2_{yy} & \sigma^2_{yz} \\ \sigma^2_{zx} & \sigma^2_{zy} & \sigma^2_{zz} \end{bmatrix} \tag{52}$$

where $\sigma^2_{xy} = \sigma^2_{yx}$, $\sigma^2_{xz} = \sigma^2_{zx}$, $\sigma^2_{yz} = \sigma^2_{zy}$.

The eigenvalues and eigenvectors for the above tensor were calculated to find the principal components and angles of rotation from the original coordinate directions. The IMSL math routine EIGBS is used to compute the eigenvalues and eigenvectors of a banded symmetric matrix after the moments and cross-moment are calculated. A program implementing the numerical calculation of moments, eigenvalues, and eigenvectors is explained and listed in Appendix A.

To facilitate the moment calculations, a program was written to create the index list of triangular subdomains over which horizontal integration occurs. This program is incidental to the integration process; the index lists can be created by manually subdividing the domain. With a large number of views however, this

part of the process can be tedious and the triangulation program (listed in Appendix B) was used in creating many of the index lists.

The moments for reactive solutes were calculated using the same approach outlined in this section. The reactive moments will also include the term, ρs, representing the adsorbed phase, along with the tracer in solution, nc. The adsorbed phase term (ρs) is calculated using an adsorption isotherm, which is assumed to be constant in space and constant over the duration of the test. The spatial moments could then be calculated for either the solute distribution (nc), the adsorbed phase distribution (ρs), or the total distribution (nc + ρs).

G. Bromide Moments

1. Data Preparation

Each set of bromide data for each sampling round was checked for completeness both horizontally and vertically. In many cases samplers did not fully penetrate the bromide cloud, and the top or bottom sampler port had concentration values above background values. For these cases values were linearly interpolated between samplers (or less frequently extrapolated) to complete the vertical profile at each sampler (table 12). In the majority of situations a single additional value was added to establish a zero concentration above or below the sampling interval. The established cut off concentration for adding points was 0.5 mg/L; if a top or bottom sampler port showed a value above 0.5 mg/L, then an additional point was added; below this value, a point wasn't added.

Table 12

Numbers of Data used in Bromide Moment Analysis

Date	No. analyses	No. added zero values	No. samplers	No. added zero samplers	No. triangles
7/85	599	10	40	3	71
8/85	1700	33	114	0	188
9/85	2175	51	146	0	254
10/85	2264	53	153	0	266
11/85	1878	21	128	0	215
12/85	1648	6	111	0	185
1/86	1649	11	111	0	187
2/86	1592	8	107	0	180
3/86	1954	8	131	7	202
4/86	1923	6	129	0	197
5/86	2268	12	152	0	243
7/86	2247	10	151	0	183
8/86	2091	9	141	0	222
9/86	2002	0	134	0	223
10/86	1641	0	110	0	183
12/86	1654	0	111	4	190
Total	29,285	238	1969	14	3,189

Additional zero concentration samplers were added to the horizontal sampler distribution for three sampling dates (July, 1985; March, 1986; December, 1986; table 12). In each of these dates part of the concentration distribution was outside the sampler array. Rather than truncate the concentration distribution after the last sampler, additional zero concentration points were added. Due to the linear interpolation in the numerical method for calculating moments, the additional zero points allow a projection of the concentration distribution beyond the measured values. For each case (3 points for July, 1985; 7 points for March 1986; 4 points for December 1986) just a few points were needed to establish a reasonable concentration distribution. After the zero points were added vertically and horizontally an index list of triangular subregions was formed. Data input to the moment generating program (Appendix A) included porosity, background correction data, concentration values, and the index list for triangles.

2. Mass in Solution

Table 13 shows the results of the moment calculations for the sixteen bromide distributions. For each date the total mass (zeroth moment), the center of mass (first moment), and variances (second moment) were calculated.

The calculated total mass for each sampling round varied between 86 to 105 percent of the total injected mass (fig. 56). The differences between the calculated total mass and the injected mass are likely due to errors made estimating porosity, analyzing bromide, and interpolating the data vertically and horizontally.

Table 13 Moment Values for Bromide (all length units in feet, angles in degrees east from south)

Date	Injection	Mass(g)	x[a]	y[b]	z[c]	Cum. Dist.	Θ_i*	Θ_T**	$\sigma^2_{x'}$	$\sigma^2_{y'}$	$\sigma^2_{z'}$	$\Theta_{yx'}$+	$\Theta_{yz'}$++
07/85	12	4442	2.5	- 24.3	40.3	24.4	5.9	5.9	16.6	69.8	4.0	18.5	8.0
08/85	32	5146	8.7	- 55.3	38.3	56.0	11.3	8.9	19.8	217.1	5.0	12.8	5.5
09/85	54	4939	9.9	- 85.0	36.3	85.7	2.3	6.6	20.7	375.1	5.4	8.9	2.7
10/85	82	4986	18.5	-127.6	34.7	129.2	11.4	8.2	26.7	564.5	7.8	9.5	3.5
11/85	110	4912	26.7	-167.1	33.8	169.5	11.7	9.1	33.8	921.5	7.9	12.5	3.3
12/85	138	4229	33.2	-211.5	33.9	214.4	8.3	8.9	37.4	1261.1	7.7	11.9	2.6
01/86	173	4318	36.5	-254.2	31.6	257.2	4.4	8.2	46.3	1443.5	11.1	11.1	0.5
02/86	202	4850	37.5	-291.4	30.8	294.5	1.5	7.3	41.4	1742.0	11.0	9.3	1.8
03/86	236	4901	38.6	-329.3	30.3	332.4	1.7	6.7	54.7	1910.4	11.3	8.0	1.4
04/86	272	4469	43.5	-375.0	30.2	378.3	6.1	6.6	55.8	2114.4	11.3	7.7	1.3
05/86	314	4808	54.8	-439.4	30.8	443.7	10.0	7.1	65.0	2590.2	14.7	10.4	2.1
07/86	348	4916	62.4	-483.8	30.7	488.8	9.7	7.3	63.2	2441.1	9.4	11.2	0.8
08/86	383	4927	71.7	-532.7	30.3	538.5	10.8	7.7	75.0	3515.7	8.8	12.9	0.4
09/86	425	4936	83.2	-592.0	29.3	598.9	11.0	8.0	82.8	3597.1	8.7	14.7	1.1
10/86	460	4998	93.7	-644.1	28.6	652.1	11.4	8.3	76.9	4003.2	10.5	15.1	1.2
12/86	496	4953	106.3	-702.1	26.6	711.5	12.3	8.6	112.5	4362.9	14.3	17.6	1.1

$$*\Theta_i = \tan^{-1}\left(\frac{\Delta\bar{x}}{\Delta\bar{y}}\right) \qquad **\Theta_T = \tan^{-1}\left(\frac{\bar{x}}{\bar{y}}\right) \qquad +\Theta_{yx'} = \tan^{-1}\left(\frac{E_{yx'}}{E_{xx'}}\right) \qquad ++\Theta_{yz'} = \tan^{-1}\left(\frac{E_{yz'}}{E_{zz}}\right)$$

where the eigenvectors are $\begin{bmatrix} E_{xz'} & E_{xx'} & E_{xy'} \\ E_{yz'} & E_{yx'} & E_{yy'} \\ E_{zz'} & E_{zx'} & E_{zy'} \end{bmatrix}$

and the principal components are $x' = \sigma^2_{x'}$, $y' = \sigma^2_{y'}$, $z' = \sigma^2_{z'}$

[a]positive is east from magnetic north, origin is the middle injection well

[b]positive is magnetic north

[c]elevation above mean sea level

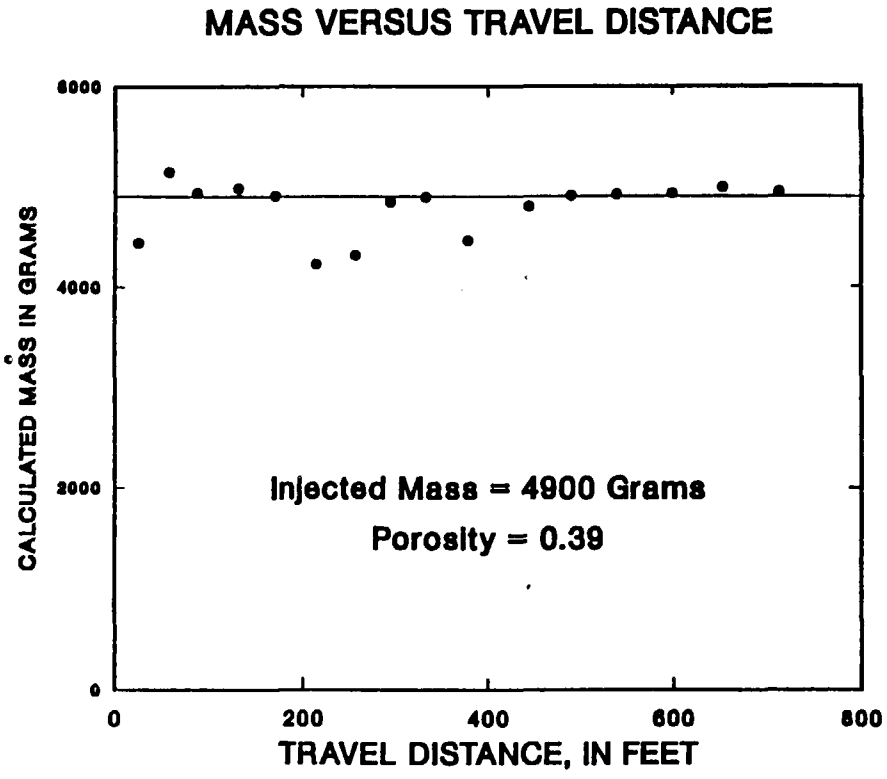

Figure 56. Calculated mass of bromide for each sampling date

The effect of errors in porosity, which was assumed to be constant in space, would be to proportionately increase or decrease all of the total mass estimates. There is supporting evidence from both the small-scale tracer tests (Section II), and published sand and gravel porosity values for the 0.39 value used in the mass calculation. Morris and Johnson (1967) show a mean value of 0.39 for medium and coarse-grained sand and the same mean value for "washed drift" (outwash) sand. Perlmutter and Lieber (1970) show a range of 0.34 to 0.41 for glacial sands on Long Island and a mean of 0.38. These data clearly indicate that the 0.39 value used in the moments calculation is reasonable for the well sorted medium and coarse-grained sand in the aquifer at the large-scale tracer test site.

The effect on mass calculations of interference corrections to the low concentration bromide values is shown in figure 57. This figure shows a comparison of two sets of mass calculations, one with bromide corrections, the other without any corrections (including any correction for background concentration). The mass values calculated using corrected bromide values do not show any trend with travel distance. This was the expected result for a nonreactive solute (it was assumed that bromide was nonreactive in the sand and gravel aquifer). The trend for the mass values calculated using uncorrected bromide values indicates an increase in total mass with travel distance. If interpreted directly this result would indicate a net production of bromide as the cloud moved through the aquifer. As this production seems unlikely, the apparent increase in mass is probably due to errors in the bromide analyses.

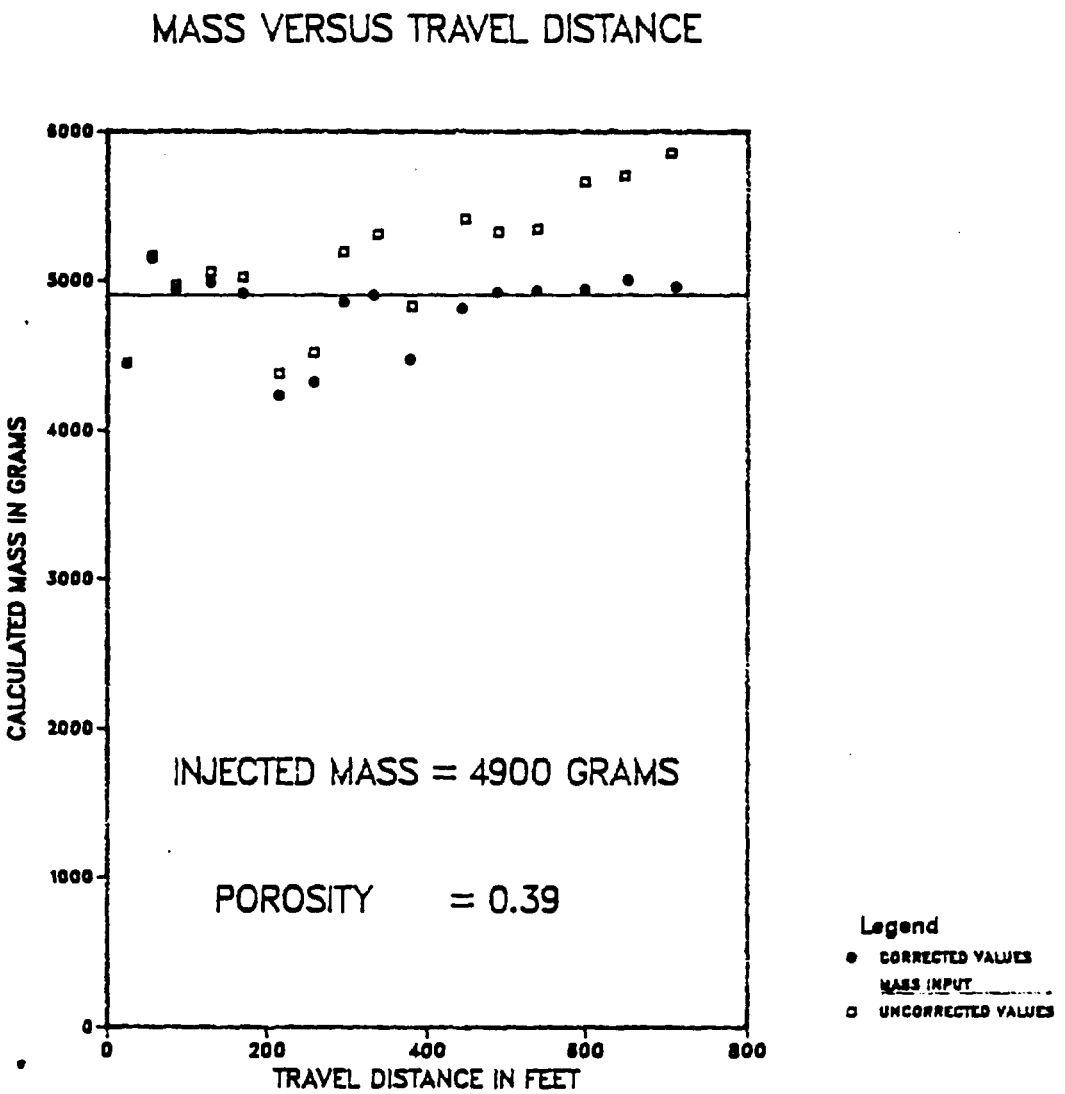

Figure 57. Calculated mass for each sampling date using corrected and uncorrected bromide data

Because the bromide cloud increases in size with travel distance, and concentrations decrease, there is a proportional increase in the total mass in the lower concentration portions of the cloud. If there is a consistent error or bias in the low-concentration analyses, then this effect should be greater in the later moment calculations. This is exactly what is observed. As indicated earlier, the effect of analysis error is to increase the apparent bromide concentration for values less than 1 mg/L. These concentration errors then cause an increased total mass. Because there is more real mass in the lower concentration parts of the bromide cloud later in the test, the result is an apparent rise in the total mass of bromide when uncorrected values are used. These observations support the need for the interference correction and validate the correction method. Although the fact that the total mass calculated using corrected values shows no trend does not uniquely confirm the correction approach, it does indicate the approach gave consistent and valid results.

The effect of sampling density on the calculated total mass is shown in table 14 and figure 58. A ratio of relative bromide cloud size to the area of each sampler can be used to illustrate the effect of sampling density. The relative bromide cloud size was calculated by multiplying the square root of the horizontal variances ($\sigma^2_{x'}$, $\sigma^2_{y'}$, table 13) together. This quantity has units of area and is a measure of the bromide cloud size or spread around the mean position. The sampling area was estimated for five zones in the sampler array in which the lateral spacing between samplers was approximately constant. The ratio of relative bromide cloud size to the area of

Table 14

Comparison of Calculated Mass to a Ratio of Bromide Cloud Standard Deviations with Average Sampling Area

		Mass	Cum. Dist.	Zone*	$\frac{\sigma'_x\sigma'_y}{\text{area}}$ *	mass <4500g
A.	JUL 85*	4442	24.4	a	1.4	*
B.	AUG 85	5146	56.0	b	2.7	
C.	SEP 85	4939	85.7	b	3.7	
D.	OCT 85	4986	126.2	b	5.1	
E.	NOV 85	4912	169.5	c	3.3	
F.	DEC 85*	4229	214.4	d	1.6	*
G.	JAN 86*	4318	257.2	d	1.9	*
H.	FEB 86	4850	294.5	d	2.0	
I.	MAR 86	4901	332.4	d	2.4	
J.	APR 86*	4469	378.3	d	2.5	*
K.	MAY 86	4808	443.7	d	3.0	
L.	JUL 86	4916	488.8	d	2.9	
M.	AUG 86	4827	538.5	d	3.8	
N.	SEP 86	4936	598.9	d	4.0	
O.	OCT 86	4998	652.1	d	4.1	
P.	DEC 86	4953	711.5	d	5.2	

average $(\sigma'_x\sigma'_y/\text{area})$ for * : 1.9; average mass = 4365g

average $(\sigma'_x\sigma'_y/\text{area})$ for others : 3.5; average mass = 4939g

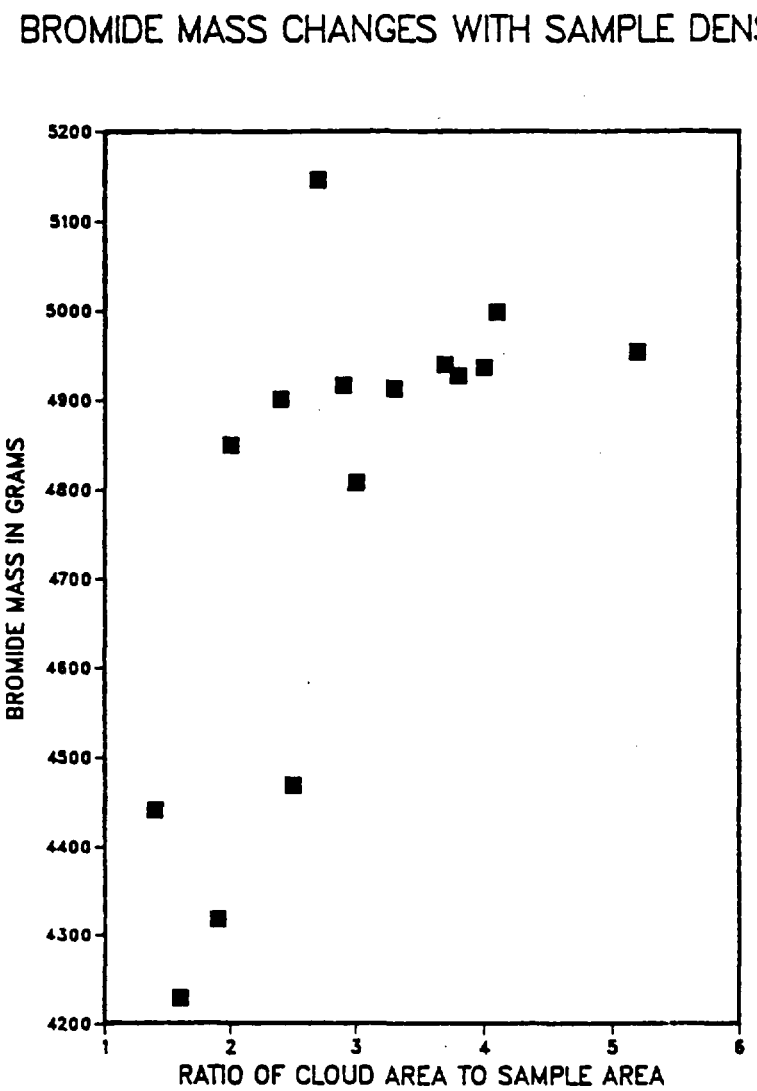

Figure 58. Bromide mass variations with respect to the ratio of cloud area to sample area

each sampler is a nondimensional measure of sampling density for each calculation of total mass. The larger this ratio is, the more likely it was to have a significant number of samplers in the bromide cloud.

There are two clusters of sampling dates shown in figure 58, a plot of mass versus the ratio of relative bromide cloud size to the area of each sampler. The cluster of four low mass values has an average ratio of 1.9, whereas the cluster of twelve mass values near the injected mass has an average ratio of 3.5. This illustrates that, on average, a closer spacing of samplers will generate a better measure of the total mass than will a larger spacing of samplers.

3. Center of Mass and Velocity

The horizontal displacement of the center of mass for bromide followed a nearly constant velocity of 1.4 ft/day (0.43 m/day). The position in space of the center of mass for each date is given in table 13 and the displacement of the cumulative travel distance with time is shown in figure 59. The movement of the horizontal location of the center of mass is shown in figure 60. The trajectory closely matches the predicted path based on the water-table configuration of August 1985. A basic finding of the tracer test has been that the average solute velocity and movement are very predictable for this sand and gravel aquifer. This result is similar to that found by LeBlanc (1984b) in which he accurately predicted the velocity and direction of the sewage plume in the same aquifer.

The strong influence of the water table on the movement of the bromide cloud is illustrated in figure 61. This figure shows the

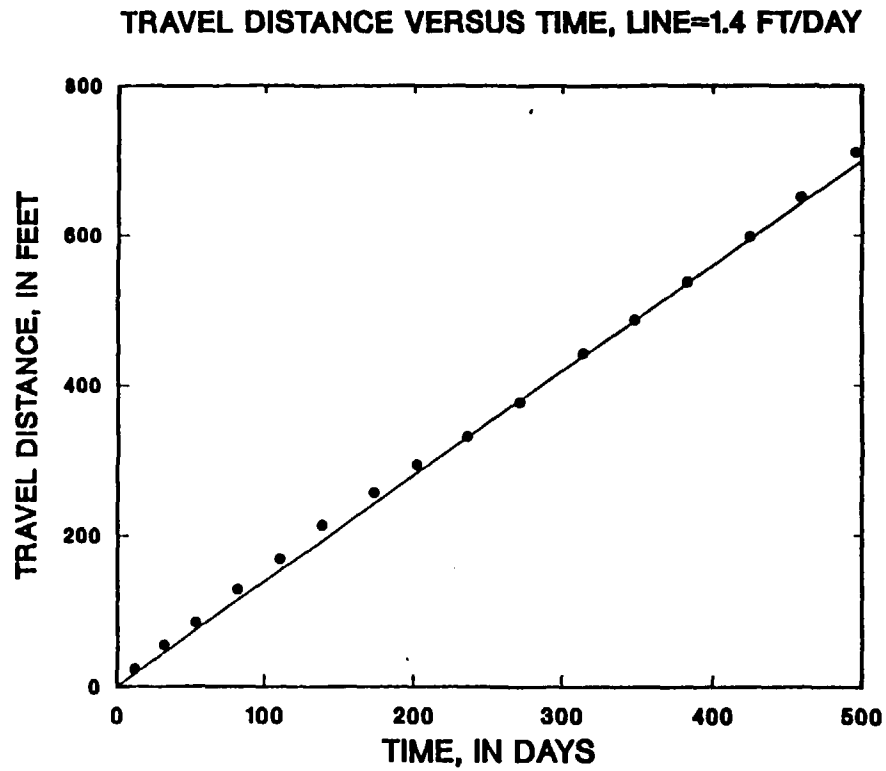

Figure 59. Distance traveled over time of the bromide center of mass

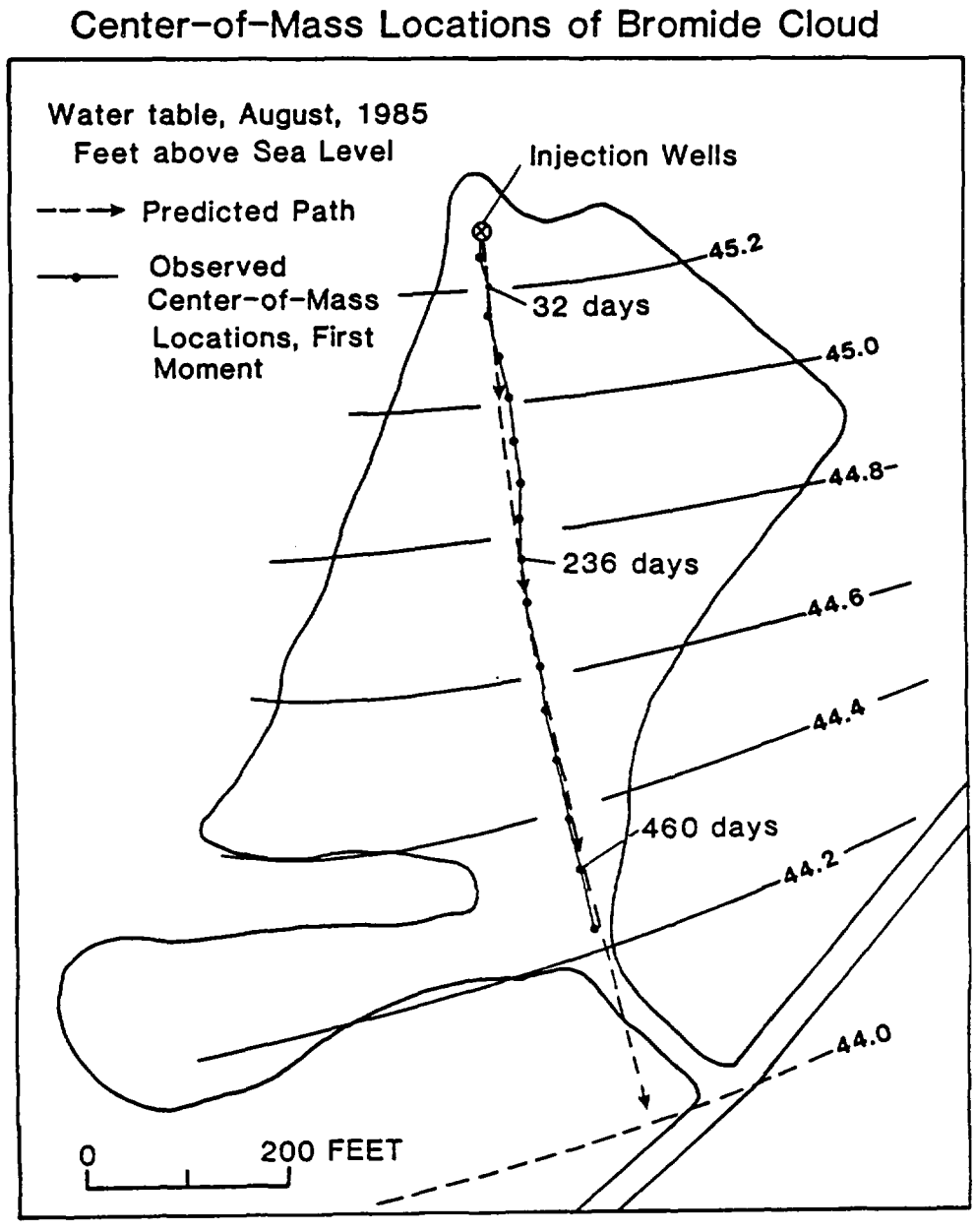

Figure 60. Trajectory of the bromide center of mass over time

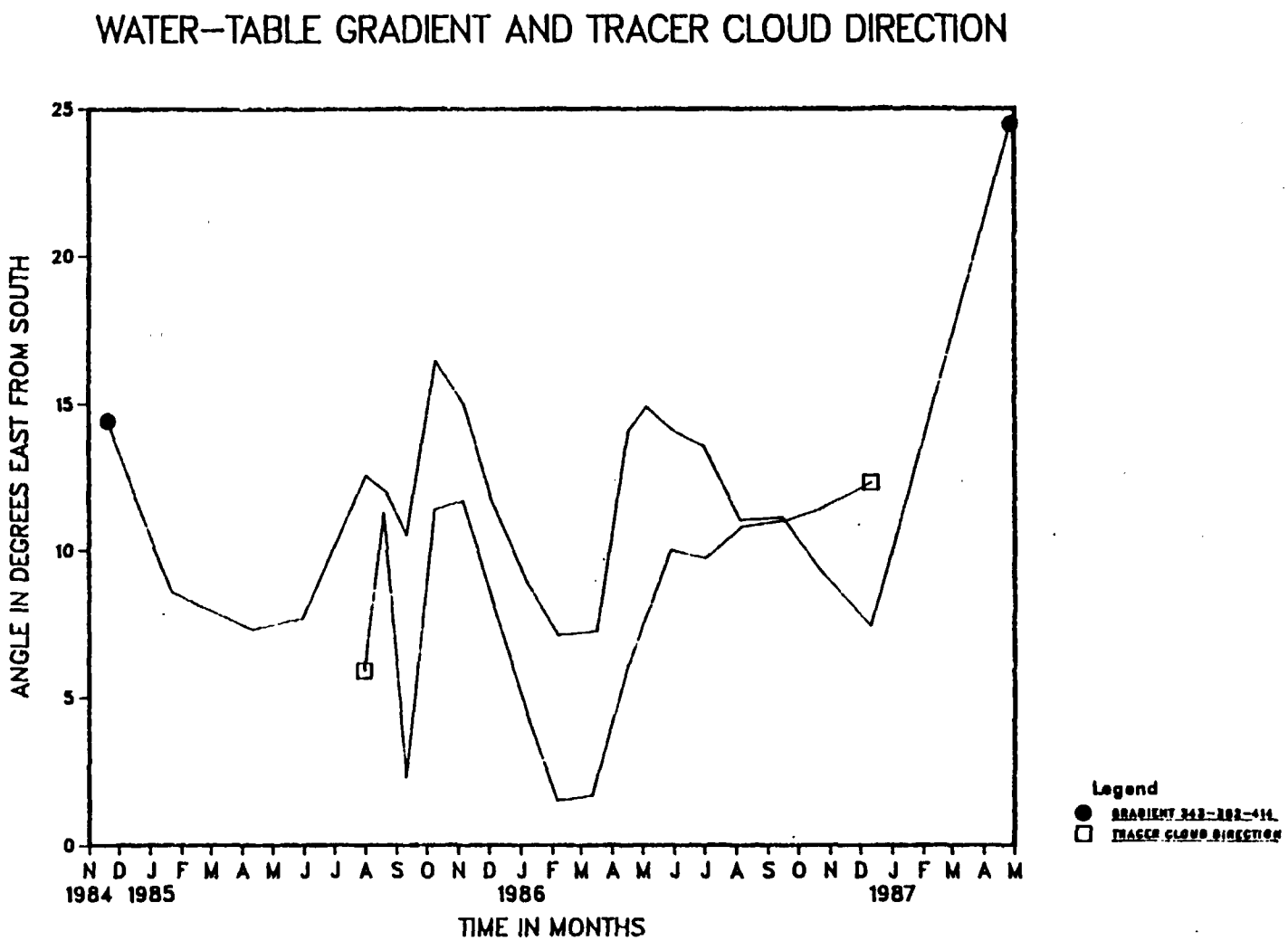

Figure 61. A comparison of the direction of the water table gradient and the direction of movement of the bromide center of mass

change over time of the direction of bromide cloud movement and the direction of the slope (gradient) of the water table. There is a close correspondence between the two directions, with the cloud shifting direction with the changes in water-table slope direction. The difference between the two directions is small, generally less than 5 degrees. This difference may be due to either the large area over which the water-table direction is calculated, or horizontal anisotropy in hydraulic conductivity.

The vertical movement of the bromide center of mass is shown in figure 62. As discussed earlier, the initial rapid downward movement of the cloud is likely due, in part, to density-driven sinking. Along with the downward movement caused by the density contrast between the tracer cloud and the ambient ground water, the accretion of recharge also caused some downward movement. Between 240 to 380 days (330 to 540 feet of travel distance) the bromide cloud showed little vertical movement, after which the cloud again began to move downward. This later movement may again be due to recharge, with the angle of vertical movement about half the angle at the beginning of the test.

4. Variance and Dispersivity

The second moments were calculated as discussed in Section III.F.3. The principal components were calculated to give variances of the bromide cloud in three directions - longitudinal, transverse horizontal, and transverse vertical. These orthogonal directions showed some variation in orientation over time (table 13), with the longitudinal direction ($\theta_{yx'}$) changing about 10 degrees over the

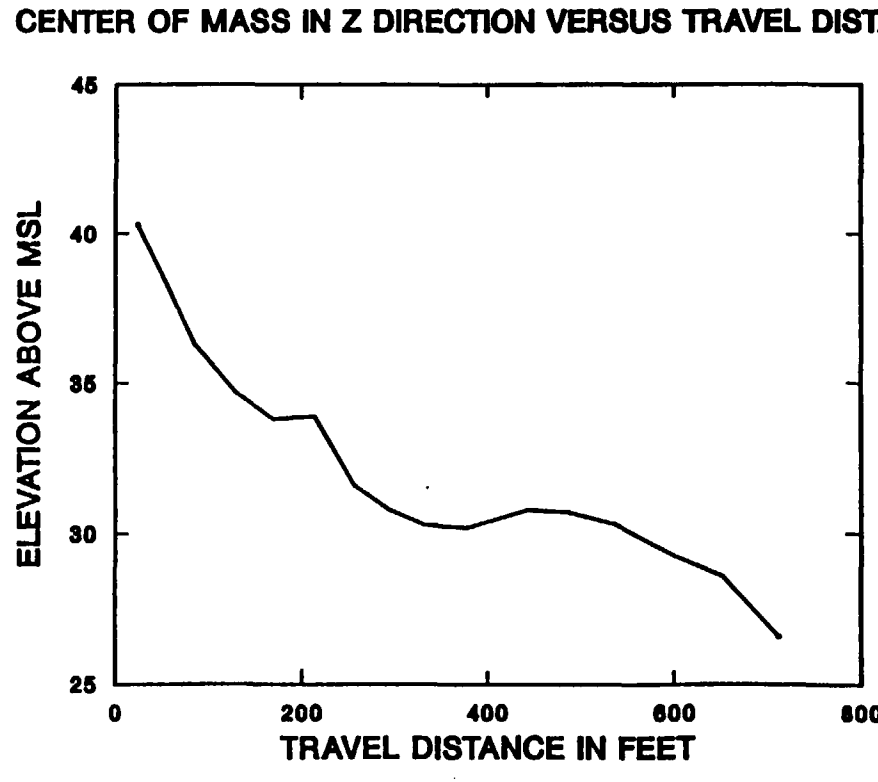

Figure 62. Elevation of the bromide center of mass with respect to the horizontal travel distance

duration of the test. The changes in longitudinal variance orientation match the changes in direction for the center of mass (fig. 63). This plot shows that as the flow direction changed the longitudinal orientation tracked these changes. Therefore, the cloud rotated toward the direction of transport as it moved through the aquifer. Figure 63 shows the cloud orientation is usually shifted a few degrees to the east relative to the direction of flow. This indicates that the cloud orientation is more directly aligned with the water-table gradient, as can be seen by comparing figure 61 to figure 63. The theoretical results reported by Gelhar and Axness (1983) indicated that the cloud orientation should be shifted toward the direction of the gradient relative to the flow direction if there was horizontal anisotropy in the hydraulic conductivity distribution (see figs. 9a and 9b of Gelhar and Axness, 1983). It is interesting to note from the Gelhar and Axness (1983) results that even a small amount of anisotropy could cause an observable difference between the flow direction and the cloud orientation.

The transverse vertical direction ($\theta_{yz'}$, table 13) initially showed about 8.0 degrees difference from the vertical. This difference decreased to about 1 degree as time progressed. The reason for these differences can be seen in the cross-sections of concentration (figs. 49-52) where it is apparent that from the beginning of the test the leading edge of the bromide cloud is higher than the trailing portion. This elevation difference shows up in the variance calculations as a rotation with a slightly positive upward tilt. As time progressed and the cloud became longer in the direction of flow, the relatively slow change in elevation difference

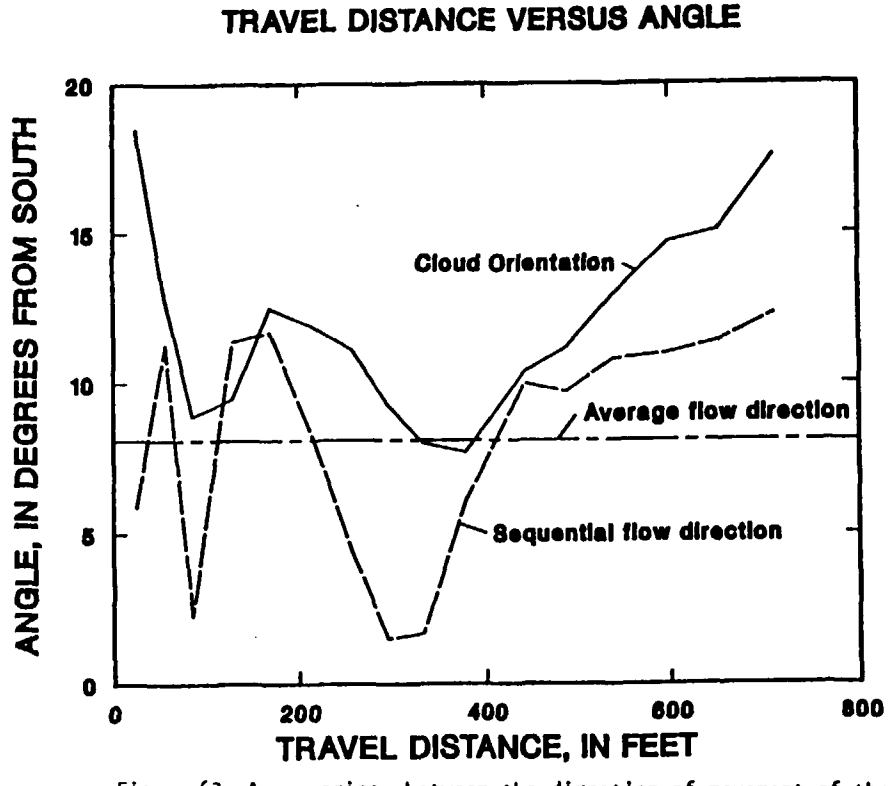

Figure 63. A comparison between the direction of movement of the bromide center of mass and the orientation of the bromide cloud

between the leading and trailing parts of the cloud resulted in a smaller angle of rotation.

The change in longitudinal variance with travel distance is shown in figure 64. There is a strong linear trend to these data, and as the velocity is nearly constant, the longitudinal dispersivity can be calculated as one half the slope of the change in variance with travel distance. The resultant dispersivity is 3.14 feet (0.96m). The strong correlation (0.994) between the longitudinal variance and travel distance indicates this trend is linear in later time and that the longitudinal dispersion process is Fickian at the scale of this test. This is an important result of this test, particularly as there have been questions raised as to whether the dispersion process in aquifers would ever be Fickian.

A nonlinear trend in the longitudinal variance was observed during the first 130 feet (40m) of distance traveled (figs. 65 and 66). Figure 65 shows the sequential change in longitudinal dispersivity from the beginning of the test. The change between July and August 1986 was omitted because these moments show first a decrease in variance and then a compensating large increase (fig. 64). Large changes in dispersivity from date to date are still apparent after omitting the July and August 1986 data. This scatter is likely due to the limitations of sampling at fixed locations. For example, if the cloud was close to but had not reached a sampler, then a zero concentration would be sampled, resulting in a smaller variance than had the cloud just reached the sampler.

When the averaging interval for the dispersivity calculations is extended by using every other date after September 1985 (again

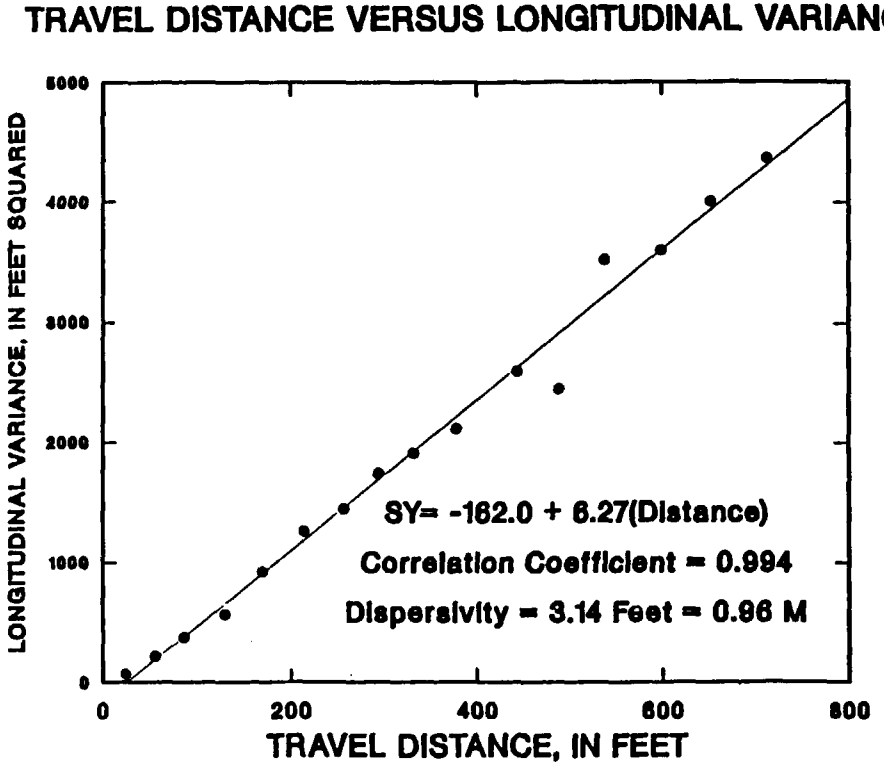

Figure 64. Change in bromide longitudinal variance with respect to travel distance

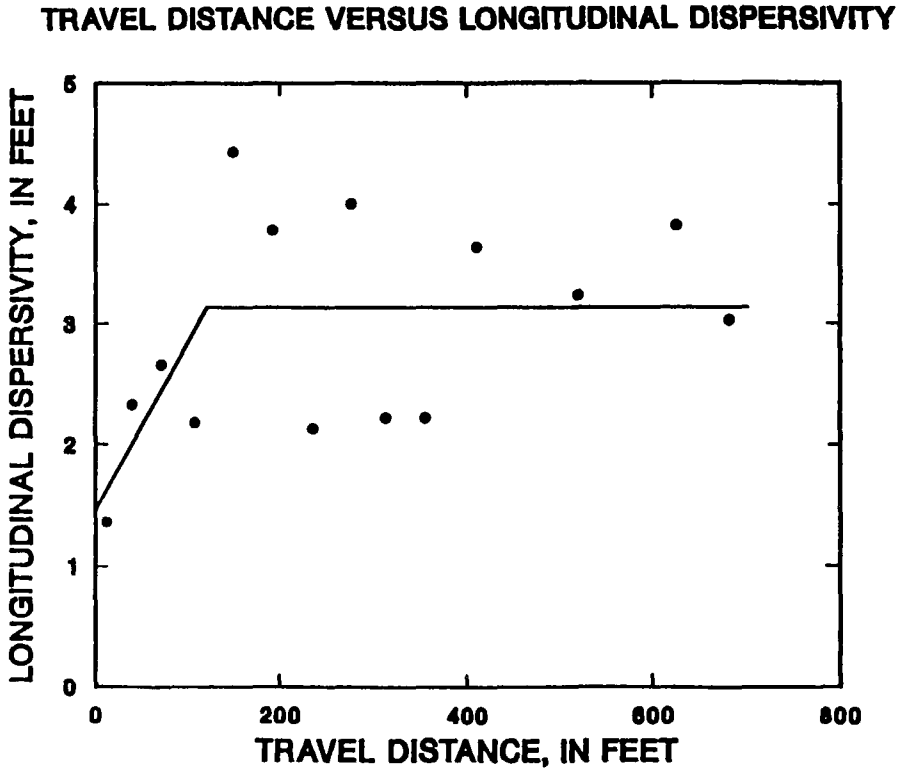

Figure 65. Sequential change in longitudinal dispersivity with travel distance

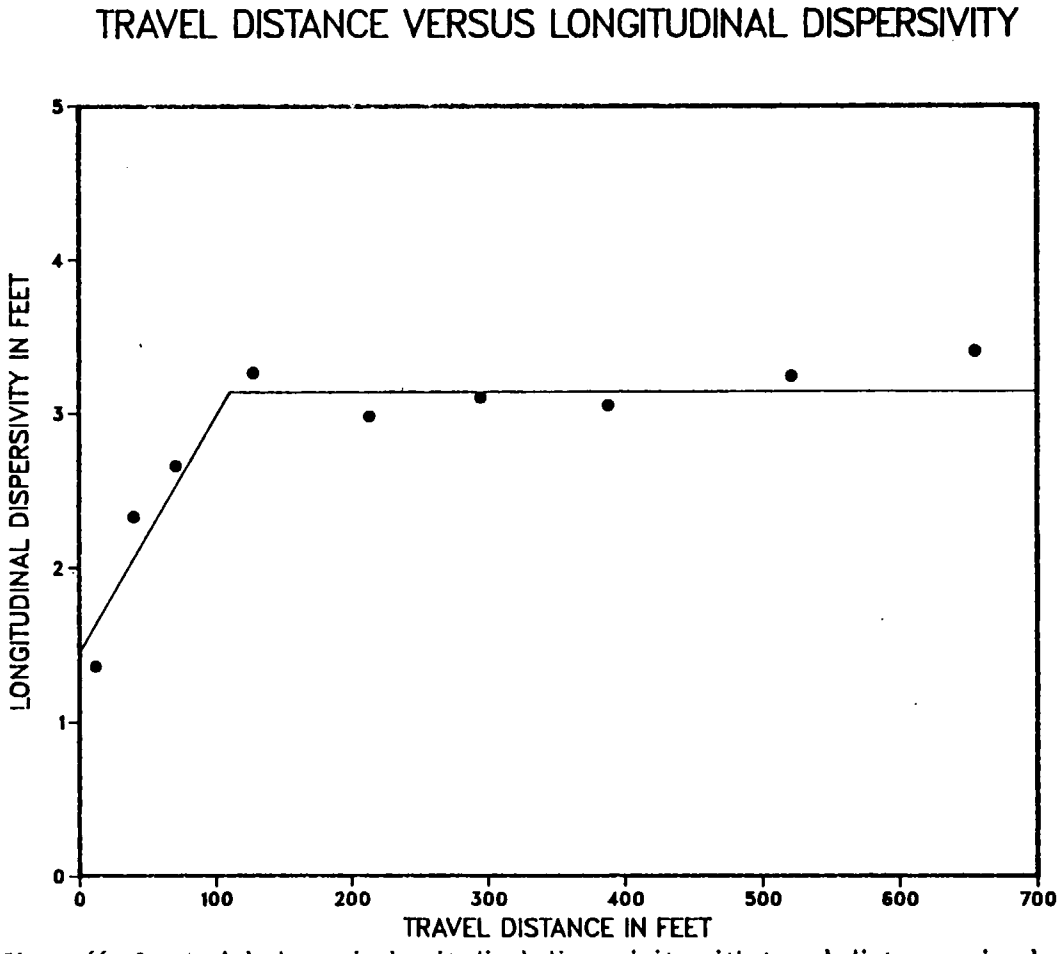

Figure 66. Sequential change in longitudinal dispersivity with travel distance using longer periods

skipping July and August 1986), the result (fig. 66) is a much smoother representation of the change in dispersivity with travel distance. Figure 66 shows a rapid rise in dispersivity with travel distance and then a leveling off of the dispersivity value. This result agrees with the theoretical results of Gelhar et al. (1979) and Dagan (1982, 1984) who show an early time in which the dispersion process is non-Fickian and the dispersivity increases with time (or travel distance). The distance at which the asymptotic value of dispersivity was reached also agrees with the theoretical results of Gelhar et al. (1979) as this occurs after about 140 feet of travel distance. This value is between the length of 10 to 100 longitudinal dispersivities (31 to 310 feet) predicted by Gelhar et al. (1979).

The effect of errors in bromide analyses on the calculated dispersivities is illustrated in figure 67, a plot of two sets of longitudinal variances against travel distance. One set of longitudinal variances was calculated using the corrected values of bromide; the other used uncorrected values. It is readily apparent that there are increasing differences between the two sets of variances, with the variances based on the uncorrected values showing a larger slope and a larger apparent dispersivity. As indicated for the mass calculations, the increasing differences between the two sets of variances are due to the larger concentration values in the low concentration range for the uncorrected bromide analyses. These larger values become increasingly more influential on the total mass and variance calculations as the cloud becomes larger, and more dilute, and more mass is shifted into the lower concentration ranges. Therefore it

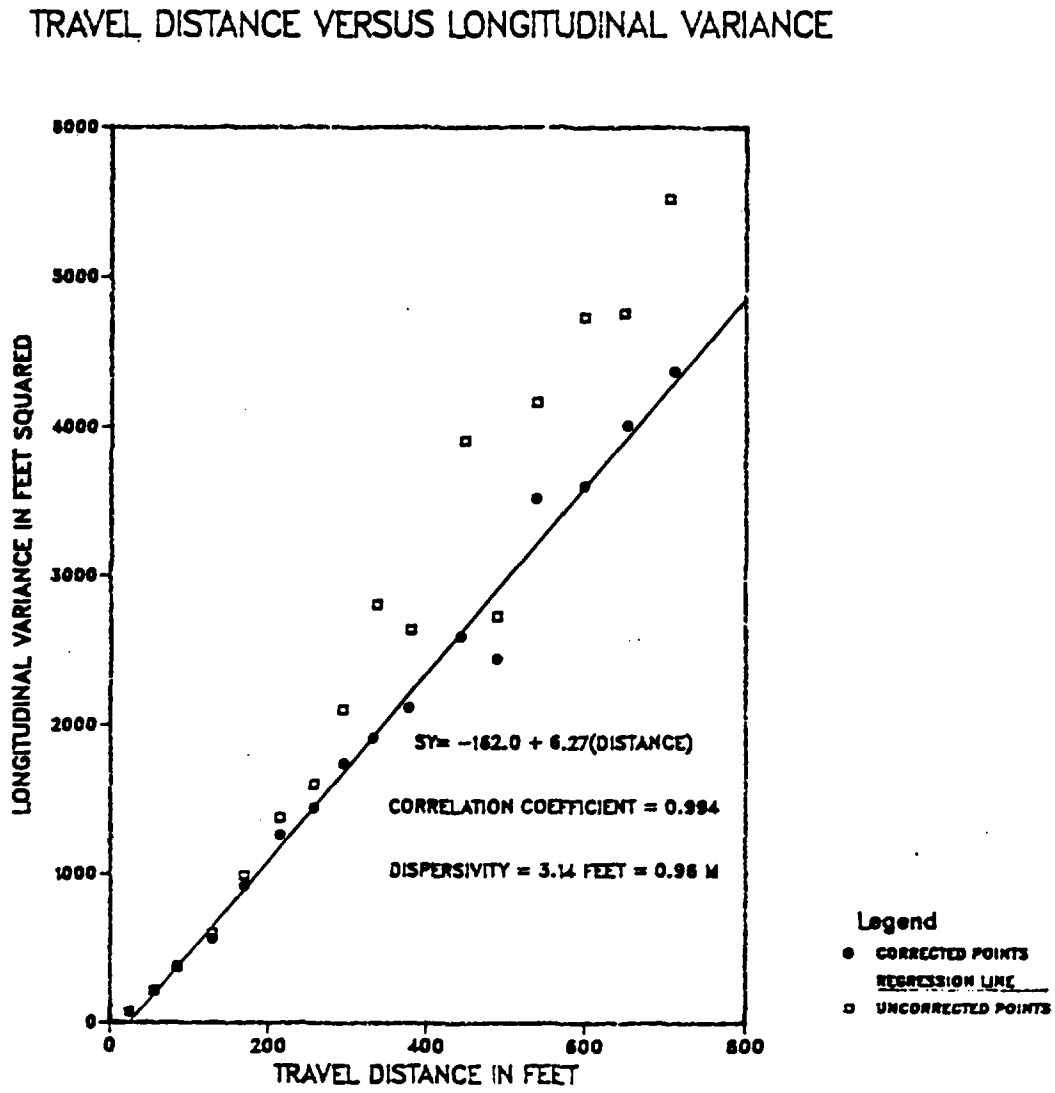

Figure 67. A comparison of the change in longitudinal variance with travel travel distance for corrected and uncorrected bromide values

was important to correct the bromide values to obtain a reasonably accurate value of dispersivity for this test. It should be noted that the errors in bromide analysis had a minimal effect on the first moments, the center of mass locations. This occurs because there are compensating errors at both the leading and trailing edge which cancel each other out. The result is very little difference in the center of mass position for corrected or uncorrected bromide concentrations.

The change in transverse horizontal variance with respect to travel distance is shown in figure 68. As with the longitudinal variance, the transverse horizontal variance shows a clearly linear trend with travel distance (correlation coefficient is 0.975). The transverse horizontal dispersivity can be calculated as one half the slope of the change in variance with travel distance, which gives 0.06 feet (1.8 cm). This value is much smaller than the longitudinal variance, with about a 50 to 1 ratio between the two. There is more scatter about this linear trend than with the longitudinal case, which can be qualitatively explained by ratios of cloud size to sampler spacing. In the later part of the test the longitudinal spacing of the samplers was about 15 feet and the lateral spacing was about 9 feet. If we take the ratio of the square root of variance to the sampler spacing, a measure of cloud size to sampler density is established. Using the October 1986 data, the longitudinal ratio is:

$$\sqrt{4003.2}/15 = 4.2,$$

and the transverse horizontal ratio is:

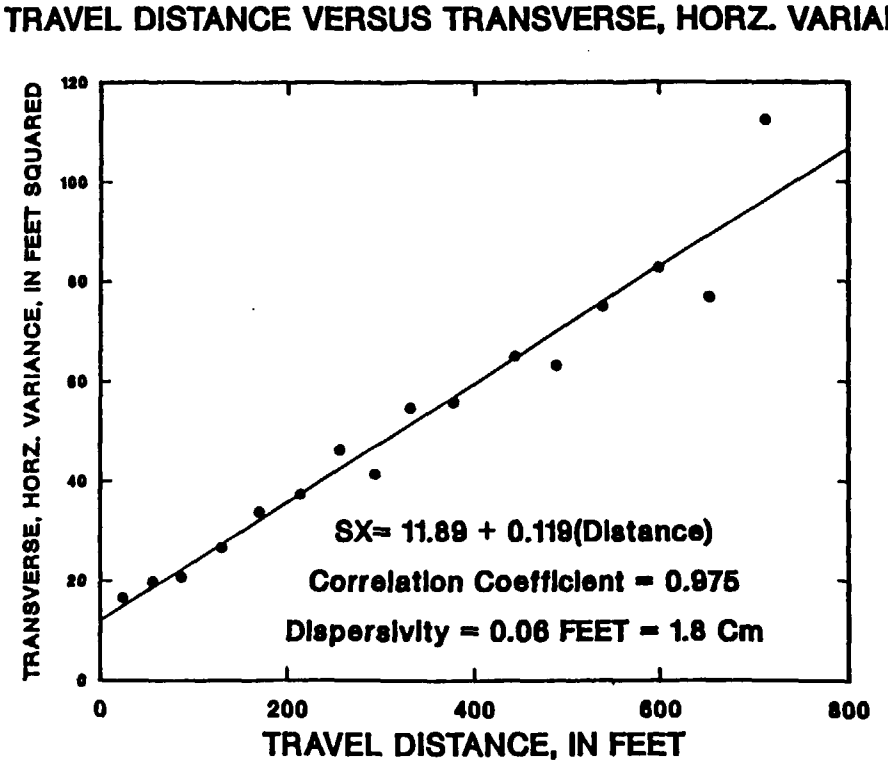

Figure 68. Change in bromide transverse horizontal variance with travel travel distance

$\sqrt{76.9}/9 = 0.97$.

It is readily apparent from these ratios that there was less resolution of the lateral extent of the cloud than along the direction of flow. Therefore it would be reasonable to expect more variation in the second moment values with a larger relative spacing between samplers in the transverse horizontal direction.

The change in transverse vertical variance with respect to travel distance is shown in figure 69. Although a linear regression line was fitted to these data, it is not clear that the variances follow a linear trend. If a dispersivity is calculated from these data, the result is 0.005 feet (0.15 cm). This value is very small in comparison with the longitudinal dispersivity, about a 640 to 1 ratio. It can be seen from the data that the slope of the initial rise in vertical variance was larger than the overall trend, giving over double the overall dispersivity (≈ 0.4 cm). This more rapid increase in variance was likely due to the sinking of the cloud in the early part of the test, causing increased vertical "smearing" of the cloud and a resultant increased spreading of the bromide cloud. After about 200 days the vertical movement of the cloud was likely dominated by the ambient flow field, and reacting to downward movement during recharge events.

5. Comparison with Borden Test

A comparison of results from the Borden site (Freyberg, 1986; Mackay and others, 1986) to the Cape Cod test is shown in table 15. There are obvious differences in the average hydraulic conductivity

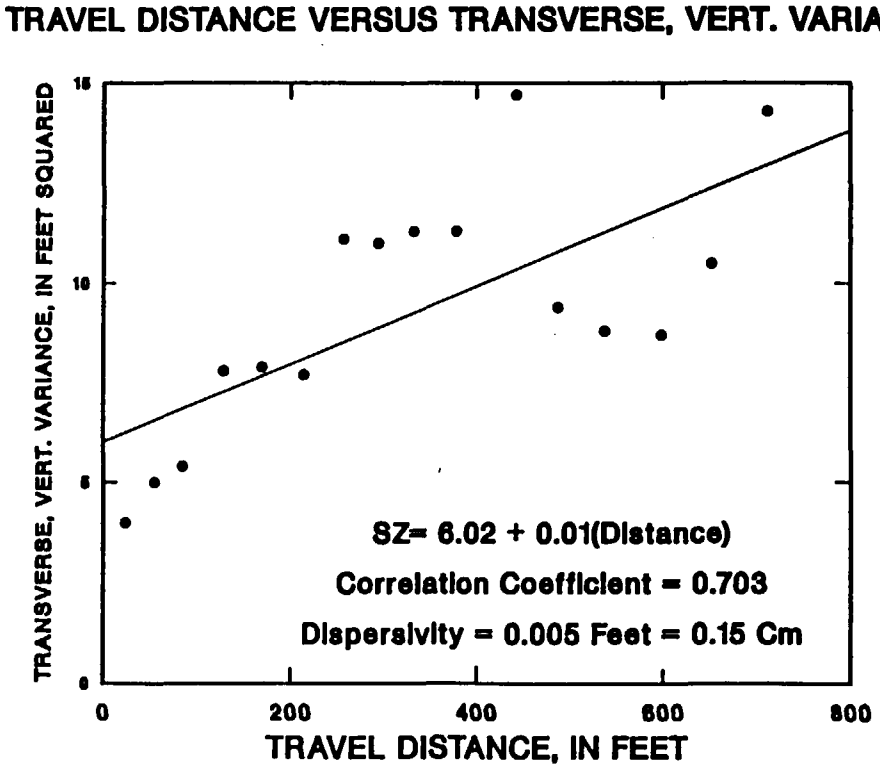

Figure 69. Change in bromide transverse vertical variance with travel distance

Table 15

Comparison of Results
from the Borden Site Tracer Test and the
Cape Cod Tracer Test

	Cape Cod	Borden
K	120 m/day	6.2 m/day
Horizontal Velocity	0.42 m/day	0.091 m/day
α_L	0.96 m	0.43 m
α_T	0.018 m	0.04 m

and velocity at the two sites, with the Cape Cod values much larger, and yet the dispersivities are very similar. The major difference in dispersivities between the two tests is the much larger ratio between the longitudinal to transverse horizontal dispersivities for the Cape Cod test (50 to 1) versus the Borden test (11 to 1). Results of both tests show that nonreactive solute concentrations are highly variable in space and difficult to predict on a small scale, but that average characteristics (i.e. moments) can be expected to change in a predictable manner.

6. Summary and Discussion

Major findings from a moments analysis of the bromide distribution are: 1) longitudinal mixing was the dominant dispersion process with dispersivity reaching a limiting value of 0.96 m after 40 m of travel distance, 2) transverse horizontal and vertical dispersivities were relatively small (1.8 cm and 0.15 cm, respectively), and 3) the horizontal displacement of the bromide cloud was accurately predicted using estimates of hydraulic conductivity, porosity, and measured hydraulic gradient.

The results from the bromide moments analysis generally are in agreement with the theoretical stochastic results of Gelhar and Axness (1983) and Dagan (1982). Careful measurements of the bromide movement and spreading show that there is an enhanced dispersion of solutes in aquifers relative to the values measured in laboratory column experiments. The order of magnitude of the longitudinal dispersivity is in good agreement with estimates presented by Gelhar and Axness (1983, table 3, item I). As predicted

by Gelhar et al. (1979) there was an early period of Non-Fickian transport, during which calculated dispersivity values increased. After traveling a distance of about 43 meters (about 45 dispersivity lengths) the longitudinal dispersivity reached an asymptotic limit, about 1 meter. The length of the early Non-Fickian period agrees with the estimate by Gelhar et al. (1979) of 10 to 100 dispersivity lengths.

The magnitude of the transverse horizontal dispersivity observed during the tracer test is about two orders of magnitude greater than that predicted by Gelhar and Axness (1983, table 3, item I). The constant value of the transverse horizontal dispersivity doesn't agree with the results presented by Dagan (1984) in which the transverse horizontal dispersivity decreases to zero at large time. This disagreement with the theoretical results indicates that there may be another mechanism, not included in the above theoretical results, which increases and maintains the transverse horizontal dispersivity value.

The observed orientation of the cloud was generally closer to the direction of the water-table gradient than the direction of flow as shown by the mean movement of the cloud. These small differences may be indicative of possibly some horizontal anisotropy in the sand and gravel aquifer. As indicated above, nearly all of the major features of the bromide cloud shape and movement conformed to that predicted by the stochastic analysis of macrodispersion.

H. Lithium Moments

1. Mass in Solution

Moments were calculated for 17 lithium distributions, one more (May 1987) than for bromide. Lithium values were directly used in the moments analysis program without any background concentration correction because the background concentration was below the analytical detection limit. The same moments calculation procedure was used for the lithium concentrations (lithium in solution) as for bromide. By assuming a form of the adsorption isotherm it was also possible to calculate moments for the adsorbed lithium. The results of the moment calculations for the lithium in solution at each sampling date are given in table 16, and the numbers of analyses and triangles used in the calculations are in table 17.

The change in mass (zeroth moment) with time is shown in figure 70. This figure shows a decline in the mass in solution over time which was rapid in early time and then became slower as the test progressed. Five views of the lithium distribution (7/85, 11/85, 1/86, 7/86, 9/86),were not included in this trend because these sampling rounds were incomplete, giving only a partial picture of the lithium distribution.

The regular decline in the mass of lithium in solution indicates that lithium ion was not involved in an instantaneous linear adsorption reaction. If the lithium ion had been involved in this type of reaction there should have been a constant mass in solution, with the mass in solution less than the injection mass. The nonlinear isotherm for lithium adsorption, discussed in Section II.D.4 (fig. 46),

Table 16

Moments for Lithium Distributions

Date	Time Days	Mass (g)	$\bar{x}$	$\bar{y}$	$\bar{z}$	Travel Dist.	σ'^2_x	σ'^2_y	σ'^2_z
JUL 87*	12	366	1.9	- 19.5	40.2	19.5	17.4	43.5	4.71
AUG 85	32	415	6.7	- 43.7	39.2	44.2	17.6	117.4	5.25
SEP 85	54	343	7.7	- 64.7	37.7	65.2	17.2	222.3	4.95
OCT 85	82	248	13.5	- 91.5	37.0	92.5	17.8	412.2	4.72
NOV 85*	110	158	21.6	-136.3	36.6	138.0	19.8	239.2	3.28
DEC 85	138	186	22.9	-147.5	36.3	149.2	19.5	1057	5.17
JAN 86*	173	108	26.0	-172.3	36.1	174.2	17.6	1790	5.31
FEB 86	202	144	26.4	-183.7	35.3	185.6	48.0	1843	6.50
MAR 86	236	121	26.1	-196.0	34.7	197.8	40.7	2272	6.98
APR 86	272	89	25.4	-195.9	34.7	297.6	29.0	2934	7.46
MAY 86	314	65	27.8	-205.7	34.8	207.6	29.7	5318	7.18
JUL 86*	348	60	31.2	-226.4	34.5	228.5	26.7	3711	7.14
AUG 86	383	67	28.7	-205.7	34.7	207.7	28.0	4544	7.18
SEP 86*	425	26	37.7	-281.3	33.6	283.8	28.8	2149	4.00
OCT 86	460	56	30.2	-223.2	34.3	225.2	32.1	5652	7.46
DEC 86	496	61	30.4	-234.9	33.9	235.9	32.0	5482	7.84
MAY 87	643	37	36.3	-163.5	33.4	266.0	23.7	8452	7.34

*Incomplete sampling, only a partial distribution was analyzed.

Table 17

Numbers of Data used in Lithium Moment Analysis

Date	# Analysis	# Triangles
JUL 85	596	65
AUG 85	1818	204
SEP 85	1800	210
OCT 85	2379	279
NOV 85	1129	132
DEC 85	1524	176
JAN 86	1278	132
FEB 86	1863	208
MAR 86	1711	187
APR 86	1711	187
MAY 86	1772	197
JUL 86	1291	132
AUG 86	1885	203
SEP 86	994	98
OCT 86	2029	222
DEC 86	2244	231
MAY 87	2289	241

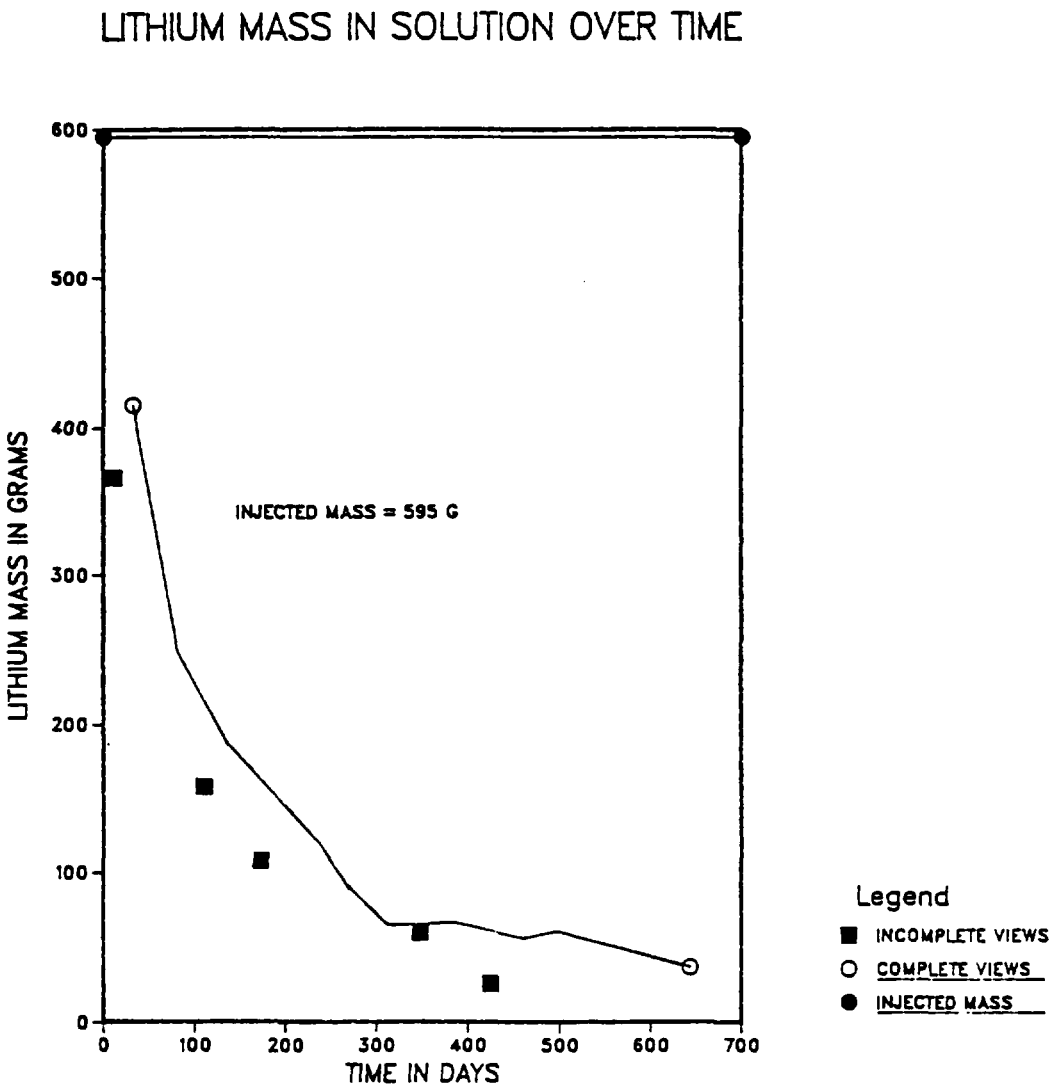

Figure 70. Lithium mass in solution over the period of the tracer test

also indicates that the lithium ion was not following a linear isotherm at concentrations greater than a few tenths of a milligram per liter (mg/L).

The total mass of lithium was calculated for each lithium distribution by assuming a form of the nonlinear isotherm. This isotherm was then used to calculate the concentration of lithium on the solid surface and subsequently the mass on the solid. The total mass of lithium is shown in figure 71 for two nonlinear isotherms. The first, $s = 0.452C^{0.316}$, is the one-day isotherm measured in the laboratory; the second, $s = 0.178C^{0.5584}$, is a fitted isotherm. The coefficients in the second isotherm were adjusted until a rough match to the injected mass was reached for those distributions which were complete. Figure 71 shows that the one-day laboratory isotherm consistently underestimates the total mass and the mass declines over time. The total mass calculated from the fitted isotherm shows a nearly constant value over time, but shows a significantly greater adsorption than the laboratory measured isotherms over the full range of lithium concentrations (fig. 72).

There is some indication that after 300 days the mass in solution is relatively constant (fig. 70). From 314 to 496 days the mass in solution varied between 65 to 61 grams (table 16), averaging about 62 grams. However, between 496 to 643 days the mass in solution dropped from 61 to 37 grams. This decrease in mass after having remained constant for 182 days may in part be due to a dilution of a significant portion of the lithium mass to below the detection limit of the analysis method. Although the last view (May 1987) indicated a decrease in the mass in solution, the change

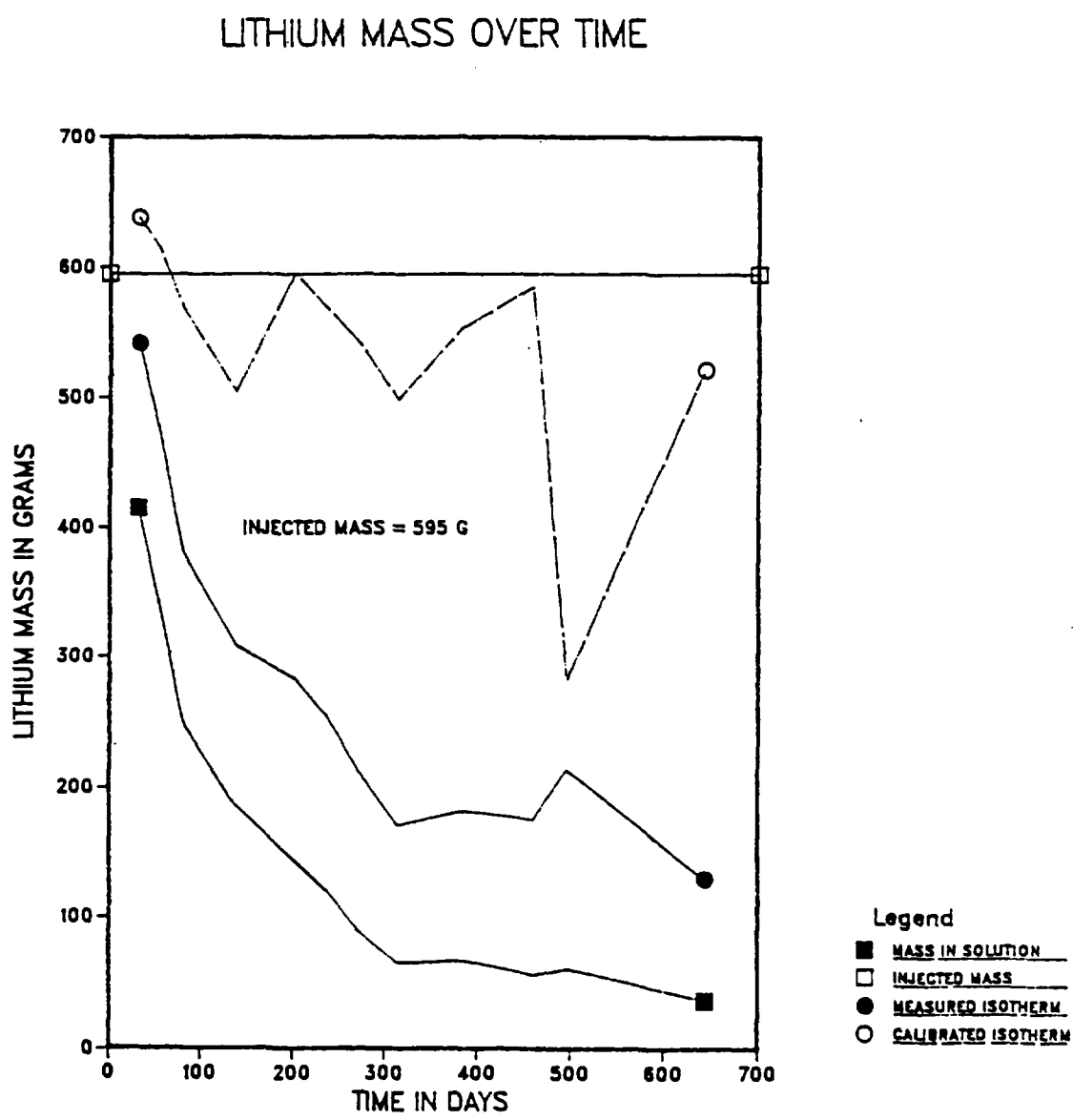

Figure 71. Lithium mass in solution compared with estimated total mass using both the measured isotherm and a calibrated isotherm

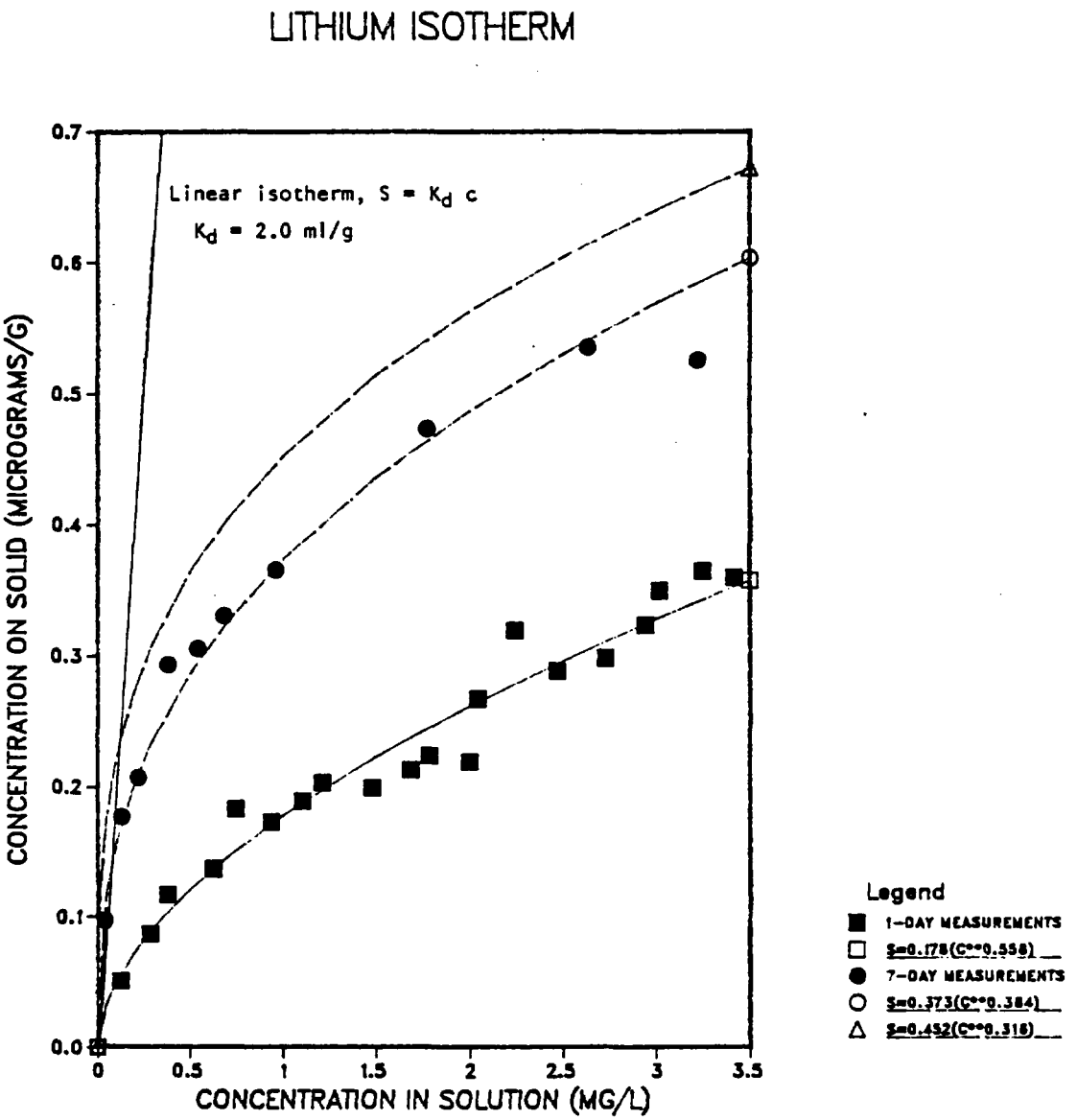

Figure 72. A comparison of three adsorption isotherms for lithium on to Cape Cod sediment, (written communication, Warren Wood, 1987)

in mass is slow. This slow change in mass may indicate that the lithium adsorption reaction is approaching a linear or quasi-linear part of the effective isotherm. There is also some indication of linear adsorption later in the test from the first moment data.

2. Center of Mass and Solute Velocity

The movement of the center of mass of the lithium in solution is shown in plan view in figure 73. The direction of the lithium movement is nearly identical to the bromide movement, indicating that the mean direction of movement of the lithium cloud also follows the direction of the water-table gradient in the test area. The lithium cloud consistently lags behind the bromide cloud.

The vertical movement of the lithium cloud is illustrated in figure 74. The center of mass for lithium also shows sinking but not as much as the bromide cloud. The rate of sinking for lithium is rapid during the first 200 days, as it is for bromide; but because the lithium cloud does not move as fast as the bromide and lags behind the more dense bromide cloud, the lithium cloud does not sink as much during the early part of the test. It is interesting to note that the vertical movement of the lithium cloud mimics the vertical movement of the bromide cloud, with about a four foot separation distance between the centers of mass between 200 to 400 days. After 400 days both clouds begin to sink again, with the separation distance increasing to seven feet. Therefore the vertical movement of the lithium cloud also lags behind the vertical movement of the bromide cloud.

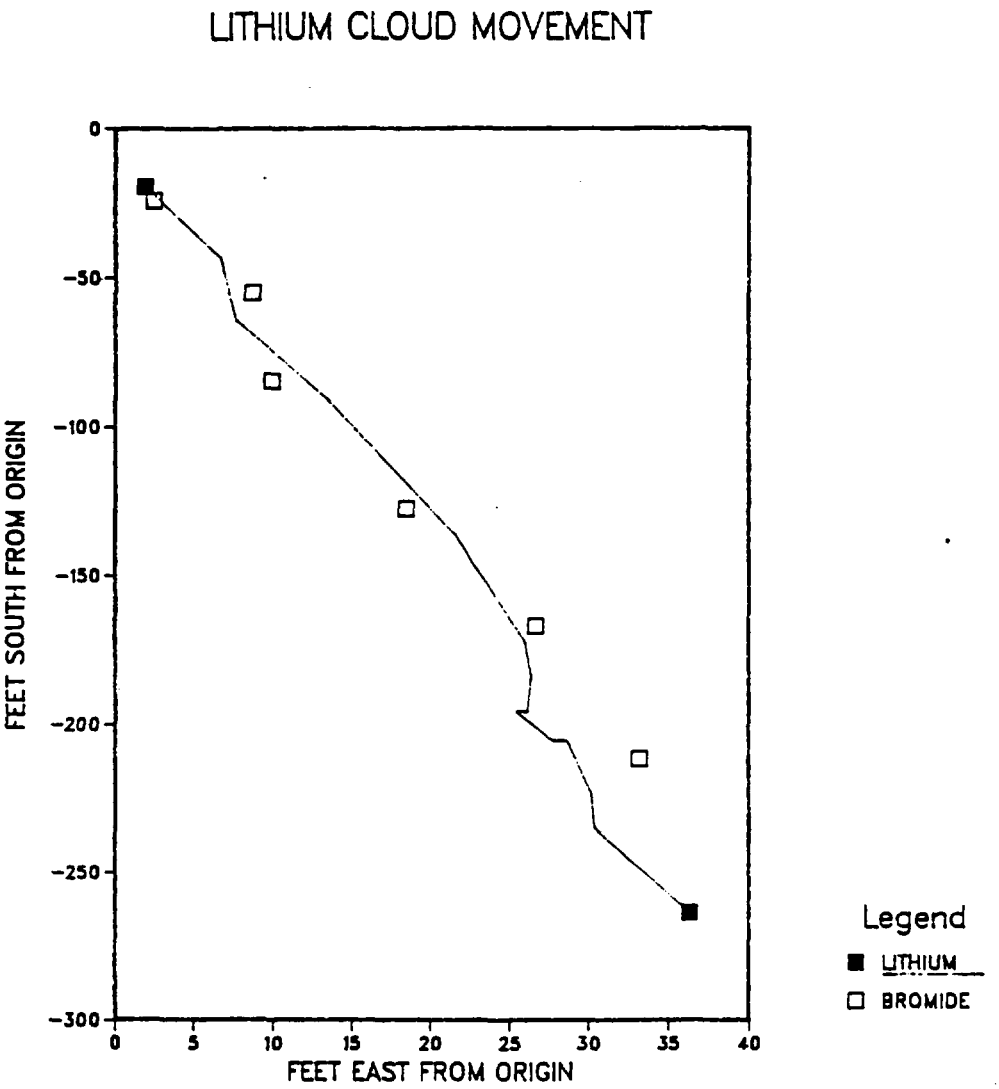

Figure 73. Trajectory of the lithium in solution in the horizontal plane.

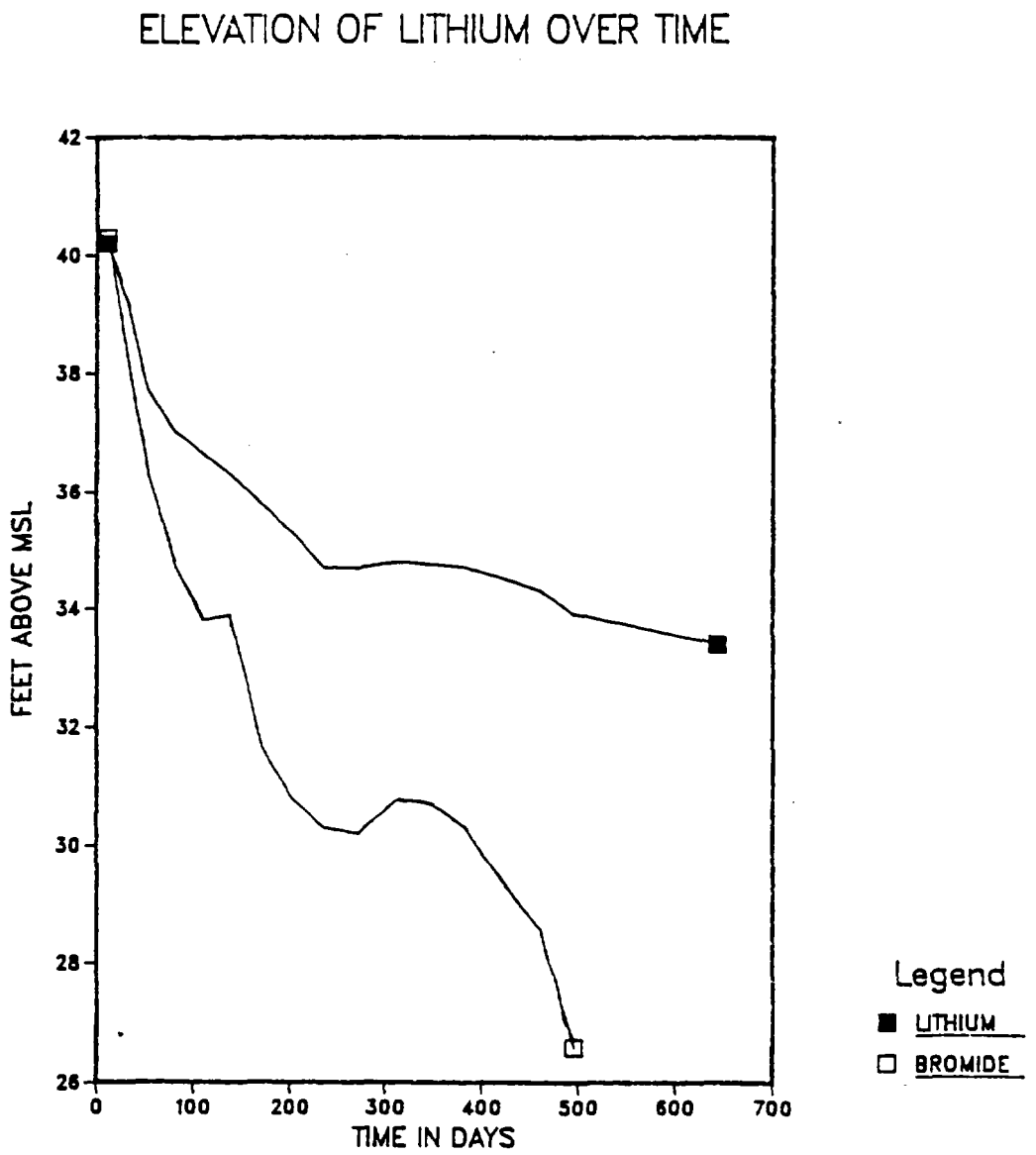

Figure 74. A comparison of the elevations of centers of mass for lithium and bromide

The horizontal displacement of the lithium cloud over time is shown in figure 75. It is evident from comparison with the constant bromide velocity (1.4 ft/day) that the velocity of the lithium cloud decreased over time. During the first 32 days of the test the lithium velocity was nearly the same as for bromide. Between 32 to 236 days the lithium velocity steadily decreased. From 236 to 383 days the lithium velocity was very slow, averaging about 0.067 ft/day. From 383 to 643 days the lithium velocity was about 0.22 ft/day. The variation in lithium velocity after 236 days may in part be due to the lateral spacing between samplers. Because the average distance between samplers at the 200 ft. travel distance was 15 feet, it would take 67 to 224 days to cover the distance between samplers with a velocity varying between 0.067 to 0.22 ft/day. Therefore the lithium distributions would tend to show intermittent jumps and discontinuities in mean displacement that are due to the lateral and transverse spacing between sampling points. It is also apparent from the travel distance of incomplete views that the mean position can be significantly influenced by the completeness of the sampling.

The nearly linear trend in the mean displacement in the later part of the test (after 236 days) is another indication of a nearly constant mass in solution. The relationship between the mass in solution and the velocity is clearly stated in equation 29, where the mean displacement is dependent on the ratio of mass in solution to total mass. Therefore if the mean displacement is steady, and the fluid velocity is steady, then the ratio of mass in solution to total mass can be assumed to be constant. If the mass in solution is

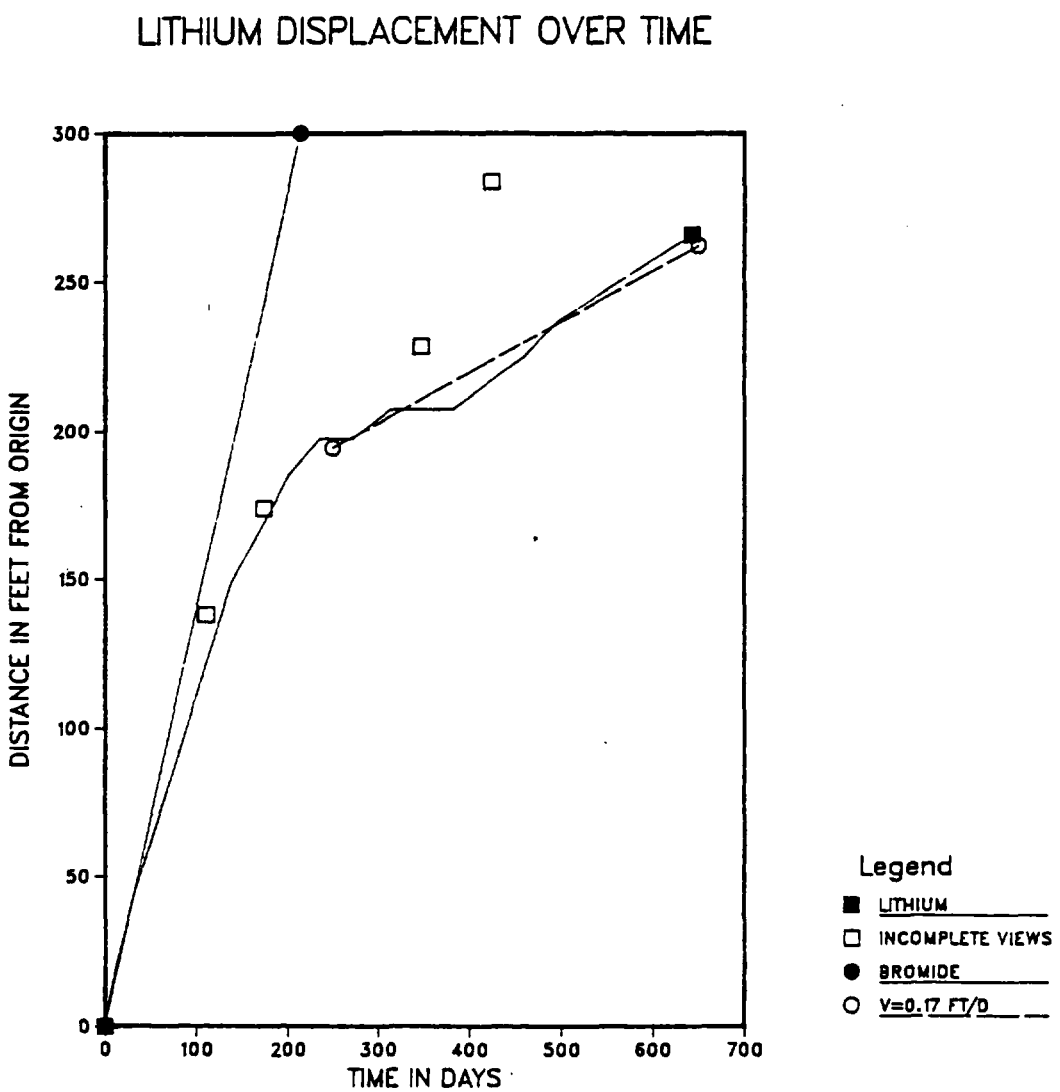

Figure 75. Displacement of the center of mass of lithium over time

constant, or nearly so, then it is likely that the adsorption reaction is approaching a linear or quasi-linear part of the isotherm.

From the ratio of total mass to the mass in solution, a retardation coefficient can be calculated for lithium during the later part of the test:

$$\text{retardation coefficient} = \frac{M_T}{M_c} = \frac{595g}{62g} = 9.6.$$

The retardation coefficient can be used to calculate the expected retarded velocity of lithium:

$$\text{retarded velocity} = \frac{M_c}{M_T} v = \frac{1.4 \text{ ft/day}}{9.6} = 0.15 \text{ ft/day}.$$

This retarded velocity is very close to the average (0.17 ft/day) for the period 236 to 643 days after injection. The above retardation coefficient would give a Kd value of about 2.0 mL/g (with n=0.39 and ρ = 1.7 g/cm^2), a value which would indicate a very steep linear adsorption isotherm (see fig. 72). It is interesting however that both the mass and first moment calculations indicate this high degree of adsorption.

3. Variance and Dispersivity

The rate of change in longitudinal variance for the lithium distributions, shown in figure 76, steadily increased over time until 272 days after injection. From 272 to 643 days the longitudinal variance showed large variations in value in a general upward trend.

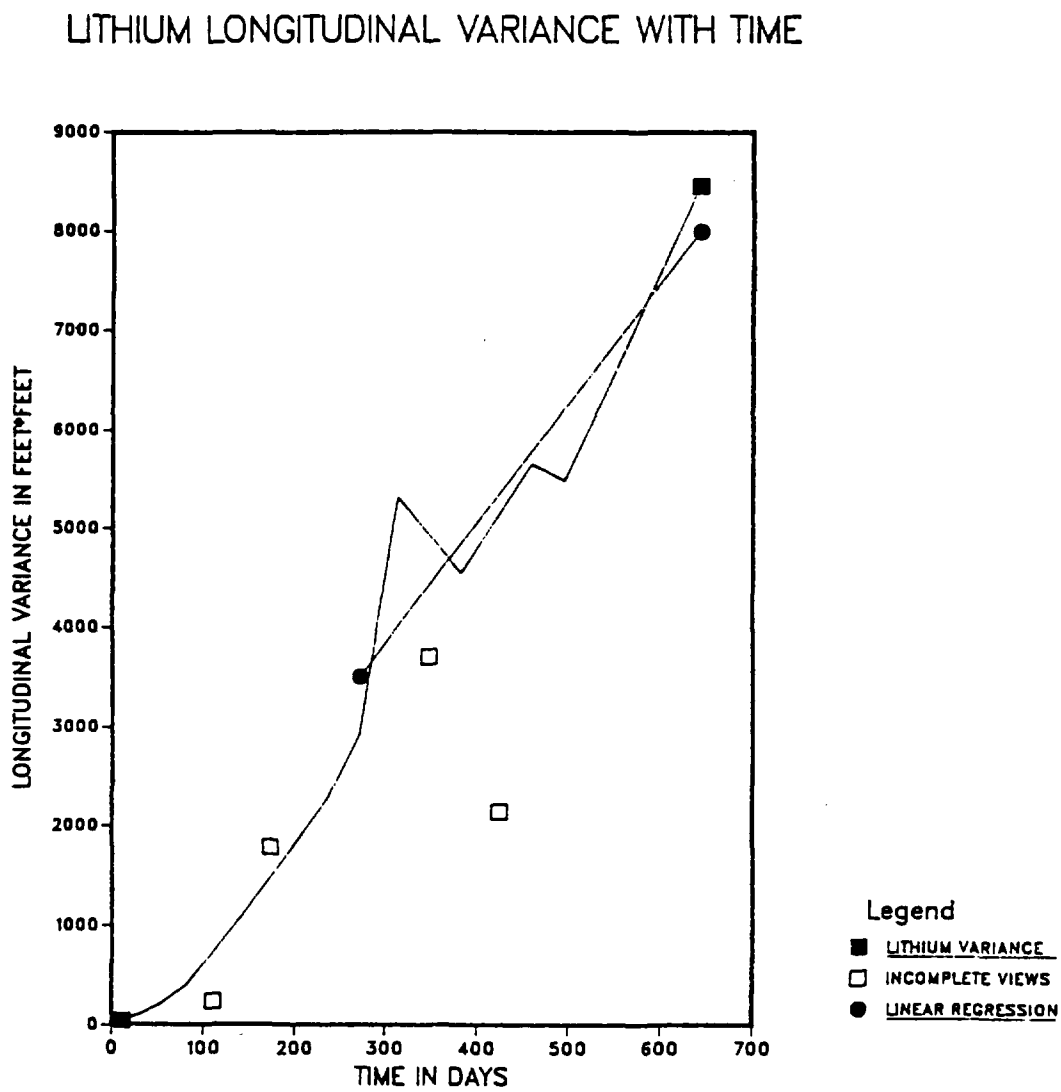

Figure 76. Change in lithium longitudinal variance over time

The variability in the variance trend is very likely due to the sampling density; as the lithium cloud moves, it would be expected that there would jumps and discontinuities in the variance calculations.

There is some evidence from these data that the change in variance over time may be linear after 272 days. The slope of the line from 236 to 272 days is about 18.4 ft^2/day and the slope of the line from 496 to 643 days is about 20.2 ft^2/day. This is a small increase in the slope and both values are larger than the slope of a linear regression over the period from 272 to 643 days (12.1 ft^2/day, only for complete views). Although these data are not definitive, the data can be interpreted as a linear trend.

The change in longitudinal variance with respect to travel distance (fig. 77) shows a similar trend as the change over time (fig. 76). The rate of change in variance steadily increased up to 200 feet of mean displacement (236 days after injection) and then showed large variations around a general upward trend. The slope of a linear regression over the period from 236 to 643 days is about 75 feet. This slope is much larger than that for the change in longitudinal variance for the bromide cloud. If the change in longitudinal variance with travel distance for lithium can be assumed to be linear, and the velocity is assumed constant over the same period (236 to 643 days), the effective longitudinal dispersivity for the lithium cloud movement is about 37 feet. This dispersivity value is over 10 times larger than the longitudinal dispersivity for bromide. Although the effect of nonlinear adsorption reactions can not be discounted as a contributor to this

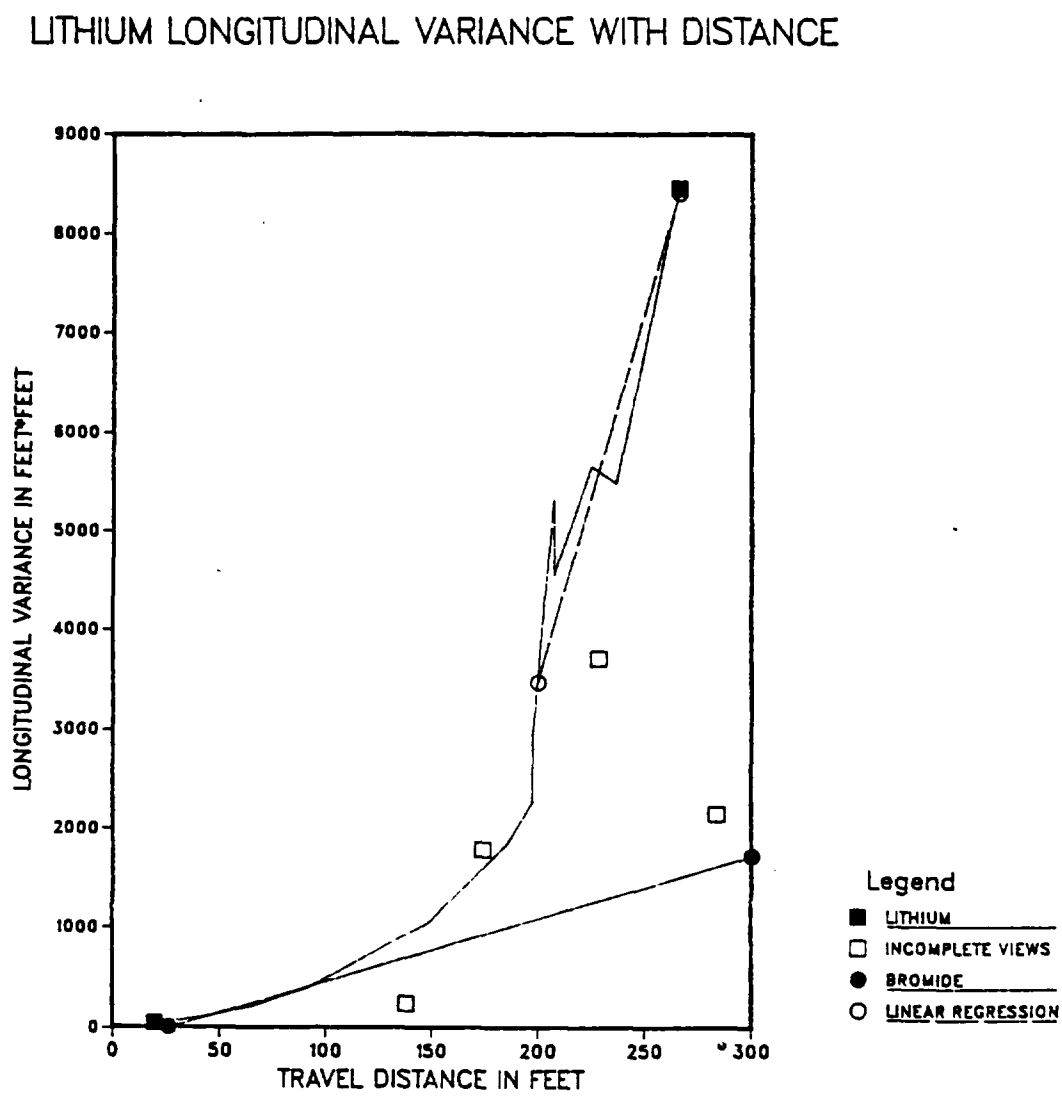

Figure 77. Change in lithium longitudinal variance with travel distance

enhanced spreading of the lithium, it would seem unlikely that all of the spreading could be caused by a nonlinear process which is approaching linearity. Therefore another process should be operating to enhance the longitudinal spreading of the lithium cloud. This other process, enhanced macrodispersion for nonconservative solutes, is examined in the next section of this report.

The changes in transverse horizontal and vertical variance with respect to travel distance are shown in figures 78 and 79, respectively. These data can be compared with the linear regression lines showing the trend in bromide variance for each direction. It is apparent that there is much more scatter around a general upward trend for the transverse horizontal variance for lithium in contrast to that for bromide (fig. 78). The slope of a linear regression of all the complete views is 0.57 feet. This value is nearly 5 times higher than that for bromide. The regression coefficient is so low (r=0.57) however, that the linear fit to these data is very poor. If two outliers (2/86, 3/86) are removed, the slope decreases to 0.066 feet, and the fit improves (r=0.83). Therefore, it would appear that there is not any clear evidence to show the lithium cloud had an effective transverse horizontal dispersivity that was much greater than that for the bromide cloud.

The change in transverse vertical variance for lithium is also very similar to the changes observed for the bromide variance (fig. 79). Here the slope of a linear regression of complete views (0.015 ft) is very similar to that found for bromide (0.01 ft), and the linear trend in the lithium variances is strong (r=0.90). The

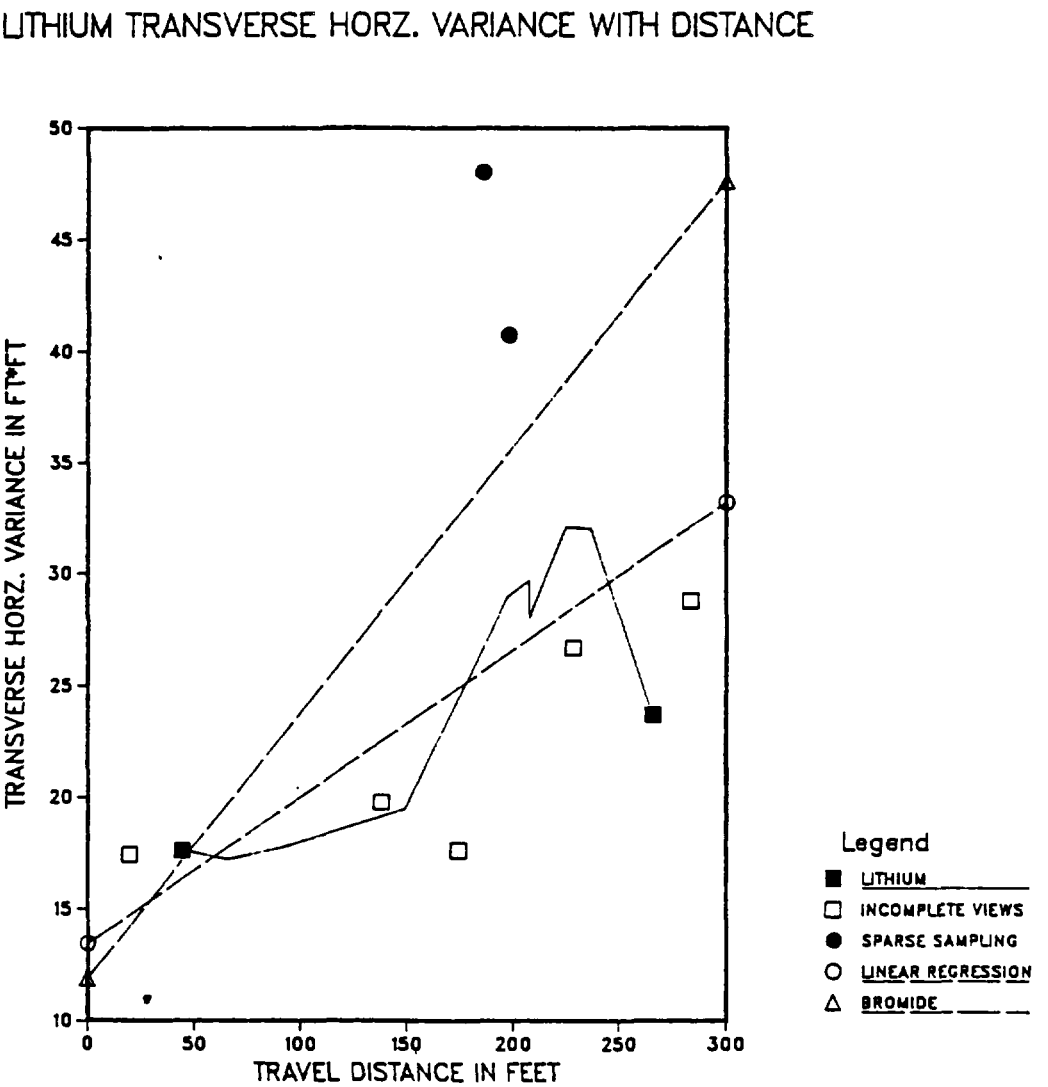

Figure 78. Change in lithium transverse horizontal variance with travel distance

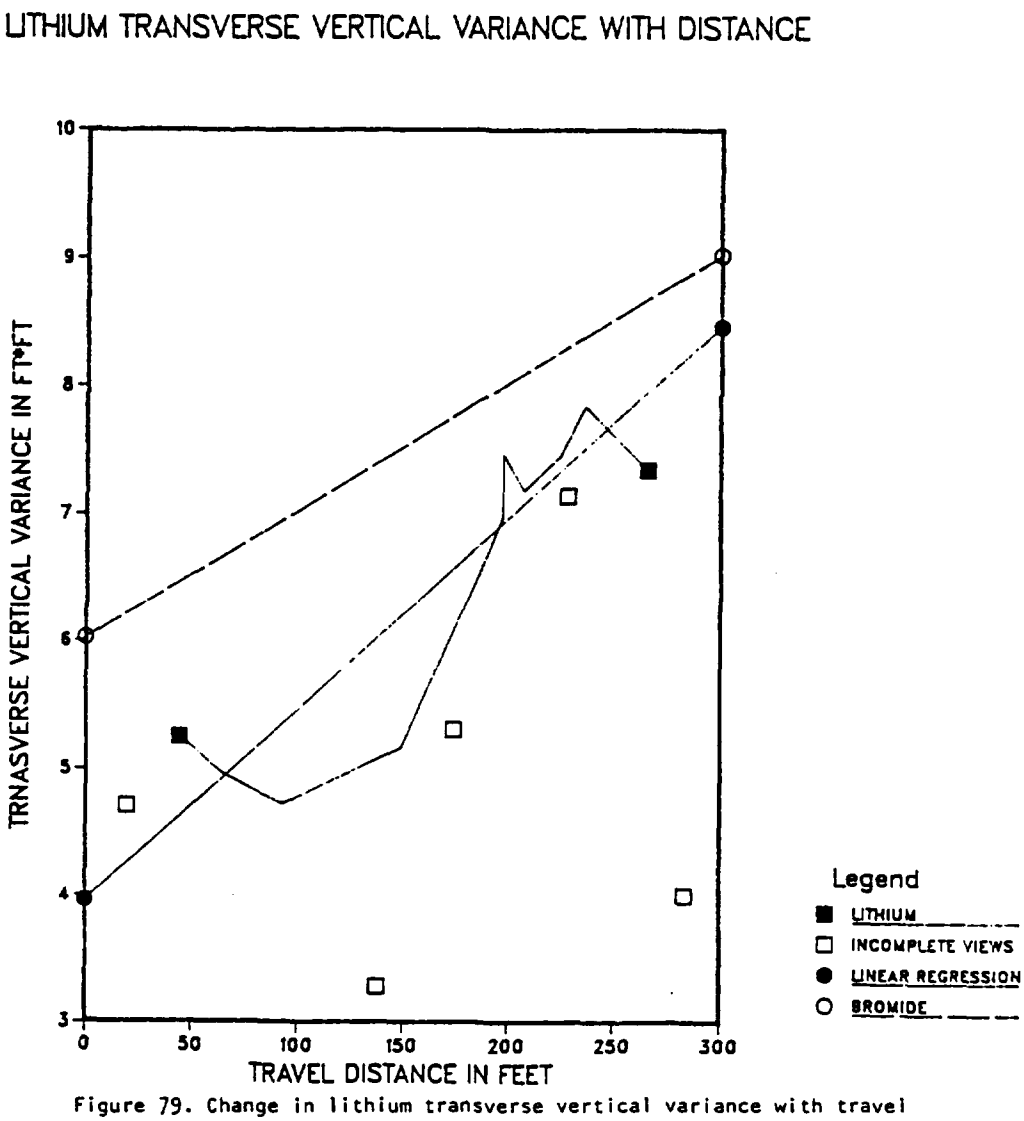

Figure 79. Change in lithium transverse vertical variance with travel distance

transverse vertical dispersivity is nearly the same for lithium as that for bromide.

The variability of each of the lithium variances (longitudinal, transverse horizontal and vertical) can be qualitatively explained by ratios of the standard deviation to sample space. Using the final view (5/87) as an example, the ratios of the longitudinal:

$$\sqrt{8452}/15 = 6.1,$$

transverse horizontal:

$$\sqrt{23.7}/9 = 0.54$$

and transverse vertical:

$$\sqrt{7.34}/2.08 = 1.3$$

directions indicate that the transverse horizontal direction had the fewest number of samples relative to the size of the cloud in that direction. This low resolution of the lithium cloud caused large variations in the transverse horizontal variance along with poor resolution of the longitudinal variance, with resultant jumps and discontinuities in both variance trends. It should be pointed out, however, that the general trends are evident for both the longitudinal and transverse horizontal variances and that the variations around these trends point out the need for not only frequent and dense point sampling but also the need for careful design for these types of field tracer experiments.

IV. Stochastic Analysis of Reactive Solute Macrodispersion in Aquifers

A. Introduction

The movement and fate of reactive solutes in aquifers has been the subject of much recent research because most of the toxic constituents in ground-water contamination problems are involved in reactions during transport. A good review of present knowledge about reactive solute geochemistry is presented by Cherry et al. (1984), in which the similarities and differences between the transport of reactive and nonreactive solutes are described. In particular Cherry et al. (pg. 50, 1984) show that many column experiments indicate a long tailing effect on the breakthrough curves for reactive solutes. Cherry et al. (1984) reference work by Van Genuchten et al. (1974, 1977a, 1977b) and by James and Rubin (1978) which indicates that this extended tailing may be due to a kinetically controlled reaction. The work by Van Genuchten et al. (1974, 1977a, 1977b) also indicates that the extended tailing effect may be caused by solute diffusion into "dead-end" pores. It is readily apparent from these studies that the extent of tailing in laboratory column breakthrough curves is related to the ratio of fluid flow to the rate of kinetically controlled reactions or slow diffusion into "dead-end" pores.

A similar tailing or extra-spreading effect has been noted in field tracer tests with reactive tracers. Figure 55 shows an extensive tailing of the lithium cloud during the large-scale tracer test, and the rapid increase in longitudinal variance for lithium

(fig. 77) also indicates enhanced spreading relative to the nonreactive solute. Another field tracer test showing the same effect was reported by Pickens et al. (1981). In this test iodide (nonreactive) and strontium (reactive) tracers were used to evaluate K_d values at the Chalk River site in Ontario, Canada. A result of this experiment is the finding of larger dispersivities for strontium relative to those for iodide. The authors attribute this increased spreading to nonequilibrium adsorption (i.e. kinetic or diffusion effects).

B. Purpose and Approach

The purpose of the following analysis is to calculate the effective retardation coefficient and to examine a mechanism by which enhanced spreading can occur for reactive solutes with an equilibrium linear adsorption reaction. The approach used in this analysis is analogous to that used by Gelhar and Axness (1983) for the calculation of macrodispersion for a nonreactive solute. The transport of the reactive solute is seen as occurring in a heterogeneous porous media, in which both the physical and geochemical properties have random variations. The variations in aquifer properties are seen as having definable covariance structure and are also related to each other. The random variations in aquifer properties cause random variations in fluid flow and solute concentrations. By using a spectral analysis method it is possible to evaluate the enhanced mixing (macrodispersion) caused by the random perturbations in fluid flow and solute concentrations. By postulating a relationship between the physical and geochemical

properties in an aquifer it is possible to calculate the effect on solute macrodispersion caused by this relationship.

It should be clearly understood that the mechanism described here is one possible explanation of the enhanced spreading effect for reactive solutes. Other causes, including kinetic reactions and diffusion into dead-end pores, may also be involved in this effect. It will be shown however, that the mechanism in the following analysis is physically realistic and may, in part, explain the enhanced spreading of reactive solutes.

C. Random Fields

1. Aquifer Hydraulic Properties

Hydraulic conductivity, because it typically is found to be log normally distributed, is described as the sum of a stationary mean and a zero mean perturbation of the log transform:

$$f(x) = \ln [K(x)], \tag{53a}$$

$$f(x) = \bar{f}(x) + f'(x) \tag{53b}$$

and

$$E[f'(x)] = 0 \tag{53c}$$

The variations represented by f' are described by a three-dimensional statistically homogeneous, but anisotropic, covariance function:

$$R_{ff}(\tau) = \sigma_f^2 \exp\left[-\left(\frac{\tau_1^2}{\lambda_3^2} + \frac{\tau_2^2}{\lambda_2^2} + \frac{\tau_3^2}{\lambda_3^2} \right)^{1/2} \right] \tag{54}$$

where τ_i = separation distance in the i direction,

σ_f^2 = variance of f',

λ_i = correlation in the i direction.

This covariance has as its spectrum:

$$S_{ff}(k) = \frac{\sigma_3^2 \lambda_1 \lambda_2 \lambda_3}{\pi^2 (1 + k_1^2 \lambda_1^2 + k_2^2 \lambda_2^2 + k_3^2 \lambda_3^2)^2} \tag{55}$$

which is the Fourier transform of the covariance function (54).

Another aquifer property is porosity, n, which is also represented by a mean and a perturbation:

$$n = \bar{n} + n' \tag{56}$$

Earlier studies by Warren and Skiba (1964), and Naff (1978) have considered the effects of porosity variations on solute transport and found the effects to be secondary to the effects of hydraulic conductivity variations. However, porosity variations are included in this analysis and a linear relationship between hydraulic conductivity and porosity, along with a random variation around the linear trend, is assumed:

$$n = a_1 + b_1 f + g \tag{57}$$

The mean of the perturbation is zero,

$$E[g] = 0, \tag{58}$$

and the cross-spectrum between f' and g is assumed zero (i.e., no correlation of the perturbations)

$$S_{fg} = 0. \tag{59}$$

The mean of equation (57) is:

$$\bar{n} = a_1 + b_1 f. \tag{60}$$

and the perturbation is:

$$n' = b_1 f' + g \tag{61}$$

2. Aquifer Geochemical Properties

The geochemical reaction treated in this analysis is the instantaneous, reversible, and linear adsorption of a solute to the solid phase of the aquifer:

$$S = K_d c \tag{62}$$

where S is the concentration on the solid (μg/g), c is the concentration in solution (mg/L), and K_d is the distribution coefficient (ml/g).

For a stochastic analysis of the distribution coefficient (K_d) variability, the coefficient is expressed as a sum of a stationary mean and perturbation:

$$\rho K_d = \rho \bar{K}_d + \rho K'_d \tag{63}$$

where ρ is the bulk density of the solid matrix (mass/volume). As with porosity, the distribution coefficient is related to hydraulic conductivity by a linear equation:

$$\rho K_d = a_2 + b_2 f + e, \tag{64}$$

the mean of the K_d perturbation is zero,

$$E[e] = 0, \tag{65}$$

and the f and e perturbations are not correlated,

$$S_{fe} = 0, \tag{66}$$

the mean is,

$$\rho \bar{K}_d = a_2 + b_2 \bar{f} \tag{67}$$

and the perturbation is,

$$\rho K'_d = b_2 f' + e \tag{68}$$

By combining porosity and the distribution coefficient, the random form of the retardation factor times porosity can be formed:

$$R_n = n + \rho K_d, \tag{69}$$

with the mean

$$\bar{R}_n = \bar{n} + \rho \bar{K}_d = a_1 + a_2 + (b_1 + b_2)\bar{f} \qquad (70)$$

and perturbation

$$R'_n = n' + \rho K'_d = g + e + (b_1 + b_2)f'. \qquad (71)$$

Note that these relations ignore the possible effects of porosity variations on the bulk density (i.e., $S_{ge} = 0$).

3. Transport Variables

The transport variables, specific discharge (q) and concentration (c) are also represented by their respective means and perturbations:

$$q_i = \bar{q}_i + q'_i \qquad (72)$$

$$c = \bar{c} + c' . \qquad (73)$$

D. Development of Stochastic Equations

1. Spectral Equations

The mass conservation equation that describes the transport of a solute with linear isotherm adsorption to the solid is (modified from eq. 7-46, Bear, 1979):

$$R_n \frac{\partial c}{\partial t} + \frac{\partial (q_i c)}{\partial x_i} = \frac{\partial}{\partial x_i}\left(E_{ij} \frac{\partial c}{\partial x_j} \right) \qquad (74)$$

where t = time,

q_i = specific discharge, (L/t),

x_i = coordinate direction ,

D_{ij} = dispersion coefficient tensor (L^2/t),

$E_{ij} = nD_{ij}$.

For low concentrations the fluid can be assumed to have a constant density. The conservation of mass for a constant density fluid is,

$$\frac{\partial q_i}{\partial x_i} = 0 . \tag{75}$$

Assuming uni-directional flow, the coordinate system is aligned such that the x_1 direction is along the direction of mean flow:

$$E[q_1] = \bar{q}_1 = q = \text{mean specific discharge} \tag{76}$$

and

$$\bar{q}_2 = \bar{q}_3 = 0 . \tag{77}$$

When the flow perturbations are relatively small ($q'_i << q$), the local (pore scale) dispersion tensor, E_{ij} is approximately constant. With this assumption the local dispersion tensor is composed of the main diagonal terms (see Naff, 1978):

$$E_{ij} = \begin{bmatrix} \alpha_L q & 0 & 0 \\ 0 & \alpha_T q & 0 \\ 0 & 0 & \alpha_T q \end{bmatrix} \tag{78}$$

where α_L is the local longitudinal dispersivity and α_T is the local transverse dispersivity. Next, the perturbed quantities for R_n, c, and q_i are submitted in equation 74 to yield:

$$(\bar{R}_n + R'_n)\frac{\partial(\bar{c}+c')}{\partial t} + \frac{\partial(\bar{q}_i + q'_i)(\bar{c}+c')}{\partial x_i} = E_{ij}\frac{\partial^2(\bar{c}+c')}{\partial x_i \partial x_j} \qquad (79)$$

For convenience the R_n term is brought inside the time derivative because it is assumed constant with respect to time. Expanding terms and taking the expectation of (79) produces the mean equation:

$$\frac{\partial \bar{R}_n\bar{c}}{\partial t} + \frac{\overline{\partial R'_n c'}}{\partial t} + \frac{\partial \bar{q}_i\bar{c}}{\partial x_i} + \frac{\overline{\partial q'_i c'}}{\partial x_i} = E_{ij}\frac{\partial^2\bar{c}}{\partial x_i \partial x_j} \qquad (80)$$

Subtracting the mean equation from (79) gives the mean-removed equation:

$$\frac{\partial \bar{R}_n c'}{\partial t} + \frac{\partial R'_n \bar{c}}{\partial t} + \frac{\partial \bar{q}_i c'}{\partial x_i} + \frac{\partial q'_i \bar{c}}{\partial x_i} - E_{ij}\frac{\partial^2 c'}{\partial x_i \partial x_j}$$

$$= -\left[\frac{\partial R'_n c'}{\partial t} - \frac{\overline{\partial R'_n c'}}{\partial t}\right] - \left[\frac{\partial q'_i c'}{\partial x_i} - \frac{\overline{\partial q'_i c'}}{\partial x_i}\right] \qquad (81)$$

Considering the perturbations to be small, their products appearing in the second-order terms on the right-hand side of equation 81 are neglected. The effect of neglecting second-order terms was examined by Dagan (1984) and found to be small relative to first-

order terms. Dropping these second-order terms produces a first-order approximation describing the concentration perturbation:

$$\frac{\partial \bar{R}_n c'}{\partial t} + \frac{\partial R'_n \bar{c}}{\partial t} + \frac{\partial \bar{q}_i c'}{\partial x_i} + \frac{\partial q'_i \bar{c}}{\partial x_i} = E_{ij} \frac{\partial^2 c'}{\partial x_i \partial x_j} \qquad (82)$$

or

$$\bar{R}_n \frac{\partial c'}{\partial t} + R'_n \frac{\partial \bar{c}}{\partial t} + \bar{q}_i \frac{\partial c'}{\partial x_i} + q'_i \frac{\partial \bar{c}}{\partial x_i} = E_{ij} \frac{\partial^2 c'}{\partial x_i \partial x_j} \qquad (82a)$$

In order to properly represent the changes in concentration, the mean (80) and mean-removed (82) equations are expressed in terms of a moving coordinate:

$$\xi_1 = x_1 - \frac{qt}{R_e}, \quad \xi_2 = x_2, \quad \xi_3 = x_3, \qquad (83)$$

and note that

$$\left.\frac{\partial}{\partial t}\right|_{x_i} = \left.\frac{\partial}{\partial t}\right|_{\xi_i} + \frac{\partial \xi_1}{\partial t}\frac{\partial}{\partial \xi_i} = \left.\frac{\partial}{\partial t}\right|_{\xi_i} - \frac{q}{R_e}\frac{\partial}{\partial \xi_1} \qquad (83a)$$

$$\left.\frac{\partial}{\partial x_i}\right|_t = \left.\frac{\partial}{\partial \xi_i}\right|_t$$

where R_e is the effective retardation factor times porosity. The mean equation is now:

$$\left[\frac{-q}{Re}\frac{\partial \bar{R}_n \bar{c}}{\partial \xi_1} + \frac{\partial \bar{R}_n \bar{c}}{\partial t}\right] + \left[\underset{(b)}{\frac{-q}{Re}\frac{\partial \bar{R}' \bar{c}'}{\partial \xi_1}} + \underset{(c)}{\frac{\partial \bar{R}' \bar{c}'}{\partial t}}\right]$$

$$+ \frac{\partial \bar{q}_i \bar{c}}{\partial \xi_i} + \underset{(a)}{\frac{\partial \overline{q'_i c'}}{\partial \xi_i}} = E_{ij}\frac{\partial^2 \bar{c}}{\partial \xi_i \partial \xi_j} \qquad (84)$$

The same change in coordinate system is also done for the mean-removed equation:

$$\bar{R}_n\left(\frac{\partial c'}{\partial t}\bigg|_{\xi_i} - \frac{q}{R_e}\frac{\partial c'}{\partial \xi_i}\right) + R'_n\left(\frac{\partial \bar{c}}{\partial t}\bigg|_{\xi_i} - \frac{q}{R_e}\frac{\partial \bar{c}}{\partial \xi_1}\right) + \bar{q}_i\frac{\partial c'}{\partial \xi_i} + q'_i\frac{\partial \bar{c}}{\partial \xi_i}$$

$$= E_{ij}\frac{\partial^2 c'}{\partial \xi_i \partial \xi_j} \qquad (85)$$

The additional terms (a), (b), and (c) in equation (84) are evaluated for their effect on the mean movement of the solute using a spectral analysis approach. Because statistical homogeneity is assumed, Fourier-Stieltjes representations may be used for the perturbed quantities:

$$c' = \int_{-\infty}^{\infty}\int\int\int \exp[ik_i x_i]\, dZ_c(k,t) = \int_{-\infty}^{\infty}\int\int\int \exp i\left[k_1\left(\xi_1 + \frac{qt}{R_e}\right) + k_2\xi_2 + k_3\xi_3\right] dZ_c(k,t)$$

(86a)

$$q'_i = \int_{-\infty}^{\infty}\int\int\int \exp\,[ik_i x_i]\, dZ_{q_i}(k) \qquad (86b)$$

$$R'_n = \int_{-\infty}^{\infty}\int\int\int \exp\,[ik_i x_i]\, dZ_{Rn}(k) \qquad (86c)$$

where $k_i = (k_1, k_2, k_3)$ is the wave number vector,

$x_i = (x_1, x_2, x_3)$ is the position vector,

$$dZ_{R_n} = dZ_{\rho K_d} + dZ_n$$

and integration is over three-dimensional wave number space. Using these representations in equation (85) with

$$G_i = -\frac{\partial \bar{c}}{\partial x_i},$$

along with the uniqueness of the spectral representation:

$$\bar{R}_n\left(ik_1 \frac{q}{R_e} dZ_c + \frac{\partial dZ_c}{\partial t}\bigg|_{\xi_i} - \frac{q}{R_e} ik_1\, dZ_c\right) + dZ_{R_n}\left(\frac{\partial \bar{c}}{\partial t}\bigg|_{\xi_1} + \frac{q}{R_e} G_1\right)$$

$$+ q_i k_1 dZ_c - G_i\, dZ_{q_i} = -E_{ij} k_i k_j dZ_c \qquad (87)$$

and then cancelling terms:

$$\bar{R}_n \frac{\partial(dZ_c)}{\partial t} + (qik_1 + E_{ij}k_ik_j)\, dZ_c + \left(\frac{q}{Re} G_1 + \frac{\partial \bar{c}}{\partial t}\right) dZ_{R_n} - G_i dZ_{q_i} = 0 \tag{88}$$

Taking the large time solution results in:

$$\frac{\partial(dZ_c)}{\partial t} \to 0\,, \quad dZ_c = \frac{-\left(\frac{qG_1}{Re} + \frac{\partial \bar{c}}{\partial t}\right) dZ_R + G_i dZ_{q_i}}{(q_i ik_1 + E_{ij}k_ik_j)} \tag{89}$$

This above equation relates the complex Fourier amplitudes for concentration, retardation, and specific discharge. The above equation is the large-time asymptotic result. An analysis of time varying macrodispersion can be found in Gelhar et al. (1979), in which it is shown that the dispersivity increases over time until it reaches an asymptotic (i.e. Fickian) limit.

In order to evaluate terms (a), (b), and (c) in equation (84), the cross spectra are calculated and integrated over the wave domain. For term (a) the cross spectrum S_{cq_i} is calculated by multiplying both sides of (89) by $dZ^*_{q_i}$ (the complex conjugate of the Fourier amplitude), taking the mean, and using the spectral representation theorem. This results in the spectral relationship:

$$S_{cq_i} = \frac{-\left(\frac{qG_1}{Re} + \frac{\partial \bar{c}}{\partial t}\right) S_{R_n q_j} + G_j S_{q_y q_i}}{(q\, ik_1 + E_{ij}k_ik_j)} \tag{90}$$

where S_{cq_i} is the cross spectrum of c and q_i, $S_{R_n q_j}$ is the cross spectrum of R_n and q_i, and $S_{q_j q_i}$ is the cross spectrum of i and j components of the specific discharge. Equation (90) relates the spectra of flow variation and retarded flow variations to that of the dispersive flux. To evaluate the term (a) in equation (84), the cross spectrum is integrated over the wave domain:

$$\overline{c'q'_i} = \int_{-\infty}^{\infty} S_{cq_i}\, dk \tag{91}$$

For terms (b) and (c) the cross spectrum of R'_n and c' are used:

$$\overline{R'_n c'} = \int_{-\infty}^{\infty} S_{R_n c}\, dk \tag{92}$$

where $S_{R_n c}$ is calculated using equation 89:

$$S_{R_n c} = \frac{-\left(\frac{qG_1}{R_e} + \frac{\partial \bar{c}}{\partial t}\right) S_{RR} + G_j S_{Rq_i}}{(qik_1 + E_{ij}k_i k_j)} \tag{93}$$

After integration over the wave domain, terms (a), (b), and (c) become:

$$\text{(a)} \quad \frac{\partial(\overline{q'_i c'})}{\partial \xi_i} = \frac{\partial}{\partial \xi_i}\left[I_1 \frac{q}{R_e} \frac{\partial \bar{c}}{\partial \xi_1} - I_1 \frac{\partial \bar{c}}{\partial t} - I_2 \frac{\partial \bar{c}}{\partial \xi_j} \right] \tag{94}$$

where

$$I_1 = \int_{-\infty}^{\infty} \frac{S_{R_n q_j}\, dk}{(q\, ik_1 + E_{ij}k_i k_j)} \tag{94a}$$

$$I_2 = \int_{-\infty}^{\infty} \frac{S_{q_j q_i}\, dk}{(q_i k_1 + E_{ij}k_i k_j)} \tag{94b}$$

(b) $$\frac{\partial(R'_n c')}{\partial \xi_1} = \frac{\partial}{\partial \xi_1}\left[I_3 \frac{q}{R_e} \frac{\partial \bar{c}}{\partial \xi_1} - I_3 \frac{\partial \bar{c}}{\partial t} - I_1 \frac{\partial \bar{c}}{\partial \xi_j} \right] \tag{95}$$

where

$$I_3 = \int_{-\infty}^{\infty} \frac{S_{R_n R_n}\, dk}{(q\, ik_1 + E_{ij}k_i k_j)} \tag{95a}$$

(c) $$\frac{\partial \overline{R'_n c'}}{\partial t} = \frac{\partial}{\partial t}\left[I_3 \frac{q}{R_e} \frac{\partial \bar{c}}{\partial \xi_1} - I_3 \frac{\partial \bar{c}}{\partial t} - I_1 \frac{\partial \bar{c}}{\partial \xi_j} \right] \tag{96}$$

The effect of each term on the mean transport equation is based primarily on the derivatives of c in the term. In the case of term (a), there are second derivatives in space and mixed derivatives:

$$\frac{\partial}{\partial \xi_i}\left(\frac{\partial \bar{c}}{\partial \xi_j}, \frac{\partial \bar{c}}{\partial t}\right) \tag{97}$$

It is apparent from an analysis of moments of terms containing these derivatives that only the second derivatives in space will affect the second moment (variance) of the concentration distribution. The mixed derivative terms will have an effect on third and higher moments (see Gelhar et al., 1979), producing asymmetry in the solute distribution.

Second derivatives in space appear in term (b) but do not appear in term (c). Therefore, only terms (a) and (b) will have an effect on solute dispersion. Also apparent in equations (94)-(95) is the lack of first derivatives in space or time for terms (a), (b), and (c) in equation 84. Therefore, the mean storage and advective terms in equation 84 will not be affected by terms (a), (b), or (c). Because the mean advective transport terms must be zero in the moving coordinate systems,

$$\frac{-q}{R_e}\frac{\partial \bar{R}_n \bar{c}}{\partial \xi_1} + \frac{\partial \bar{q}_i \bar{c}}{\partial \xi_i} = 0 \tag{98}$$

where

$$\frac{\partial \bar{q}_i \bar{c}}{\partial \xi_i} = q\frac{\partial \bar{c}}{\partial \xi_1} \tag{99}$$

from equations 76 and 77 and, therefore, R_e must equal R_n. The effective retardation coefficient is thus the arithmetic mean. This now leaves the mean equation as:

$$\frac{\partial \overline{R}_n \overline{c}}{\partial t} + \frac{\partial \overline{q'_i c'}}{\partial \xi_i} - \frac{q}{R_e} \frac{\partial \overline{R'_n c'}}{\partial \xi_1} + \frac{\partial \overline{R'_n c'}}{\partial t} = E_{ij} \frac{\partial^2 \overline{c}}{\partial \xi_i \partial \xi_j} \qquad (100)$$

2. Solution with Statistically Isotropic Media

Equations 94a, 94b, and 95a are integrated using spectral relationships between lnK, q_i, and R_n. The specific discharge spectrum is developed using the Darcy equation with locally isotropic hydraulic conductivity (Gelhar and Axness, (1983)).

$$q_i = -K \frac{\partial \phi}{\partial x_i} = -K_\ell \exp(f') \frac{\partial \phi}{\partial x_i} = K_\ell \left(1 + f' + \frac{f'^2}{2} + \ldots \right) \left(\frac{\partial H}{\partial x_i} + \frac{\partial h}{x_i} \right) \qquad (101)$$

where $K_\ell = \exp[E(\ln K)]$ and $\phi = H + h$, $(E[h] = 0)$ is the hydraulic head. If small perturbations are assumed then products of perturbed quantities can be dropped, leading to the mean-removed equation:

$$q'_i = -K_\ell \left(f' \frac{\partial H}{\partial x_i} + \frac{\partial h}{\partial x_i} \right) \qquad (102)$$

Using Fourier-Stieltjes representations the complex Fourier amplitude is:

$$dZ_{q_i} = K_{\ell}(J_i dZ_f - i\, k_i dZ_h) \tag{103}$$

where $J_i = -\dfrac{\partial H}{\partial x_i}$ is the mean hydraulic gradient in the x_i direction.

The three-dimensional equation for head perturbations is (Bakr et al., 1978):

$$\nabla^2 h = J_i \frac{\partial f}{\partial x_i} \tag{104}$$

and using Fourier-Stieltjes representations is:

$$dZ_h = \frac{-i\, J_i\, k_i\, dZ_f}{k^2} \tag{105}$$

where $k2 = k_1 2 + k_2 2 + k_3 2$. Using equations 103 and 105 produces a relation between specific discharge and log hydraulic conductivity:

$$dZ_{q_i} = K_{\ell}\left(J_i - \frac{J_i k_i k_j}{k^2}\right) dZ_f \tag{106}$$

With unidirectional mean flow ($\bar{q}_2=\bar{q}_3=0$), a statistically isotropic lnK field ($\lambda = \lambda_1 = \lambda_2 = \lambda_3$), and zero transverse mean hydraulic gradients, the spectrum of the specific discharge becomes:

$$S_{q_j q_i} = \frac{q^2}{\gamma^2}\left(\delta_{i1} - \frac{k_1 k_i}{k^2}\right)\left(\delta_{j1}\, \frac{-k_1 k_j}{k^2}\right) S_{ff} \tag{107}$$

where δ_{ij} is the dirac delta function and $\gamma = \frac{q}{K_\ell J_1}$ which in this case of an isotropic lnK field is $\gamma = 1 + \frac{\sigma_f^2}{6}$ (eq. 28b, Gelhar and Axness, 1983).

For the spectrum $S_{R_n R_n}$ and the cross spectrum S_{Rq_i} equation (71) is used with Fourier-Stieltjes representations:

$$dZ_{R_n} = dZ_g + dZ_e + (b_1 + b_2)\, dZ_f \tag{108}$$

which can immediately be used to form the spectrum:

$$S_{R_n R_n} = S_{gg} + S_{ee} + (b_1 + b_2)^2\, S_{ff} \tag{109}$$

and cross spectrum:

$$S_{R_n q_i} = (b_1 + b_2)\, K_\ell \left(J_i - \frac{J_j k_i k_j}{k^2} \right) S_{ff} \tag{110}$$

which after using $\gamma = \frac{q}{K_\ell J_1}$ is:

$$S_{R_n q_i} = (b_1 + b_2)\, \frac{q}{\gamma} \left(\delta_{ij} - \frac{k_1 k_i}{k^2} \right) S_{ff} \tag{111}$$

To solve for the longitudinal macrodispersivity term, A_{11}, integrals I_1, I_2, I_3 (eq. 94 and 95) are evaluated using the spectrum and cross spectrum (eq. 107, 109, 111) and the spectrum of lnK, S_{ff} (eq. 55). An approximate solution can be found by assuming the local dispersivity (α_L, α_T) is small compared to the correlation scale (λ). This assumption is valid if the ratio of α_L to λ is .01 or smaller (see Gelhar and Axness, 1983). Following through term by term:

$$I_1 = \int_{-\infty}^{\infty} \frac{(b_1+b_2)\,\frac{q}{\gamma}\left(\delta_{i1} - \frac{k_1-k_i}{k^2}\right) S_{ff}dk}{(q\,ik_1 + E_{ij}k_ik_j)} \qquad (112)$$

Using the diagonal form of the local dispersion coefficient (eq. 78), eliminating the specific discharge, and multiplying through by

$$[-i\,k_1 + \{\alpha_L k_1^2 + \alpha_T(k_2^2 + k_3^2)\}]$$

produces

$$I_1 = \int_{-\infty}^{\infty} \frac{(b_1+b_2)\left(\delta_{i1} - \frac{k_1k_i}{k^2}\right)(-i\,k_1 + (\alpha_L k_1^2 + \alpha_T(k_2^2+k_3^2)))S_{ff}dk}{\gamma(k_1^2 + (\alpha_L k_1^2 + \alpha_T(k_2^2 + k_3^2))^2)} \qquad (113)$$

The integral is evaluated in Appendix C with the result:

$$I_1 = \frac{(b_1 + b_2)\,\sigma_f^2\,\lambda}{\gamma} \qquad (114)$$

Now proceeding to solve for I_2 using equations 94a and 107:

$$I_2 = \int_{-\infty}^{\infty} \frac{q^2\left(\delta_{i1} - \frac{k_1 k_i}{k^2}\right)\left(\delta_{j1} - \frac{k_1 k_j}{k^2}\right) S_{ff}\, dk}{\gamma^2 (q\, i k_1 + E_{ij} k_i k_j)} \qquad (115)$$

this equation is identical to the term used in the analysis by Gelhar and Axness (1983) and is integrated following the same procedure as was used for I_1; with the result:

$$I_2 = \frac{q\, \sigma_f^2\, \lambda}{\gamma^2} \qquad (116)$$

For I_3 the procedure is again repeated, this time using equations 95 and 109:

$$I_3 = \int_{-\infty}^{\infty} \frac{S_{gg} + S_{ee} + (b_1 + b_2)^2 S_{ff}\, dk}{(q\, i k_1 + E_{ij} k_i k_j)} \qquad (117)$$

Both S_{gg} and S_{ee} are assumed to have spectrum similar to S_{ff} (i.e., a negative exponential covariance function):

$$S_{gg} = \frac{\sigma_g^2\, \lambda_g^3}{\pi^2 (1 + \lambda_g^2\, k_i^2)} \qquad (118)$$

$$S_{ee} = \frac{\sigma_e^2 \lambda_e^3}{\pi^2 (1 + \lambda_e^2 k_i^2)} \tag{119}$$

Following through the procedure produces:

$$I_3 = \frac{1}{q} (\sigma_g^2 \lambda_g + \sigma_e^2 \lambda_e^2 + (b_1+b_2)^2 \sigma_f^2 \lambda) \tag{120}$$

Combining all the terms in the mean equation (84) which contains second derivatives of $\bar{c}$ with respect to ξ_1 produces dispersive terms in ξ_1

$$\text{(a)} \quad \frac{\partial}{\partial \xi_1} \left[\frac{(b_1+b_2)\sigma_f^2 \lambda}{\gamma} \frac{q}{R_n} \frac{\partial \bar{c}}{\partial \xi_1} - \frac{q \sigma_f^2 \lambda}{\gamma^2} \frac{\partial \bar{c}}{\partial \xi_1} \right] \tag{121}$$

$$\text{(b)} \quad \frac{-q}{R_n} \frac{\partial}{\partial \xi_1} \left[\frac{1}{R_n} (\sigma_g^2 \lambda_g + \sigma_e^2 \lambda_e + (b_1+b_2)\sigma_f^2 \lambda) \frac{\partial \bar{c}}{\partial \xi_1} - \frac{(b_1+b_2)\sigma_f^2 \lambda}{\gamma} \frac{\partial \bar{c}}{\partial \xi_1} \right] \tag{122}$$

with no terms added from part (c).

All longitudinal dispersive terms are combined such that the dispersive term is

$$A_{11} \left(-q \frac{\partial^2 \bar{c}}{\partial \xi_1^2} \right), \tag{123}$$

and

$$A_{11} = \frac{(\sigma_g^2 \lambda_g + \sigma_e^2 \lambda_e)}{R_n^2} + \frac{\sigma_f^2 \lambda}{\gamma^2} \left(1 - \frac{\gamma(b_1+b_2)}{R_n} \right)^2 \qquad (124)$$

is the asymptotic longitudinal macrodispersivity for a reactive solute with linear adsorption onto the solid matrix. In the case of a conservative solute ($b_2 = 0$), with a constant porosity in the aquifer ($b_1 = 0$), the longitudinal macrodispersivity is equivalent to the result in Gelhar and Axness, 1983 ($A_{11} = \sigma_f^2 \lambda / \gamma^2$). The quadratic (i.e., parabolic) relationship between the reactive solute macrodispersivity and the ($b_1 + b_2$) parameter is shown in Figure 80. It is readily apparent that if the ($b_1 + b_2$) parameter is negative, the macrodispersivity is increased, and as indicated in Appendix C, the slope of the K_d, lnK relationship (b_2) should be negative for most cases. It is conceivable, however, that the ($b_1 + b_2$) parameter could be positive due to a positive correlation between porosity and lnK. For this case (i.e., $b_1 + b_2 > 0$) the macrodispersivity could decrease until it is equal to zero. This case of a zero macrodispersivity represents the possibility in which the retarded velocities are exactly balancing the variations in fluid velocities caused by local variations in hydraulic conductivity. The offsetting retardation would then create a uniform velocity field for the reactive solute. The uniform velocity field would not have any of the velocity perturbations which cause macrodispersivity and the reactive solute macrodispersivity would be equal to zero. The resulting dispersion of the reactive solute would be due solely to the local dispersion which occurs in homogeneous porous media. Note that there is an

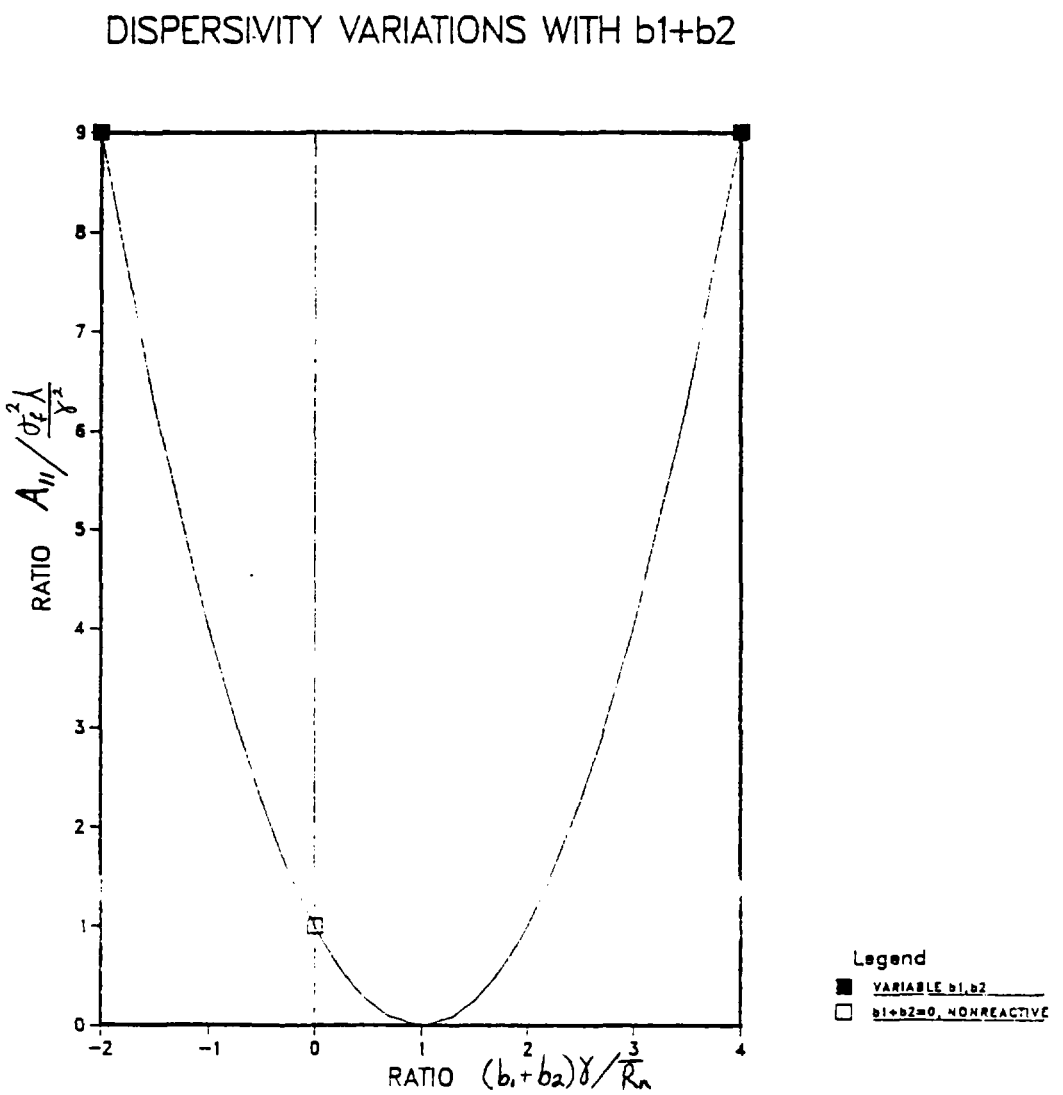

Figure 80. Variation in dispersivity with parameters b_1+b_2

increase in the macrodispersivity due to the random variations in porosity and K_d even if these variations are not correlated with hydraulic conductivity. These factors,

$$(\sigma_g^2 + \sigma_e^2 \lambda_e)/\bar{R}_n^2 .$$

will be dependent on both the variance of the porosity and K_d variations and the length over which the variations are correlated. In combination with the most likely case of increased dispersion due to negatively correlated lnK and K_d variations it appears that this development may provide an explanation for increased macrodispersivities for reactive solute transport.

The transverse macrodispersivity terms for the isotropic lnK case are produced by again examining equations (94-95) for terms with the transverse concentration gradients

$$\frac{\partial^2 \bar{c}}{\partial x_2^2} \text{ and } \frac{\partial^2 \bar{c}}{\partial x_3^2}.$$

In the case of I_1 in equations (94a) and (113), it is immediately apparent that with $k_1 = k_2$ or $k_i = k_3$ the equation will be odd in these wave numbers and will integrate to zero over the domain ($-\infty$ to ∞). As I_3 is not involved in any of the transverse terms, this leaves the single remaining term:

$$-\frac{\partial}{\partial \xi_i}\left(I_2 \frac{\partial \bar{c}}{\partial \xi_j}\right)$$

where

$$I_2 = \int_{-\infty}^{\infty} \frac{S_{q_j q_i}\, dk}{(q\, ik_1 + E_{ij}k_i k_j)}$$

This term is identical to that used in the analysis by Gelhar and Axness (1983, eq. 36) with the result that

$$A_{22} = A_{33} = \frac{\sigma_f^2\, \alpha_L}{15\, \gamma^2}\left(1 + \frac{4\alpha_T}{\alpha_L}\right) \qquad (125)$$

Therefore, these results indicate the variability in the distribution coefficient and porosity only affects the longitudinal macrodispersivity for the isotropic lnK covariance case.

3. Solution with Statistically Anisotropic Media

For the more generalized analysis of arbitrary orientation of flow relative to the stratification in a statistically anisotropic lnK field, equations (94) and (95) indicate differing contributions by I_1, I_2, and I_3 to the macrodispersivity tensor. The quantity I_1 will contribute to the longitudinal terms A_{11}, A_{12}, and A_{13}; it should be noted that the macrodispersivity tensor is symmetric and $A_{12}=A_{21}$, $A_{13}=A_{31}$.

The quantity I_2 contributes to all terms of the tensor and the analysis of this integral is identical to that used in Gelhar and Axness (1983). The quantity I_3 will only contribute to the longitudinal term, A_{11}.

To solve for each macrodispersivity term, A_{ij}, integrals I_1, I_2, and I_3 are evaluated after the spectrum $S_{R_nq_j}$, $S_{q_iq_j}$ and $S_{R_nR_n}$ are found for the specific flow conditions. The cross-spectrum $S_{R_nq_j}$ is found by using equation (103).

$$dZ_{q_j} = K_I \left(J_j - J_n \frac{k_j k_n}{k^2} \right) dZ_f$$

multiplying by the quantity:

$$dZ^*_{R_n} = dZ^*_g + dZ^*_e + (b_1+b_2)dZ^*_f$$

and application of the expectation operator produces

$$S_{R_nq_j} = (b_1+b_2)K_I J_n \left(\delta_{jn} - \frac{k_j k_n}{k^2} \right) S_{ff} \qquad (126)$$

The spectrum for specific discharge, $S_{q_iq_j}$ is found by applying (106) twice to produce:

$$S_{q_iq_j} = K_I^2 J_m J_n \left(\delta_{im} - \frac{k_i k_m}{k^2} \right) \left(\delta_{jn} - \frac{k_j k_n}{k2} \right) S_{ff} \qquad (127)$$

The spectrum for R, $S_{R_nR_n}$, is the same as before

$$S_{R_nR_n} = S_{gg} + S_{ee} + (b_1+b_2)^2 S_{ff}. \qquad (128)$$

Following the approach of Gelhar and Axness (eq. 63, 1983), integrals I_1, I_2, and I_3 are evaluated. For I_1 the components of A_{ij} are:

$$I_1 = -\frac{1}{R_n}\int_{-\infty}^{\infty} \frac{S_{R_n R_j}\, dk}{q(i\,k_1 + {}_L k_1^2 + \alpha_T(k_2^2 + k_3^2))} \tag{129}$$

$$= \frac{-1}{R_n}\int_{-\infty}^{\infty} \frac{(b_1+b_2)\; K_\ell J_n \left(\delta_{jn} - \dfrac{k_j k_n}{k^2}\right) S_{ff}\, dk}{q(i\,k_1 + \alpha_L k_1^2 + \alpha_T\,(k_2^2 + k_3^2))} \tag{130}$$

$$= (b_1+b_2)[J_j P - J_j Q_{ij}]/J_1 \gamma R_n \tag{131}$$

where

$$P = \int_{-\infty}^{\infty} \frac{S_{ff}\, dk}{B} \tag{132}$$

$$Q_{ij} = \int_{-\infty}^{\infty} \frac{k_i k_j S_{ff} dk}{k^2 B} \tag{133}$$

$$B = (i\,k_1 + \alpha_L\, k_1^2 + \alpha_T\,(k_2^2 + k_3^2)) \tag{134}$$

$$\gamma = \frac{q}{K_\ell J_1} \tag{135}$$

For I_2 the components of A_{ij} are (see Gelhar and Axness, 1983, eq. 62,63):

$$I_2 = \int_{-\infty}^{\infty} \frac{S_{q_j q_i}\, dk}{q^2 (i\, k_1 + \alpha_L k_1^2 + \alpha_T (k_2^2 + k_3^2))} \tag{136}$$

$$= [J_j J_i P - J_j J_n Q_{in} - J_m J_i Q_{jm} + J_m J_n R_{ijmn}] \Big/ J_1^2 \gamma^2 \tag{137}$$

where P, Q_{ij}, B, and γ are as in equations (132) through (135) and

$$R_{ijmn} = \int_{-\infty}^{\infty} \frac{k_i k_j k_m k_n\, S_{ff}\, dk}{k^4 B} \tag{138}$$

For I_3 the components of A_{ij} are:

$$I_3 = \frac{1}{R_n^2} \int_{-\infty}^{\infty} \frac{S_{R_n R_n}\, dk}{(i\, k_1 + \alpha_L k_1^2 + \alpha_T (k_2^2 + k_3^2))} \tag{139}$$

$$= \frac{1}{R_n^2} [\sigma_g^2 \lambda_g + \sigma_e^2 \lambda_e + (b_1 + b_2)^2 P] \tag{140}$$

Following the approach outlined in Gelhar and Axness (1983), the integrals P, Q_{ij}, and R_{ijmn} are of the form

$$I_g = \int_{-\infty}^{\infty} \frac{c(k)\, S_{ff}\, dk}{(i\, k_1 + \alpha_L\, k_1^2 + \alpha_T (k_2^2 + k_3^2))} \tag{141}$$

where

$$c(k) = 1,\ k_i k_j / k^2 \text{ or } k_i k_j k_m k_n / K^4$$

By assuming that α_L / λ_1 goes to zero, as in the isotropic ln K covariance case, equation 141 is now:

$$I_g \equiv \pi \int_{-\infty}^{\infty}\int c(0, k_2, k_3)\, S_{ff}(0, k_2, k_3)\, dk_2 dk_3 \qquad (142)$$

Note that if any one of the subscripts in Q_{ij} or R_{ijmn} are 1, the integral will be zero because $C(0, k_2 k_3) = 0$. This asymptotic analysis should be quite accurate for $\alpha_f/\lambda_1 < 0.01$ (see Gelhar and Axness, 1983, figure 1). The integrals in the form of equation (142) were evaluated in polar coordinates (Gelhar and Axness, 1981) and are given in an appendix in Gelhar and Axness, 1983.

An example of the use of this analysis is the special case of $\gamma_1 = \gamma_2$ (isotropy in the plane of stratification, with mean flow inclined at an angle (θ) with the bedding (see case 1. Gelhar and Axness. 1983). Using the solution outlined above. with $J_2 = 0$. the following nonzero components of A_{ij} are obtained:

$$A_{11} = \frac{\sigma_f^2 \lambda_1 \mu}{W\gamma^2}\left[1 - \frac{\gamma(b_1+b_2)}{R_n}\right]^2 + \frac{\sigma_g^2 \lambda_g + \sigma_e^2 \lambda_e}{R_n^2} \qquad (143a)$$

$$A_{22} = \frac{\sigma_f^2 \lambda_1 \mu J_3^2}{[2\,(1+W)^2 \gamma^2 J_1^2]} \qquad (143b)$$

$$A_{33} = \frac{\sigma_f^2 \lambda_1 J_3^2 (1 + 2W)}{[2(1 + W)^2 \gamma^2 J_1^2]} \qquad (143c)$$

$$A_{13}=A_{31}= \frac{\sigma_f^2 \lambda_1 \mu J_3}{[(1 + W)\gamma^2 J_1]}\left[1 - \frac{\gamma(b_1+b_2)}{R_n}\right] \qquad (143d)$$

where

$$\gamma = \frac{q}{K_\ell J_1}, \quad \mu = \frac{\lambda_3}{\lambda_1}, \quad W = (\sin^2\theta + \mu^2\cos^2\theta)^{1/2}$$

It should be noted that the factor

$$\left[1 - \frac{\gamma(b_1+b_2)}{R_n}\right]$$

again affects the macrodispersivity tensor, with the longitudinal term affected the greatest. If it is assumed that the sum of (b_1 + b_2) is negative, then the longitudinal macrodispersivity of a nonconservative solute is increased relative to the transverse terms. The result will be a stronger orientation of the largest principal macrodispersivity term toward the direction of flow.

E. Application of Reactive Solute Macrodispersivity

1. Chalk River Tracer Test

A comparison of nonreactive and reactive solute macrodispersivities can be made for a radial tracer test in which

both nonreactive (^{131}I) and reactive (^{85}Sr) solutes were used as tracers.

Pickens et al. (1981) conducted the single well injection and pumping tracer test in a fluvial sand aquifer at the Chalk River site in Ontario, Canada. The breakthrough of nonreactive tracer, ^{131}I, was used to develop groundwater velocities and dispersion coefficients. Strontium 85 was also injected and was found to be significantly absorbed by the aquifer materials relative to ^{131}I (Figure 81, from Pickens, et al., 1981). The dispersivities for the ^{85}Sr movement were found to be 2-5 times greater than those calculated from the ^{131}I breakthrough curves (table 18). The authors attribute this increased spreading to nonequilibrium adsorption effects and include these effects in the dispersion coefficient because good agreement was obtained between the analytical solution and the field data (Figure 81). Another example of the increased spreading of ^{85}Sr relative to ^{131}I is shown in the breakthrough curve for the withdrawal phase of the test (figure 82).

Laboratory batch and column tests for K_d values were made and are shown in tables 19 and 20 (from Pickens, et al., 1981). K_d values vary a good deal and are likely due to the variation in mineralogy and grain size in the individual strata in the aquifer. K_d values were also calculated from the tracer test (table 18) and are compared with batch and column tests in table 21. It was found that batch and column tests generally yielded higher K_d values than those calculated from breakthrough curves. The authors attribute this to increased accessibility to adsorption sites in the batch tests and greater time to achieve equilibrium conditions.

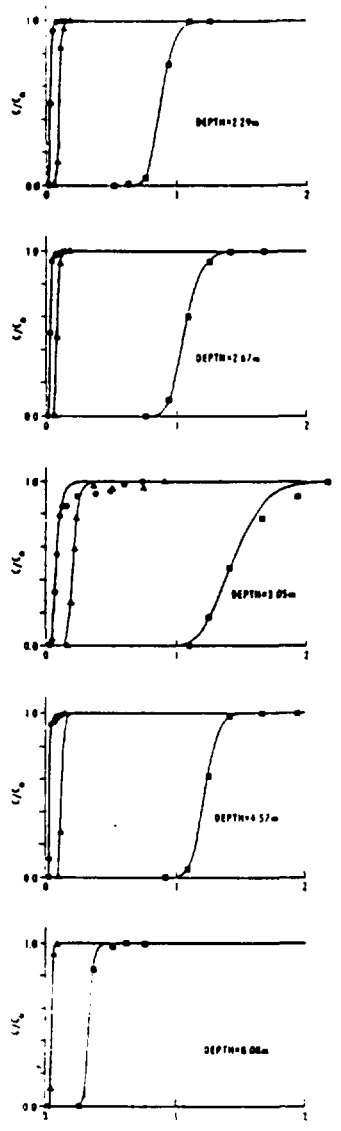

Fig. 7. Comparison of measured ^{131}I breakthrough curves at distances of 0.36 m (solid circles), 0.66 m (solid triangles), and 2.06 m (solid squares) with the Gelhar and Collins analytical solution (solid lines). Parameter values are listed in Table 4.

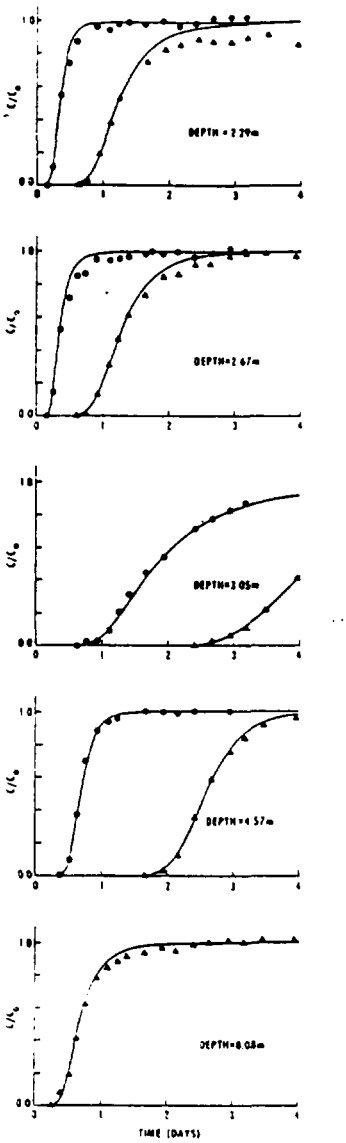

Fig. 8. Comparison of measured ^{85}Sr breakthrough curves at distances of 0.36 m (solid circles) and 0.66 m (solid triangles) with the Gelhar and Collins analytical solution (solid lines). Parameter values are listed in Table 4.

Figure 81. Illustrations from Pickens et al., 1981

Table 18. Dispersivity values, from Pickens et al., 1981

TABLE 4. Parameter Values Obtained From Analysis of ^{131}I and ^{85}Sr Breakthrough Curves

Radial Distance, m	^{131}I			^{85}Sr			
	$\bar{t}$, days	Q/b, m^2/day	α, cm	$\bar{t}$, days	Q/b, m^2/day	α, cm	K_d, ml/g
			2.29-m Depth				
0.36	0.028	5.53	0.7	0.35	0.442	1.4	2.6
0.66	0.094	5.53	0.7	1.23	0.423	2.6	2.7
2.06	0.88	5.74	0.7	...	...	...	...
			2.67-m Depth				
0.36	0.028	5.53	0.7	0.35	0.442	1.6	2.6
0.66	0.085	6.12	0.7	1.29	0.403	2.2	3.2
2.06	1.06	4.78	0.7	...	...	...	...
			3.05-m Depth				
0.36	0.087	1.78	1.5	1.84	0.084	3.0	4.5
0.66	0.213	2.44	0.7	4.20*	0.124	1.5	4.2
2.06	1.43	3.54	1.5	...	...	...	...
			4.57-m Depth				
0.36	0.038	4.07	0.4	0.68	0.228	0.7	3.8
0.66	0.132	3.94	0.4	2.57	0.202	0.7	4.1
2.06	1.22	4.15	0.4	...	...	...	...
			8.08-m Depth				
0.66	0.053	9.81	0.7	0.68	0.765	3.3	2.6
2.06	0.34	14.90	0.7	...	...	...	...

*Extrapolated.

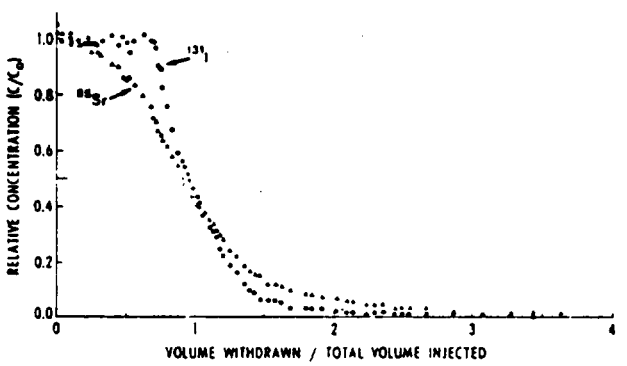

Fig. 9. Breakthrough curves for ^{131}I (solid circles) and ^{85}Sr (open triangles) for the middle sand aquifer well during the withdrawal phase.

Figure 82. Illustration from Pickens et al., 1981

Table 19. Strontium distribution coefficients, from Pickens et al.,1981

TABLE 5. K_d^{Sr} Values Obtained From Analysis of Sediment Cores

Average Depth, m	Core 1 Radioactivity, dpm/g	Core 1 Radioactivity, dpm/ml	Core 1 K_d^{Sr} ml/g	Core 2 Radioactivity, dpm/g	Core 2 Radioactivity, dpm/ml	Core 2 K_d^{Sr}, ml/g
2.24	3046	530	5.8	3557	727	4.9
2.30	3281	691	4.8	3187	739	4.3
2.36	3564	740	4.8	3072	662	4.6
2.42	3885	703	5.5	3175	727	4.4
2.48	3429	715	4.8	3110	688	4.5
2.54	4193	666	6.3	3086	497	6.2
2.60	3238	713	4.5	3905	559	7.0
2.66	3081	713	4.3	3224	632	5.1
2.72	3383	737	4.6	3030	669	4.5
2.78	3190	725	4.4	3333	693	4.8
2.84	3600	713	5.0	3066	705	4.3
2.90	4422	725	6.1	3358	645	5.2
2.96	3892	602	6.5	3863	703	5.5
3.02	949	220	4.3	2456	536	4.6
3.08	5028	719	7.0	281	24	11.7
3.14	5571	719	7.7	5259	536	9.8
3.20	5710	776	7.4	5260	815	6.5
3.26	5085	695	7.3	5427	871	6.2

Mean of 36 core K_d^{Sr} is 5.7 ml/g; standard deviation is 1.6 ml/g.

Table 20. Batch distribution coefficients, from Pickens et al., 1981

TABLE 8. K_d^{Sr} Values Obtained From Batch Experiments

Average Depth, m	First Sample C_f, dpm/ml	First Sample K_d^{Sr}, ml/g	Second Sample C_f, dpm/ml	Second Sample K_d^{Sr}, ml/g	Average K_d^{Sr}, ml/g
2.30	998	3.1	1032	2.9	3.0
2.66	1044	2.8	...	...	2.8
3.02	517	10.7	515	10.8	10.7
3.08	826	4.8	830	4.8	4.8

C_i is the initial concentration in solution, equal to 1623 dpm/ml. C_f is the final concentration in solution. Three center dots indicate that there was insufficient sediment for a duplicate analysis.

Table 21. Comparison of Kd values, from Pickens et al., 1981

TABLE 9. Comparison of K_d^{Sr} Values Obtained From Field Breakthrough Curves, Sediment Cores, and Batch Experiments

Average Depth, m	K_d^{Sr} Value, ml/g: Breakthrough Curves r_{SP} = 0.36 m	Breakthrough Curves r_{SP} = 0.66 m	Sediment Cores Core 1	Sediment Cores Core 2	Batch*
2.30	2.6	2.7	4.8	4.3	3.0
2.66	2.6	3.2	4.3	5.1	2.8
3.05	4.5	4.2	5.7	7.9	7.8

Here r_{SP} is the radial distance to the sampling points.
*Sediments used are from core 1.

In order to estimate the increase in macrodispersivity due to a correlation between K_d and ln K, values of ln K and K_d were used from reported results by Sudicky, et al. (1985) and Starr, et al. (1985). These articles report results of laboratory sand box experiments, although the natural sediments used in these experiments may not represent the conditions at the Chalk River site, both the grain size (sand and silt) and ^{85}Sr K_d values are similar to these parameters reported for the Chalk River test site. As shown in table 22, the slope of the K_d, ln K relationship is negative, as is postulated in Appendix D.

A comparison between the ratio of reactive solute dispersivity to nonreactive solute dispersivity, for the tracer experiment and the calculated ratio based on the measured b_2 value is shown in table 23. The two sets of ratios match closely, particularly as many of the parameters must be estimated from limited data. The most important conclusion that can be reached is that there is a significant increase in the reactive solute macrodispersivity relative to nonreactive solute dispersivity and that the theoretical development presented in this paper offers an explanation of this behavior. Although several criticisms can be leveled on this use of the experiment data, particularly for the short travel distance and nonuniform radial flow field, there is a good indication that the general effect (that an exaggerated velocity variations due to K_d, ln K correlation) is present. Therefore, this analysis should be tested on a field test in which the assumptions used in this analysis (uniform steady flow over long travel distances) are applicable.

Table 22

Value of b_2 for ^{85}Sr

material	K Sudicky et al., 1985	Kd (batch experiments) Starr, et al., 1985
sand	2.3×10^{-4} m/s	1.65 mL/g
silt	6.0×10^{-8} m/s	12.5 mL/g

$$b_2 = \frac{\Delta Kd}{\Delta \ln K} = \frac{-10.0}{3.3} = -1.3$$

Table 23

Ratio of Reactive to Nonreactive Dispersivity for Radial Test

depth (m)	distance (m) Calculated*		Kd	Field
			α_{Sr}/α_I	A_{Sr}/A_I
2.29	.36	2.6	2.0	2.7
	.66	2.7	3.7	2.7
2.67	.36	2.6	2.3	2.7
	.66	3.2	3.1	2.4
3.05	.36	4.5	2.0	1.9
	.66	4.2	2.1	2.0
4.57	.36	3.8	1.8	2.1
	.66	4.1	1.8	2.0
8.08	.66	2.6	4.7	2.7
	Average		2.6	2.4

* $A_{Sr}/A_I = \left(1 - \frac{\gamma b_2}{R_n}\right)^2$

2. Cape Cod Tracer Test

The application of the theoretical results to the longitudinal dispersivity observed for lithium during the large-scale tracer test is difficult because: I) It is not certain that equilibrium (i.e., instantaneous) linear adsorption is occurring for lithium, even for the later part of the test. 2) It is not clear that a Fickian limit (i.e. a constant dispersivity) has been reached for dispersion of the reactive solute. The Fickian limit should be reached after a travel distance of 10 to 100 dispersivity lengths (Gelhar et al., 1979) which in this case would mean a minimum travel distance of about 350 feet. The center of mass of lithium has only traveled about 250 feet during the test. Therefore there may be early-time effects on the lithium distribution which can not be explained by the asymptotic results presented in this report. 3) It has not been established that there is a correlation between hydraulic conductivity and adsorption at the tracer test site for lithium.

With the above difficulties and limitations in mind, a ratio of reactive to nonreactive solute dispersivities can be estimated for the large-scale test. Using the same approach as for the Chalk River tracer test,

$$\frac{A_{11}^{L_i}}{A_{11}^{B_r}} = \left(1 - \frac{\gamma(b_1+b_2)}{R_h}\right)^2$$

is the ratio of reactive to nonreactive solute dispersivities. As shown in table 24, the result of this calculation (using Appendix D for the lnk-K_d correlation) is a ratio of reactive to nonreactive

Table 24

Ratio of Reactive to Nonreactive Solute Macrodispersivity

$$\frac{A_{11}^{Li}}{A_{11}^{Br}} = \left(1 - \frac{\gamma (b_1 + b_2)}{\bar{R}_n} \right)^2$$

where $b_1 = 0$, (no porosity variations)

$$b_2 = \rho \frac{d(K_d)}{d(\ln k)} = -\rho \frac{K_d}{2}, \text{ from Appendix D}$$

$$\gamma = \frac{\exp\left(\sigma_f^2 \left(\frac{1}{2} - g_{33} \right) \right)}{\sin^2\theta + \beta \cos^2\theta}, \text{ (eq. 67, Gelhar and Axness, 1983)}$$

$$\bar{R}_n = n + \rho K_d.$$

If the following parameters are assumed:

K_d = 2.0 ml/g

ρ = 1.7 g/cm3

n = 0.39

σ_f^2 ≅ 1.1

Table 24 Continued

then the ratio $\frac{A_{11}^{Li}}{A_{11}^{Br}}$ is 2.2. If $\rho K_d \ll n$, then

$$\frac{A_{11}^{Li}}{A_{11}^{Br}} \cong \left(1 + \frac{\gamma p K_d}{2n}\right)^2$$

If $\rho K_d \gg n$, then, $\frac{A_{11}^{Li}}{A_{11}^{Br}} \cong \left(1 + \frac{\gamma}{2}\right)^2$ and if γ range is 1 – 4, then the last relation gives a range of $\frac{A_{11}^{Li}}{A_{11}^{Br}}$ from 2 to 9.

solute dispersivities of about 2.2. This value is much lower than the observed ratio of about 10. The reasons for the difference could be: 1) The observed spreading is due to a combination of both chemical (i.e. nonlinear adsorption and kinetic reaction) effects and that from a spatial variation of geochemical properties in the aquifer. 2) The relation between lnk and K_d may be quite different than that inferred using the results shown in Appendix D. If the value of b_2 is more negative, the ratio will be increased. 3) There could be a contribution to the reactive solute macrodispesivity from the porosity and distribution coefficient variability which was not included in the above calculation (see equation 124).

The results of this analysis indicate that part of the enhanced longitudinal spreading of the lithium cloud may be due to the correlation of hydraulic conductivity and adsorption in the aquifer. It should also be noted that the stochastic analysis correctly predicted that the reactive solute transverse dispersivities would be similar to those for the nonreactive solute. Although these results were not definitive, there were encouraging signs that spatial variability of geochemical properties can induce enhanced spreading of reactive solutes and further work on this mechanism is warranted.

V. Summary and Conclusions

A large-scale tracer test was conducted in a sand and gravel aquifer on Cape Cod, Massachusetts by injecting a known mass of four tracers (4,900 g of bromide, 380 g of fluoride, 595 g of lithium, and 610 g of molybdenum as molybdate), and then monitoring the movement of the tracers with a three-dimensional sampling network. Sixteen views of the spatial distribution of bromide, from July 1985 to December 1986, were analyzed by calculating the zeroth (total mass), first (mean position), and second (variance) moments. The second moment analysis was particularly important as it was shown that the dispersivity is equal to one half the change in variance with travel distance if the fluid velocity is constant.

Calculated total mass of bromide for each sampling date varied between 86 and105 percent of the total injected mass. The differences between the calculated total mass and the injected mass are likely due to errors made estimating porosity, analyzing bromide, and interpolating the data. The lack of any trend in the calculated mass with travel distance confirms conservative transport of the bromide ion.

The horizontal displacement of the center of mass for bromide followed a nearly constant velocity of 0.43 m/d (meters per day). The center of mass moved rapidly downward during the first 200 days. This pattern of vertical movement indicates that vertical flow of the solute cloud depends on density contrasts early in the test before the solute cloud has mixed with native ground water.

A nonlinear trend in bromide longitudinal variance with travel distance was observed during the first 40 m (meters) of distance

traveled, indicating a non-Fickian dispersion process in the early part of the test. However, the change in longitudinal variance with travel distance followed a linear trend after the solute cloud had traveled 40 m and it is clear that a Fickian limit was reached. The longitudinal dispersivity, given by one-half the slope of the least squares regression line, is about 0.96 m. The strong correlation (0.99) indicates that the change in variance with travel distance is linear, and thus dispersion is Fickian. Some scatter is observed around the linear trend at later times. This scatter appears to be due to errors in the chemical analyses at low concentrations, primarily in the leading and trailing edges of the cloud, which can significantly affect the second moment calculations. The change in transverse horizontal and vertical variance with travel distance shows a significant scatter around linear trends. This scatter is probably due to sampling density relative to the size of the solute cloud. Transverse horizontal dispersivity is about 1.8 cm (centimeters) and transverse vertical dispersivity is about 0.15 cm.

Major conclusions from the bromide moments analysis for the Cape Cod tracer test are: (1) longitudinal mixing was the dominant dispersion process, reaching a Fickian limit after 40 m; (2) transverse horizontal and vertical dispersion were relatively small; and (3) the horizontal displacement of the solute cloud was accurately predicted using estimates of hydraulic conductivity, porosity, and measured hydraulic gradient. A comparison of results from tracer tests at a site in Ontario, Canada (Freyberg, 1986; Mackay and others, 1986) and the Cape Cod site shows uniform velocity of the nonreactive solute, similar values of longitudinal

dispersivity (0.43 m for the Canadian site, 0.96 m for Cape Cod), and small values of transverse dispersivity. Differences between the two tests include: 1) a much higher flow rate (about four times greater) for the Cape Cod tracer test, 2) a longer travel distance (over 2 times greater) for the Cape Cod tracer test, 3) a distinct Fickian limit reached by the longitudinal dispersivity value during the Cape Cod tracer test, and 4) transverse vertical dispersivity values reported by the Cape Cod tracer test. Results of both tests show that, although nonreactive solute concentrations are highly variable and difficult to predict on a small scale, the average characteristics (i.e., moments) can be predicted.

The distribution and movement of the reactive solute, lithium, was strongly affected by adsorption to the aquifer sediments. The mass of lithium in solution showed a large decrease during the first 300 days of transport until about 10 percent of the injected mass remained in solution. Between 300 to 500 days the mass remained relatively constant and then showed a small decrease from 500 to 640 days. The velocity of the lithium in solution showed a similar pattern, starting at about the same rate as bromide (1.4 ft/day) and then decreasing with time. Between 200 and 300 days the lithium in solution attained a relatively constant velocity of 0.17 ft/day. Both the slow change in mass with time and relatively constant velocity indicate that the adsorption reaction may be closer to linear. Although the laboratory adsorption isotherm is nonlinear, at low concentrations the second derivative may be small and the first derivative relatively constant, giving a quasi-linear nature to the reaction. The distribution coefficient was estimated to be about 2.0

mL/g for the later part of the test, based on the observed ratio of the total mass to the mass in solution.

The change in longitudinal variance with travel distance for lithium in solution showed distinct differences in comparison to that for bromide. The change in longitudinal variance for bromide showed a very linear trend with a slope of about 2 meters. The change in longitudinal variance for lithium showed a nonlinear trend, concave upward, which in the later part of the test had a slope of over 20 meters. This information would indicate that the longitudinal dispersivity for the lithium in solution is over ten times larger than that for bromide. In contrast, the values of the transverse horizontal and vertical variances did not differ greatly from those for bromide. Although there was a large scatter around the change in transverse variance with travel distance, the slopes and resultant dispersivities for the lithium transverse directions also did not appear to differ greatly from those for bromide.

The large-scale natural-gradient tracer test results clearly demonstrate the applicability of the stochastic approach (Gelhar and Axness, 1983; Dagan, 1982) to the analysis of the dispersive movement of nonreactive solutes in aquifers. Nearly every major feature of the nonreactive tracer (bromide) cloud shape and movement conformed to that predicted by the stochastic analysis of macrodispersion. Along with the successful results from the nonreactive tracer part of the test, interesting, more complex results from the reactive tracer (lithium) part of the test were obtained. Although the distribution and movement of the reactive tracer is not as fully understood as the nonreactive case, it is clear

that enhanced spreading is occuring. A stochastic analysis of the variability of geochemical properties of the aquifer may help in explaining this observation.

A theoretical analysis of reactive solute macrodispersion was presented to explain, in part, the enhanced spreading of reactive solutes relative to that for nonreactive solutes. The approach used in this analysis was to postulate correlations between hydraulic conductivity and both porosity and the distribution coefficients. Both the hydraulic and geochemical properties were assumed to have stationary means and random perturbations around the means. Using a spectral analysis method it was found that, for both isotropic and anisotropic porous media, the longitudinal dispersivity can be significantly affected by the correlation of K to K_d. In the case of increasing adsorption with decreasing grain size and resultant decreasing K, there would be a negative correlation between K and K_d. This negative correlation produces an increased dispersivity for reactive solutes. It was also found that the effective retardation coefficient is the arithmetic mean.

The results of the stochastic analysis of reactive solute macrodispersion can be cautiously applied to the observed lithium distribution in the large-scale test. Although the theoretical analysis provides an explanation of the enhanced longitudinal mixing for lithium, the same enhanced spreading may be due to a kinetically controlled reaction. An obvious need is for further work on defining the applicable chemical reaction in the aquifer. An extended stochastic analysis to include early-time effects could also help explain the asymmetry of the lithium distribution. The observed

enhanced spreading for a reactive solute is an important aspect of the tracer test as it indicates both a rapid dilution of the reactive solute and a potentially rapid movement of the leading edge of the solute front. Therefore the first arrival of a reactive solute might be much sooner than would have been predicted using average retarded velocities when the enhanced spreading occurs. This early arrival time of reactive solutes has serious implications for the transport of highly toxic chemicals in aquifers.

References

Anderson, M.P., 1979, Using models to simulate the movement of contaminants through groundwater flow systems, CRC Crit. Rev. Environ. Control, 9, 97-156.

Aris, R., 1956, On the dispersion of a solute in a fluid flowing through a tube, Proc. R. Soc. London, Ser. A, 235, 67-78.

Bakr, A.A., L.W. Gelhar, A.L. Gutjahr, and J.R. MacMillan, 1978, Stochastic analysis of spatial variability in subsurface flows, 1, Comparison of one- and three-dimensional flows, Water Resour. Res., 14(2), 263-271.

Bear, J., 1972, Dynamics of Fluids in Porous Media, American Elsiever, New York.

Bear, J., 1979, Hydraulics of Groundwater, McGraw-Hill, New York.

Cherry, J.A., R.W. Gillham, J.F. Barker, 1984, Contaminants in groundwater: Chemical processes, in Groundwater Contamination, National Research Council, National Academy Press.

Dagan, G., 1982, Stochastic modeling of groundwater flow by unconditional and conditional probabilities, 2, The solute transport, Water Resour. Res., 18(4), 835-848.

Dagan, G., 1984, Solute transport in heterogeneous porous formations, J. Fluid Mech., 145, 151-177.

Freeze, R.A., 1975, A stochastic-conceptual analysis of one-dimensional groundwater flow in nonuniform homogeneous media, Water Resour. Res., 11(5), 725-741.

Freeze, R.A., and J.A. Cherry, 1979, Groundwater, Prentice-Hall, Inc., Englewood Cliffs, New Jersey.

Freyberg, D.L., 1986, A natural gradient experiment on solute transport in sand aquifer, 2, spatial moments and the advection and dispersion of non reactive tracers, Water Resour. Res., 22(13), 2031-2046.

Gelhar, L.W., A.L. Gutjahr, and R.L. Naff, 1979, Stochastic analysis of macrodispersion in a stratified aquifer, Water Resour. Res., 15(6), 1387-1397.

Gelhar, L.W. and C.L. Axness, 1981, Stochastic analysis of macrodispersion in three-dimensionally heterogeneous aquifers, Rep. H-8, 140 pp., Hydrol. Res. Program, N.M. Inst. of Mining and Technol., Socorro.

Gelhar, L.W., 1982, Analysis of two-well tracer tests with a pulse input, Department of Energy, RHO-BW-CR-131 P.

Gelhar, L.W., and C.L. Axness, 1983, Three-dimensional stochastic analysis of macrodispersion in aquifers, Water Resour. Res., 19(1), 161-180.

Gelhar, L.W., A. Mantoglou, C.Welty, and K.R. Rehfeldt, 1985, A review of field-scale physical solute transport processes in saturated and unsaturated porous media, Final Proj. Rep. EPRI EA-4190, Elec. Power Res. Inst., Palo Alto, CA.

Guswa, J.H., and D.R. LeBlanc, 1985, Digital models of ground-water flow in the Cape Cod aquifer system, Massachusetts, U.S. Geological Survey Water-Supply Paper 2209.

Hubbert, M.K., 1953, Entrapment of petroleum under hydrodynamic conditions, Bul. Am. Assoc. Pet. Geologists, 37(8), 1954-2026.

James, R.V., and J. Rubin, 1978, Applicability of the local equilibrium assumption to transport through soils of solutes affected by ion exchange, in Proceedings 176th American Chemical Society National Meeting, 225-235.

Konikow, L.F., and Bredehoeft, J.D., 1978, Computer model of two-dimensional solute transport and dispersion in ground water: U.S. Geological Survey Techniques of Water-Resources Investigations, book 7, Chap. C2, 90 p.

LeBlanc, D.R., 1982, Sewage plume in a sand and gravel aquifer, Cape Cod, Massachusetts: U.S. Geological Survey Open-File Report 82-274, 35 p.

LeBlanc, D.R., 1984a, Sewage plume in a sand and gravel aquifer, Cape Cod, Massachusetts: U.S. Geological Survey Water-Supply Paper 2218, 28 p.

LeBlanc, D.R., 1984b, Digital modeling of solute transport in a plume of sewage-contaminated ground water: U.S. Geological Survey Open-File Report 84-475, 11-43.

LeBlanc, D.R., Garabedian, S.P., Quadri, R.D., Morin, R.H., Teasdale, W.E., and Paillert, F.L., 1985, Hydrogeologic controls on solute transport in a plume of sewage-contaminated ground water, Cape Cod, Massachusetts, in U.S. Geological Survey Open-File Report 86-481, Ragone, S.P., ed.

LeBlanc, D.R., Garabedian, S.P., Wood, W.W., Hess, K.M. and Quadri, R.D., 1987, Natural-gradient tracer test in sand and gravel: Objective, approach, and overview of tracer movement in U.S. Geological Survey Open-File Report 87-109, B9-12.

Mackay, D.M., D.L. Freyberg, P.V. Roberts, and J.A. Cherry, 1986, A natural gradient experiment on solute transport in a sand aquifer, 1, Approach and overview of plume movement, Water Resour. Res., 22(13), 2017-2029.

Matheron, G., and G. deMarsily, 1980, Is transport in porous media always diffusive? A counterexample, Water Resour. Res., 16(5), 901-917.

McDonald, M.G., and A.W. Harbaugh, 1984, A modular three-dimensional finite-difference ground-water flow model, U.S. Geological Survey Open-File Report 83-875.

Morris, D.A., and Johnson, A.J., 1967, Summary of hydrologic and physical properties of rock and soil materials as analyzed by the Hydrologic Laboratory of the U.S. Geological Survey, 1948-60; U.S. Geological Survey Water-Supply paper 1839-D, 42 p.

Naff, R.L., 1978, A continuum approach to the study and determination of field longitudinal dispersion coefficients, Ph.D. dissertation, N.M. Inst. of Mining and Technol., Socorro.

Neuman, S.P., 1972, Theory of flow in unconfined aquifers considering delayed response of the water table, Water Resour. Res. 8 1031-1045.

Neuman, S.P., 1973, Supplementary comments on theory of flow in unconfined aquifers considering delayed response of the water table, Water Resour. Res. 9, 1102-1103.

Neuman, S.P., 1974, Effect of partial penetration on flow in unconfined aquifers considering delayed gravity response, Water Resour. Res. 10, 303-312.

Neuman, S.P., 1975, Analysis of pumping test data from anisotropic unconfined aquifers considering delayed gravity response, Water Resour. Res 11(2), 329-342.

Oldale, R.N., 1969, Seismic investigations on Cape Cod, Martha's Vineyard and Nantucket, Massachusetts, and a topographic map of the basement surface from Cape Cod Bay to the Islands: U.S. Geological Survey Professional Paper 650-B, p. B122-B127.

Orion Research, 1982, Halide electrode instruction manual, Orion Research, Cambridge, Massachusetts.

Perlmutter, N.M., and Lieber, M., 1970, Dispersal of Plating wastes and sewage contaminants in ground water and surface water. South Farmingdale-Massapequa area, Nassau County, New York: U.S. Geological Survey Water Supply Paper 1879-G 67 p.

Pickens, J.F., and G.E. Grisak, 1981, Scale-dependent dispersion in a stratified granular aquifer, Water Resour. Res., 17(4), 1191-1211.

Pickens, J.F., and R.E. Jackson, and K.J. Inch, 1981, Measurement of distribution coefficients using a radial injection dual-tracer test, Water Resour. Res. 17(3), 529-544.

Roberts, P.V., M.N. Goltz, and D.M. Mackay, 1986, A natural gradient experiment on solute transport in a sand aquifer, 3, Retardation estimates balances for organic solutes, Water Resour. Res., 22(13), 2047-2058.

Sampson, R.J., 1978, SURFACE II graphics systems, revision one, 240 pp., Kans. Geol. Surv., Lawrence.

Schwartz, F.W., 1977, Macroscopic disperison in porous media: The controlling factors, Water Resour. Res., 13(4), 743-752.

Smith, L., and F.W. Schwartz, 1980, Mass transport, 1, A stochastic analysis of macroscopic dispersion, Water Resour. Res., 16(2), 303-313.

Standard Methods for the examination of water and waste water, 1980, 15th edition, American Public Health Assoc.

Starr, R.C., R.W. Gillham, and E.A. Sudicky, 1985, Experimental investigation of solute transport in stratified porous media, 2, The reactive case, Water Resour. Res. 21(7), 1043-1050.

Stollenwerk, K.G., and D.B. Grove, 1987, Natural-gradient tracer test in sand and gravel: nonconservative transport of molybdenum, U.S. Geological Survey, Open-File Report 87-109, B17-B22.

Sudicky, E.A., and J.A. Cherry, 1979, Field observations of tracer dispersion under natural flow conditions in an unconfined sandy aquifer, Water Pollut. Res. Can., 14, 1-17.

Sudicky, E.A., R.W. Gillham, and E.O. Frind, 1985, Experimental investigation of solute transport in stratified porous media, 1, The nonreactive case, Water Resour. Res. 21(7), 1035-1041.

Sudicky, E.A., 1986, A natural gradient experiment on solute transport in a sand aquifer: Spatial variability of hydraulic conductivity and its role in the dispersion process, Water Resour. Res., 22(13), 2069-2082.

Taylor, G.I., 1953, The dispersion of matter in solvent flowing slowly through a tube, Proc. R. Soc. London Ser. A., 219, 189-203.

Thurman, E.M., Barber, L.B., II, Ceazan, M.L., Smith, R.L. Brooks, M.G., Schroeder, M.P., Keck, R.J., Driscoll, A.J., LeBlanc, D.R., and Nichols, W.J., Jr., 1984, Sewage contaminants in ground water: U.S. Geological Survey Open File Report, 84-475, LeBlanc, D.R. ed.

Van Genuchten, M.T., J.M. Davidson, and P.J. Wierenga, 1974, An evaluation of kinetic and equilibrium equations for the prediction of pesticide movement through porous media, Soil Sci. Soc. Amer. Proc., 38, 29-35.

Van Genuchten, M.T., and P.J. Wierenga, 1977a, Mass transfer studies in sorbing porous media: II. Experimental evaluation with Trithium, Soil Sci., Soc. Am. J., 41, 272-277.

Van Genuchten, M.T., P.J. Wierenga, and G.A. O'Connor, 1977b, Mass transfer studies in sorbing porous media: III. Experimental evaluation with 2, 4, 5-T, Soil Sci. Soc. Am. J., 41, 278-285.

Appendix A

Moments Program Description and Listing

The generalized logic flow for the moments program is as follows:

A. Input
   1. Read in the number of samples, the number of triangular subdomains, and the porosity.
   2. For each sampler, read in the concentration, x, y, and z position, and a flag for the type of analysis method.
   3. Make background corrections to the concentration data using subroutine BCT.
   4. Read in the index list for triangles.

B. Integrate over the vertical for the zeroth and first moments.
   1. Call Subroutine ZINT for vertical integration of concentration (CI).
   2. Call ZINT for integration of concentration times Z (CZ) for average vertical position.

C. For each triangle integrate over the horizontal.
   1. Calculate the area of the triangle.
   2. Call Subroutine XYINT for horizontal integration of vertically integrated concentration (CI) for total mass.
   3. Call XYINT for horizontal integration of CI for average x and y positions
   4. Call XYINT for horizontal integration of CZ for average Z position.

5. Sum moments of each triangle to obtain the domain totals, resulting in total mass (M_T), $\bar{x}$, $\bar{y}$, and $\bar{z}$.
6. Output the results.

D. Integrate over the vertical for the second moments
1. Call ZINT for integration of concentration times $(Z-Z)^2$, (CCZ), for σ^2_{zz}.

E. For each triangle integrate over the horizontal.
1. Call XYINT for horizontal integration of CI for

$$\sigma^2_{xx}, \sigma^2_{xy}, \sigma^2_{yy}, \sigma^3_{xxx}, \sigma^3_{yyy}, \sigma^4_{xxxx}, \sigma^4_{yyyy}.$$

2. Call XYINT for horizontal integration of CZ for σ^2_{xz}, σ^2_{yz}.
3. Call XYINT for horizontal integration of CCZ for σ^2_{zz}.
4. Sum moments of each triangle to obtain the domain totals.
5. Output results.

F. Calculate the principal components of the variance tensor using subroutine EIGBS and output results.

G. Subroutines
1. Subroutine ZINT is a direct implementation of equations (43) and (44).
2. Subroutine XYINT uses a repeated application of equation (51) to solve (50). The power to which each basic function (ϕ_i) is raised is calculated, along with the corresponding coefficients. The integral (eq.

50) then is the sum of 3^{i+j+1} components of the sub-integral)eq. 51).

3. Subroutine REIGBS calls IMSL subroutine EIGBS to calculate the eigenvalues and eigenvectors of the solute variance tensor.
4. Subroutine BCT reads in the background concentrations to be subtracted from the input concentrations. The background values are allowed to vary by depth and by range of concentration. The differing corrections by depth and range are due to a spatial variation of interfering ions. Each sample concentration is checked for depth and concentration range and an appropriate correction value is subtracted.

```
C APPENDIX A: PROGRAM FOR GENERATING VALUES OF CONCENTRATION MOMENTS
```

```
C APPENDIX A: PROGRAM FOR GENERATING VALUES OF CONCENTRATION MOMENTS
C     UNITS: X,Y,Z IN FEET. CONCENTRATION IN MG/L
C     MINIMUM VALUES: C) .001 MG/L.  Z) -50.0 FT
C     Z MUST BE IN DECREASING ORDER FOR EACH SAMPLER
C     SAMPLERS MUST BE TRIANGULATED FOR X-Y INTEGRATION
      DIMENSION CI(200),CZ(200),CC(200,17),X(200),Y(200),Z(200,17),
     1XX(3),YY(3),C(3),ZZ(17),CCZ(17),FL(12),IT(300,3)
     2,CZ2(200),TX(3),TY(3),TZ(3),A(3,3)
      REAL*8 TOTM,TOTX,TOTY,TOTZ,TX,TY,TZ,TXY,TXZ,TYZ,CZ2,AVX,AVY,AVZ
      REAL*8 A,CI,CZ,CC,X,Y,Z,FL,XX,YY,C,ZZ,CCZ,TOT,TOTI,SUM,AR
C     INITIALIZE ARRAYS
      DO 10 I=1,200
      CI(I)=0.0
      CZ(I)=0.0
      CZ2(I)=0.0
      X(I)=0.0
      Y(I)=0.0
      DO 10 J=1,17
      CC(I,J)=0.0
   10 Z(I,J)=-100.0
      FL(1)=1.0
      DO 11 I=2,12
   11 FL(I)=FL(I-1)*I
C     READ DATA
      IFL=0
      READ(5,900)NS,NT,PR
      WRITE(6,1000)NS,NT,PR
      CALL BCT(CT,ZT,BC,IFL)
      NXY=0
      XL=0.0
      YL=0.0
      ICCW=0
      DO 100 N=1,NS
      READ(5,911)CT,XT,YT,ZT,ICCK
      IF(XT.EQ.XL.AND.YT.EQ.YL.AND.N.GT.1)GO TO 110
      IS=0
      NXY=NXY+1
      X(NXY)=XT
      Y(NXY)=YT
      XL=X(NXY)
      YL=Y(NXY)
  110 IS=IS+1
```

```
C APPENDIX A: PROGRAM FOR GENERATING VALUES OF CONCENTRATION MOMENTS


      Z(NXY,IS)=ZT
      IF(ICCK.LE.0.AND.IFL.GT.0)GO TO 114
      CC(NXY,IS)=CT
      GO TO 99
  114 CALL BCT(CT,ZT,BC,IFL)
      CC(NXY,IS)=CT-BC
   99 IF(CC(NXY,IS).LT.0.0)CC(NXY,IS)=0.0
      IF (CC(NXY,IS).GT.0.0)ICQW=ICQW+1
  100 WRITE(6,910)CC(NXY,IS),X(NXY),Y(NXY),Z(NXY,IS),CT,BC,ICCK
      WRITE(6,2000)ICQW
      DO 120 N=1,NT
      READ(5,920)IT(N,1),IT(N,2),IT(N,3)
  120 WRITE(6,920)IT(N,1),IT(N,2),IT(N,3)
C     CALCULATE C INTEGRATION OVER Z
      DO 130 N=1,NXY
      DO 140 I=1,17
      CCZ(I)=CC(N,I)
  140 ZZ(I)=Z(N,I)
      ZB=0.0
      K=0
      CALL ZINT(CCZ,ZZ,ZB,K,SUM)
C     WRITE(6,930)SUM
      CI(N)=SUM
      ZB=0.0
      K=1
      CALL ZINT(CCZ,ZZ,ZB,K,SUM)
C     WRITE(6,930)SUM
      CZ(N)=SUM
      WRITE(6,940)N,CI(N),CZ(N)
  130 CONTINUE
C     CALCULATE INTEGRATION OVER XY PLANE
      TOT=0.0
      TOTZ=0.0
      TOTX=0.0
      TOTY=0.0
      DO 150 N=1,NT
      DO 160 I=1,3
      XX(I)=X(IT(N,I))
      YY(I)=Y(IT(N,I))
  160 C(I)=CI(IT(N,I))
C     CALCULATE MASS INTEGRATION
      II=0
```

```
C APPENDIX A: PROGRAM FOR GENERATING VALUES OF CONCENTRATION MOMENTS


      JJ=0
      AR=.5*((XX(2)*YY(3)-YY(2)*XX(3))-XX(1)*(YY(3)-YY(2))+YY(1)*
     1(XX(3)-XX(2)))
      CALL XYINT(XX,YY,C,II,JJ,AR,FL,SUM)
C     WRITE(6,940)N,SUM
      TOT=TOT+SUM
C     CALCULATE FIRST MOMENT VALUES (AVERAGE POSITION)
      II=1
      JJ=0
      CALL XYINT(XX,YY,C,II,JJ,AR,FL,SUM)
      TOTX=TOTX+SUM
      II=0
      JJ=1
      CALL XYINT(XX,YY,C,II,JJ,AR,FL,SUM)
      TOTY=TOTY+SUM
      DO 170 I=1,3
  170 C(I)=CZ(IT(N,I))
      II=0
      JJ=0
      CALL XYINT(XX,YY,C,II,JJ,AR,FL,SUM)
      TOTZ=TOTZ+SUM
      WRITE(6,940)N,AR,TOT,TOTX,TOTY,TOTZ
  150 CONTINUE
      AVX=TOTX/TOT
      AVY=TOTY/TOT
      AVZ=TOTZ/TOT
      WRITE(6,931)
      TOTM=TOT*PR/35.3147
      WRITE(6,930)TOT,TOTM,AVX,AVY,AVZ
C     CALCULATE SECOND MOMENT INTEGRATION OVER Z
      DO 180 N=1,NXY
      DO 181 I=1,17
      CCZ(I)=CC(N,I)
  181 ZZ(I)=Z(N,I)
      K=2
      CALL ZINT(CCZ,ZZ,AVZ,K,SUM)
      CZ2(N)=SUM
C     WRITE(6,940)N,SUM
  180 CONTINUE
C     CALCULATE HIGHER MOMENTS
      DO 190 I=1,3
      TX(I)=0.0
```

```
C APPENDIX A: PROGRAM FOR GENERATING VALUES OF CONCENTRATION MOMENTS


      TY(I)=0.0
  190 TZ(I)=0.0
      TXY=0.0
      TXZ=0.0
      TYZ=0.0
      DO 200 N=1,NT
      DO 210 I=1,3
      XX(I)=X(IT(N,I))-AVX
      YY(I)=Y(IT(N,I))-AVY
  210 C(I)=CI(IT(N,I))
      AR=.5*((XX(2)*YY(3)-YY(2)*XX(3))-XX(1)*(YY(3)-YY(2))
     1+YY(1)*(XX(3)-XX(2)))
      DO 220 I=2,4
      II=I
      JJ=0
      CALL XYINT(XX,YY,C,II,JJ,AR,FL,SUM)
      TX(I-1)=TX(I-1)+SUM
      II=0
      JJ=I
      CALL XYINT(XX,YY,C,II,JJ,AR,FL,SUM)
  220 TY(I-1)=TY(I-1)+SUM
      II=1
      JJ=1
      CALL XYINT(XX,YY,C,II,JJ,AR,FL,SUM)
      TXY=TXY+SUM
      DO 230 I=1,3
  230 C(I)=CZ2(IT(N,I))
      II=0
      JJ=0
      CALL XYINT(XX,YY,C,II,JJ,AR,FL,SUM)
      TZ(1)=TZ(1)+SUM
      DO 240 I=1,3
  240 C(I)=CZ(IT(N,I))
      II=1
      JJ=0
      CALL XYINT(XX,YY,C,II,JJ,AR,FL,SUM)
      TXZ=TXZ+SUM
      II=0
      JJ=1
      CALL XYINT(XX,YY,C,II,JJ,AR,FL,SUM)
      TYZ=TYZ+SUM
  200 CONTINUE
```

C APPENDIX A: PROGRAM FOR GENERATING VALUES OF CONCENTRATION MOMENTS

```
      WRITE(6,932)
      DO 250 I=1,3
      SUMX=TX(I)/TOT
      SUMY=TY(I)/TOT
      SUMZ=TZ(I)/TOT
  250 WRITE(6,940)I+1,SUMX,SUMY,SUMZ
      SUMXY=TXY/TOT
      SUMXZ=TXZ/TOT
      SUMYZ=TYZ/TOT
      WRITE(6,933)
      WRITE(6,930)SUMXY,SUMXZ,SUMYZ
      DO 300 I=1,3
      DO 300 J=1,3
  300 A(I.J)=0.0
      A(1,3)=TX(1)/TOT
      A(2,2)=TXY/TOT
      A(2,3)=TY(1)/TOT
      A(3,1)=TXZ/TOT
      A(3,2)=TYZ/TOT
      A(3,3)=TZ(1)/TOT
      CALL REIGBS(A)
      STOP
  900 FORMAT(2I5,F10.2)
 1000 FORMAT(1X,'NS, NT, PR'.2I5,F10.2)
  910 FORMAT(21X.6F8.2,I2)
  911 FORMAT(21X,4F8.2,I2)
  920 FORMAT(5X,3I5)
  930 FORMAT(10F10.2)
  931 FORMAT(1X,'TOTAL, TOTAL MASS, XBAR, YBAR, ZBAR')
  932 FORMAT(1X,'MOMENT NO., SUMX, SUMY, SUMZ')
  933 FORMAT(1X,'CROSS MOMENTS, XY, XZ, YZ')
  940 FORMAT(I5,10G12.4)
  950 FORMAT(1X,'DIAGONALIZED VARIANCE VALUES, SX,SY,SZ',3F12.4)
  960 FORMAT(1X,'THETA ANGLE VALUES, X-Y, Z-Y, Z-X',3F12.4)
 2000 FORMAT(1X,'NUMBER OF CONC ABOVE BACKGROUND',I10)
      END
      SUBROUTINE ZINT(C,Z,ZB,K,SUM)
      DIMENSION C(17),Z(17)
      REAL*8 C,Z,ZB,A,B,P1,P2,PT,Q1,Q2,QT,R1,R2,RT,SUM
      K1=K+1
      PT=0.0
      QT=0.0
```

```
C APPENDIX A: PROGRAM FOR GENERATING VALUES OF CONCENTRATION MOMENTS


      RT=0.0
      SUM=0.0
      DO 10 I=1,16
      A=0.0
      B=0.0
      P1=0.0
      P2=0.0
      Q1=0.0
      Q2=0.0
      IF(C(I).LE.1.0E-3.AND.C(I+1).LE.1.0E-3)GO TO 10
      IF(Z(I).EQ.Z(I+1)) GO TO 10
      IF(Z(I).LE.-50.0.OR.Z(I+1).LE.-50.0)GO TO 10
      A=(C(I)-C(I+1))/(Z(I)-Z(I+1))
      B=C(I)-A*Z(I)
      P1=((Z(I)-ZB)**K1)*B/K1
      P2=((Z(I+1)-ZB)**K1)*B/K1
      PT=P1-P2+PT
      Q1=((Z(I)-ZB)**K)*(Z(I)**2)*A/2
      Q2=((Z(I+1)-ZB)**K)*(Z(I+1)**2)*A/2
      QT=Q1-Q2+QT
      IF(K.LT.1)GO TO 10
      SM=1.0
      SN=2.0
      DO 20 J=2,K1
      R1=0.0
      R2=0.0
      J1=J+1
      IP=K1-J
      IS=(-1)**J1
      SS=SM*(IP+1)
      SM=SS
      SS=SN*J1
      SN=SS
      R1=(Z(I)**J1)*((Z(I)-ZB)**IP)
      R2=(Z(I+1)**J1)*((Z(I+1)-ZB)**IP)
      RT=RT+(R1-R2)*A*IS*SM/SN
   20 CONTINUE
   10 CONTINUE
      SUM=PT+QT+RT
      RETURN
      END
      SUBROUTINE XYINT(X,Y,C,II,JJ,AR,FL,SUM)
```

```
C APPENDIX A: PROGRAM FOR GENERATING VALUES OF CONCENTRATION MOMENTS


      DIMENSION X(3),Y(3),C(3),FL(12),IW(20),NP(3),IX(3),IY(3)
      REAL*8 X,Y,C,FL,AR,SI,SS,ST,SUM
C     CALCULATE NUMBER OF MULTIPLICATIONS
C     WRITE(6,900)(X(I),Y(I),C(I),I=1,3)
C     WRITE(6,910)II,JJ,AR,SUM
      IP=II+JJ+1
      IT=3**IP
      DO 20 I=1,IP
   20 IW(I)=1
      SUM=0.0
      DO 30 I=1,IT
      DO 40 J=1,3
      NP(J)=0
      IX(J)=0
   40 IY(J)=0
      DO 50 J=1,IP
      NP(IW(J))=NP(IW(J))+1
      IF(J.GT.1) GO TO 51
      IC=IW(J)
      GO TO 50
   51 II1=II+1
      IF(J.GT.II1) GO TO 52
      IX(IW(J))=IX(IW(J))+1
      GO TO 50
   52 IY(IW(J))=IY(IW(J))+1
   50 CONTINUE
C     CALCULATE INTEGRATION
      NT=2
      ST=C(IC)
      DO 60 J=1,3
      NT=NT+NP(J)
      XT=X(J)**IX(J)
      YT=Y(J)**IY(J)
      SS=ST*XT*YT
      ST=SS
   60 IF(NP(J).LE.0)NP(J)=1
      SI=2.0*AR*ST*FL(NP(1))*FL(NP(2))*FL(NP(3))/FL(NT)
      SUM=SUM+SI
C     WRITE(6,920)AR,ST,SI,I,(IW(J),J=1,IP),(NP(L),L=1,3),(IX(M),M=1,3)
C    1,(IY(N),N=1,3)
      IN=IP+1
      DO 70 J=1,IP
```

C APPENDIX A: PROGRAM FOR GENERATING VALUES OF CONCENTRATION MOMENTS

```
      IN=IN-1
      IF(J.EQ.1)GO TO 71
      IF(IW(IN+1).GT.3)GO TO 71
      GO TO 70
   71 IW(IN)=IW(IN)+1
   70 CONTINUE
      DO 80 J=1,IP
   80 IF(IW(J).GT.3)IW(J)=1
   30 CONTINUE
C     WRITE(6,900)SUM
  900 FORMAT(9G12.4)
  910 FORMAT(2I5,2G12.4)
  920 FORMAT(3G10.3,15I5)
      RETURN
      END
      SUBROUTINE REIGBS(A)
      REAL*8 A(3,3),D(3),Z(3,3),WK(100)
      N=3
      IZ=3
      IA=3
      IJOB=-3
      NC=2
      M=3
      CALL EIGBS(A,N,IA,IJOB,NC,M,D,Z,IZ,WK,IER)
      WRITE(6,110)IER
  110 FORMAT(1X,'IER',I5)
      WRITE(6,120)(D(I),I=1,3)
  120 FORMAT(1X,'EIGENVALUES',10F12.4)
      DO 20 I=1,3
   20 WRITE(6,130)(Z(I,J),J=1,3)
  130 FORMAT(1X,'Z',3G15.5)
      STOP
      END
      SUBROUTINE BCT(CT,ZT,BC,IFL)
      DIMENSION Z(6),C(6),DC(5,5)
      IF(IFL.GT.0)GO TO 50
      READ(7,100)NZ,NC
      WRITE(6,100)NZ,NC
      IF(NZ.LE.1.OR.NC.LE.1)IFL=-1
      IF(IFL.LT.0)RETURN
      NZ1=NZ-1
      NC1=NC-1
```

```
C APPENDIX A: PROGRAM FOR GENERATING VALUES OF CONCENTRATION MOMENTS


      READ(7,110)(Z(I),I=1,NZ)
      WRITE(6,110)(Z(I),I=1,NZ)
      READ(7,110)(C(I),I=1,NC)
      WRITE(6,110)(C(I),I=1,NC)
      DO 10 I=1,NZ1
      READ(7,110)(DC(I,J),J=1,NC1)
   10 WRITE(6,110)(DC(I,J),J=1,NC1)
      IFL=1
      RETURN
   50 BC=0.0
      IF(CT.LT.C(NC).OR.CT.GT.C(1))GO TO 80
      IF(ZT.LT.Z(NC).OR.ZT.GT.Z(1)) GO TO 80
      DO 60 I=1,NZ1
      I1=I+1
      IF(ZT.GT.Z(I).OR.ZT.LT.Z(I1))GO TO 60
      DO 61 J=1,NC1
      J1=J+1
      IF(CT.GT.C(J).OR.CT.LT.C(J1))GO TO 61
      BC=DC(I,J)
   61 CONTINUE
   60 CONTINUE
   80 RETURN
  100 FORMAT(2I5)
  110 FORMAT(8F10.2)
      END
```

Appendix B

Triangulation Program Description and Listing

The following program creates triangles from a set of points in a two-dimensional space. The program moves sequentially through the set of points creating triangles by relating three points and checking this trial triangle against a master list of triangles that have already been created. If the trial triangle area does not intersect the area of any on the master list, it is placed on the master list. A limit on distances between point pairs is used to prevent creating large triangles. A limit on the ratio between the triangle perimeter distance squared and the triangle area (aspect ratio) is used to prevent creating long, thin triangles. These two limits prevent undesirably large or thin triangles and allow some flexibility on the appearance of triangles.

The logic flow of the program is as follows:

Main Program

1. Point locations are read.
2. Distance limit, aspect ratio limit, and output flag are read.
3. For each point (i) do the following:
   a. Calculate the distance from the point to all other points, putting the distances in increasing order (subroutine DISRT).
   b. Starting with the nearest neighboring point each possible triangle with (i) is checked for the distance limit.

c. The trial triangle index is put into counterclockwise order (subroutine INDX).

d. The trial triangle perimeter distance and area are calculated (subroutine ARP).

e. The trial triangle aspect ratio is checked against the limit.

f. The trial triangle is compared to the triangles that are on a master list (subroutine TRCK). If the triangle area does not intersect any previously created triangles on the master list, the index of the trial triangle is placed on the master list.

4. The index of the new triangle is output to a file.

Subroutines

5. Subroutine DISRT calculates distances between points and sorts these distances in increasing order. Distances are calculated by subroutine DST.

6. Subroutine INDX puts the three points defining each triangle into counterclockwise order. The point with the smallest x value will always be first. This insures that those three points, no matter what the input order, will also have the same counterclockwise output order.

7 Subroutine ARF calculates the area and perimeter distance of a triangle.

8. Subroutine TRCK checks two triangles for area intersection. This is done by checking each triangle for line intersections. If any two lines intersect at a point midway between the line end points then the triangle

areas overlap. As a final check, the triangles are evaluated to find if one triangle is fully contained within the other. A flag is returned to indicate if the triangle areas intersect.

A comparison between manually produced triangles and those produced using the program indicate that a majority of the triangles from each method were identical. Most of the differences between the two methods are due to use of different diagonals spiltting a quadrilateral. A few additional triangles are created using the automatic method because these triangles fall within the distance and aspect ratio limits. Additional triangles may also be created with sampling points that were ignored during the manual method. The automatic method does a good job of forming an index list and was used in producing many of the index lists for the bromide moments and all of those for the lithium moments.

```
C APPENDIX B: PROGRAM FOR GENERATING TRIANGLE INDEX LIST
```

```
C APPENDIX B: PROGRAM FOR GENERATING TRIANGLE INDEX LIST
      DIMENSION X(300),Y(300),DS(300),ID(300),ITR(900,3),ITP(3)
     1,IT(20,3),XR(3),YR(3),XT(3),YT(3),XMN(900),YMN(900),XMX(900)
     2,YMX(900)
      COMMON PRC
      XL=0.0
      YL=0.0
      I=0
   10 READ(5,100,END=20)XX,YY
      IF(XX.EQ.XL.AND.YY.EQ.YL.AND.I.NE.0)GO TO 10
      I=I+1
      WRITE(6,110)I,XX,YY
      X(I)=XX
      Y(I)=YY
      XL=XX
      YL=YY
      GO TO 10
   20 NPT=I
      NPT1=NPT-1
      NT=0
      READ(7,120)DLM,PAL,PRC
      WRITE(6,120)DLM,PAL,PRC
      DO 30 I=1,NPT
      CALL DISRT(X,Y,DS,ID,I,NPT)
      DO 15 J=1,NPT
      IF(PRC.GT.0.0)WRITE(6,130)J,ID(J)
   15 IF(PRC.GT.0)WRITE(6,120)X(ID(J)),Y(ID(J)),DS(J)
      DO 31 IP2=2,NPT1
      I2=ID(IP2)
      IF(DS(IP2).GT.DLM)GO TO 31
      IP21=IP2+1
      DO 32 IP3=IP21,NPT
      I3=ID(IP3)
      IF(DS(IP3).GT.DLM)GO TO 32
      ITP(1)=I
      ITP(2)=I2
      ITP(3)=I3
      XT(1)=X(I)
      XT(2)=X(I2)
      XT(3)=X(I3)
      YT(1)=Y(I)
      YT(2)=Y(I2)
```

```
C APPENDIX B: PROGRAM FOR GENERATING TRIANGLE INDEX LIST


      YT(3)=Y(I3)
      CALL INDX(XT,YT,ITP,XMIN,YMIN,XMAX,YMAX)
      CALL ARP(XT,YT,AR,P)
      DO 90 J=1,3
   90 IF(PRC.GT.0)WRITE(6,120)XT(J),YT(J),AR,P
      IF(P.LE.0.0.OR.AR.LE.0.0)GO TO 32
      TARP=P*P/AR
      IF(TARP.GT.PAL)GO TO 32
      IF(NT.LT.1)GO TO 51
      DO 45 J=1,NT
      IW=0
      IF(XMAX.LE.XMN(J).OR.XMIN.GE.XMX(J))GO TO 45
      IF(YMAX.LE.YMN(J).OR.YMIN.GE.YMX(J))GO TO 45
      DO 46 K=1,3
      MP=ITR(J,K)
      XR(K)=X(MP)
      YR(K)=Y(MP)
   46 IF(ITP(K).EQ.ITR(J,K))IW=IW+1
      IF(IW.GE.3)GO TO 32
      CALL TRCK(XT,YT,XR,YR,IWF)
      IF(IWF.GT.0)GO TO 32
   45 CONTINUE
   51 NT=NT+1
      XMN(NT)=XMIN
      YMN(NT)=YMIN
      XMX(NT)=XMAX
      YMX(NT)=YMAX
      DO 50 J=1,3
   50 ITR(NT,J)=ITP(J)
      WRITE(6,130)NT,(ITP(J),J=1,3),AR,P,TARP
   32 CONTINUE
   31 CONTINUE
   30 CONTINUE
      STOP
  100 FORMAT(29X,2F8.2)
  110 FORMAT(I5,2F10.2)
  120 FORMAT(12F10.2)
  130 FORMAT(4I5,3G12.3)
      END
      SUBROUTINE DISRT(X,Y,DS,ID,IPT,NPT)
      DIMENSION X(300),Y(300),DS(300),ID(300)
      COMMON PRC
```

```
C APPENDIX B: PROGRAM FOR GENERATING TRIANGLE INDEX LIST


      X0=X(IPT)
      Y0=Y(IPT)
      IF(PRC.GT.0.0)WRITE(6,100)IPT,X0,Y0
      DO 10 I=1,NPT
      ID(I)=I
      CALL DST(X0,Y0,X(I),Y(I),DS(I))
      IF(PRC.GT.0.0)WRITE(6,100)I,DS(I)
   10 CONTINUE
C     SORT
      TDS=DS(1)
      DS(1)=DS(IPT)
      DS(IPT)=TDS
      ID(IPT)=1
      ID(1)=IPT
      NPT1=NPT-1
      IF(PRC.GT.0.0)WRITE(6,100)ID(1),DS(1)
      DO 20 I=2,NPT1
      DMIN=DS(I)
      I1=I+1
      ITT=I
      DO 30 J=I1,NPT
      IF(DS(J).GE.DMIN)GO TO 30
      ITT=J
      DMIN=DS(J)
   30 CONTINUE
      IL=ID(ITT)
      ID(ITT)=ID(I)
      ID(I)=IL
      TDS=DS(I)
      DS(I)=DS(ITT)
      DS(ITT)=TDS
      IF(PRC.GT.0.0)WRITE(6,100)ID(I),DS(I)
   20 CONTINUE
      RETURN
  100 FORMAT(I5,10F10.2)
      END
      SUBROUTINE ARP(X,Y,AR,P)
      DIMENSION X(3),Y(3)
      AR=.5*((X(2)*Y(3)-Y(2)*X(3))-X(1)*(Y(3)-Y(2))+Y(1)*(X(3)-X(2)))
      CALL DST(X(1),Y(1),X(2),Y(2),P1)
      CALL DST(X(1),Y(1),X(3),Y(3),P2)
      CALL DST(X(2),Y(2),X(3),Y(3),P3)
```

C APPENDIX B: PROGRAM FOR GENERATING TRIANGLE INDEX LIST

```
      P=P1+P2+P3
      RETURN
      END
      SUBROUTINE DST(X1,Y1,X2,Y2,D)
      DIFX=X1-X2
      DIFY=Y1-Y2
      XS=DIFX*DIFX
      YS=DIFY*DIFY
      SUM=XS+YS
      D=SQRT(SUM)
      RETURN
      END
      SUBROUTINE INDX(X,Y,ID,XMIN,YMIN,XMAX,YMAX)
      DIMENSION X(3),Y(3),ID(3)
      XMIN=X(1)
      YMIN=Y(1)
      XMAX=X(1)
      YMAX=Y(1)
      IXM=1
      DO 10 I=2,3
      IF(X(I).GT.XMIN)GO TO 10
      IF(Y(I).GT.YMIN.AND.X(I).EQ.XMIN)GO TO 10
      XMIN=X(I)
      YMIN=Y(I)
      IXM=I
   10 CONTINUE
      IF(IXM.EQ.1)GO TO 15
      XT=X(1)
      YT=Y(1)
      IT=ID(1)
      X(1)=X(IXM)
      Y(1)=Y(IXM)
      ID(1)=ID(IXM)
      X(IXM)=XT
      Y(IXM)=YT
      ID(IXM)=IT
   15 CONTINUE
      DX1=X(1)-X(2)
      IF(DX1.EQ.0.0)GO TO 25
      DX2=X(1)-X(3)
      IF(DX2.EQ.0.0)GO TO 20
      R1=(Y(1)-Y(2))/DX1
```

```
C APPENDIX B: PROGRAM FOR GENERATING TRIANGLE INDEX LIST


      R2=(Y(1)-Y(3))/DX2
      IF(R1.LT.R2)GO TO 20
   25 XT=X(2)
      YT=Y(2)
      IT=ID(2)
      X(2)=X(3)
      Y(2)=Y(3)
      ID(2)=ID(3)
      X(3)=XT
      Y(3)=YT
      ID(3)=IT
   20 CONTINUE
      DO 30 I=1,3
      IF(X(I).LT.XMIN)XMIN=X(I)
      IF(X(I).GT.XMAX)XMAX=X(I)
      IF(Y(I).LT.YMIN)YMIN=Y(I)
   30 IF(Y(I).GT.YMAX)YMAX=Y(I)
      RETURN
      END
      SUBROUTINE TRCK(XT,YT,XR,YR,IWF)
      DIMENSION XT(3),YT(3),XR(3),YR(3),CX(2).CY(2).X(2,4),Y(2,4)
     1,XW(3),YW(3)
      COMMON PRC
      IWF=0
      DO 10 I=1,4
      I1=I
      IF(I.EQ.4)I1=1
      X(1,I)=XT(I1)
      X(2,I)=XR(I1)
      Y(1,I)=YT(I1)
   10 Y(2,I)=YR(I1)
      DO 11 I=1,2
      CX(I)=0.0
   11 CY(I)=0.0
      DO 12 I=1,2
      DO 12 J=1,3
      CX(I)=CX(I)+X(I,J)/3.0
   12 CY(I)=CY(I)+Y(I,J)/3.0
      DO 20 I=1,3
      A1=1.0E10
      I1=I+1
      IF(X(1,I).EQ.X(1,I1))GO TO 25
```

C APPENDIX B: PROGRAM FOR GENERATING TRIANGLE INDEX LIST

```
      A1=(Y(1,I)-Y(1,I1))/(X(1,I)-X(1,I1))
   25 B1=Y(1,I)-A1*X(1,I)
      XSI=X(1,I)
      XMI=X(1,I1)
      IF(XSI.LE.XMI)GO TO 26
      XSI=X(1,I1)
      XMI=X(1,I)
   26 CONTINUE
      DO 30 J=1,3
      IPS=0
      DO 37 K=1,2
      KK=I+K-1
      DO 37 M=1,2
      MM=J+M-1
   37 IF(X(1,KK).EQ.X(2,MM).AND.Y(1,KK).EQ.Y(2,MM))IPS=1
      IF(IPS.GT.0)GO TO 30
      A2=1.0E10
      J1=J+1
      IF(X(2,J).EQ.X(2,J1))GO TO 35
      A2=(Y(2,J)-Y(2,J1))/(X(2,J)-X(2,J1))
   35 B2=Y(2,J)-A2*X(2,J)
      IF(A1.EQ.A2)GO TO 30
      XSJ=X(2,J)
      XMJ=X(2,J1)
      IF(XSJ.LE.XMJ)GO TO 36
      XSJ=X(2,J1)
      XMJ=X(2,J)
   36 CONTINUE
      XI=(B2-B1)/(A1-A2)
      IF(XI.GT.XSI.AND.XI.LT.XMI.AND.XI.GT.XSJ.AND.XI.LT.XMJ)IWF=1
      IF(PRC.GT.0.0)WRITE(6,100)I,J,IWF,A1,B1,A2,B2,XI
  100 FORMAT(3I5,5F10.2)
      IF(IWF.GT.0)GO TO 99
   30 CONTINUE
   20 CONTINUE
      DO 40 K=1,2
      KK=2
      IF(K.EQ.2)KK=1
      ICK=0
      DO 50 I=1,3
      I1=I+1
      XW(1)=X(K,I)
```

```
C APPENDIX B: PROGRAM FOR GENERATING TRIANGLE INDEX LIST


      YW(1)=Y(K,I)
      XW(2)=X(K,I1)
      YW(2)=Y(K,I1)
      XW(3)=CX(KK)
      YW(3)=CY(KK)
      CALL ARP(XW,YW,AR,P)
   50 IF(AR.GT.0.0)ICK=ICK+1
      IF(ICK.GE.3)IWF=1
      IF(IWF.GT.0)GO TO 99
   40 CONTINUE
   99 RETURN
      END
```

Appendix C

Solution of Spectral Integrals

Equation 113 is solved by recognizing that the lnk spectrum (eq. 55) is even in k_i so that any odd powers of k_i will integrate to zero. Substituting in

$$u_i = \lambda k_i\,,\ \varepsilon = \alpha_L / \lambda,\ \mathcal{K} = \alpha_T / \alpha_L$$

$$I_1 = \int_{-\infty}^{\infty} \frac{(b_1+b_2)\left(1-\dfrac{u_1^2}{u^2}\right)\dfrac{\varepsilon}{\lambda}\,(u_1^2 + \mathcal{K}\,(u_2^2+u_3^2))\,\dfrac{S_{ff}}{\lambda^3}\,dk}{\gamma\left[\dfrac{u_1^2}{\lambda^2}+\dfrac{\varepsilon}{\lambda^2}\,(u_1^2+\mathcal{K}(u_2^2+u_3^2))^2\right]} \qquad \text{(C1)}$$

Now substitute in $v = u_3/\varepsilon$,

$$I_1 = \int_{-\infty}^{\infty} \frac{(b_1+b_2)\left(1-\dfrac{\varepsilon^2 v^2}{u^2}\right)(v^2\varepsilon^2 + \mathcal{K}(u_2^2+u_3^2))\,S_{ff}\,dv\,du_2\,du_3}{\gamma\lambda^2\,(v^2 + (\varepsilon^2 v^2 + \mathcal{K}(u_2^2+u_3^2))^2)} \qquad \text{(C2)}$$

The ratio of the local dispersivity to the lnk correlation scale is now allowed to go to zero ($\varepsilon \to 0$) and the substitution $a = \mathcal{K}\,(u_2^2 + u_3^2)$ is made:

$$I_1 = \int_{-\infty}^{\infty} \frac{(b_1+b_2)a\ S_{ff}(o, u_2, u_3)dv\ du_2\ du3}{\gamma\lambda^2(v^2+a^2)} \qquad (C3)$$

The first integration over v (reintroducing k_2 and k_3) produces:

$$I_1 = \iint_{-\infty}^{\infty} \frac{\pi(b_1+b_2)\ S_{ff}\,(o, k_2, k_3)\,dk_2\,dk_3}{\gamma} \qquad (C4)$$

Substituting in equation 55 for S_{ff} and converting to polar coordinates:

$$k_2 = r\cos\phi,\ k_3 = r\sin\phi,\ k^2 = r^2\ dk_2dk_3 = rdrd\phi$$

produces:

$$I_1 = \frac{\pi(b_1+b_2)}{\gamma} \int_0^{2\pi}\int_0^{\infty} \frac{\sigma_f^2\,\lambda^3\,rdr\ d\phi}{\pi^2(1+\lambda^2r^2)} \qquad (C5)$$

Integrating over r:

$$\int_o^{\infty} \frac{rdr}{(1+\lambda^2r^2)} = \frac{1}{2\lambda^2}, \text{ and } \phi : \int_o^{2\pi} d\phi = 2\pi,$$

produces the result:

$$I_1 = \frac{(b_1+b_2)\sigma_f^2\lambda}{\gamma} \qquad (C6)$$

Appendix D

Relationship between Hydraulic Conductivity and the Distribution Coefficient using Spherical Grains

If it is assumed that the solid matrix of an aquifer is composed of uniform spheres, with constant surface properties, the slope of the ln K - K_d relationship can be inferred. Hydraulic conductivity is assumed to be proportional to the square of the grain radius (r) (Freeze and Cherry, 1979):

$$K = Ar^2 , \tag{D1}$$

and the natural logarithm is:

$$\ln K = \ln A + 2 \ln r \tag{D2}$$

where A is a constant with units of (length • time)$^{-1}$.

If porosity is assumed constant then the ratio of the volume of grains to the volume of porous media is a constant:

$$n = \frac{\text{volume of grains}}{\text{volume of porous media}} = \frac{ng \cdot \text{volume of one grain}}{\text{volume of porous media}} \tag{D3}$$

where ng is the number of grains in the volume of porous media.

The amount of solute adsorption to the solid phase is assumed to be proportional to the surface area per volume of porous media:

$$S = W \cdot \frac{(\text{surface area})}{(\text{volume of porous media})} \cdot C \qquad \text{(D4)}$$

where

S is the concentration on the solid,

W is a constant, and

C is the concentration of the solute.

The distribution coefficient, K_d, is then defined:

$$K_d = \frac{W \cdot (\text{surface area})}{(\text{volume of porous media})}, \qquad \text{(D5)}$$

and (D3) substituted in:

$$K_d = \frac{W \cdot ng \cdot (\text{surface area of one grain})}{ng \cdot (\text{volume of one grain})/n}. \qquad \text{(D6)}$$

Substituting in the quantities for area and volumes results in the relation between K_d and r:

$$K_d = \frac{W\, ng\, 4\pi r^2}{ng\, \frac{4}{3}\pi r^3/n} = \frac{3Wn}{r}. \qquad \text{(D7)}$$

Taking the derivatives with respect to radius for equations D2 and D7 results in the derivative of K_d with respect to hydraulic conductivity:

$$\frac{d(K_d)}{d(\ln K)} = \frac{d(K_d)/dr}{d(\ln K)/dr} = \frac{-3Wn/r^2}{2/r} = \frac{-3Wn}{2r}. \qquad \text{(D8)}$$

By substituting the value of K_d back into equation D8 it is possible to define the derivative in terms of K_d:

$$\frac{d(K_d)}{d(\ln K)} = \frac{-K_d}{2} . \qquad \text{(D9)}$$

This analysis indicates that the slope of the lnK, K_d relationship should be negative in sign and related to the value of K_d. Because of the limitations of the assumptions involved an empirical relationship for lnK and K_d would likely give better field results for an application to field conditions.